# Modelling Stress Accumulation and Dissipation in Subducting Lithosphere and the Origin of Double and Triple Seismic Zones

Thesis submitted in accordance with the requirements of the University of Liverpool for the degree of Doctor in Philosophy by Anna Fry

October 2010

This thesis is dedicated to my family.

**Abstract**

Stress accumulation in the subducting lithosphere is responsible for Wadati-Benioff zone seismicity observed worldwide. Stresses are generated by mechanisms such as slab pull and slab resistance, bending and unbending, thermal expansion, and the basalt to eclogite phase transformation. These in turn are influenced by plate age, dip angle, plate velocity, rollback velocity, and slab curvature. The resulting patterns of seismicity are complex and double or triple seismic zones are often observed. To investigate the accumulation and dissipation of stress in the subducting lithosphere that generates such multi-layered features, I use two independent but complementary models.

The 2D model uses coupled finite element thermal and mechanical solvers, and a viscous rheology with a yield stress. The model has kinematic boundary conditions, but dynamic driving forces. I investigate the development of stress within the lithosphere and its sensitivity to slab age, megathrust geometry and dip, plate velocity, and rollback velocity. The model generates realistic magnitudes of trench dynamic topography, and predicts double and triple layers of stress within the slab that correlate to observations.

The 1D model represents a vertical segment of oceanic lithosphere, following it in a Lagrangian manner as it is subducted. The rheology is viscoelastic, and includes temperature and stress dependence, stress memory, and stress advection. A simple finite difference scheme couples this viscoelasticity with kinematic thermal conditions. The model determines stresses arising from slab pull, slab bending and unbending, the basalt to eclogite transition and thermal stresses, and predicts downdip bands of tensile and compressive stress consistent with observations of double and triple seismic zones.

Together, the models investigate the development of stresses in the subducting lithosphere and their sensitivity to various parameters. Both models are applied to the specific examples of north Chile and northeast Japan, generating stresses using estimated parameter values. Both models predict intermediate depth seismicity to be dominated by slab unbending, due either to prior bending, or to circulation in the mantle wedge. Both models also predict an additional band of tension in the slab crust due to decoupling or phase transition, which can occur at intermediate depths. These results are in agreement with the majority of observation of double and triple Wadati-Benioff zones; double seismic zones that have an alternative stress pattern may show the top two, or top and bottom, bands of a triple layered structure.

# Contents

# Acknowledgments

I could not have completed this work without the help and support of a number of people.

I have been immensely fortunate to have Nick Kusznir and Andreas Rietbrock as my PhD supervisors. Nick has been an endless source of enthusiasm and encouragement, and Andreas has provided some excellent discussions, and the opportunity for some field experience in Sumatra.

I'd like to thank the many other members of staff and post-grads in the department for all the favours I've asked over the years, as well as all the members of my research group, past and present. Special thanks also go to my colleagues in Oslo, particularly Marcin who has been enormously generous with his time and expertise.

I could not have undertaken this PhD without financial support from NERC, and I owe them a huge debt of gratitude that I was able to continue my education this far.

And finally, I am eternally grateful to all the members of my extended family, who have kept me sane with their love, support, and cups of tea. Especially Rod and Poppy, who have listened patiently to more monologues about subduction than I care to remember.

I hereby declare that the work contained in this thesis is my own, except where due reference is made.

# Chapter 1

# Introduction

Nearly a hundred years have passed since the first observations of Wadati-Benioff zone seismicity, yet the mechanisms of stress accumulation and dissipation that generate such seismicity remain enigmatic. The subduction of the oceanic plate into the mantle causes seismicity by frictional sliding at shallow depths, but this failure is inhibited by high confining pressures below approximately 50km depth. The causes of seismicity beneath this depth has subsequently been the subject of much speculation.

The earthquakes caused by subduction of the oceanic lithosphere are among the most devastating natural disasters known to man, costing dearly in terms of destruction and loss of life. The better the causes and triggers for seismicity are understood, the more hope there is for developing accurate predictions and early warning systems to mitigate such catastrophes.

Understanding what processes cause Wadati-Benioff zone seismicity is also an important facet of our knowledge about the Earth and its structure. Seismicity is the end result of a multitude of interacting components, including force balance, rheology, driving conditions, temperature, and mineralogy, so investigation in one area of research such as subduction zone seismicity contributes to the understanding of the Earth system as a whole.

Improvements in pinpointing the location of earthquakes has revealed that a number of subduction zones worldwide have their seismicity organised into two or three distinct bands (Hasegawa et al., 1978; Igarashi et al., 2001). Focal mechanisms indicate that the stresses in these bands are usually aligned downdip, and are of opposite polarity. The most common stress pattern of double Wadati-Benioff zones is compression over tension (Kao and Rau, 1999; Brudzinski et al., 2007), although observations from some seismic zones show tension over compression (Comte and Suarez, 1994) or tension in both bands (Rietbrock and Waldhauser, 2004; Brudzinski et al., 2007). The

seismicity beneath northeast Japan shows a triple layer structure, where the common double seismic zone pattern of compression over tension has an additional layer of tensile stresses located in the slab crust (Igarashi et al., 2001). The existence of these multi-layered structures under so many different conditions indicates that they are a fundamental feature of subduction.

There are many theories about the causes of double and triple seismic zones, based on the various possible mechanisms of stress accumulation and dissipation. Stresses are generated by body forces and deformation in the slab, including buoyancy, bending, and changes in volume with temperature or mineralogy, and the viscoelasticity of the slab means the stresses accumulate through stress memory and are advected with the slab. Earthquakes are generated when these stresses are dissipated seismically, via mechanisms such as dehydration (Green and Houston, 1995; Kirby et al., 1996), shear instabilities (Ogawa, 1987; Karato et al., 2001), or transformational faulting (Kirby, 1987; Green and Burnley, 1989). Any hypothesis about the causes of Wadati-Benioff zone seismicity also needs to account for the separation between the bands of stress and the restriction of seismicity to intermediate depths. This is often attributed to the thermal state of the slab (House and Jacob, 1982), but there remains disagreement about the details (Molnar et al., 1979; Wiens and Stein, 1983; Kirby, 1995).

The accumulation of stresses in the subducting lithosphere leads to Wadati-Benioff zone seismicity; these stresses are generated by slab pull and slab resistance, bending and unbending, thermal expansion, and the basalt to eclogite transition. These are in turn influenced by subduction convergence rate, dip angle, plate age, rollback, curvature rate, temperature, mantle viscosity, and deeper phase transitions. To investigate how these stresses develop and interact, and how such stress interactions lead to double and triple seismic zones, I have developed two complementary computational models.

The first model is two-dimensional, covering a domain 6,000km wide and extending from the Earth's surface to the core-mantle boundary. The rheology is dependent on temperature and stress, and incorporates diffusion creep, dislocation creep, and a yield stress. Kinematic boundary conditions such as convergence rate and rollback are externally applied, but temperature-dependent viscosity and density control the system internally.

The second model is one-dimensional and represents a vertical slice of lithosphere, following its development in a Lagrangian manner as it is subducted. It has a viscoelastic rheology which is temperature and stress dependent, and includes stress memory and stress advection. The model calculates stresses arising from slab pull, bending and unbending, thermal expansion and the basalt-to-eclogite transition, and

the redistribution of stresses due to creep and brittle failure.

Using these two models I investigate the development of the subducting lithosphere, looking at how double and triple layers of stress can form in the slab. The sensitivity of the models to the parameters of slab age, dip angle, plate velocity, roll-back velocity, and slab curvature is explored, looking at how variations in these affects outputs such as stress pattern, slab shape, and dynamic topography. Then both models are applied to the case studies of north Chile and northeast Japan to try and replicate observations. Using the models to predict stresses and comparing these results to observations, the causes of double and triple Wadati-Benioff zones are explored.

# Chapter 2

# Seismicity in Wadati-Benioff Zones: background and context

## 2.1 Introduction

Two historic papers by Wadati in the early twentieth century provided the foundations for research into the field of subduction zone earthquakes. In the first paper, seismic observations and geometry were used to show that some earthquakes recorded at stations in Japan originated hundreds of kilometers below the surface (Wadati, 1928). In the second paper, he demonstrated that this seismic activity occurred in sloping planes reaching from the ocean trenches down to 660km (Wadati, 1935). Twenty years later in America, drawing on the database of seismic events published by Gutenberg and Richter, Benioff also plotted earthquakes as a function of depth, revealing the same sloping structures extending deep into the earth (Benioff, 1954) as shown in figure 2.1. These bands of seismicity are now known as Wadati-Benioff Seismic Zones. Despite these zones being identified and named, their significance was not immediately realised.

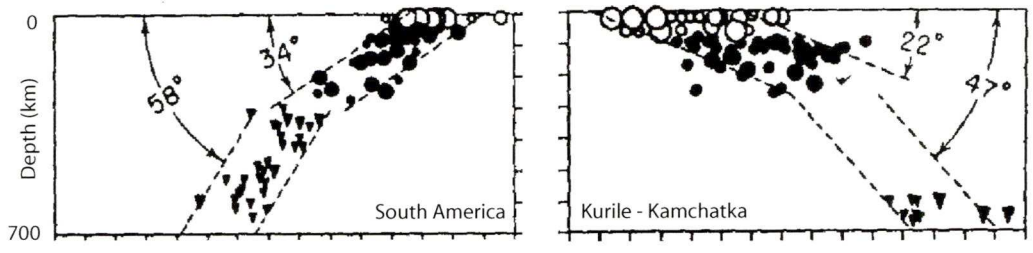


Figure 2.1: Wadati-Benioff zones from South America and Kuril-Kamchatka (Benioff, 1954)

The 1964 earthquake in Alaska was the largest earthquake ever to be recorded in America. An uplift of of several metres over an area of 60,000 square kilometers gave one of the first solid pieces of evidence for the underthrusting of the oceanic plate beneath the continental plate (Plafker, 1965). Further work into the location of earthquake hypocentres confirmed that the observed seismicity was indicative of a large scale structure reaching down more than 650km below the Earth's surface (Sykes, 1966).

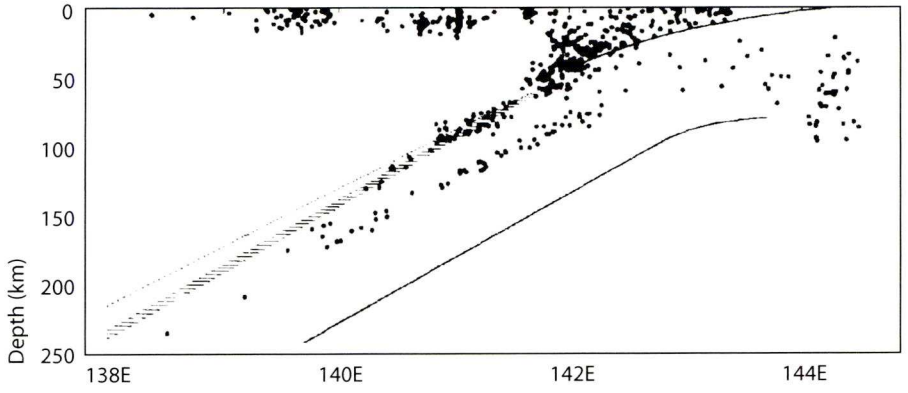


Figure 2.2: Seismicity defining a double-layered Wadati-Benioff zone in Tohoku, north-east Japan (Hasegawa et al., 1978)

Improvements in observational techniques led to better resolution of earthquake hypocentres, and more details of the seismic zone became clear. The improved focal mechanism plots revealed that some Wadati-Benioff zones were in fact split into two layers, as shown in figure 2.2 (Hasegawa et al., 1978), where the upper layer is at the top of the slab, and the lower layer is deeper in the slab and runs parallel. Stress analyses show that in the majority of these double seismic zones the upper plane is in downdip compression and the lower layer in is downdip tension (Fujita and Kanamori, 1981). Further improvements in focal mechanism resolution have revealed the double seismic zone beneath Japan to be a triple seismic zone, as shown in figure 2.3, where an additional layer of downdip tension is apparent at the top of the slab (Igarashi et al., 2001). The origin of these double and triple Wadati-Benioff Zones is still unclear, and this thesis is presented as a numerical investigation into the stress accumulation and dissipation leading to such seismicity.

## 2.2 Stress patterns in seismic zones

The direct cause of seismicity in the subduction zones is the release of stresses in the subducting slab. At convergent plate boundaries, the stick-slip movement of one plate

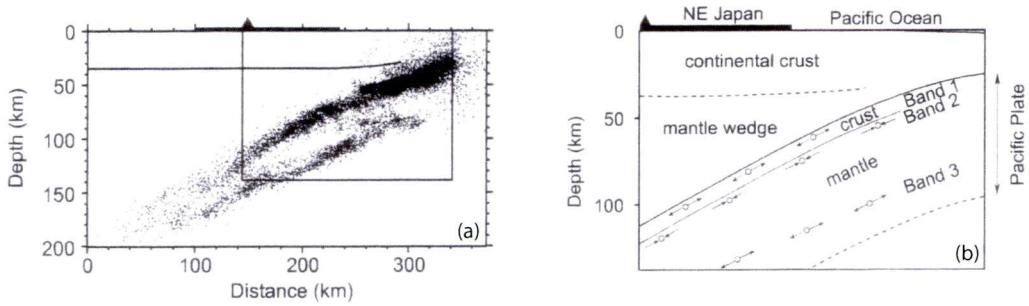


Figure 2.3: Triple-layered Wadati-Benioff zone in north-east Japan (Igarashi et al., 2001; Wang, 2002).

against another causes earthquakes at the surface; however, below about 50km depth lithostatic pressure is too high to permit any further frictional sliding. Yet seismicity in subduction zones extends from the surface down to nearly 700km, demanding alternative explanations. Slab pull, slab resistance, bending, unbending, thermal stresses and metamorphism have all been cited as means of generating stress in the slab; dehydration, thermal instabilities and transformational faulting have been proposed as ways of producing seismicity from these stresses. These are summarised in table 2.1.

| Stress accumulating mechanisms | Stress dissipating mechanisms |
|---|---|
| Slab pull, slab resistance | Dehydration |
| Bending, unbending | Thermal instabilities |
| Thermal stresses | Transformational faulting |
| Metamorphism | |

Table 2.1: Stress accumulating and dissipating mechanisms

Early analyses of focal mechanisms suggested that slabs sinking under their own weight tend to have stresses in downdip tension until they reach greater depths, whereupon resistance is encountered and the stresses become downdip compression, as shown in figure 2.4 (Isacks and Molnar, 1971; Chen et al., 2004). Further investigation along these lines supported these observations, showing that compressional stress in the slab increases with convergence rate, and decreases with slab age. Many subduction zones that were recognised as having 'mixed' stress states were revealed to be double and triple seismic zones by improved observations (Fujita and Kanamori, 1981).

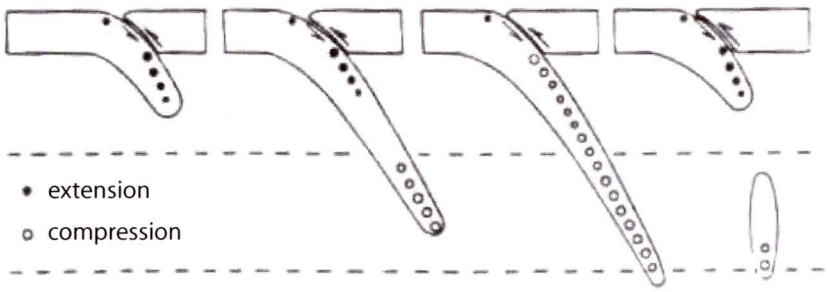


Figure 2.4: Stress states indicating stage of subduction (Isacks and Molnar, 1971)

### 2.2.1 Stresses within double and triple seismic zones

Most double seismic zones follow the same stress pattern: downdip compression in the upper band of seismicity, and downdip tension in the lower band (Sleep, 1979; Fujita and Kanamori, 1981), for example, Japan (Hasegawa et al., 1978), Tonga (Kawakatsu, 1986), Mariana (Samowitz and Forsyth, 1981), Aleutians (Engdahl and Scholz, 1977), Kuril (Kao and Chen, 1994) and Kamchatka (Gorbatov et al., 1994).

| Stress pattern | Region |
|---|---|
| Downdip compression in upper band, downdip tension in lower band | NE Japan<br>Tonga<br>Mariana<br>Kuril<br>Kamchatka<br>N Chile |
| Downdip tension in both planes | Alaska<br>Taiwan<br>Mendocino<br>New Zealand<br>New Britain<br>N Chile |

Table 2.2: Stress patterns in different double seismic zones

However, there are a number of double seismic zones which are characterised by downdip tension at intermediate depths for both upper and lower seismic bands, including Alaska (Ratchkovsky et al., 1997), Taiwan (Kao and Rau, 1999), New Zealand (Reyners and Robinson, 1997), New Britain McGuire and Wiens (1995), and Mendocino (Smith et al., 1993).

Additionally, the subduction zone beneath the central Andes has been reported as having a stress pattern of tension over compression (Comte and Suarez, 1994) or

extension in both planes (Rietbrock and Waldhauser, 2004). The occurrence of double seismic zones despite a variety of stress patterns indicates a trigger for seismicity that exists regardless of stress state. These results are summarised in table 2.2.

The seismic zone of northeast Japan shows three distinct bands of seismicity: normal faulting in the very top band, downdip compression 5-20km below, and downdip tension 40km below that (Igarashi et al., 2001). Any explanation of the origins of double seismic zones needs to be able to account for the differences between observed stress patterns, and the rarer occurrence of triple seismic zones.

## 2.3 The depth dependency of seismicity

The mechanisms of stress accumulation and dissipation in the subduction zone are heavily dependent on ambient conditions of pressure and temperature, which are primarily controlled by depth. Subduction zones are usually divided into three depth ranges: shallow (0-50km), intermediate (50-300km), and deep (300-700km). In a plot of earthquake frequency against depth (figure 2.5), there is a peak at shallow depths, followed by a decrease in seismicity through intermediate depths to a minimum at 300km, then a small resurgence in activity peaking at about 550km.

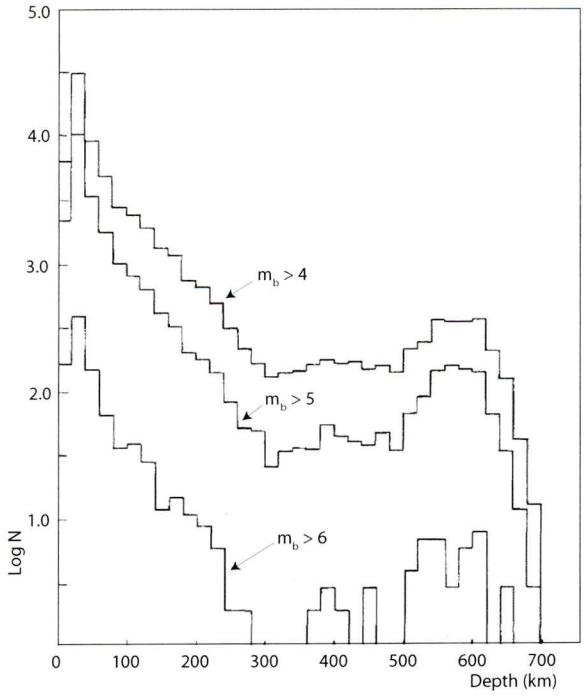


Figure 2.5: The relationship between earthquake frequency and depth (Vassiliou et al., 1984)

At shallow depths, seismicity is due to stick-slip behaviour between the downgoing and overriding plates. This frictional sliding ends when the ambient temperature and pressure become too high, at about 50km; any seismicity below this point is due to failure within the subducting slab (Kirby et al., 1996). Double seismic zones are principally a feature of intermediate depth seismicity, although some have been reported to extend as deep as 460km in exceptionally cold slabs (Wiens et al., 1993).

## 2.4 The role of temperature in seismicity

The lithosphere is created from hot upwelling material at mid-ocean ridges and subsequently cools as it ages and moves away from the ridge. At the point of subduction, the older the slab is, the colder it will be. Figure 2.6 shows some typical geotherms for the oceanic lithosphere. As it subducts back into the hot mantle, the slab will begin to heat up through conduction. The faster the cool material is advected into the mantle, the deeper the cold slab geotherms will penetrate into the mantle. The temperature of the subduction zone is therefore dominated by the two parameters of plate age and subduction velocity (McKenzie, 1969; Molnar et al., 1979).

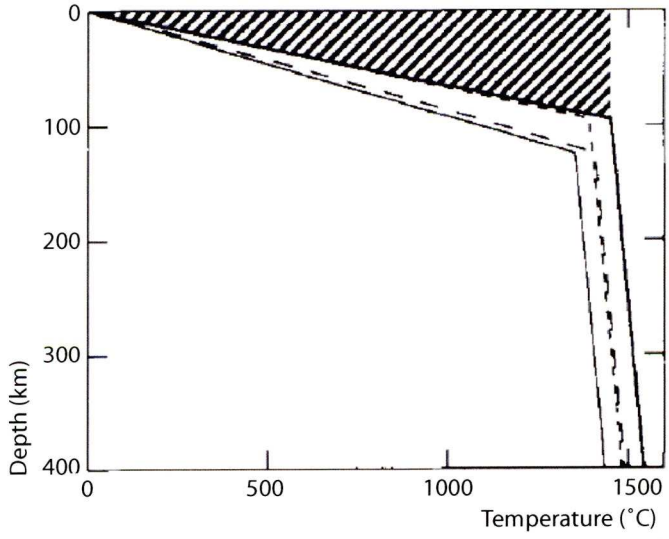


Figure 2.6: A range of oceanic lithosphere geotherms from the models of Stein and Stein (1992). The upper solid line is for a lithosphere of approximately 100Myr, the lower solid line for 150Myr

A plot of the isotherms across the subduction zone indicates a strong relationship between seismicity and thermal structure (figure 2.7). Intermediate depth seismicity only occurs in regions which are cooler than about 600°C (Wortel, 1982; Chen and

Molnar, 1983) or 800°C (Wiens and Stein, 1983). The origin of this temperature constraint upon the regions of seismicity is still controversial. It has been proposed that this temperature is the point at which the material enters the viscous regime where it is unable to retain stresses (Molnar et al., 1979), or is rapidly weakened (Wiens and Stein, 1983). Alternatively, it marks the maximum temperature of phase transformation or dehydration (Kirby, 1995).

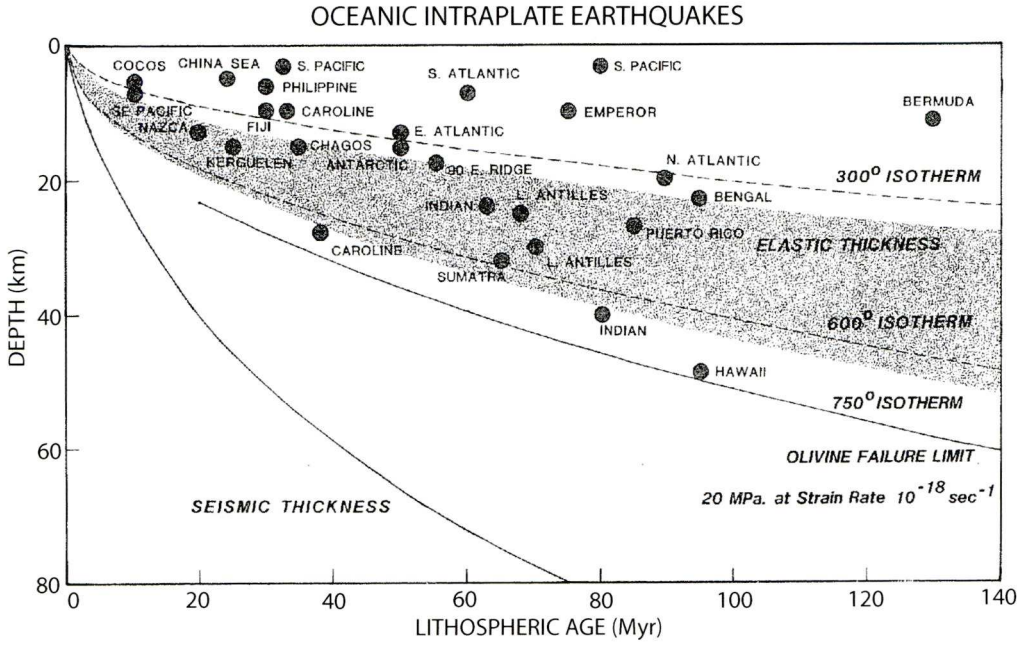


Figure 2.7: The relationship between plate age, temperature, and maximum depth of seismicity. (Wiens and Stein, 1983)

Double seismic zones appear on either side of the cold core of the subducting slab and converge at depth, which coincides well with the slab isotherms. There is also a relationship between the separation of the bands and the age of the plate, shown in figure 2.8 (Brudzinski et al., 2007), due to the dependency of the thermal state of the slab upon the plate age at the time of subduction.

## 2.5 Stress accumulation in the subducting slab

### 2.5.1 Slab pull and slab resistance

The subducting slab is colder and thus denser than the mantle, and this negative buoyancy makes the slab sink; this downward force is known as slab pull (McKenzie, 1969).

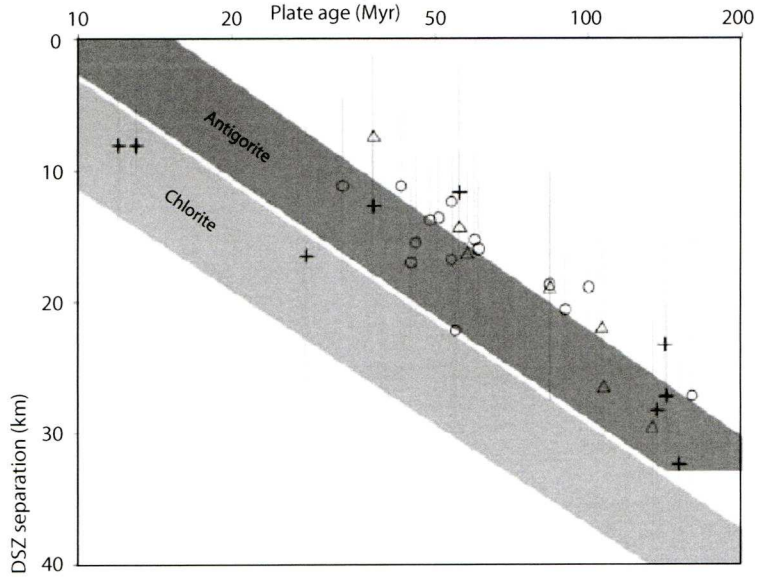


Figure 2.8: The relationship between plate age and double seismic zone separation (Brudzinski et al., 2007)

If the mineralogy of the slab changes through metamorphism, the density and therefore the slab pull is affected too.

Forsyth and Uyeda (1975) find slab pull to be the most important force acting on the slab, followed by its opposing force, slab resistance. Slab resistance arises from the increase in mantle viscosity with depth, making it increasingly difficult for the slab to subduct.

### 2.5.2 Bending and unbending in the slab

The subducting slab is required to bend at the surface so that subduction can begin; it then unbends at depth. The large stresses this causes have frequently been cited as the origins of double Wadati-Benioff zone seismicity as the stresses associated with unbending - compression on top, extension underneath - correlate to the stress patterns observed in most double seismic zones (Engdahl and Scholz, 1977). However, the seismic zone is seen to continue even after the slab has finished unbending (Fujita and Kanamori, 1981), but if the slab is viscoelastic and retains a stress memory this is still a plausible mechanism for seismicity deep in the mantle (Wang, 2002).

### 2.5.3 Thermal stresses in the slab

As soon as the cold slab enters the mantle, it begins to heat up. The expansion of the material due to the increase in temperature induces thermal strains, and the non-

uniformity of this expansion causes deformation.

The thermal structure of the subduction zone is also important in terms of mineralogy. Temperature and pressure govern mineral density, grain size, and transformation, which directly affects viscosity and density, and therefore buoyancy and slab pull (Guest et al., 2003).

The termination of seismicity at depth and the merging of the layers in a double seismic zone has been attributed to thermal stresses which are dependent upon slab temperatures (House and Jacob, 1982), but it seems that the associated strain rates alone are too small to account for the stress release observed in double seismic zones (Wang, 2002).

### 2.5.4 Metamorphism in the slab

The metamorphism of minerals in the subducting slab can cause stresses in two different ways. First, phase changes such as the basalt to eclogite transition in the subducting oceanic crust are associated with a decrease in volume, which in a continuous medium will lead to deformation, inducing deviatoric tension in the crust and deviatoric compression in the lithosphere. Second, a decrease in volume implies an increase in density, increasing slab pull (Kirby et al., 1996).

## 2.6 Stress dissipation in the subducting slab

Various mechanisms have been invoked to explain the observed stress patterns in double seismic zones. The 'classic' stress pattern of compression in the upper band and tension in the lower band has often been attributed to the unbending of the slab (Sleep, 1979) following the severe bending at subduction initiation. The transition of basalt to eclogite would induce tension in the crust and compression in the mantle (Kirby et al., 1996). Similarly, the phase transformation of olivine to spinel to perovskite would induce localised tension due to the associated volumetric reduction (Guest et al., 2003). If subduction zone seismicity extends to great depths, it is often associated with downdip compression due to the resistance of the highly viscous lower mantle; conversely, if the seismicity is shallow or discontinuous, it is usually associated with downdip tension due to the negative buoyancy of the slab (Isacks and Molnar, 1971; Chen et al., 2004). But these are all mechanisms of stress accumulation and each is insufficient to cause observed seismicity in the slab; with no other mechanism involved they would simply produce ductile deformation.

### 2.6.1 Transformational faulting

A change in the temperature and pressure conditions of a mineral often means a change in phase, for example, the transformation of olivine to wadsleyite at the 410km discontinuity. Observations of transformations in ice and tremolite indicate that in certain circumstances this transformation may occur instantaneously with an associated stress drop, which has become known as transformational faulting (Kirby, 1987). Since these transformations are facilitated rather than inhibited by high pressure it has been suggested that transformational faulting could explain intermediate and deep seismicity.

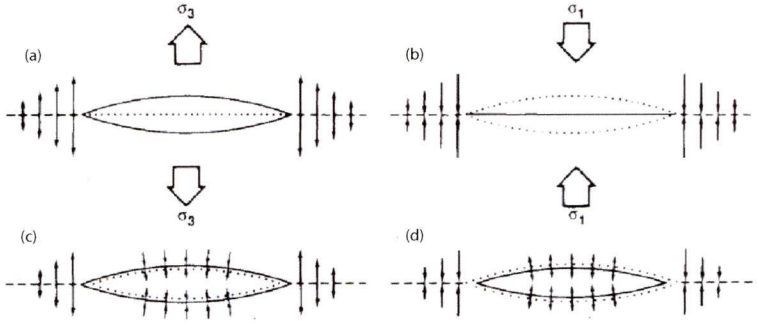


Figure 2.9: Comparison of mode I cracks and anticracks. The diagram shows (a) a crack, (b) an empty anticrack, (c) transformation of a material involving an increase in volume (d) transformation of material involving a decrease in volume, producing a filled anticrack (Green and Burnley, 1989)

The prerequisite for transformational faulting is the existence of a meta-stable olivine wedge at the core of the cold subducting slab (Kirby et al., 1991). The low temperature means the olivine is transported deeper than would be stable at equilibrium temperatures, but as it warms up it begins to change phase (Green and Houston, 1995). Under this hypothesis, the end of seismicity at 660km is accounted for by end of transformation of olivine to spinel (Kirby, 1995).

In the initiation of transformational faulting, lenses of the new denser phase form within the old phase; called anticracks, they have a similar geometry but opposite stress sign to cracks, as shown in figure 2.9. Instability comes about through a high density of anticracks, leading to failure if the anticracks join up (figure 2.10), if heat is released and drives the reaction (Green and Burnley, 1989), or if the transformation propagates at the lens tips (Kirby, 1987).

Transformational faulting has been claimed to be the source of intermediate depth seismicity (Kao and Liu, 1995), but other analyses show that of the two possible reactions this would involve, the transformation of aluminous enstatite occurs too slowly,

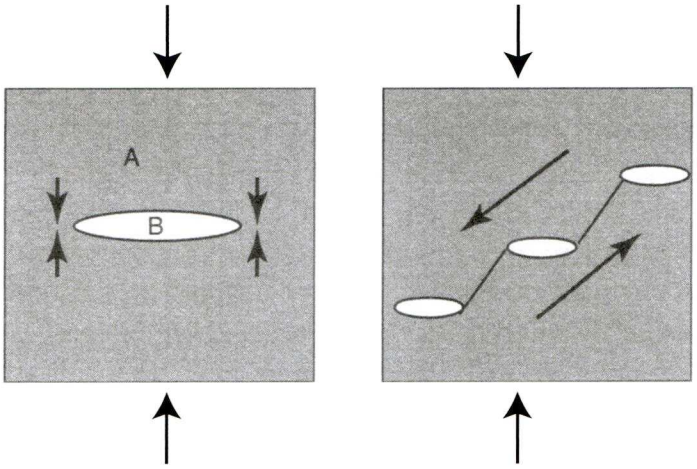


Figure 2.10: Transformational faulting (Karato, 2003).

and the transformation of olivine occurs at too great a depth (Hacker et al., 2003). Aftershocks and repeating seismicity are difficult to explain with transformational faulting, since transformation can only occur once (Karato et al., 2001); there is also evidence of aftershocks occurring beyond the bounds of the predicted olivine wedge (Wiens et al., 1994).

### 2.6.2 Dehydration

Dehydration embrittlement is a mechanism which is proposed to facilitate brittle faulting at intermediate depths. When hydrated minerals in the oceanic lithosphere are subducted, at some point the temperature and pressure conditions will cause them to dehydrate. The fluid released in the reaction increases pore pressure, reducing the amount of shear stress needed for the rock to fail (Raleigh, 1967), enabling brittle faulting under conditions that might otherwise be expected to produce ductile flow (Green and Houston, 1995; Kirby et al., 1996). This can be written

$$\tau = \tau_0 + \mu(\sigma_n - P) \tag{2.1}$$

where $\tau$ is shear stress at failure, $\tau_0$ is cohesive stress, $\mu$ is the coefficient of friction, $\sigma_n$ is normal stress, and P is pore pressure; hence when normal stress approaches the pore pressure, the shear stress tends towards the cohesive stress (Raleigh and Paterson, 1965; II, 2007).

The dehydration reaction occurring in the upper layer of double seismic zones is usually ascribed to the basalt to eclogite transition (Kirby et al., 1996; Hacker et al.,

2003; Brudzinski et al., 2007). In the lower layer, the reaction has been suggested to be the dehydration of antigorite (Peacock, 2001; Brudzinski et al., 2007), chlorite (Hacker et al., 2003) or mantle serpentine (Hacker et al., 2003; Yamasaki and Seno, 2003). But the increase in pore pressure in itself is not enough to cause seismicity; it is merely a mechanism which allows stresses to cause brittle failure rather than ductile deformation.

Kirby et al. (1996) attributes the upper band of double seismic zones to the dehydration of basalt to eclogite, which increases pore pressure and decreases volume, causing extensional stresses in the crust and compression beneath. Wang (2002) proposes that this metamorphism is the cause of the very top band in triple seismic zones, and the lower two bands (the two bands seen in double seismic zones) are due to unbending in the presence of dehydration, producing a band of compression above a band of tension in accordance with the majority of observations. Rietbrock and Waldhauser (2004) cite the interaction of slab pull with dehydration to be the cause of the double seismic zone beneath the central Andes, which shows downdip extension in both layers.

Dorbath et al. (2008) has another interpretation for the lower band, proposing that tensile stresses below the neutral fibre of the slab force fluids upwards but they are unable to enter the compressive region above, therefore they collect at the neutral fibre, causing seismicity that can show either extension or compression depending on the local conditions, particularly the radius of curvature. However, by definition the neutral fibre is a minimum in the local stress regime, a condition unlikely to promote seismicity.

One of the main difficulties of the dehydration hypothesis is how the minerals are able to be hydrated in the first place. The hydration of minerals in the shallow oceanic crust likely occurs through exposure to sea water through pre-subduction faulting (Kirby, 1995); however, the hydration of minerals 40km deeper in the oceanic lithosphere is more difficult to explain. There are two main proposals: deep normal faulting at the site of slab bending allows seawater to penetrate (Peacock, 2001; Kirby, 1995), or the slab is hydrated from beneath when it passes over a hydrated plume (Seno and Yamanaka, 1996), although both are theories unsupported by observations at this point.

### 2.6.3 Shear Instabilities

A third proposed mechanism for intermediate-depth seismicity is shear instability. In many materials, viscous heating and temperature-dependent viscosity positively in-

fluence each other (Schubert and Turcotte, 1972), causing deformation and possibly failure.

Catastrophic shearing is one way in which failure may occur; as a mechanism for stress release it originates from metallurgy, but it may be equally appropriate to apply it to the subducting lithosphere. Hobbs and Ord (1988) proposed that a critical temperature exists which defines the boundary between strain rate softening and strain rate hardening. Above the critical temperature the material is stable; below it, a fluctuating strain rate causes weakening of the material, leading to catastrophic plastic shear and causing earthquakes. Whether this is a plausible process under subduction zone conditions is as yet unconfirmed.

An alternative to plastic shearing is thermal runaway (Ogawa, 1987; Karato et al., 2001). High strain rates cause deformation, which releases heat in the material. However, if the heat is unable to diffuse away quickly enough, the rise in temperature lowers the viscosity, weakening the material and making it susceptible to further deformation. Above critical values of temperature and strain rate, this causes catastrophic failure (Kelemen and Hirth, 2007; John et al., 2009).

Thermal runaway instability is cited as the cause of the deep-focus 1994 Bolivian earthquake (Kanamori et al., 1998), but has also been applied to intermediate-depth seismicity. The presence of narrow veins of psudotachylite in blueschist to eclogite facies supports thermal runaway as a failure mechanism (Andersen et al., 2008); estimates of stress drops are in the right region, easily achieving 750MPa in a few milliseconds (John et al., 2009). The favourable conditions for such instabilities are large deformation in areas of high strength and low temperature, and so the presence of such conditions being found on either side of the cold core of the slab could implicate thermal runaway in the production of double seismic zones (Karato et al., 2001).

## 2.7 Investigating stress accumulation and dissipation with numerical modelling

One of the most useful methods of investigation into how stresses accumulate and dissipate within a subducting slab is through numerical modelling.

A study by Kaus et al. (2009) models the Taiwanese subduction zone to predict the long-term stress state. Although visco-elastic-plastic code is used, the elasticity is ignored, giving a visco-plastic rheology. Temperatures are taken from a static profile calculated from the cooling plate model. The bending of the subducting plate together with a weak lower crust explains the observed and predicted extensional stresses, but

a double stress zone was not reported.

Babeyko and Sobolev (2008) study the subduction zone with a 2D visco-elastic-plastic thermomechanical model. They use a 'zoomed-in' version of a previous model (Sobolev and Babeyko, 2005), where the domain is 350km wide by 160km deep with an increase in resolution to 5-10km. This small window, however, renders the model very much kinematic: boundary conditions at the edges of the domain are enforced to simulate plate advance via rollback and slab pull. With a combined rheology of diffusion, dislocation, and Peierls creep, double and triple bands of stress are observed with values up to 1.5GPa, which are attributed to slab unbending.

Similar kinematic boundary conditions are also applied to the restricted domain of Dorbath et al. (2008), which is 1800km wide by 300km deep and investigates the subduction of the Nazca plate beneath north Chile. They use an elastic-viscous-brittle rheology, and a stratified model with different parameters for each layer. A steady-state temperature condition is used, as the model only runs for 2Myr. The pressure and stress plots for the subducting slab show a double-layer feature, where both layers are attributed to dehydration. They locate the upper band in the slab crust and the lower band in the neutral core where they postulate fluids to accumulate, and predict lower plane seismicity to exhibit a range of focal mechanisms. However, some observations do not support these predictions (Rietbrock and Waldhauser, 2004), and the low stress regime of the neutral core seems unlikely to promote seismicity.

Cížková et al. (2007) use a two-dimensional visco-plastic model with a much larger domain of 2,000km deep, and either 5,000km or 12,000km wide. Subduction is initiated using kinematic boundary conditions until the slab tip reaches 200km, then the models are run with either kinematic or free slip surface conditions. In the free-slip models, the slab sinks at speeds around 10cm/yr until the tip passes the 410km phase transition, after which it moves at speeds up to 38cm/yr. In the interests of comparing similar models, these velocities are imposed onto the slab in the kinematic models, however, they are far beyond any slab velocities observed in nature. Double stress zones are apparent in all their models and attributed to slab bending and unbending together with buoyancy forces due to phase transitions, although these do not occur at intermediate depths and the pattern is dependent on the model setup. Decoupling between the subducting and overriding plates is achieved through the use of a free-slip fault from the surface to 150km depth, and a low viscosity slab crust leading into a low viscosity mantle wedge which ends at 190km depth. Although full decoupling occurs, enforcing such conditions to these depths may exert too great an influence on the slab behaviour.

These models all examine subduction in different ways to investigate the causes

of stress in the lithosphere, but only Cížková et al. (2007) evolves temperature with time. In a situation where the temperature-dependent rheology is so important, the temperature profile has a strong influence on the total stress state. Also, none of the models domains are deeper than 2,000km and some are as shallow as 160km, which is also likely have an effect on the predicted stresses through the interaction between the slab and the lower mantle. A model that can incorporate an evolving temperature structure into a thermo-mechanical model, and combine this with a realistic viscosity structure that reaches down to the core-mantle boundary would therefore be a useful addition to the current research outlined here.

# Chapter 3

# Modelling stress development in the subducting lithosphere using the two-dimensional viscous model

## 3.1 Introduction

Subduction zones are an integral part of the mantle convection system, and the source of the largest and most destructive earthquakes that occur; therefore an understanding of subduction zone initiation and development, and the processes that cause seismicity, is an important area of geodynamics. The physical inaccessibility and the large time scale of subduction mean that direct observations are limited, but numerical modelling can provide insights into physical processes that would otherwise be unobtainable.

The earliest subduction models used small domains with low resolution and simple numerical techniques (Andrews and Sleep, 1974; Toksoz and Hsui, 1978; Sleep, 1979). With the advancement of knowledge in geodynamics, increasingly sophisticated computational methods, and the rise in desktop computing power, modelling has become an important subset of subduction zone studies. Models can be formulated to study large-scale processes such as mantle convection (Tackley, 2000; Billen and Gurnis, 2001), or small-scale specifics like plate decoupling depths (Wada and Wang, 2009) and the effects of slab mineralogy (Marton et al., 1999).

The vast array of models used to study subduction zones is a testament to their usefulness. An overview of types of models is presented here, followed by the formulation of my two-dimensional viscous model, including a discussion of important parameters and their effects on subduction.

### 3.1.1 Types of model

Subduction zone models can be constructed to study a broad range of features, and there are certain fundamental parameters such as dimension, reference frame, driving force, and numerical method which will influence the modelling approach.

Subduction zone models are generally performed in one, two, or three dimensions, plus time. One dimensional models require many assumptions and give a limited picture of the system under consideration, but are usually the easiest to implement and therefore can often be performed at very high resolution and with a complex rheology. Three dimensional models can give the best representation of the system as a whole, but computing restrictions and mathematical complexities mean they are often restricted on resolution and rheology. Two dimensional models are a compromise; they can provide a good understanding of the subduction zone system but can still operate with high resolution and complex parameters.

Models are generally either Eulerian or Lagrangian. Models set in the Eulerian reference frame have boundary conditions that are usually easier to initialise, although creating truly free surfaces is a challenge (Schmeling et al., 2008). Models using the Lagrangian frame of reference are better for implementing a free surface, and more accurate at material boundaries because the mesh dividing up the model is advected with the material, so interpolating between time steps is not necessary (Deubelbeiss and Kaus, 2008). The drawback of the mesh advection is that remeshing is often needed, which is computationally expensive and introduces inaccuracy.

The choice between dynamic and kinematic models is also quite important. Kinematic models have imposed velocity conditions, driving the system according to predetermined parameters (Ponko and Peacock, 1995; Dorbath et al., 2008). Dynamic models impose the initial conditions for a system but then allow it to evolve in an internally self-consistent way (Gurnis and Hager, 1988; Capitanio et al., 2007). Han and Gurnis (1999) investigated these two types of model and found them to be very similar except that their kinematic model introduced significantly more work into the system, although other studies have not found such good agreement (Cížková et al., 2007).

One of the most popular numerical methods for solving the partial differential equations describing a model is the finite difference method (Majumdar, 2005; Guest et al., 2004; Dorbath et al., 2008). The domain is covered with a regular rectangular grid, specifying function values at each node. The difference between nodal values gives an approximation to the derivative, so the differential equations can be solved. This method is discussed in more detail in chapter 5. The other most common method is the finite element method (Zienkiewicz et al., 2005; Dabrowski et al., 2008; Capitanio et al., 2007). Here the domain is divided into discrete elements, each of which

obey global equations and local conditions, then the governing differential equations are solved for each element. This method is covered more fully in section 3.2.3.

The work discussed in this chapter and chapters 4, 7 and 8 is based on my two-dimensional thermo-mechanical finite element model, which is Eulerian and pseudo-dynamic. I first discuss the general theory behind the finite element method, then the details of the parameters I use in my model in the context of subduction modelling as a whole.

## 3.2 Thermo-viscous model formulation

### 3.2.1 Constitutive equations

The 2D thermo-viscous subduction model predicts the flow of a viscous, incompressible fluid that convects according to its temperature-dependent viscosity and density.

The thermal part of the model uses the thermal advection-diffusion equation, which can be written

$$\frac{\partial T}{\partial t} = \frac{1}{\rho C_p}\nabla.(k\nabla T) - \underline{v}.\nabla T \tag{3.1}$$

where T is temperature, $C_p$ is specific heat capacity, k is is thermal conductivity, and $v$ is the velocity vector (Turcotte and Schubert, 2002). The viscous flow of the material obeys the incompressibility condition, so the conservation of mass can be written

$$\nabla \cdot \underline{v} = 0 \tag{3.2}$$

Assuming a viscous rheology and force balance, the Navier-Stokes equation can be written as

$$\rho\left(\frac{\partial \underline{v}}{\partial t} + \underline{v}\cdot\nabla\underline{v}\right) = -\nabla P + \eta\nabla^2\underline{v} + F \tag{3.3}$$

where $\rho$ is density, $t$ is time, $v$ is velocity, $P$ is pressure, $\eta$ is viscosity, and $F$ is the body force.

The stress $\sigma$ in a fluid can be found from

$$\sigma = \eta\dot{\varepsilon} \tag{3.4}$$

where $\eta$ is the viscosity and $\dot{\varepsilon}$ is the strain rate. The total stress is the sum of the pressure and the deviatoric stresses,

$$\sigma_{ij} = \tau_{ij} - P_{ij}\delta_{ij} \tag{3.5}$$

where $\tau$ is deviatoric stress, and $\delta$ is the Kroneker delta. This can be written in tensor form as

$$\begin{bmatrix} \sigma_{xx} & \sigma_{xy} \\ \sigma_{yx} & \sigma_{yy} \end{bmatrix} = \begin{bmatrix} \tau_{xx} - P & \tau_{xy} \\ \tau_{yx} & \tau_{yy} - P \end{bmatrix} \tag{3.6}$$

The deviatoric stresses are found from the product of the viscosity and the rate of deformation,

$$\tau_{ij} = \eta D_{ij} \tag{3.7}$$

where

$$D_{ij} = \left( \frac{\partial u_i}{\partial x_j} + \frac{\partial u_j}{\partial x_i} \right) \tag{3.8}$$

In tensor form the deviatoric stresses can be written

$$\begin{bmatrix} \tau_{xx} & \tau_{xy} \\ \tau_{yx} & \tau_{yy} \end{bmatrix} = \begin{bmatrix} 2\eta \frac{\partial u}{\partial x} & \eta \left( \frac{\partial u}{\partial y} + \frac{\partial v}{\partial x} \right) \\ \eta \left( \frac{\partial u}{\partial y} + \frac{\partial v}{\partial x} \right) & 2\eta \frac{\partial v}{\partial y} \end{bmatrix} \tag{3.9}$$

The eigenvalues of the total stress tensor give the principal stresses, and the eigenvectors give the principal stress axes. These describe the stress ellipse, which can be translated back to Cartesian coordinates for convenience (figure 3.1).

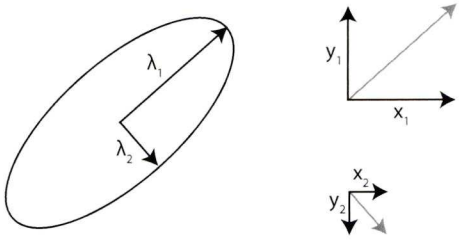


Figure 3.1: Prinicipalised stress axes describing the stress ellipse, and their conversion to Cartesian coordinates

### 3.2.2 Thermo-mechanical coupling

The two-dimensional model is based on a thermal finite element solver and a mechanical finite element solver coupled together as shown in figure 3.2.

The thermal solver determines the new temperatures, which are used to calculate temperature-dependent densities and viscosities. These densities and viscosities are passed to the mechanical solver, which uses them to calculate pressure and velocity. These velocities are used to update the domain by advecting the temperature field,

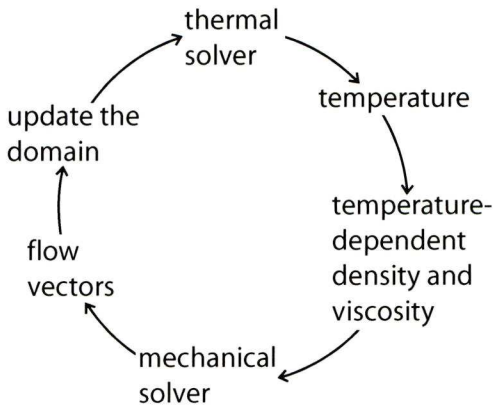


Figure 3.2: Coupling thermal and mechanical solvers together

and the new configuration is passed back to the thermal solver for the next time step.

I use the thermal and mechanical solvers from the finite element package 'MILAMIN' (Dabrowski et al., 2008) as the basis of my viscous model. The code is originally Lagrangian, but here I use an Eulerian version for ease of boundary condition implementation. The thermal code has also been changed from steady state to a transient solution. A brief summary is given here of the finite element method in general and the specific formulation used in my model, but more detail can be found in the paper by Dabrowski et al. (2008).

### 3.2.3 The finite element method

Finite element modelling is a powerful technique whereby the domain under consideration is divided into discrete, non-overlapping elements, and the behaviour of each element according to the governing equations is found. The behaviour of the whole system is then given by the assembly of these element-wise solutions.

The discretisation of the domain is here performed using a package called 'Triangle' (Shewchuck, 1996). Triangle divides the domain into 7-noded triangular elements, where the corner nodes are shared with a varying number of triangles, the side nodes are shared between two adjacent triangles, and the centre node is unique (figure 3.3). The speed and accuracy of the solution is determined by the size of the elements: a fine mesh with many small elements will give a more accurate answer but will be more computationally expensive. It is also possible to use a mesh which is refined in certain areas to give more detail.

For a differential equation **A** with boundary conditions **B**, we require an unknown

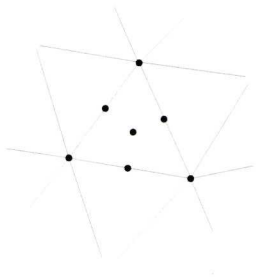

Figure 3.3: The triangular mesh used to discretise the domain

function $\mathbf{u}$ that solves the equation sets (Zienkiewicz et al., 2005)

$$\mathbf{A}(\mathbf{u}) + \mathbf{B}(\mathbf{u}) = 0 \tag{3.10}$$

The function $\mathbf{u}$ can be approximated over an element by

$$u(x, y) \approx u^e(x, y) = \sum_{i=1}^{n} N_i^e(x, y) u_i^e \tag{3.11}$$

where $u_i$ is the value of $u^e$ at the $i$th node of the element, and $N_i^e$ are interpolation functions. Each approximation function $u^e$ would need to be differentiable as many times as the partial differential equation involving $u$, but in the weighted residual finite element method the weak form of the governing equation is used, which moves some of the differentiation to a weighting function.

The weak form of the governing equations is found by multiplying the differential equation by a weighting function $w$ and integrating by parts

$$\int_\Omega wA(u)d\Omega + \int_\Gamma wB(u)d\Gamma = 0 \tag{3.12}$$

where $\Omega$ is the domain and $\Gamma$ is the boundary. This can then be manipulated into the form

$$\int_\Omega C_1(w)C_2(u)d\Omega + \int_\Gamma D_1(w)D_2(u)d\Gamma = 0 \tag{3.13}$$

where operators $C_1$, $C_2$, $D_1$ and $D_2$ in the weak form are of lower order derivatives than A and B. In the following derivations the Galerkin method is used, where the shape functions are used as the weighting functions, that is, $w = N_i$.

Manipulation of equation 3.13 allows the weak form to be written for each element in the form

$$\mathbf{K^e u^e} + \mathbf{F^e} = \mathbf{0} \tag{3.14}$$

where **K** is known as the coefficient, or 'stiffness' matrix, and **F** are the forces acting on the element. Assembling the system from the sum of the elements gives

$$\mathbf{Ku} + \mathbf{F} = \mathbf{0} \tag{3.15}$$

The unknown $u$s can then be retrieved from the solution of this equation.

MILAMIN uses Cholesky factorisation to solve simultaneous equations. Ensuring that **K** is symmetric and positive definite, it can be written as

$$\mathbf{K} = \mathbf{LL}^* \tag{3.16}$$

where **L** is the lower triangular matrix, and **L*** is its conjugate transpose. Then solving $\mathbf{Ly} = \mathbf{F}$ to get **y**, **u** can be recovered from $\mathbf{L}^*\mathbf{u} = \mathbf{y}$, where the equations are then easy to solve using forward substitution.

### Thermal problem

For the thermal code, the transient heat conduction equation can be written (Reddy and Gartling, 2001)

$$\rho C_p \frac{\partial T}{\partial t} - \left[ \frac{\partial}{\partial x}\left( k_x \frac{\partial T}{\partial x} \right) + \frac{\partial}{\partial y}\left( k_y \frac{\partial T}{\partial y} \right) \right] = 0 \tag{3.17}$$

over the domain $\Omega$, where $T$ is temperature, $t$ is time, $\rho$ is density, $C_p$ is specific heat capacity, and $k$ is thermal conductivity. Using the method of weighted residuals, this equation is multiplied by the weight function and integrated over the element. Some manipulation using integration by parts and the divergence theorem allow this equation to be re-cast into the weak form,

$$\begin{aligned} \int_{\Omega^e} \left[ w\left( \rho C_p \frac{\partial T}{\partial t} \right) + k_x \frac{\partial w}{\partial x}\frac{\partial T}{\partial x} + k_y \frac{\partial w}{\partial y}\frac{\partial T}{\partial y} \right] dx dy \\ - \oint_{\Gamma^e} w\left( k_x \frac{\partial T}{\partial x} n_x + k_y \frac{\partial T}{\partial y} n_y \right) ds = 0 \end{aligned} \tag{3.18}$$

where $w$ is the weight function, $\Omega^e$ is the element domain, and $\Gamma^e$ is the element boundary.

Substituting $N_i$ for $w$ and writing

$$M_{ij}^e = \int_{\Omega^e} \rho C N_i N_j dxdy \tag{3.19}$$

$$K_{ij}^e = \int_{\Omega^e} \left( k_x \frac{\partial N_i}{\partial x}\frac{\partial N_j}{\partial x} + k_y \frac{\partial N_i}{\partial y}\frac{\partial N_j}{\partial y} \right) dxdy \tag{3.20}$$

$$q_i^e = \oint_{\Gamma^e} k_x \frac{\partial T}{\partial x} n_x + k_y \frac{\partial T}{\partial y} n_y ds \tag{3.21}$$

the finite element model can be described as a summation over all $n^e$ elements

$$\sum_{j=1}^{n_e} \left( M_{ij}^e \frac{dT_j^e}{dt} + K_{ij}^e T_j^e \right) - q_i^e = 0 \tag{3.22}$$

This can then be solved as a series of simultaneous equations.

**Viscous problem**

For a viscous incompressible flow, the Stokes equations are

$$\frac{\partial u_i}{\partial x_i} = 0 \tag{3.23}$$

$$\rho \left( \frac{\partial u_i}{\partial t} + u_j \frac{\partial u_i}{\partial x_j} \right) - \frac{\partial}{\partial x_j} \left[ -P\delta_{ij} + \eta \left( \frac{\partial u_i}{\partial x_j} + \frac{\partial u_j}{\partial x_i} \right) \right] + \rho f_i = 0 \tag{3.24}$$

where $u$ is velocity, $P$ is pressure, and $f_i$ is body force. Multiplying by weight functions $w'$ and $w$ respectively, and integrating over the element, the weak form of these equations can be written as (Reddy and Gartling, 2001)

$$\int_{\Omega^e} w' \frac{\partial u_i}{\partial x_i} dxdy = 0 \tag{3.25}$$

$$\begin{aligned} \int_{\Omega^e} \left[ \rho_0 w_i \left( \frac{\partial u_i}{\partial t} + u_j \frac{\partial u_i}{\partial x_j} \right) + \frac{\partial w_i}{\partial x_j} \left[ -P\delta_{ij} + \eta \left( \frac{\partial u_i}{\partial x_j} + \frac{\partial u_j}{\partial x_i} \right) \right] + \rho_0 w_i f_i \right] dxdy \\ - \oint_{\Gamma^e} w_i \sigma_i . \hat{n}\, ds = 0 \end{aligned} \tag{3.26}$$

where $\eta$ is viscosity. Using the relationships of

$$u_i(x, y, t) = \mathbf{N^T u_i} \tag{3.27}$$

$$P(x, y, t) = \mathbf{\Pi^T P} \tag{3.28}$$

$$\tag{3.29}$$

where $\mathbf{u_i}$ and $\mathbf{P}$ are the nodal values of velocity and pressure, and $\mathbf{N}$ and $\mathbf{\Pi}$ are the respective shape functions, equations 3.25 and 3.26 can be rewritten as

$$\left(\int_{\Omega^e} \Pi \frac{\partial N^T}{\partial x_i} dxdy\right) u_i = 0 \tag{3.30}$$

$$\begin{aligned} &\left[\int_{\Omega^e} \rho_0 \mathbf{N}\mathbf{N}^T dxdy\right] \dot{\mathbf{u}}_i + \left[\int_{\Omega^e} \rho_0 \mathbf{N}(\mathbf{N}^T \mathbf{u}_j) \frac{\partial \mathbf{N}^T}{\partial x_j} dxdy\right] \mathbf{u}_i \\ &- \left[\int_{\Omega^e} \frac{\partial \mathbf{N}}{\partial x_j} \mathbf{\Pi}^T dxdy\right] \mathbf{P} + \left[\int_{\Omega^e} \eta \frac{\partial \mathbf{N}}{\partial x_j} \frac{\partial \mathbf{N}^T}{\partial x_j} dxdy\right] \mathbf{u}_i + \left[\int_{\Omega^e} \eta \frac{\partial \mathbf{N}}{\partial x_j} \frac{\partial \mathbf{N}^T}{\partial x_i} dxdy\right] \mathbf{u}_j \\ &- \left[\int_{\Omega^e} \rho_0 \mathbf{N} f_i dxdy\right] - \left[\oint_{\Gamma^e} \sigma_i . \hat{n} \mathbf{N} dxdy\right] = 0 \end{aligned} \tag{3.31}$$

If the following matrices are defined:

$$\mathbf{Q}_i = \int_{\Omega^e} \Pi \frac{\partial N^T}{\partial x_i} dxdy \tag{3.32}$$

$$\mathbf{M} = \int_{\Omega^e} \rho_0 \mathbf{N}\mathbf{N}^T dxdy \tag{3.33}$$

$$\mathbf{C}(\mathbf{u}) = \int_{\Omega^e} \rho_0 \mathbf{N}(\mathbf{N}^T u_j) \frac{\partial \mathbf{N}^T}{\partial x_j} dxdy \tag{3.34}$$

$$\mathbf{K}_{ij} = \int_{\Omega^e} \eta \frac{\partial \mathbf{N}}{\partial x_j} \frac{\partial \mathbf{N}^T}{\partial x_i} dxdy \tag{3.35}$$

$$\mathbf{F}_i = \int_{\Omega^e} \rho_0 \mathbf{N} f_i dxdy + \oint_{\Gamma^e} \sigma_i . \hat{n} \mathbf{N} dxdy \tag{3.36}$$

then equations 3.30 and 3.31 can be combined to give

$$\begin{bmatrix} \mathbf{M} & 0 \\ 0 & 0 \end{bmatrix} \begin{bmatrix} \dot{\mathbf{u}} \\ \dot{\mathbf{P}} \end{bmatrix} + \begin{bmatrix} \mathbf{C}(\mathbf{u}) + \mathbf{K}(\mathbf{u}) & -\mathbf{Q} \\ -\mathbf{Q}^{\mathbf{T}} & 0 \end{bmatrix} \begin{bmatrix} \mathbf{u} \\ \mathbf{P} \end{bmatrix} = \begin{bmatrix} \mathbf{F} \\ 0 \end{bmatrix} \tag{3.37}$$

which can be condensed to the form

$$\bar{\mathbf{M}}\dot{\mathbf{U}} + \bar{\mathbf{K}}\mathbf{U} = \bar{\mathbf{F}} \tag{3.38}$$

where $\mathbf{U} = \mathbf{u}, \mathbf{v}, \mathbf{P}$, and the superposed dot indicates a time derivative. Imposing the boundary conditions, the system of equations can then be solved.

These two solvers coupled together provides a solid basis on which to build a thermo-mechanical subduction zone model to investigate stresses in the slab. The mechanical MILAMIN solver has already been implemented in a subduction setting, as part of the FEMS-2D code used in a benchmark comparison of subduction zone

models (Schmeling et al., 2008), where it performed favourably. Tests of the viscous and thermal codes used here are included in appendix A.

## 3.3 Important parameters in the 2D model

### 3.3.1 Rheology

The Earth's outer layers of mantle and crust are probably best described as visco-elastic-plastic: over short time frames there is an elastic response, over longer time periods there is viscous flow, and under certain conditions of stress there is also plastic deformation. Reasonable models to study the the Earth do not necessarily need to have the full visco-elasto-plastic complement; some do use this rheology (Kaus and Becker, 2008; Babeyko and Sobolev, 2008), but many choose only visco-elastic (Gurnis et al., 1996; Capitanio et al., 2007), visco-plastic (Cížková et al., 2007; Billen and Hirth, 2005), or just viscous (van Keken et al., 2002). Viscous models are often an acceptable approximation because viscous flow is the prevalent form of deformation in the lithosphere and asthenosphere; only under exceptional circumstances does brittle failure occur. Visco-plastic models allow a reduction in strength in areas of high stress but low temperature, like the lithosphere.

#### Viscosity structure of the mantle

The viscosity structure of the mantle has been a contentious issue in geophysics. Viscosity broadly increases with depth, but there is much disagreement about the details. Various analyses of data have been used to determine the viscosity structure of the Earth, including gravity spectra (Steinberger and Holme, 2002), geoid anomalies (Hager, 1984), post-glacial rebound (Cathles, 1975), and plate velocity (Forte et al., 1991), as well as techniques such as geoid inversion (King and Masters, 1992), joint inversion (Mitrovica and Forte, 2004), and Monte Carlo inversion (Ricard et al., 1989).

From the literature and the sensitivity tests shown in figure 3.6, I choose the background viscosity structure shown in figure 3.4 which resembles the viscosity structure from Steinberger and Holme (2002) most closely, but is more simplified in that it has a single viscosity for each of the transition zone ($10^{22}$) and the lower mantle ($10^{23}$). Figure 3.5 shows a schematic diagram of how the viscosity of the different model domains is defined.

Figure 3.6 shows temperature and stress plots for models with different viscosities for the transition zone and lower mantle. The bottom boundary of the model does

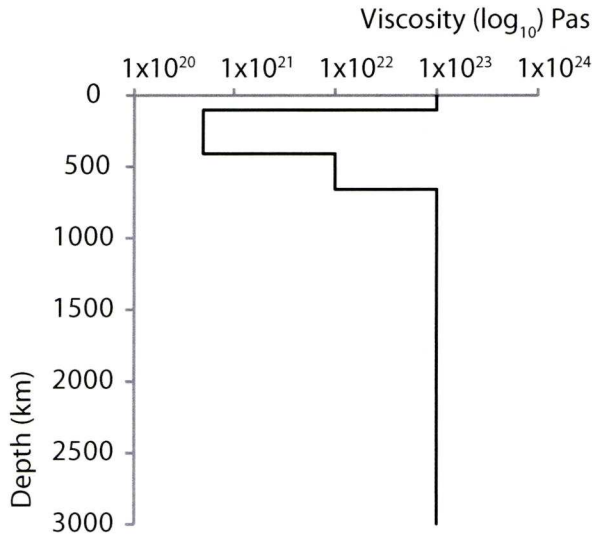


Figure 3.4: Adopted viscosity structure for my 2D model

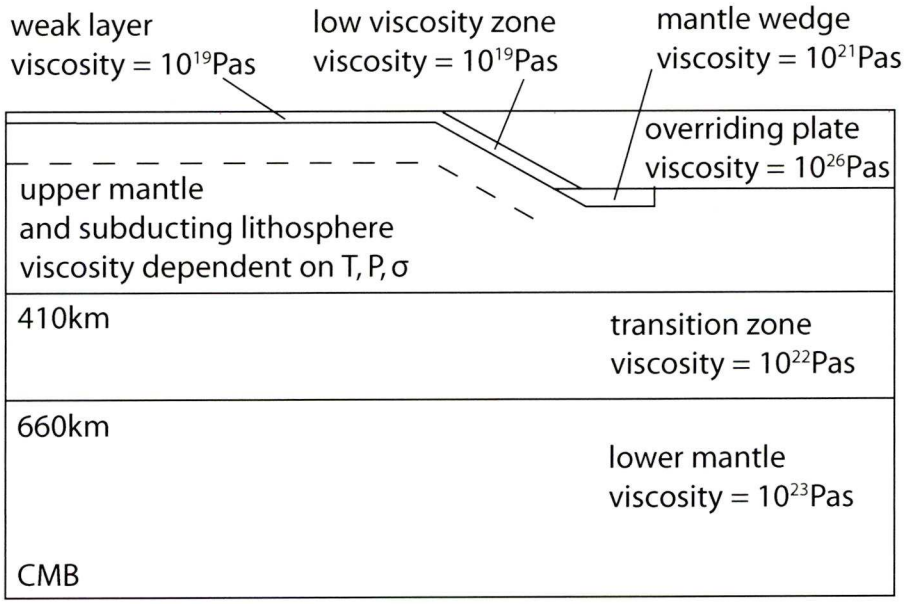


Figure 3.5: Viscosity initialisation by depth and area

not allow vertical velocity, as a representation of the high density contrast of the core-mantle boundary. The shape of the slab and its regions of high stress change depending on the viscosity of the transition zone and lower mantle; the higher these values, the more the slab is supported from underneath.

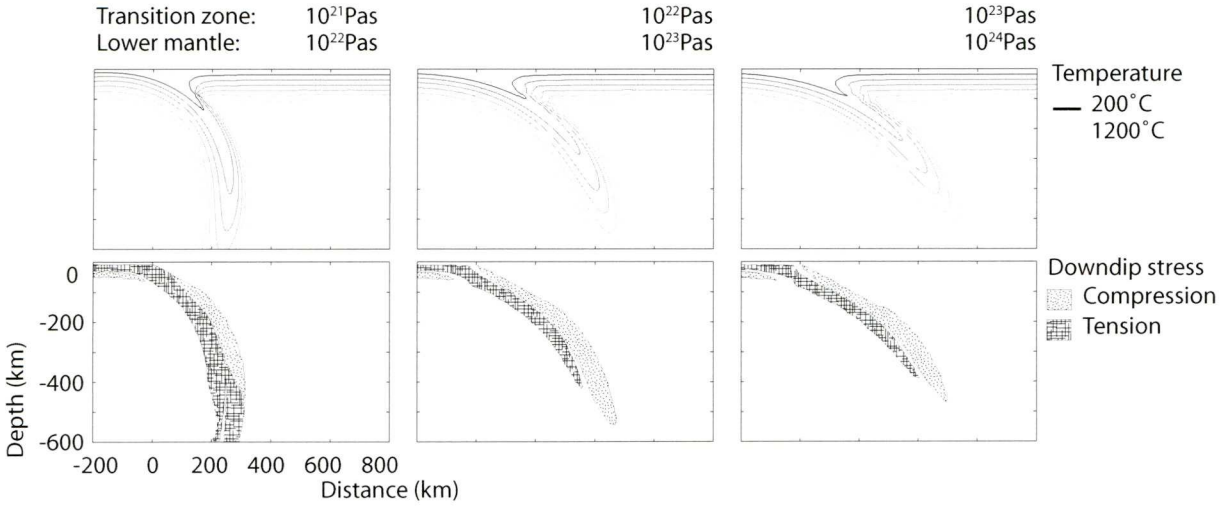


Figure 3.6: Comparison of models at 40Myr with different viscosities for the transition zone 410-660km, and the lower mantle below 600km. Stress contours show magnitudes greater than 250MPa. A full discussion of slab evolution and associated temperatures and stresses is given in chapter 4.

### Mantle viscosity, diffusion creep, and dislocation creep

Viscosity in the mantle is achieved through either diffusion or dislocation creep. Diffusion creep is dominant at high temperatures and pressures but low stress levels (Turcotte and Schubert, 2002). On the microscopic level, deformation is due to the movement of vacancies along grain boundaries or through the lattice and results in linear, Newtonian rheology. Dislocation creep, on the other hand, occurs at high stress levels. The movement of dislocations in the crystalline lattice results in power-law, non-Newtonian rheology. Previous models have found that the inclusion of dislocation creep in the viscosity formulation makes subduction initiation easier by decreasing hydrodynamic stresses on the slab (Billen and Hirth, 2005). The dominant rheology at a given temperature and pressure is the one which gives the higher strain rate (Karato and Wu, 1993).

The rheology of a viscous fluid is described by (Karato and Wu, 1993; Turcotte and Schubert, 2002)

$$\dot{\varepsilon}_{ij} = A\sigma^{n-1}\sigma_{ij}\exp\left(-\frac{E_a + PV_a}{RT}\right) \tag{3.39}$$

where all symbols and values are given in 3.1. The viscosity of a Newtonian fluid depends primarily on its temperature, whereas the viscosity of a non-Newtonian fluid is also controlled by the shear stress. In a general formulation, the viscosity can be

| Symbol | Meaning | Diffusion | Dislocation | Units |
|---|---|---|---|---|
| $\eta$ | viscosity | | | Pa s |
| T | temperature | | | K |
| P | pressure | | | Pa |
| $\sigma$ | shear stress | | | MPa |
| $\dot{\varepsilon}$ | shear strain rate | | | $s^{-1}$ |
| G | rigidity | 80 | | GPa |
| b | lattice spacing | 0.5 | | nm |
| h | grain size | 3 | | mm |
| R | gas constant | 8.314 | | $JK^{-1}$ $mol^{-1}$ |
| C | prefactor | $8.7\times10^{15}$ | $3.5x10^{22}$ | $s^{-1}$ |
| m | grain size exponent | 2.5 | 0 | |
| n | stress exponent | 1 | 3.5 | |
| $E_a$ | activation energy | 300 | 540 | kJ $mol^{-1}$ |
| $V_a$ | activation volume | $6\times10^{-6}$ | $20\times10^{-6}$ | $m^3$ $mol^{-1}$ |
| A | pre-exponential factor | $1.92\times10^{-11}$ | $2.42\times10^{-16}$ | $Pa^{-1}s^{-1}$ |

Table 3.1: Symbols, meanings and values used in viscosity calculations (Karato and Wu, 1993; Turcotte and Schubert, 2002)

described as shear stress ($\sigma$) divided by shear strain rate ($\dot{\varepsilon}$), so it can be described by

$$\eta = A^{-\frac{1}{n}} \dot{\varepsilon}_2^{\frac{1}{n}-1} \exp\left(\frac{E_a + PV_a}{nRT}\right) \tag{3.40}$$

where $A = \frac{C}{G^n}\left(\frac{b}{d}^m\right)$.

The presence of water reduces the viscosity of olivine (Hirth and Kohlstedt, 1996), and causes partial melting, reducing the viscosity further. Regions that are particularly hydrated, for example, the mantle wedge, will therefore have viscosities up to an order of magnitude lower than would normally be expected (Hirth and Kohlstedt, 2003). The existence of such a low viscosity wedge is supported by observed data such as gravitational anomalies and topography (Billen and Gurnis, 2001), and may help to lubricate tectonic movement.

### Plasticity and yield stress

Temperature and pressure dependent rheology gives a good representation of the majority of the mantle, but some regions of the subduction zone require further constraints. In cold regions such as near the Earth's surface or in the centre of slabs, the predicted viscosity can be so unrealistically high that it stops the numerical model running, let alone giving meaningful results. A practical way of dealing with this problem is to cap the viscosity at some high value, such as $10^{23}$Pas (van Hunen et al., 2000), or

1000 times the viscosity at 1300°C (Conrad and Hager, 1999). The justification for this cutoff is that at such high viscosities the material can no longer be considered to be viscous, and other deformation mechanisms would take over such as brittle failure or Peierl's creep. A map of dominating deformation mechanism under various conditions of stress and temperature is shown in figure 3.7.

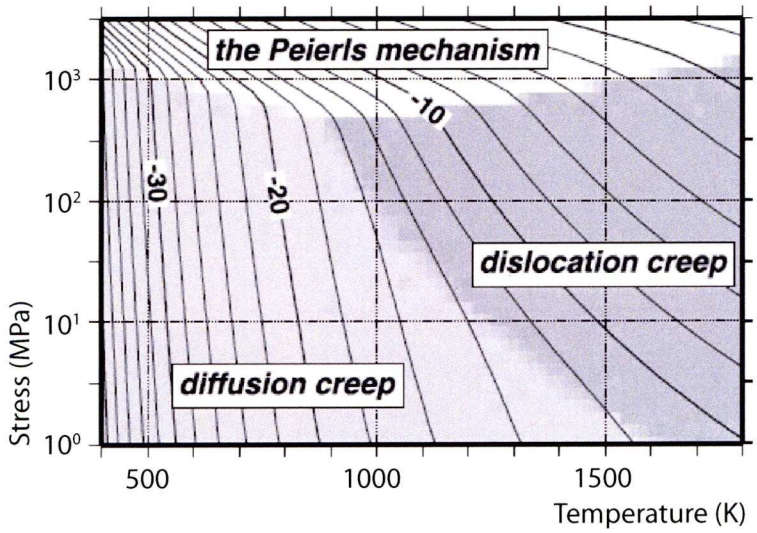


Figure 3.7: Deformation mechanism map for grain size 0.1mm. The contour lines indicate constant strain rate, the labels are log(strain rate) in units of $s^{-1}$ (Kameyama et al., 1999)

An alternative approach to applying a cutoff viscosity is to introduce a yield stress, a critical value beyond which a material will undergo irreversible plastic deformation even at low temperatures. A simple formulation of a stress limiting viscosity is (Kameyama et al., 1999; Cížková et al., 2007)

$$\eta_{\text{yield}} = \tau \dot{\varepsilon}_{\text{yield}}^{-1/n_y} \dot{\varepsilon}^{1/n_y - 1} \tag{3.41}$$

where $\tau$ is the yield stress at a particular strain rate $\dot{\varepsilon}$, $\dot{\varepsilon}_{\text{yield}}$ is the reference strain rate, and $n_y$ is the powerlaw index. Cížková et al. (2002) estimate $\dot{\varepsilon}_{\text{yield}}$ to be $10^{-15}s^{-1}$ and use $n_y = 5$, which are the values that are adopted here. This viscosity formulation has the effect of reducing the viscosity of cold regions under high stresses, and is a more elegant solution to the problem of high viscosities at cold temperatures than capping viscosity at an arbitrary value. Figure 3.8 shows the models using a yield stress of 100, 500 and 1000MPa. All three models produce very similar slab shapes and temperature contours, but the yield stress directly affects the magnitude of the stress distribution across the slab. In my model I use a yield stress of 500MPa.

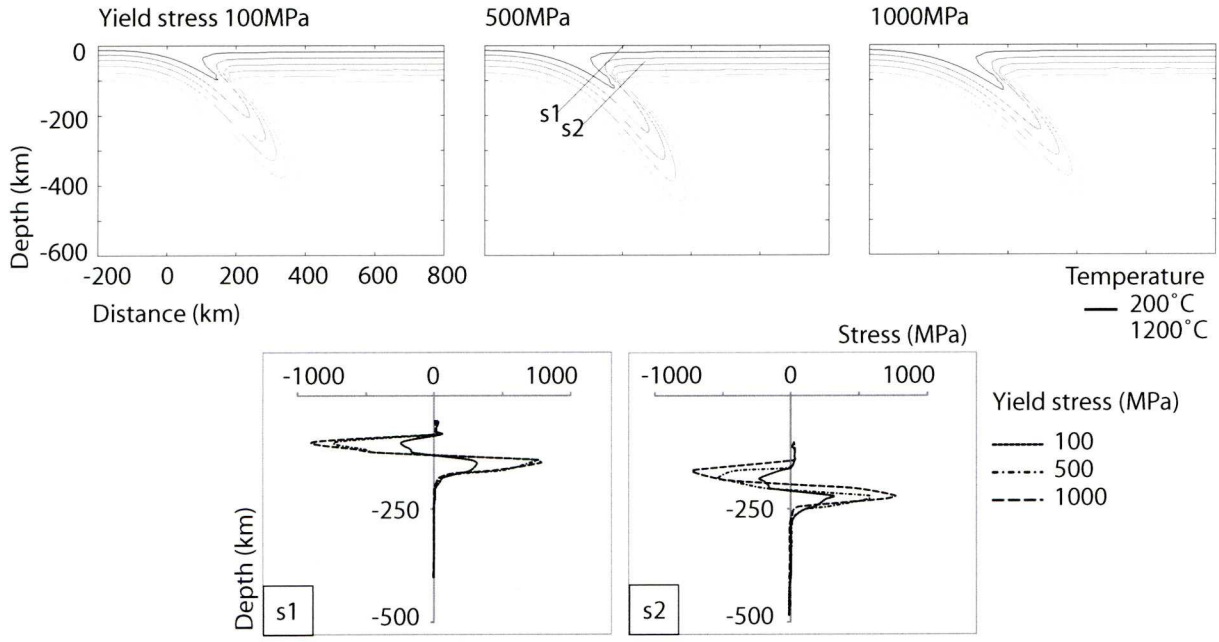


Figure 3.8: Comparison of models at 30Myr with a yield stress of 100, 500, and 1000 MPa. The top plots show temperature contours of the slab, and the site of the slices s1 and s2. The bottom plots show the stresses along these two slices.

The inclusion of the various deformation mechanisms into my 2D model results in a complex viscosity calculated using

$$\eta_{\text{effective}} = \left( \frac{1}{\eta_{\text{diffusion}}} + \frac{1}{\eta_{\text{dislocation}}} + \frac{1}{\eta_{\text{yield}}} \right)^{-1} \tag{3.42}$$

where the effective viscosity is a combination of diffusion creep, dislocation creep, and low-temperature plastic yield.

### 3.3.2 Decoupling the overriding and subducting plates

In the subduction zone, the downgoing and overriding plates are decoupled from each other, allowing relative movement between them. This decoupling is facilitated by a low strength layer, which results from a combination of accretionary wedge sediments, basaltic oceanic crust, hydrated minerals and high pore pressure, and localised strain (Cloos, 1982; Cížková et al., 2002; Manea and Gurnis, 2007; Wada et al., 2008). This layer can be seen in the form of a low velocity layer along the megathrust in many subduction zones (Abers et al., 2006; Chen et al., 2007). Observations and numerical experiments put the low viscosity zone between 7 and 50km wide, and extending from the surface to depths of 75-300km (Cížková et al., 2002; Chen et al., 2007; Wada and

Wang, 2009). The viscosity is usually estimated as one to three orders of magnitude less than the mantle wedge (Hirth and Kohlstedt, 2003; Wada et al., 2008).

In the 2D viscous model, the depth of the low viscosity zone is quite important; if it is only 100km deep, the high viscosities associated with the low temperature lithosphere can appear beneath the low viscosity zone, eventually halting subduction. Extending the low viscosity zone deeper avoids this problem but becomes quite prescriptive. The width and the viscosity of the decoupling zone are also primary controls on the development of the subduction zone. If the layer is too narrow or too high viscosity, the oceanic and continental plates are not sufficiently decoupled, resulting in much higher stresses, and unrealistically high values of dynamic topography. I use a layer 10km wide and 150km deep with a viscosity of $10^{19}$Pas to adequately decouple the plates whilst allowing as much freedom as possible for the slab to evolve self-consistently.

**Decoupling and the mantle wedge**

The mantle wedge typically has a lower viscosity than would normally be assumed for its temperature and pressure conditions because of the presence of water from the dehydration of the slab (Hirth and Kohlstedt, 2003). It is this low viscosity that allows hot material from the mantle to be pulled into the subduction zone and down with the slab, helping to decouple the overriding and subducting plates. In the 2D viscous model, if the mantle wedge is not specified as being of a lower viscosity than normal, the whole area cools in a feedback loop: the wedge becomes more viscous, so hot material is not advected as much, so the area cools and becomes even more viscous, eventually halting subduction.

Figure 3.9 shows the sensitivity of the model to the mantle wedge. If there is no mantle wedge present, subduction is much slower, cooling the whole area and ultimately halting subduction despite the presence of a low-viscosity zone. If the mantle wedge begins immediately below the continental plate at 80km depth, its vertical extent has a significant effect on subduction zone development. A mantle wedge from 80km to 100km depth partially decouples overriding and subducting plates, but models with a mantle wedge from 80km to 150km depth fully decouple the two plates, allowing a stable well-behaved slab to develop, hence these are the conditions imposed upon my model.

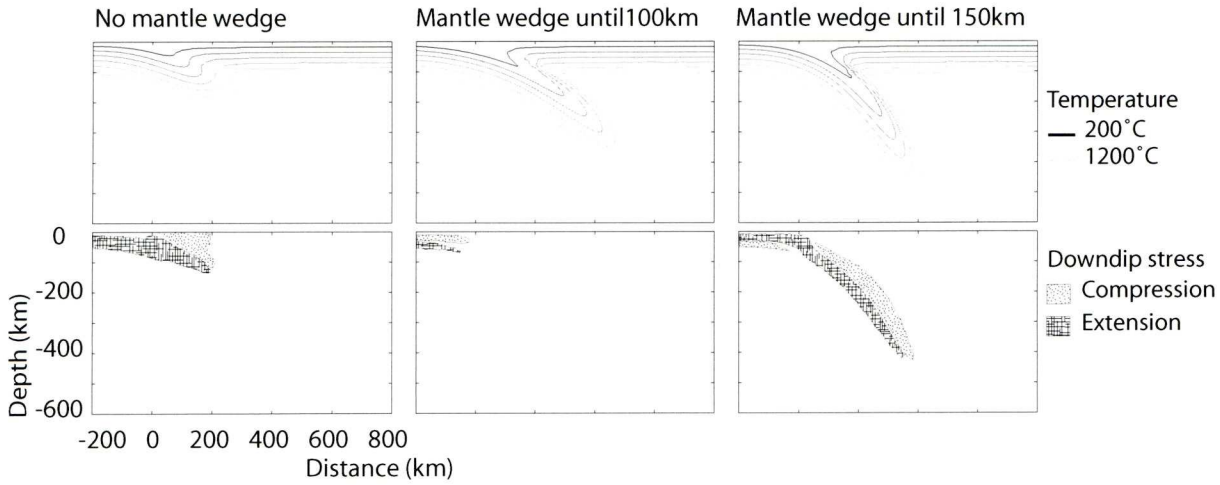


Figure 3.9: Comparison of models at 30Myr without a low-viscosity mantle wedge, with a mantle wedge extending to 100km depth, and with a mantle wedge until 150km depth. Stress contours show magnitudes greater than 250MPa.

### 3.3.3 Surface boundary conditions

The boundary condition with the most influence in subduction zone modelling is that of the top surface of the subducting plate, and is generally either free-slip or free-surface. Free-slip means that the plate is free to move horizontally but not vertically; free-surface means unrestricted movement in both directions.

Free-slip is easier to implement in Eulerian code; free-surface is easier in Lagrangian code. Although the two formulations are similar, they do not give quite the same results (Zhong et al., 1996), and a free surface is assumed to be the better model. As the 2D viscous model uses an Eulerian formulation, one approximation to a free surface is to use a lithosphere with a weak top layer, referred to as a 'sticky air' layer by Schmeling et al. (2008). This layer partially decouples the lithosphere from the top surface of the model, and may also ease subduction by accommodating upwards motion of the lithosphere at the outer rise (Goes, 2009). The weak layer is partially drawn down into the subduction zone, where it becomes part of the low viscosity decoupling zone.

Figure 3.10 shows results with and without the weak top layer. The shapes of the slab at 30Myr are very different as a result of the enhanced decoupling and freedom of movement. The bottom plot shows a close-up of the velocity vectors around the trench; in the model with a crustal layer, a return flow in the accretionary wedge can clearly be seen, as predicted by Cloos (1982). I include the weak layer in my model because it gives better results for predicted slab shape and stress profile.

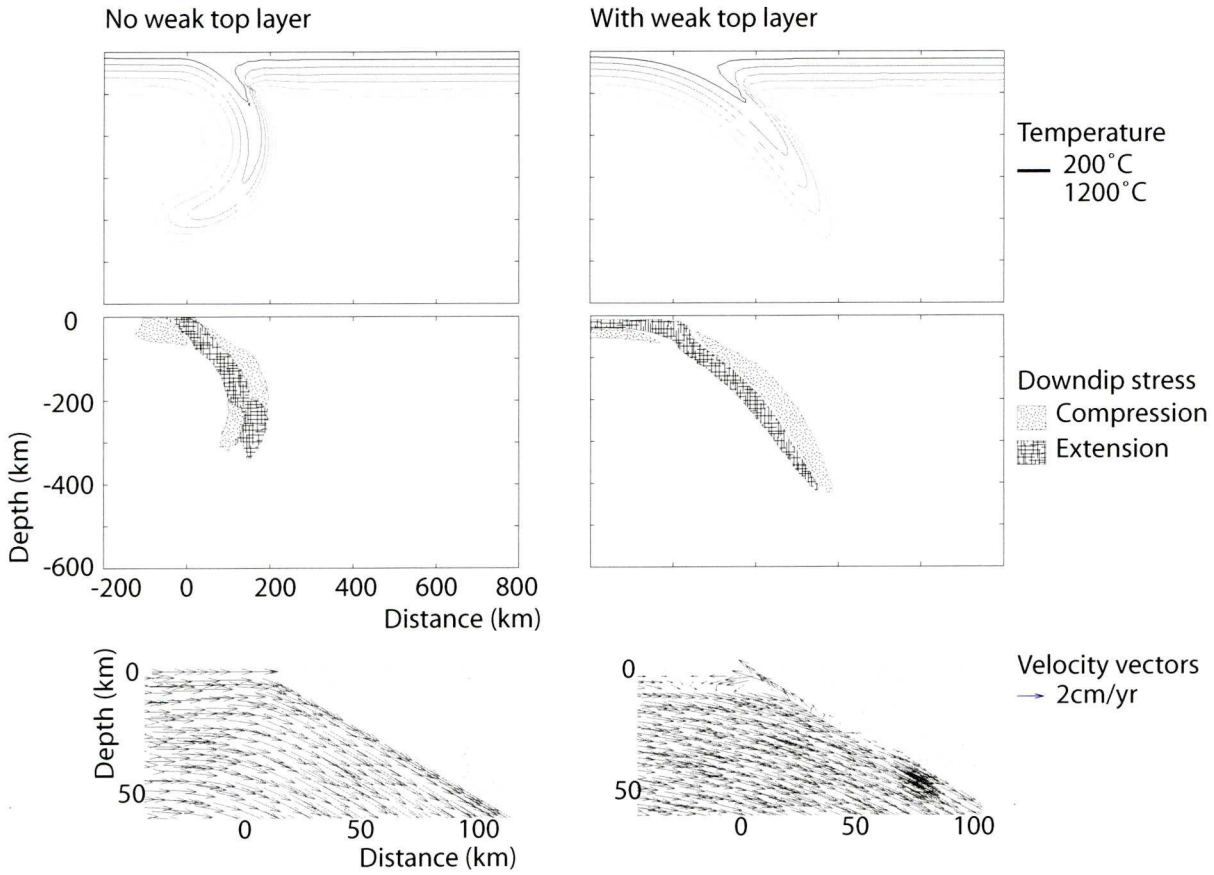


Figure 3.10: Comparison of models at 30Myr (a) without weak layer and (b) with weak layer

### 3.3.4 Negative thermal buoyancy and density contrast

Density is dependent on composition, temperature, and pressure. In the subduction zone, the slab is more dense than the surrounding mantle, causing slab pull due to the mass excess. This is primarily controlled by temperature, and the change in density of a material with respect to temperature can be formulated as

$$\Delta\rho = -\rho_0 \, \alpha \, \Delta T \tag{3.43}$$

where $\rho_0$ is a reference density, 3300 $kg/m^3$, and $\alpha$ is the thermal expansion coefficient, $3\times10^{-5}$ °C$^{-1}$ (Turcotte and Schubert, 2002). In this model I use density contrast rather than absolute density, eliminating pressure dependence: material at a given depth is compared to the typical value of the mantle at that point.

The value for $\alpha$ in the mantle is in the range 1-5$\times10^{-5}$K$^{-1}$ (Schubert et al., 2001; Chopelas and Boehler, 1992), but depends on temperature, pressure, and mineralogy. For simplicity I use a constant coefficient of thermal expansion of $3\times10^{-5}$K$^{-1}$, which

is an average value commonly chosen for subduction zone modelling (Cížková et al., 2007; Babeyko and Sobolev, 2008), appropriate for both slab and mantle. I perform sensitivity tests on my model by varying $\alpha$ between 2 and $4\times10^{-5}\mathrm{K}^{-1}$, as shown in figure 3.11. Changing $\alpha$ has an effect on the shape of the subducting slab: since the change in density is directly proportional to $\alpha$, a bigger $\alpha$ means the slab is more dense, increasing the effects of slab pull and accelerating the slab's descent into the mantle.

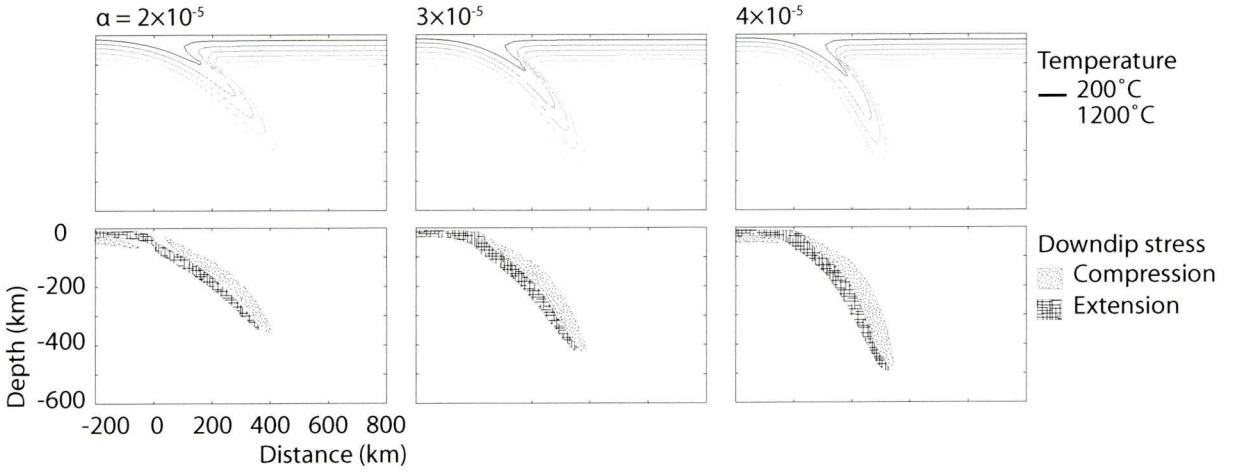


Figure 3.11: Sensitivity testing of model to $\alpha$, the coefficient of thermal expansion, shown at 30Myr. Comparison of $\alpha$ = 2, 3 and $4\times10^{-5}\mathrm{K}^{-1}$

The mantle density is estimated to have a reference value of 3300 kg $\mathrm{m}^{-3}$ at the surface, increasing with depth (Stuwe, 2002; Turcotte and Schubert, 2002). Figure 3.12 shows the model using 3300 kg $\mathrm{m}^{-3}$ compared with reference densities of $\pm10\%$, 3000 and 3600 kg $\mathrm{m}^{-3}$. This has much less effect on the slab temperature and stress evolution than $\alpha$.

### 3.3.5 Thermal conductivity

Although a constant thermal conductivity has been used in thermal modelling and gives an adequate approximation, a more accurate formulation is dependent on temperature, pressure and mineralogy. Variable conductivity can be calculated as Hofmeister (1999):

$$\kappa(P,T) = \kappa_{298}\frac{298^{a}}{T} \times \exp\left(-(4\gamma + 1/3)\int_{298}^{T}\alpha\,(\theta)\,d\theta\right) \times (1 + \frac{K_0' P}{K_0}) + K_{rad} \qquad (3.44)$$

where the meanings and typical values for olivine are given in table 3.3.5. This produces the relationship between conductivity and temperature as shown in fig 3.13. For

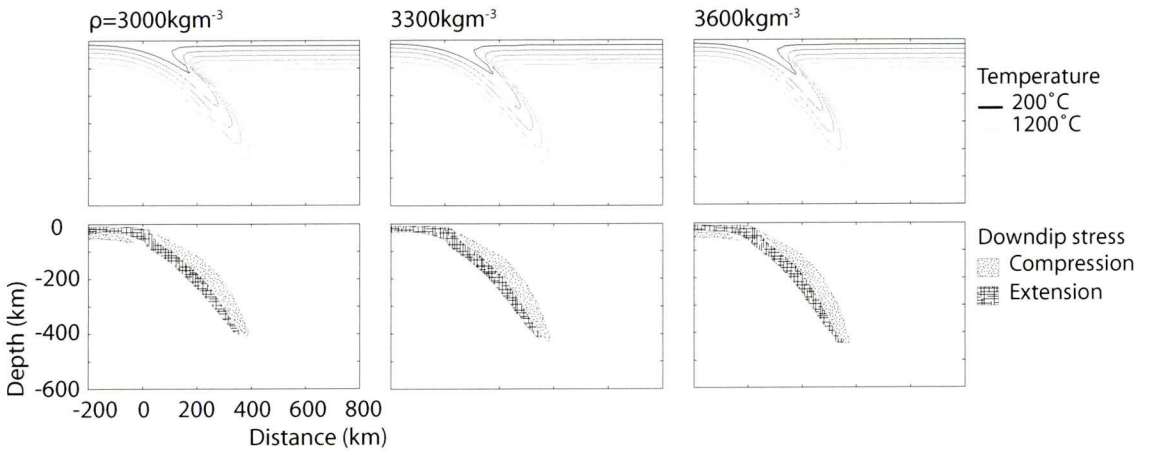


Figure 3.12: Sensitivity testing of model to $\rho$, the reference density, shown at 30Myr. Comparison of models with $\rho$ = 3000, 3300, and 3600kgm$^{-3}$.

| Symbol | Meaning | Value | Units |
|---|---|---|---|
| $\kappa$ | thermal conductivity | | W/m.K |
| P | pressure | | Pa |
| T | temperature | | K |
| $\kappa_{298}$ | thermal conductivity at the surface | 4.61 | W/m.K |
| a | fitting parameter | 0.33 | |
| $\gamma$ | thermal Grüneisen parameter | 1.25 | |
| $\alpha$ | volumetric coefficient of thermal expansion | $37.52 \times 10^{-6}$ | $K^{-1}$ |
| $K_0$ | reference isothermal bulk modulus | $128 \times 10^9$ | Pa |
| $K_0'$ | $dK/dP$ | 4.3 | |
| $\kappa_{rad}$ | radiative contribution | | W/m.K |
| | $= 0.01753 - 0.00010365T + 2.2451T^2/10^7 - 3.407T^3/10^{11}$ | | |

Table 3.2: Symbols, meanings and values used to calculate thermal conductivity

temperatures less than about 700°, the variable conductivity is higher than the typical 3.3Wm$^{-1}$ K$^{-1}$ often used for olivine (Turcotte and Schubert, 2002). These temperatures are not commonly found in the mantle, but do exist within the cold core of the subducting slab.

The inclusion of variable thermal conductivity may have some profound implications: in numerical models it appears to increases the temperature of the subducting slab so much that transformational faulting of metastable olivine as an earthquake mechanism can be virtually ruled out Hauck et al. (1999), Marton et al. (2005).

Figure 3.14 shows a comparison between a model using variable thermal conductivity, and one which uses a constant thermal conductivity of 3.3Wm$^{-1}$ K$^{-1}$ (Turcotte and Schubert, 2002). The temperature, pressure and velocity plots for both models are very similar; the variable conductivity model is a fraction colder and slower, but

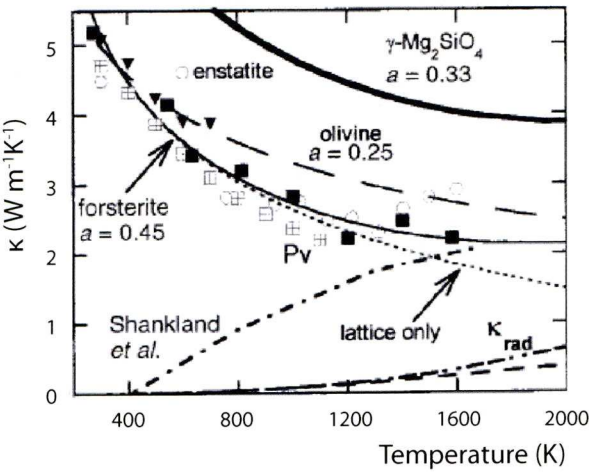


Figure 3.13: The variation of thermal conductivity with temperature (Hofmeister, 1999)

there is very little difference between them. This is in contrast to other workers who have found their models to be significantly affected by variable thermal conductivity, but these models centred around changes in phase, which is not modelled here. For completeness, variable conductivity is included in my model.

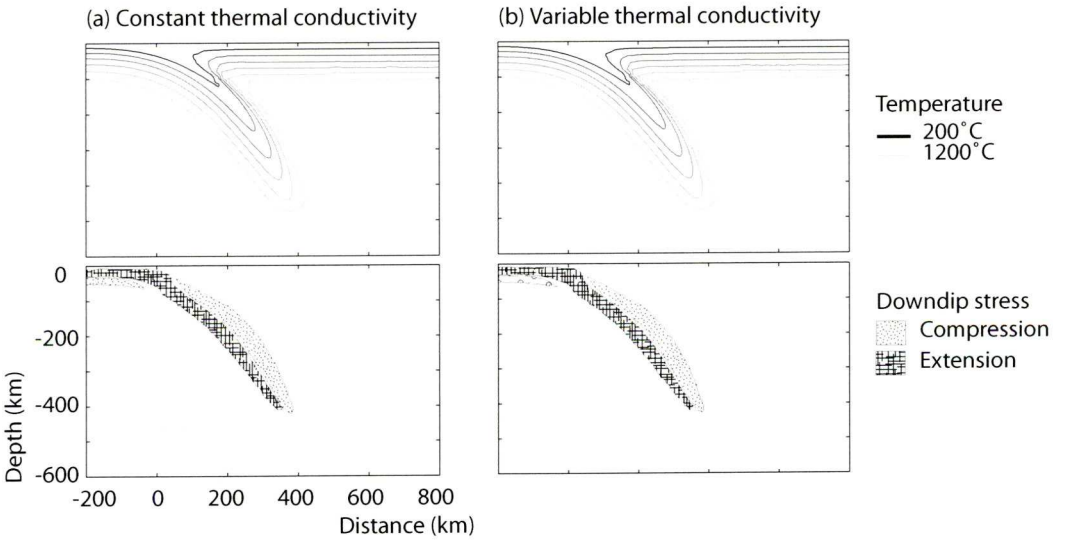


Figure 3.14: Comparison of models with a thermal conductivity that is (a) constant $3.3 \mathrm{Wm}^{-1}\mathrm{K}^{-1}$ (b) variable, dependent on temperature and pressure. Models here are shown at 30Myr.

## 3.4 Summary of the 2D viscous model

I have presented here a formulation of a viscous thermo-mechanical model which will be used to study the processes that occur in subduction zones and the mechanisms by which stresses accumulate in the downgoing slab, leading to seismicity. The model is two-dimensional and dynamic with kinematic boundary conditions. Thermal and mechanical finite element solvers are coupled together through their outputs of velocity, temperature-dependent density, and temperature-dependent viscosity. The rheology of the lithosphere and upper mantle is described by a combination of diffusion creep, dislocation creep, and yield stress. A low viscosity zone aided by a low viscosity mantle wedge decouples the overriding and subducting plates, and a partially free surface is implemented by the use of a weak zone overlying the oceanic lithosphere.

This model is used to investigate stress accumulation in subduction zones, focussing on the origin of double and triple seismic zones. The sensitivity of the model to its four key parameters of plate velocity, rollback velocity, plate age and slab dip are presented in chapter 4; the application of this model to the specific cases of north Chile and northeast Japan are presented in chapters 7 and 8.

# Chapter 4

# Predicting subduction zone stresses using the 2D viscous thermo-mechanical model

## 4.1 Introduction

The viscous model introduced in chapter 3 is formulated to investigate the behaviour of a subduction zone, and to predict stresses accumulated in the slab. The model uses a two-dimensional coupled thermal-mechanical finite element code, and implements a rheology that combines diffusion creep, dislocation creep, and yield stress. It is a hybrid dynamic-kinematic model, where plate motion and rollback are imposed as boundary conditions, but the internally generated body forces drive the system. Using this model, the evolution of the subducting slab and the response of slab development to a range of subduction parameters can be explored. The temperatures and stresses that are produced in the slab provide an insight into the mechanisms leading to Wadati-Benioff zone seismicity.

The global mantle convection system is represented through four key parameters. The horizontal movement of the oceanic plate away from a spreading ridge is represented by a plate velocity applied to the upper lithosphere some distance from the trench. The lower boundary of the model has horizontal movement to represent trench rollback, and no vertical movement as an approximation to the core-mantle boundary. The dip angle of the slab in the first 100km is imposed in the model by the domain geometry and the low viscosity zone, and the temperature of the oceanic lithosphere controls the age of the slab at the point of subduction.

This chapter presents the results from the 2D viscous subduction zone model. The

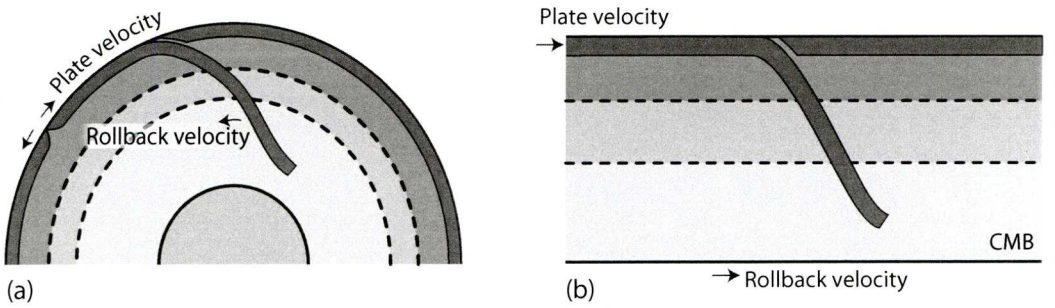


Figure 4.1: The global earth system and the model representation

four key parameters of plate age, dip angle, plate velocity and rollback velocity control the slab development and the stresses within it. Investigation into the relationships between these parameters and the stresses that are generated give insight into the processes governing Wadati-Benioff zone seismicity.

## 4.2 Governing parameters in the 2D subduction model

The four governing variables used in the viscous model are plate age, dip angle, plate velocity and rollback velocity as shown in figure 4.2; however they are not completely independent.

The lithospheric plate age at the point of subduction is defined by its temperature. As plates age they cool, approaching an equilibrium geotherm. The temperature of the oceanic plate is calculated using an analytical solution (McKenzie, 1969). Because the viscosity is temperature-dependent, this temperature structure dictates the thickness and viscosity of the oceanic lithosphere, which controls the ease with which the slab can bend (Griffiths et al., 1995). A thick, stiff plate will be difficult to bend, so will have a large radius of curvature, meaning a low dip angle (Bellahsen et al., 2005). In a fully dynamic model this would dictate the dip angle, however in my model the dip angle is imposed via the geometry of the low viscosity zone and the overriding plate, so care is taken to select dip angles that are reasonable and appropriate.

It is generally accepted that slabs sink due to their negative buoyancy, and this slab pull is countered by slab resistance at depth as the viscosity of the mantle increases. The resultant of these two forces gives the speed at which the slab will subduct. In this viscous model the plate velocity is imposed kinematically at the surface by pushing the upper oceanic lithosphere towards the trench; as the slab develops, the slab becomes more dynamically driven through its temperature-dependent density creating the slab pull, and the temperature and stress dependent viscosity of the mantle providing the

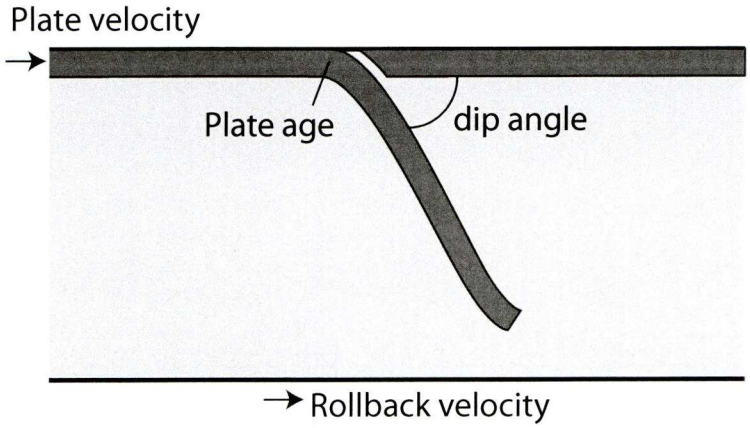


Figure 4.2: The governing parameters in the subduction model

slab resistance. For a given plate age and rheology, there is an optimum plate velocity that gives smooth subduction, where a slab develops without thickening and warping, or thinning and detaching.

Rollback, the retreat of the trench position, is treated here as an independent variable, although like the plate velocity there is a window of reasonable values that give sensible results. Here, rollback is imposed as horizontal movement of the bottom of the model representing the core-mantle boundary, creating a reference frame in which the overriding plate is stationary.

## 4.3 Dynamic topography

A good quality check on the validity of a subduction model comes from dynamic topography. Dynamic topography is the surface expression of stresses arising from buoyancy forces in the mantle, and is the source of trench bathymetry (Zhong and Gurnis, 1994). The depth of the trench has been correlated to subduction rate (Grellet and Dubois, 1982), plate age, and the plate dip angle for the first 100km (Jarrard, 1986). Zhong and Gurnis (1994) calculate dynamic topography for a model with a free slip upper boundary as

$$h = \frac{\sigma_y}{\Delta \rho g} \tag{4.1}$$

where $h$ is dynamic topography, $\sigma_y$ is the vertical component of stress at the top lithosphere boundary, $\Delta\rho$ is the density difference between the lithosphere and the loading media (air or water), and $g$ is gravity. The dynamic topography calculated by Zhong and Gurnis (1994) across the trench is shown in figure 4.3a. It has an outer rise of about 300m, a narrow trench about 100km wide and 5km deep, and a secondary depression

behind the trench which slowly decreases to zero. Dynamic topography is also calculated by Billen and Gurnis (2001), as shown in figure 4.3b, although the magnitudes of their trench subsidence and topographic high are rather large.

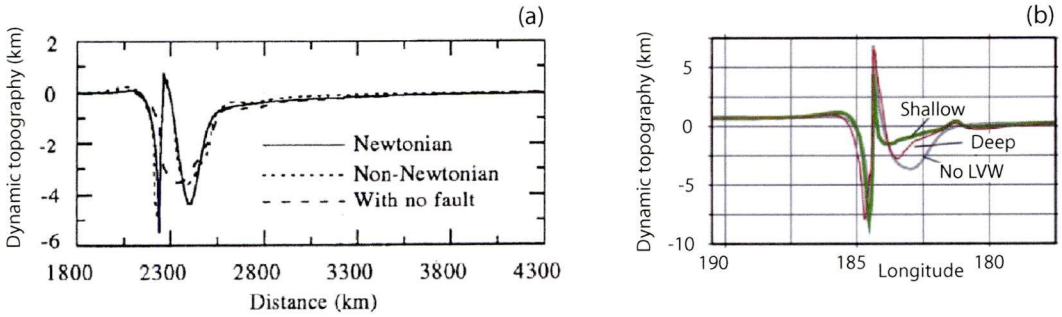


Figure 4.3: Dynamic topography (a) calculated by Zhong and Gurnis (1994) (b) calculated by Billen and Gurnis (2001) (converted to the same polarity as (a) for comparison)

Figure 4.4 shows a typical plot of dynamic topography generated by a model with a plate velocity of 2cm/yr, a dip angle of 30°, and a plate age of 100Myr, which has 80Myr of development time. It has a trench depth of approximately 3.5km, followed by a high of 1km, then a second depression of 2.5km which decreases away from the trench. The shape and magnitudes are in good agreement with observations of subduction zones, as well as the published dynamic topography of Zhong and Gurnis (1994), supporting the validity of the viscous model.

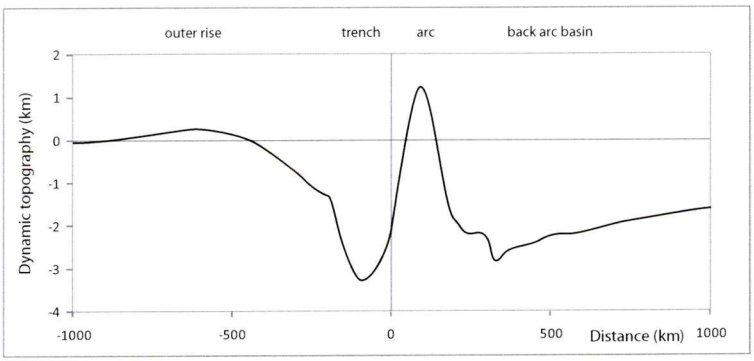


Figure 4.4: Dynamic topography from the reference model at 80Myr

## 4.4 Modelling a developing subduction zone

The reference model used here has a plate velocity of 2cm/yr, zero rollback velocity, a 30° dip angle, and a plate age of 100Myr. Figure 4.5 shows this reference model as it evolves with time.

The temperature plots in figure 4.5a show how the slab approaches a quasi-steady state by 80Myr due to the interplay between the speed of subduction and heat conduction. The temperature plots also show that the mantle wedge remains warm throughout because its low viscosity allows it to draw in hot material, which helps keep the plates decoupled.

Figure 4.5b plots the downdip stress in the subduction zone. These are calculated from the principal stresses using

$$\sigma_{x'x'} = \sigma_{xx} \cos^2 \theta + \sigma_{yy} \sin^2 \theta \tag{4.2}$$

where $\sigma_{x'x'}$ is the stress in the downdip direction, $\sigma_{xx}$ and $\sigma_{yy}$ are the principal stresses, and the angle $\theta$ is specified by the imposed megathrust geometry and is constant throughout. Figure 4.5c plots principal total stresses in more detail between 100 and 300km. The stress plots show that initially the downdip stress pattern is extension on top and compression underneath as the slab bends to begin subduction; this inverts as the slab straightens. As it is not a viscoelastic model it cannot be said to 'unbend' in the true sense since it does not have any stress memory, but it does exhibit the associated stress pattern of compression over tension.

The dynamic topography shows the presence of the trench immediately after subduction is initiated, while the arc takes longer to develop. These plots indicate the model is steady-state by about 50Myr.

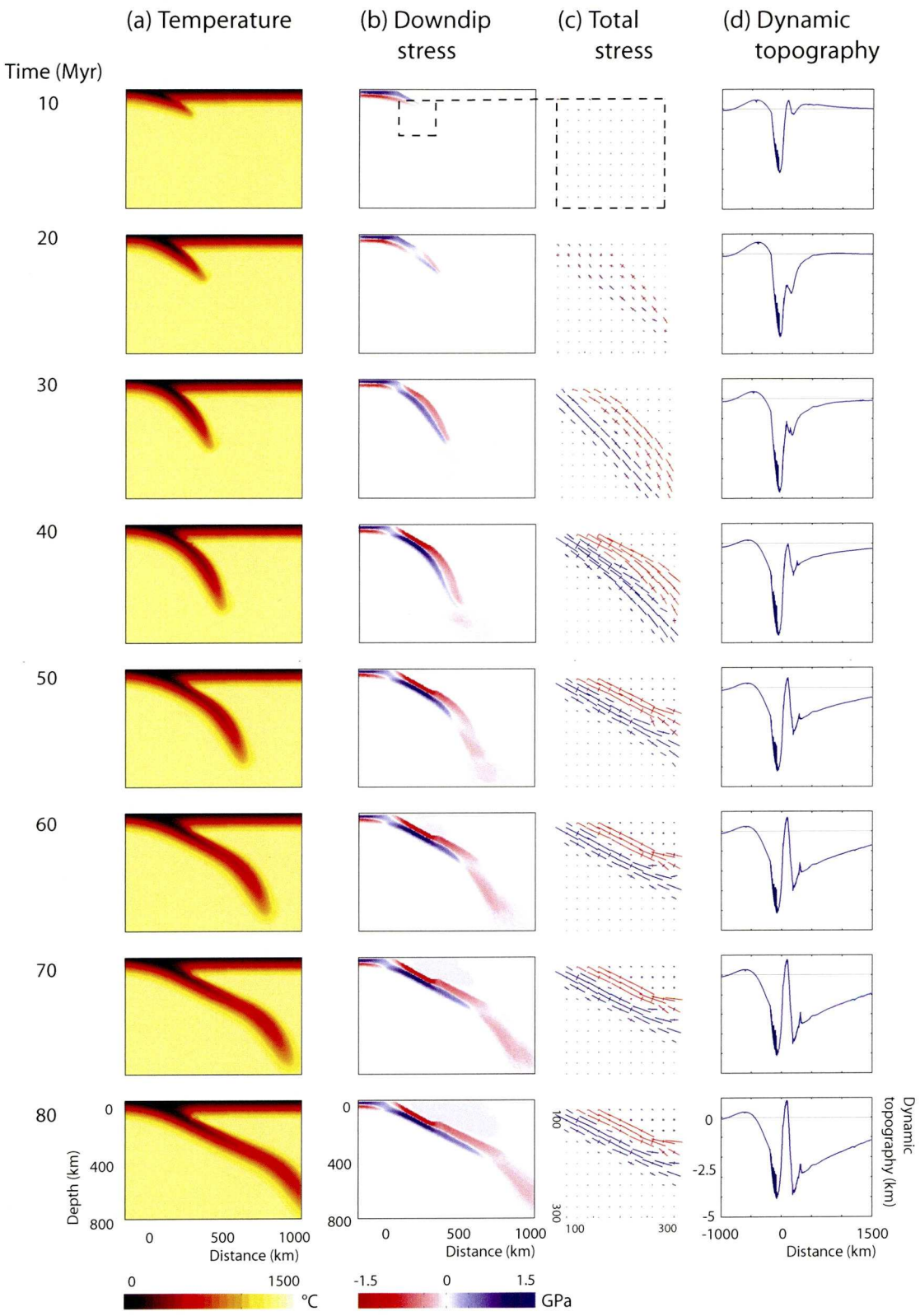


Figure 4.5: Evolution of the subduction zone over 80Myr: (a) temperature (b) downdip stress (c) principal total stress (d) dynamic topography. In the stress plots, red indicates compression, blue tension.

## 4.5 Sensitivity of slab stresses in the viscous model to the key parameters

### 4.5.1 Dependence of stresses on the age of the oceanic lithosphere

The age of the oceanic plate at the point of subduction dictates the thermal structure of the slab, which in turn controls the density and viscosity. The temperature-dependent density controls the slab pull, maintaining subduction and affecting the stresses in the slab. The temperature-dependent viscosity controls the effective width of the slab and the ease with which it can bend, which also affects the stresses within the subducting slab.

Figure 4.6 shows the difference between models with an oceanic plate age of 25Myr, 50Myr, and 100Myr at the point of subduction. All three have the same downdip stress pattern of compression over extension, although the 100Myr model reverses this trend over the top 50km due to the increased slab pull. The slab pull is dependent on the size and density of the slab; these are both controlled by the temperature. An older slab is colder, thicker, and more dense, it will therefore sink faster and penetrate further into the mantle.

### 4.5.2 Dependence of stresses in the slab on prescribed dip angle

The angle at which the oceanic plate subducts in this model is prescribed during initialisation; this angle is imposed for the first 150km by the low-viscosity zone and the mantle wedge, after which the slab is free to develop. Using a single angle for subduction initiation rather than a shallow then a deep angle or a curve is perhaps more simplistic than usually observed in subduction zones but it is also easier to examine what effect this angle has on the observed outputs.

Figure 4.7 compares models with dip angles of 20°, 30°, and 40°. The 20° model subducts well but the slab is slightly distorted along its upper edge due to the vigorous circulation occurring in the mantle wedge. The 40° model has an area of high stress along its upper edge due to the interaction with the overriding plate; below this point it is interesting to note how similar it is to the 30° model. The bulge underneath the low viscosity mantle wedge appears to be due to the small-scale convection mantle convection on the arc side of the slab.

Figure 4.8 shows the stress plots for a model with the same plate velocity as before, but a much younger oceanic plate of 25Myr. As the dip angle increases, so does the stress, as the oceanic plate is bent and forced down into the mantle by the overriding

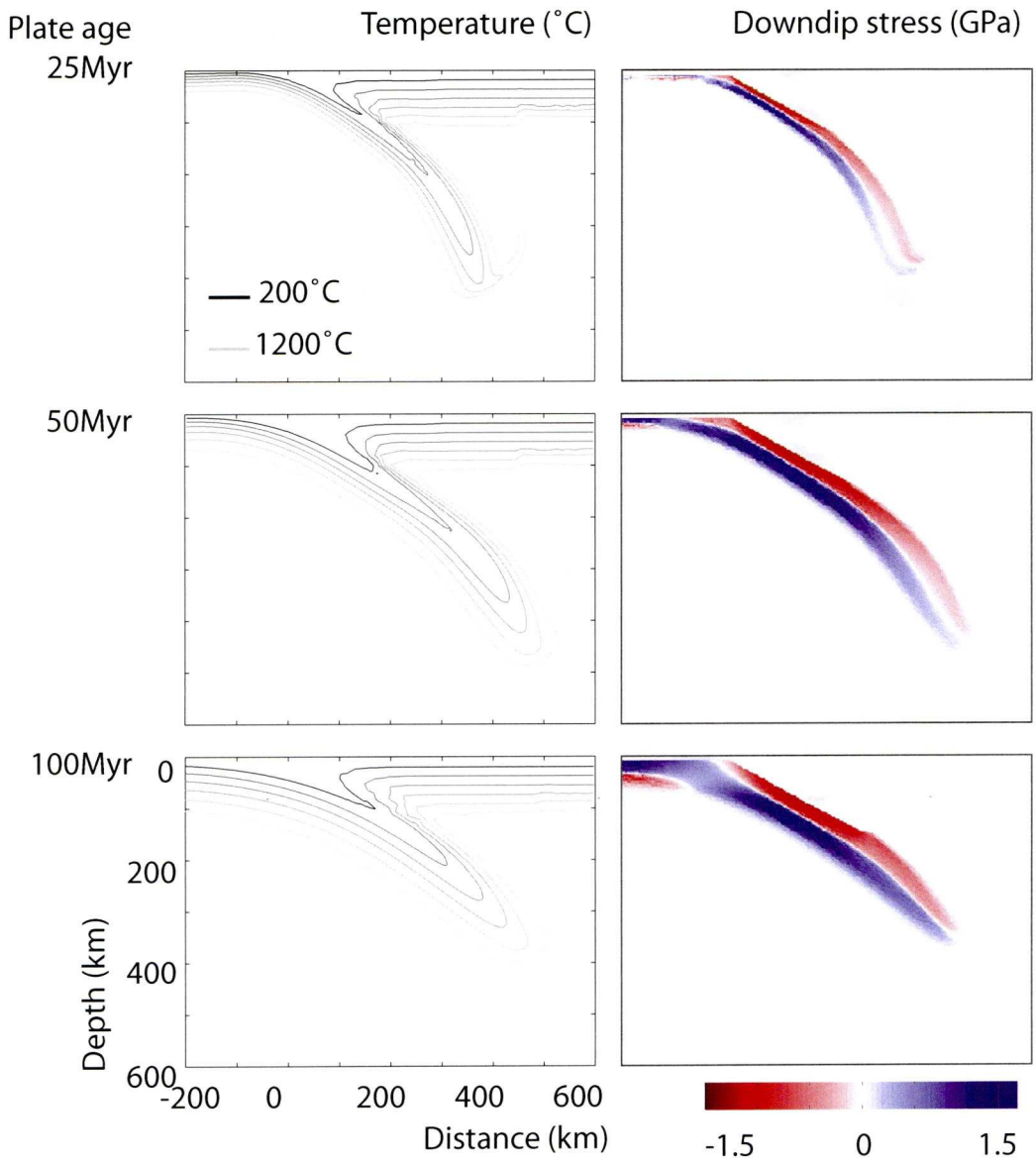


Figure 4.6: Comparison of models with different oceanic plate ages at the point of subduction: 25, 50, and 100Myr. The contours show temperature contours; the coloured areas show downdip stress (red is compression, blue is tension). Dip angle = 30°, $v_{plate}$ = 2cm/yr, $v_{rollback}$ = 2.

plate. Models with a shallow dip angle bend the least so subduction is easier to initiate than in models with high dip angles, where the large amount of bending significantly affects the stresses and geometry of the slab.

The low viscosity wedge is important in maintaining the decoupling of the overriding and subducting plates, but introduces a somewhat artificial boundary that affects the stress patterns. As the slab passes the end of the prescribed low viscosity wedge, circulation in the wedge causes the slab to bulge out underneath. This drawback of

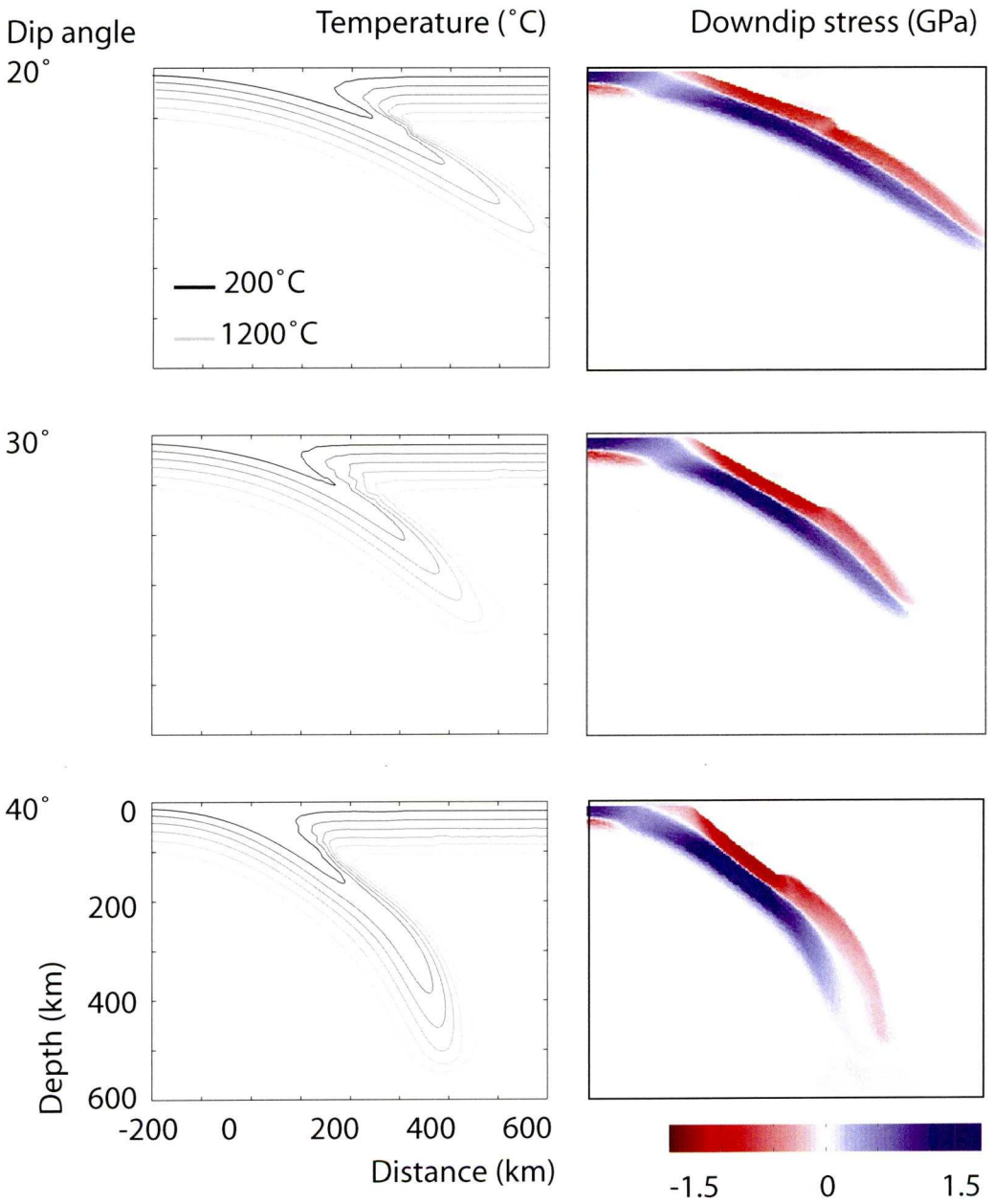


Figure 4.7: Comparison of models with dip angles of 20°, 30°, and 40°. The contours show temperature contours; the coloured areas show downdip stress (red is compression, blue is tension). Plate age = 100Myr, $v_{plate}$ = 2cm/yr, $v_{rollback}$ = 2.

including a static mantle wedge can also be seen in the models of Manea and Gurnis (2007), however the models with low dip angles are here unaffected by this distortion.

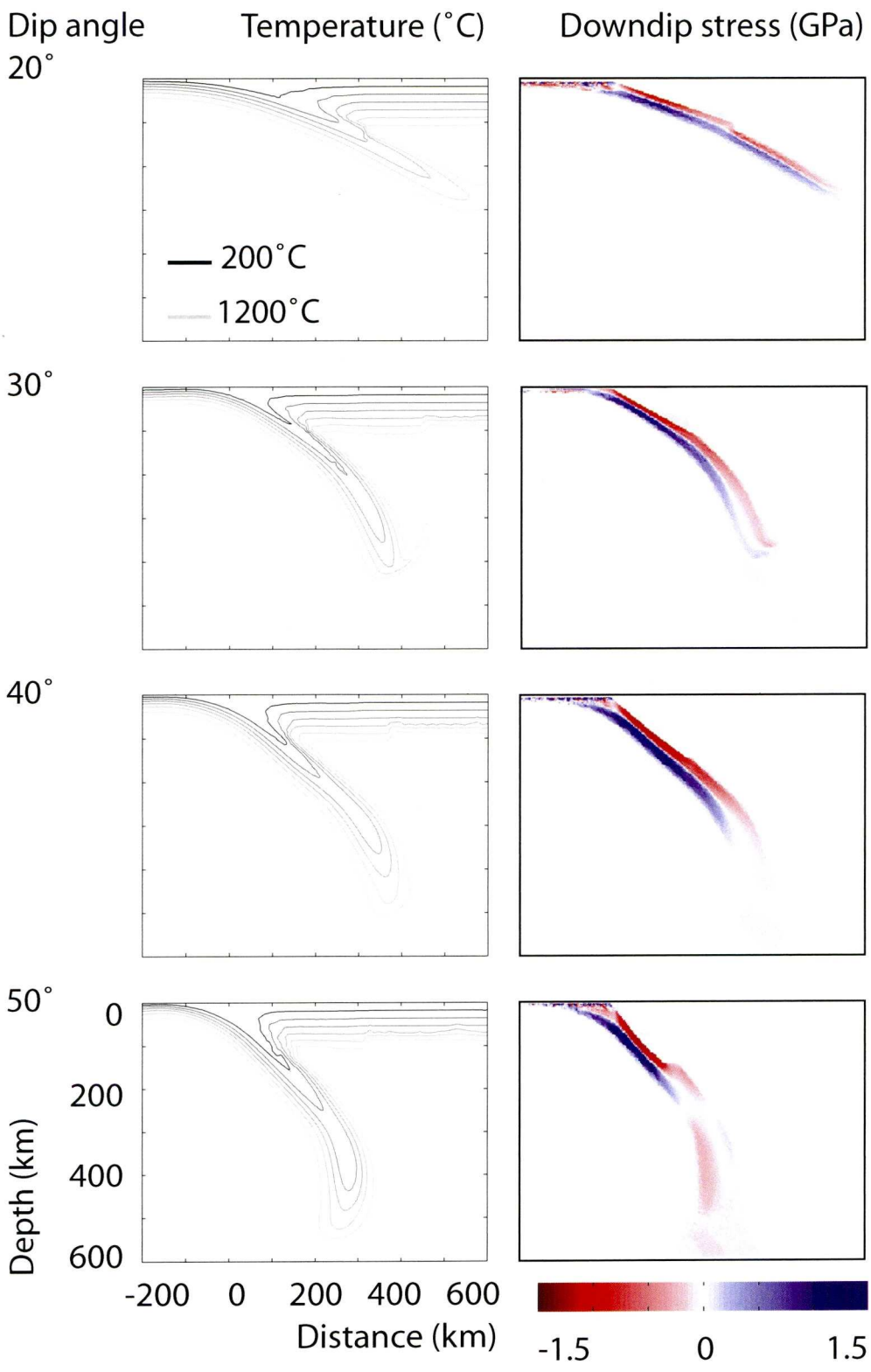


Figure 4.8: Comparison of models with dip angles of 20°, 30°, 40°, and 50°. The contours show temperature contours; the coloured areas show downdip stress (red is compression, blue is tension). Plate age = 25Myr, $v_{plate}$ = 2cm/yr, $v_{rollback}$ = 2.

### 4.5.3 Dependence of stresses in the slab on plate velocity

The primary control on subduction zone development in these models is the plate velocity, which is prescribed kinematically by a horizontal movement of the upper oceanic lithosphere towards the trench. Figure 4.9 shows models at 40Myr with different values for plate velocity.

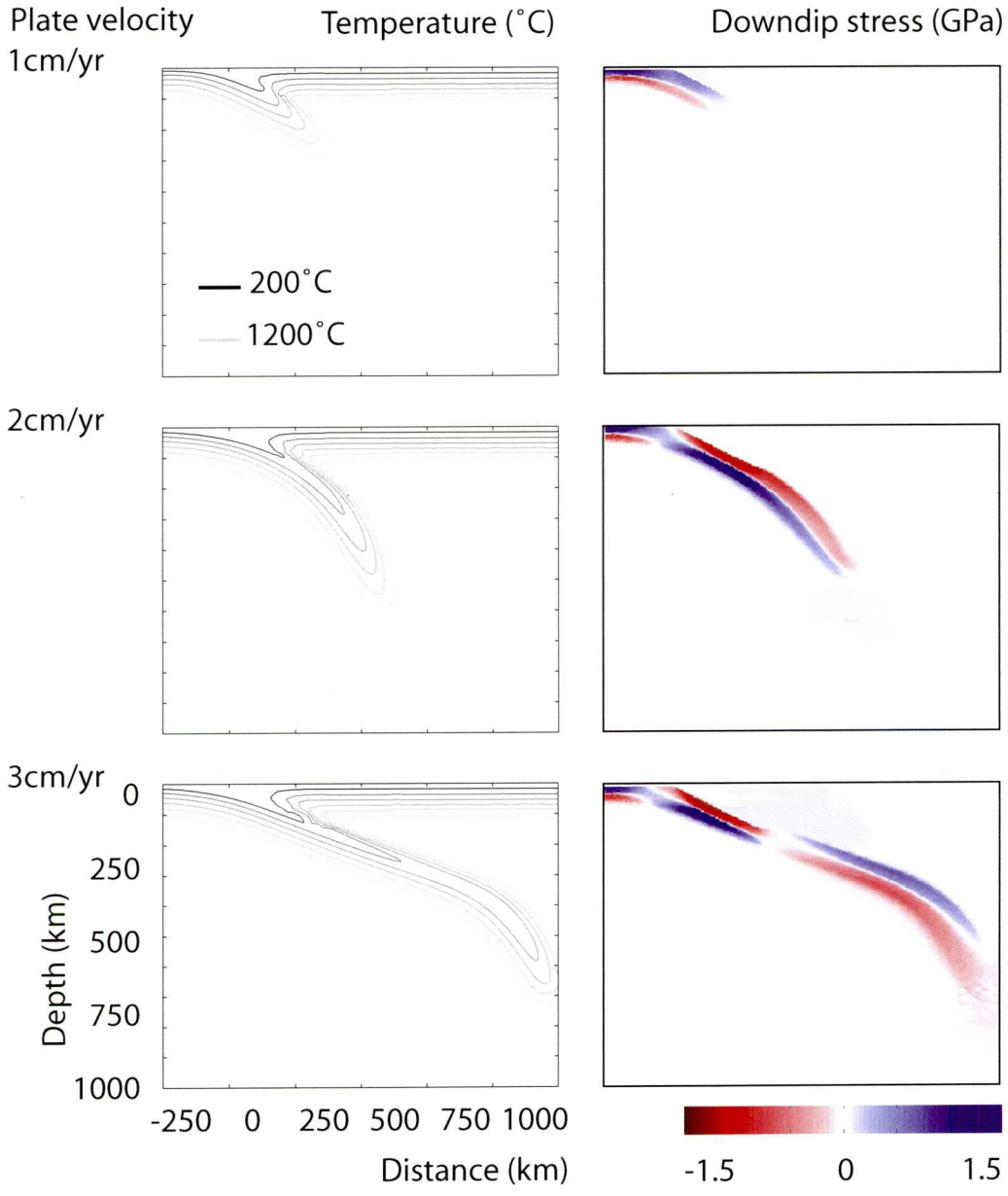


Figure 4.9: Comparison of models with plate velocity=1cm/yr, 2cm/yr and 3cm/yr. The contours show temperature contours; the coloured areas show downdip stress (red is compression, blue is tension). Plate age = 100Myr, $v_{rollback}$ = 0. All models shown at 40Myr.

Although it might be expected that a model at 40Myr with 1cm/yr would be the same as a model at 20Myr with 2cm/yr, comparison with figure 4.5 shows that this is not the case, and the 1cm/yr model appears to develop more slowly in relative terms. A more direct comparison is shown in figure 4.10. Models in figure 4.10a are shown after 60 'net' Myr of development, ie 60Myr for the 1cm/yr model, 30Myr for the 2cm/yr model, and 20Myr for the 3cm/yr model.

In figure 4.10a the 1cm/yr model is significantly less developed than the 3cm/yr model after the same net time; it has not reached as great a depth and the stresses are smaller. Figure 4.10b shows the models after 120 net Myr of development. The fastest plate motion here of 3cm/yr has not only travelled further horizontally than the other models in the same net time, but also shows an inversion of the stress pattern in the slab below approximately 200km depth.

The flow velocities for the 120 net Myr models are shown in figure 4.11: the arrows are the flow vectors, with the background colour indicating the magnitude. These vectors help to explain the differences between the models. As the slab penetrates the mantle, it induces a mantle flow, and the faster the plate velocity, the more vigorous the induced mantle flow is. The bottom boundary of the model representing the core-mantle boundary is free-slip, and therefore offers no resistance to horizontal motion. This induced mantle flow appears to assist the subduction, accelerating the progress of the faster models.

There is also a circulatory flow in the mantle wedge which can be seen in all three models. This draws in warm mantle, helping to decouple the slab from the overriding plate. It may also influence the slab development through the force it exerts on the region, and appears to act on the top edge of the slab, pulling it upwards, which is sometimes referred to as trench suction or slab suction (Forsyth and Uyeda, 1975). In the absence of stress memory, it is possible that this circulation is the cause of the slab unbending.

Figure 4.12 shows the viscosities for these models. The combination of diffusion creep, dislocation creep, and yield stress gives the slab a high-viscosity core. If the flow in the mantle wedge acts to pull the slab upwards, the slab would flex about this stiff core, producing the opposite-signed layers of stress observed in figure 4.10.

The 3cm/yr model changes from the unbending stress pattern back to bending again at approximately 200km depth as shown in figure 4.10b; if the circulation in the mantle wedge causes slab unbending, it is possible that this is the point where the slab pull becomes greater than the slab suction, and the slab begins to fall under its own weight once more.

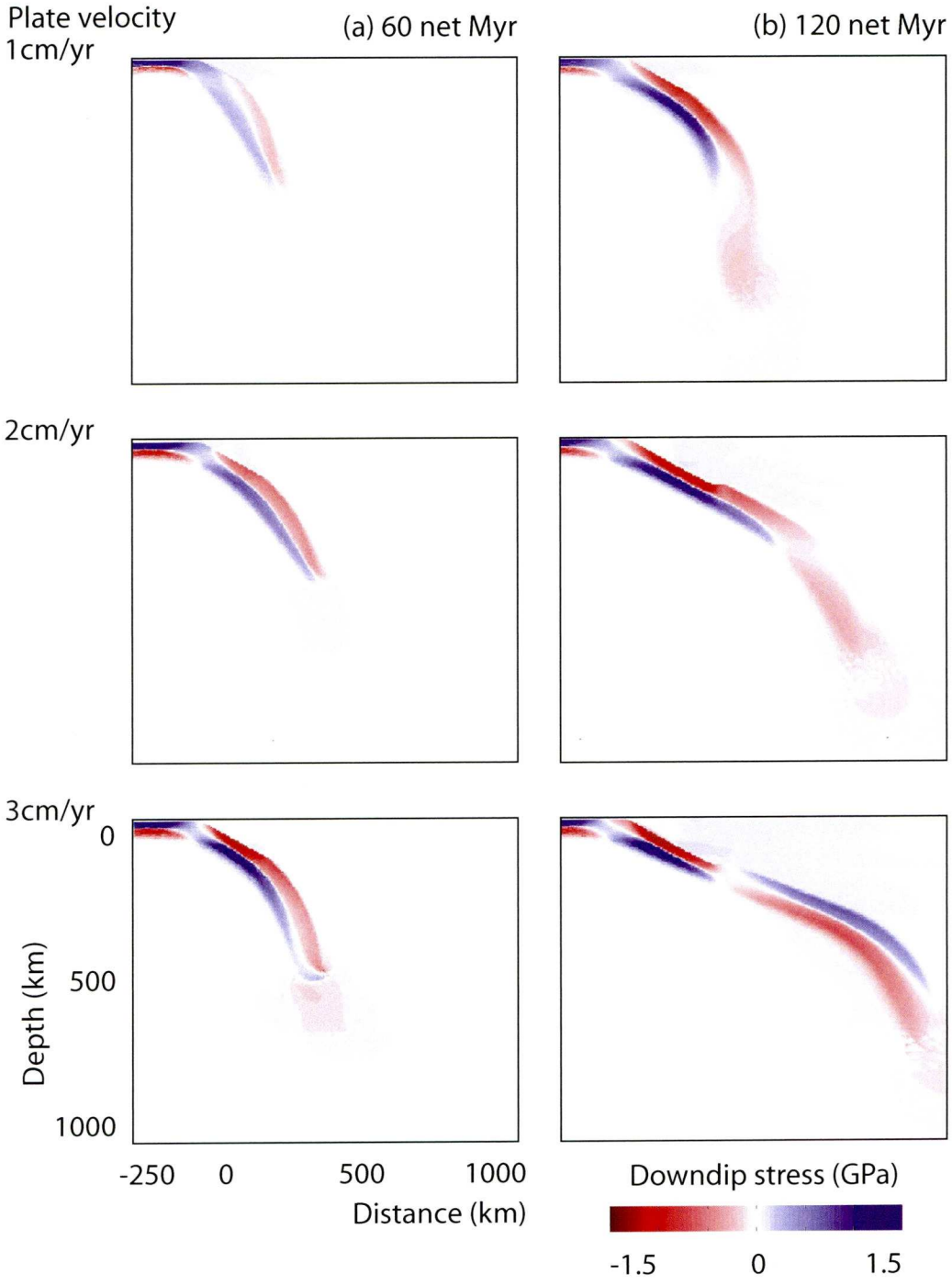


Figure 4.10: Comparison of models with plate velocity=1cm/yr, 2cm/yr and 3cm/yr. The contours show temperature contours; the coloured areas show downdip stress (red is compression, blue is tension). Plate age = 100Myr, $v_{rollback} = 0$.

### 4.5.4 Dependence of stresses in the slab on rollback velocity

In addition to the plate velocity driving the oceanic lithosphere towards the collision zone, trench rollback is also often observed in subduction zones. In this model, the

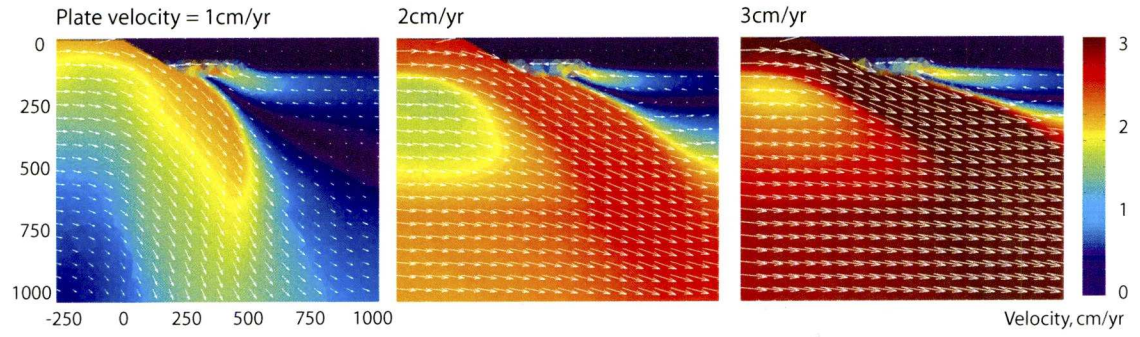


Figure 4.11: Velocities associated with models shown in figure 4.10b, at 120 net Myr. The arrows show the vectors, the background colour indicates the magnitude.

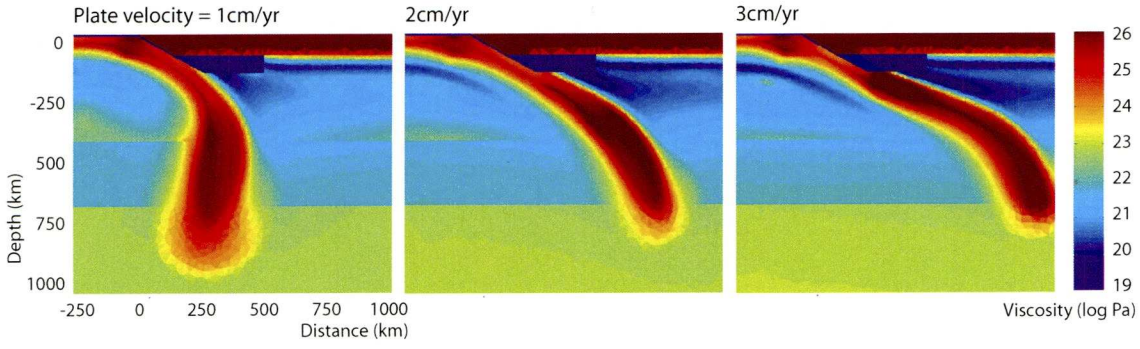


Figure 4.12: Viscosities associated with models shown in figure 4.10b, at 120 net Myr.

rollback velocity is imposed by a relative movement between the bottom of the model and the overriding plate. In conjunction with a prescribed plate velocity it can significantly affect the slab geometry and stresses; alternatively when combined with a free-slip upper boundary condition for the oceanic plate, can initiate subduction in its own right, as shown in figure 4.13. Figure 4.13a shows the model driven by prescribed motion of the top of the oceanic plate and no rollback, ie free slip on the lower boundary; figure 4.13b shows the model with free slip on the upper boundary and rollback driving subduction initiation. The disadvantage of the second model is that there is no way to impose an additional plate motion, reducing the number of governing parameters from four to three.

Figure 4.14b shows the model with a plate velocity of 2cm/yr and no rollback. Figure 4.14c is the model with a rollback velocity of 2cm/yr; figure 4.14a shows a model with a rollback of -2cm/yr for comparison, that is, a 'roll-forward'. The reference model and the $v_{roll}$=2cm/yr are very similar in geometry and stress pattern, but the slab in the rollback model has more lateral movement due to the viscous coupling of the mantle with the core-mantle boundary. The model with the 'roll-forward' is quite

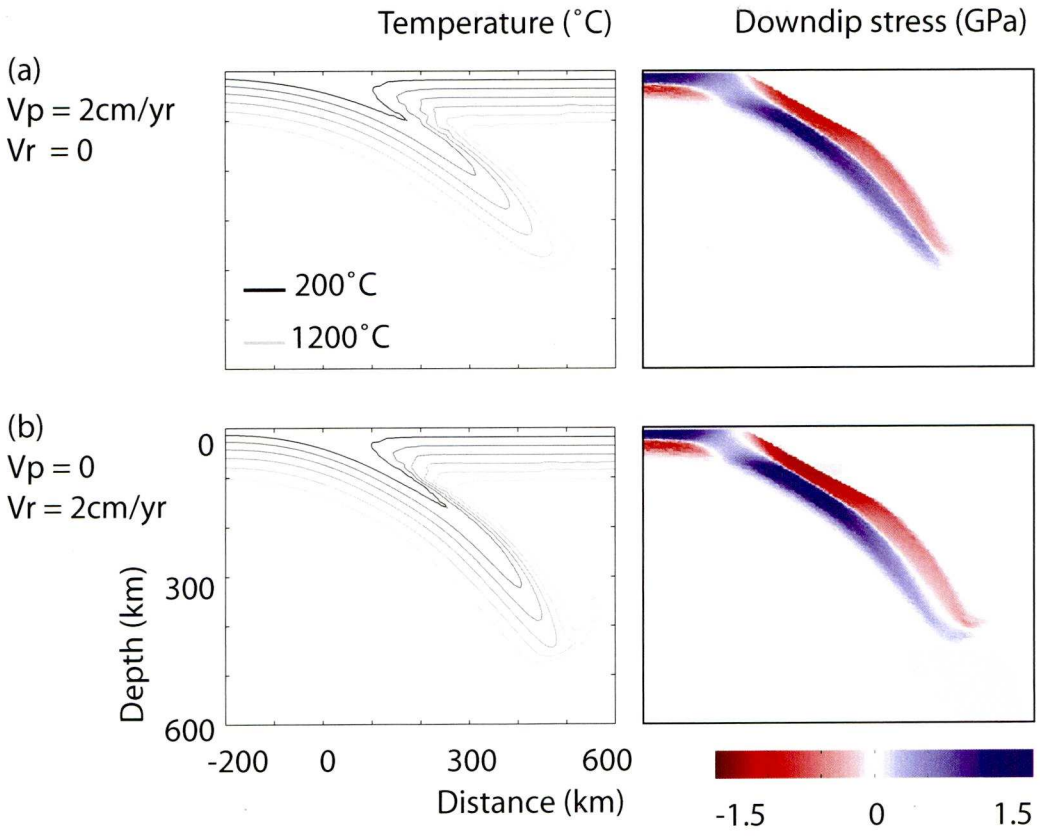


Figure 4.13: Comparison of models with convergence velocity prescribed by either (a) plate velocity or (b) rollback. Plate age = 100Myr, dip angle = 30°.

a different shape, but it is interesting to note that the double stress zone still shows the same polarity as the other two models, with compression overlaying tension, which is surprising given the geometry of the slab. Figure 4.15 showing mantle flow velocities helps to explain this phenomenon. The subduction of the slab into the mantle induces small-scale convection, and this mantle flow appears to influence the slab stress state. The low-viscosity mantle wedge encourages more vigorous circulation on the arc side of the slab, creating flows that effectively unbend the slab and produce a compressive layer over a tensile layer.

The influence rollback has on model development also depends on the other slab parameters such as plate age. Figure 4.16 shows models with young oceanic plates of only 25Myr, which are consequently hotter and with lower viscosities in the subducting slab. Figure 4.17 shows the velocities that help explain these stresses.

For a plate age of 25Myr, the slab in the model with no rollback velocity droops down under its own weight, changing the downdip stress pattern to mostly compressive, reflecting the fact that the slab is being supported by the higher viscosity tran-

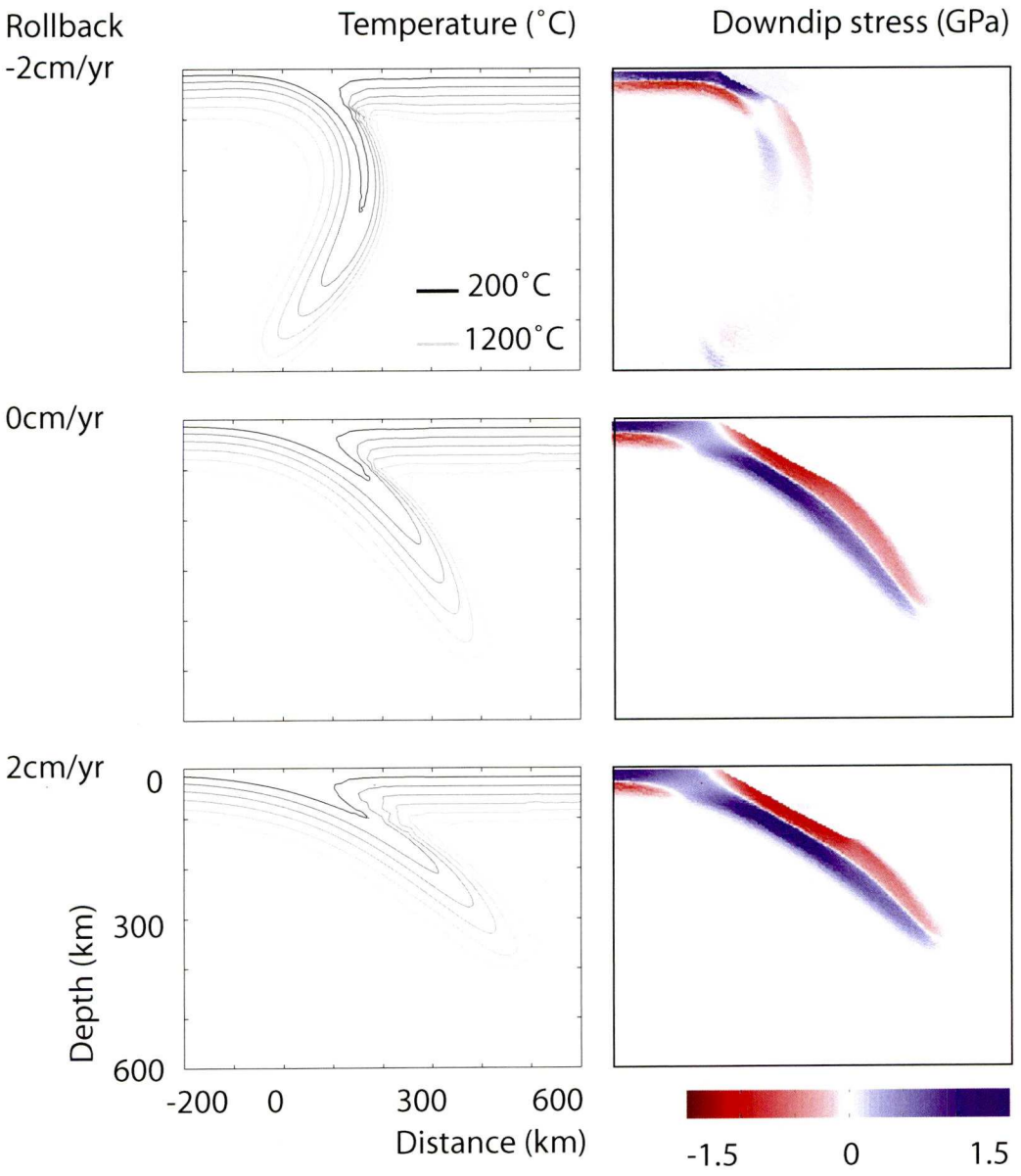


Figure 4.14: Comparison of models with rollback velocity -2cm/yr, zero, and 2cm/yr. Plate age = 100Myr, dip angle = 30°, $v_{plate}$ = 2cm/yr.

sition zone. The addition of a rollback velocity completely changes the stress pattern observed; the circulation in the arc side of the mantle is much stronger and the whole slab is swept along in the flow, which means that the slab is straightened and has a downdip stress pattern of compression over extension along its whole length.

The induced mantle flow also affects the plate velocity. Although this is initialised at 2cm/yr for both models in figure 4.16, the model with a $v_{roll}$=2cm/yr induces a vigorous mantle flow that accelerates the motion of the slab to 3cm/yr through viscous coupling.

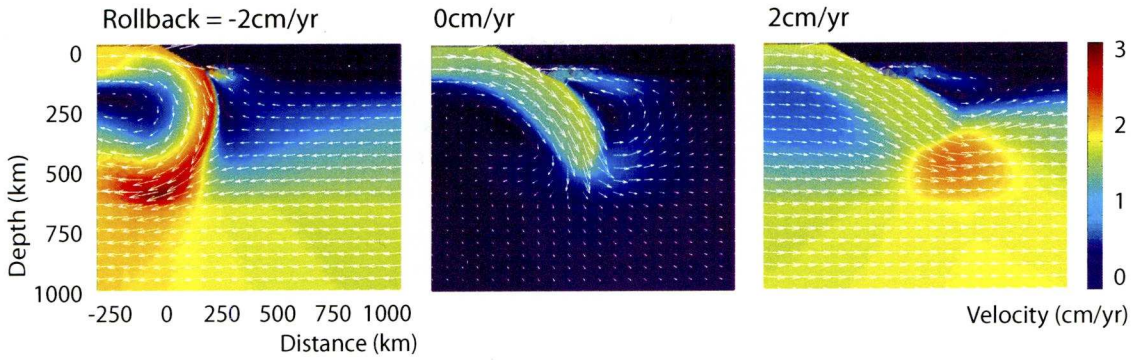


Figure 4.15: Velocities for models with rollback velocity -2cm/yr, zero, and 2cm/yr. Background color is magnitude, arrows show vectors.

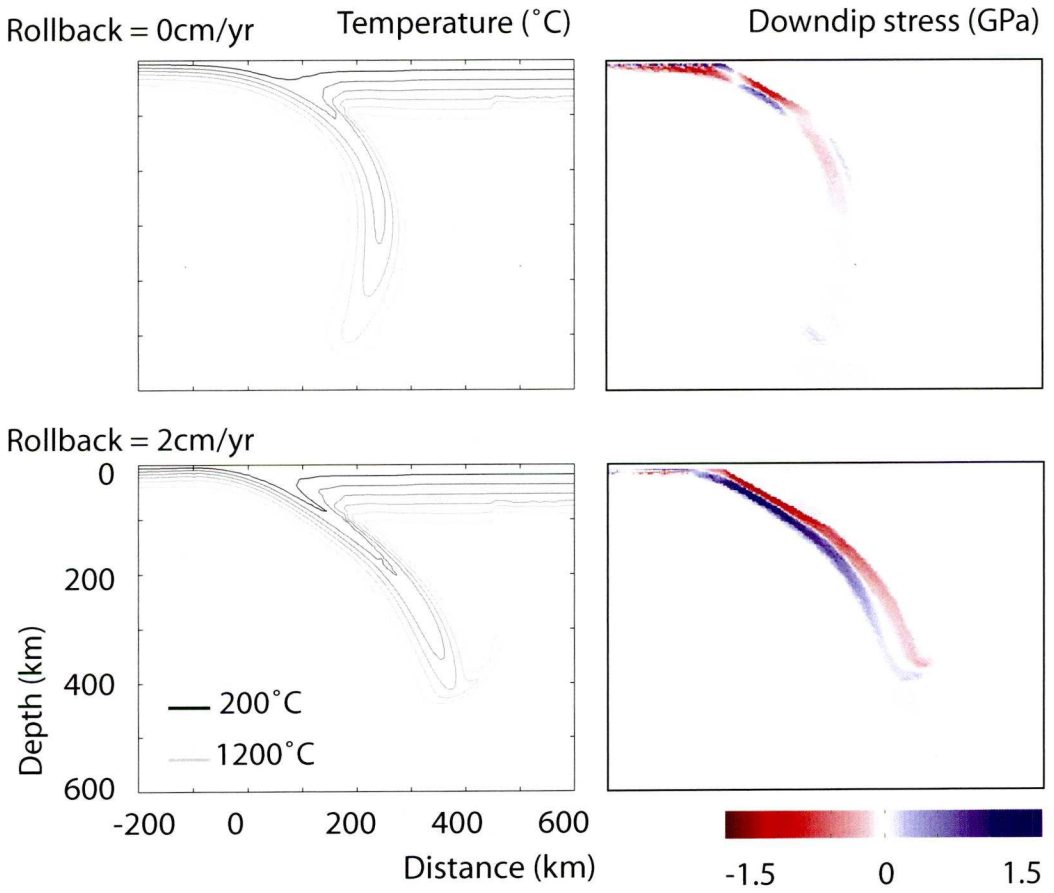


Figure 4.16: Comparison of models with and without rollback using a young, hot slab. Plate age = 100Myr, dip angle = 30°, $v_{plate}$ = 2cm/yr

The major difference between figures 4.14 and 4.16 is that the younger hotter subducting lithosphere is easier to bend, and is affected much more by the presence of rollback. The older plate is thicker and stiffer, and is affected far less. The stronger

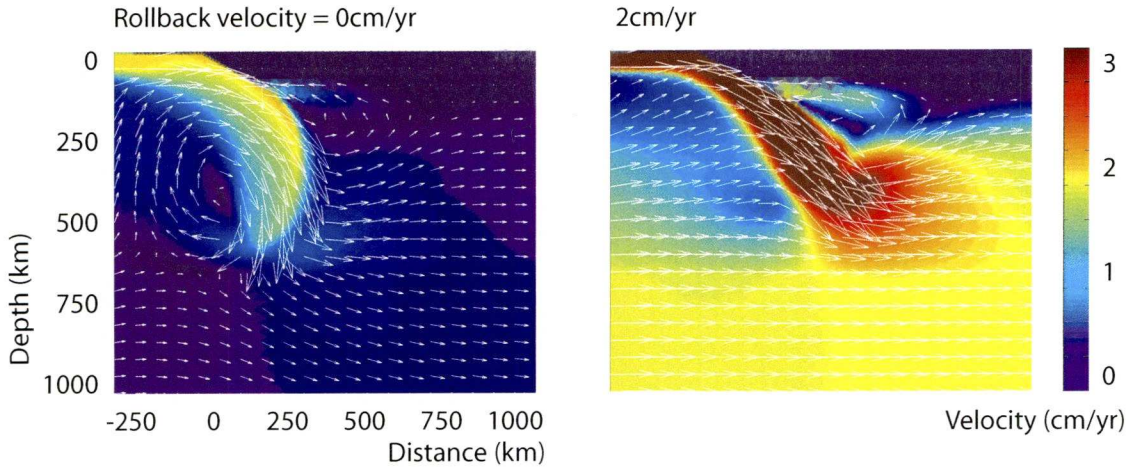


Figure 4.17: Velocities for models with rollback velocity of zero and 2cm/yr, for a plate age of 25Myr. Background color is magnitude, arrows show vectors.

influence of the rollback on the younger plate also results in variations in the stress patterns observed, whereas the older plate has a same pattern of compression over extension throughout.

## 4.6 Summary of subduction zone development and slab stresses using the 2D viscous thermo-mechanical model

The viscous thermo-mechanical model is used to develop a subduction zone under the controlling parameters of plate age, dip angle, plate velocity and rollback velocity, and the temperatures, stresses, and dynamic topographies that are produced give an insight into the processes that may occur inside the slab.

The temperature of the oceanic lithosphere at the start of subduction is controlled by the age of the plate, and this also affects the stresses that develop. Older slabs are colder and more dense, increasing their slab pull. In this model, the older slabs show tensile stresses in the top 50km of the subduction zone due to this downwards force. This increased slab pull in a cold slab, however, is accompanied by higher rigidity due to the temperature-dependent viscosity. Models comparing slabs of different ages but keeping the other parameters the same all show the same stress pattern of compression over tension after 30Myr of development. This is the 'unbending' stress pattern, but in a viscous model the unbending appears to result from flow in the mantle rather than stress memory.

The slab dip is imposed upon the model rather than being free to evolve, which

introduces some artificiality. The constraints of the model set-up geometry are hard to avoid, but for the various model parameters of plate age and velocity, a range of appropriate dip angles exist. Younger slabs are easier to bend because of their low viscosity, making subduction initiation easier, and hence they are able to subduct over a greater range of angles in this model. Within the range of angles appropriate for each model, the downdip stress patterns for each model appear quite constant.

The plate velocity and the rollback velocity of the subduction zone are distinct but related parameters; the interplay between them is one of the major controls on the stress pattern observed in the slab. The plate velocity drives the oceanic plate but also has an effect on the flow in the mantle, which affects the slab geometry and stresses. Faster plate velocities increase the mantle flow, which increases the horizontal motion of the slab and the generated stresses.

The rollback velocity has a more subtle effect on the slab and stress development. A rollback velocity equal to approximately half of the plate velocity is enough to change the flow in the mantle and with it the way the slab subducts; more rollback means a straighter slab and more horizontal subduction, less rollback means the slab subducts more vertically. This effect is minor for old plates with very high viscosities, but young plates that are less viscous are very susceptible to a change in rollback, drooping downwards under their own weight and showing a reversed stress pattern of tension over compression for their lower regions.

The stresses generated by the 2D model are always in the form of two parallel layers running down the length of the slab. The most common pattern found here is compression in the upper layer and tension beneath, although there is some variety depending on model development time. The best explanation for these results appears to be that they are a result of flow in the mantle wedge together with a visco-plastic rheology. The rheology used in the 2D model is a combination of diffusion creep, dislocation creep, and plasticity, so the implemented viscosity is both temperature and stress dependent, meaning that the slab has a high-viscosity core running down its length. The movement of the slab into the mantle induces a circulatory flow in the low-viscosity mantle wedge, which coincides with the unbending of the slab. If this circulation is strong enough to exert a significant force on the slab, it could be the cause of the slab unbending; if the slab unbends about a stiff central core, this would create a band of stress on either side of the core, with compression in the top band and tension underneath, as occurs in most of the models presented here. In models that travel significant distance horizontally, this unbending appears to continue until it is exceeded by the slab pull force, at which point it droops downwards again reversing the stress pattern to tension over compression.

The 2D viscous thermo-mechanical model presented here investigates the effects on slab development and slab stresses to the four key parameters of plate age, slab dip, plate velocity and rollback velocity that are used to represent aspects of the global mantle convection system. The magnitudes and polarities of the double stress pattern observed in these models is in good agreement with observations recorded at many seismic zones. The ubiquity of the unbending stress pattern of compression over tension is attributed to flow in the mantle, particularly in the mantle wedge, which increases with plate velocity, rollback, and dip. The dynamic topography provides an additional quality check on the models, confirming their validity, and allows conclusions drawn here about stress accumulation to be extrapolated to subduction zones worldwide.

# Chapter 5

# Modelling stress development in the subducting lithosphere using the one-dimensional visco-elastic model

## 5.1 Introduction

The Earth's mantle can be described as viscoelastic: on time scales of hundreds to millions of years, it behaves as a viscous fluid, whereas on time scales of a few seconds to hours it behaves as an elastic solid. Both of these behaviours are important to subduction zone modelling. The relative viscosities of the slab and the mantle control the movement of the slab during subduction, and it is the flow in the low-viscosity mantle wedge that helps to decouple the overriding and subducting plates. However, stress memory and stress accumulation in the lithosphere are the consequences of elasticity that lead to seismicity, and it is this behaviour that a viscoelastic model is able to explore.

A viscoelastic material accommodates deformation through elastic and viscous deformation, depending on local conditions. The brittle strength of the lithosphere increases with confining pressure and depends on its composition, which is controlled by temperature and pressure. If the lithosphere is subjected to an external lateral force, the lower lithosphere will deform by creep, transferring its stresses to the elastic upper lithosphere (Kusznir and Bott, 1977) until its brittle strength is exceeded and the lithosphere fractures (Kusznir, 1977; Mithen, 1982).

Unlike viscous fluids, viscoelastic materials have a stress memory, that is, induced stresses in cold elastic regions persist until they are either acted upon by other processes or the material heats up and enters the viscous regime. This means that stresses

are able to accumulate in the cold lithosphere and are advected with the slab, affecting the slab's development, for example, bending stresses induced in the slab as it begins to subduct also help the slab to unbend at depth. The interaction of advected stresses is likely to play an important role in the generation of earthquakes in the slab (Wang, 2002).

To investigate the accumulation of stresses in the subducting lithosphere I wrote two numerical models: a one-dimensional viscoelastic model and a two-dimensional thermal model; both models are my original work. The viscoelastic model follows a vertical slice of lithosphere through its subducting history which, despite the restriction to one dimension, still provides a useful insight into the processes of stress accumulation responsible for seismicity in the slab. The thermal model generates the temperatures for the viscoelastic calculation.

The one-dimensional viscoelastic model follows a vertical slice of lithosphere through its journey from ocean floor to subducting slab, as shown in figure 5.1. Between the ridge and the trench, the lithosphere accumulates stresses from cooling and the ridge push force. When the lithosphere begins to subduct, it acquires further stresses from bending, metamorphism, heating, and slab pull. Additionally, the viscoelastic nature of the slab redistributes stresses that decay through creep. I use the 1D model to investigate the effects of these mechanisms upon the overall slab stress state, and the relationship of this to seismicity.

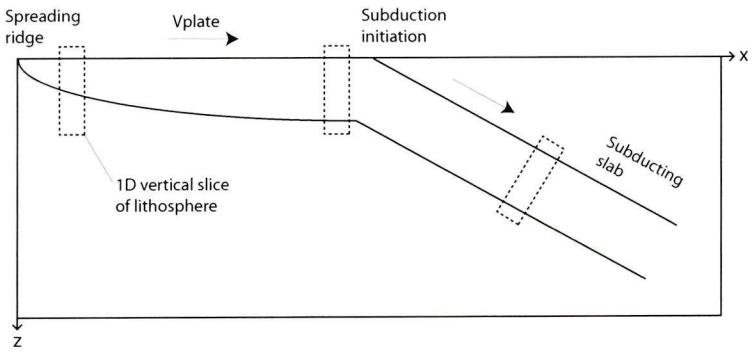


Figure 5.1: A 1D slice of lithosphere is followed on its journey from the spreading ridge to the subducting slab

## 5.2 Viscoelastic model formulation

The lithosphere accumulates stresses during both its cooling and subducting periods which ultimately generate Wadati-Benioff zone seismicity. By formulating a one-

dimensional viscoelastic model which is advected with the slab, the depth and time evolution of horizontal stresses can be investigated.

### 5.2.1 Constitutive equations of stress and strain in the lithosphere

In the Maxwell model of viscoelasticity, elastic strain $\varepsilon^e$ and viscous strain $\varepsilon^v$ are combined in series to give the total strain $\varepsilon$

$$\varepsilon = \varepsilon^e + \varepsilon^v \tag{5.1}$$

The principal stress component $\sigma$ produces an elastic strain of $\varepsilon^e = \frac{\sigma}{E}$ in the same direction and $\varepsilon^e = -\frac{\nu\sigma}{E}$ in the orthogonal directions. The total strain can be written

$$\varepsilon_x = \frac{1}{E}(\sigma_x - \sigma_x^0) - \frac{\nu}{E}(\sigma_y - \sigma_y^0) - \frac{\nu}{E}(\sigma_z - \sigma_z^0) + \varepsilon_x^v \tag{5.2}$$

$$\varepsilon_y = -\frac{\nu}{E}(\sigma_x - \sigma_x^0) + \frac{1}{E}(\sigma_y - \sigma_y^0) - \frac{\nu}{E}(\sigma_z - \sigma_z^0) + \varepsilon_y^v \tag{5.3}$$

$$\varepsilon_z = -\frac{\nu}{E}(\sigma_x - \sigma_x^0) - \frac{\nu}{E}(\sigma_y - \sigma_y^0) - \frac{1}{E}(\sigma_z - \sigma_z^0) + \varepsilon_z^v \tag{5.4}$$

$$\tag{5.5}$$

where $\varepsilon$ is total strain, $\varepsilon^v$ is viscous strain, $\sigma$ is stress, $\sigma^0$ is initial stress for brittle failure, $E$ is Young's modulus, and $\nu$, is Poisson's ratio.

Representing the lithosphere as a block of viscoelastic material to which a constant horizontal force is applied, the force balance equation can be written

$$F_x = \int_0^L \sigma_x \, dz = \text{constant} \tag{5.6}$$

where $L$ is the thickness of the lithosphere (Kusznir, 1977). If it is it assumed that the lithosphere is continuous so that all layers suffer the same total horizontal strain then we can write

$$\frac{d\varepsilon_x}{dz} = 0 \tag{5.7}$$

The viscous strain rates are given by

$$\dot{\varepsilon}_x^v = \frac{2\sigma_x - \sigma_y - \sigma_z}{6\eta} \tag{5.8}$$

$$\dot{\varepsilon}_y^v = \frac{-\sigma_x + 2\sigma_y - \sigma_z}{6\eta} \tag{5.9}$$

$$\dot{\varepsilon}_z^v = \frac{-\sigma_x - \sigma_y + 2\sigma_z}{6\eta} \tag{5.10}$$

The free surface of the Earth implies vertical stress is zero, ie $\sigma_z = 0$. Using equations 5.8 and 5.9, and the time derivatives of equations 5.2 and 5.3, some algebraic manipulation gives the change in stress with time in the x and y directions as

$$\dot{\sigma}_x = \frac{1}{L}\int_0^L \left(E\dot{\varepsilon}_v - \dot{\sigma}_x^0\right) dz - E\dot{\epsilon}_v + \dot{\sigma}_x^0 \tag{5.11}$$

$$\dot{\sigma}_y = \nu(\dot{\sigma}_x - \dot{\sigma}_x^0) - E\left(\frac{2\sigma_y - \sigma_x}{6\eta}\right) + \dot{\sigma}_y^0 \tag{5.12}$$

Integrating over time, stresses in the x and y directions can then be written as

$$\sigma_x = \int_0^T \frac{E}{(1-\nu^2)}\left(\frac{1}{L}\int_0^L \dot{\varepsilon}^v dz - \dot{\varepsilon}^v\right) dt - \frac{1}{L}\int_0^L \sigma_x^0\, dz + \sigma_x^0 \tag{5.13}$$

$$\sigma_y = \int_0^T \left(\nu\dot{\sigma}_x - E\frac{2\sigma_y - \sigma_x}{6\eta}\right) dt + \sigma_y^0 - \nu\sigma_x^0 \tag{5.14}$$

where t is time, T is total time, and the superposed dots indicate time derivatives.

The 1D viscoelastic model requires additional constraints in order to calculate the stresses in the lithosphere. Here I assume the condition of plane stress ($\sigma_y$=0), reasoning that the subducting lithosphere would be so fractured that horizontal sections would be mechanically dissociated from one another.

### 5.2.2 Viscous strain

Viscous strain is calculated from

$$\dot{\varepsilon}_x^v = \sigma_x/3\eta \tag{5.15}$$

where $\sigma_x$ is stress in the x-direction, and $\eta$ is viscosity, dependent on temperature, pressure, and stress. Viscosity is calculated for both diffusion and dislocation creep using

$$\eta = A^{-\frac{1}{n}}\dot{\varepsilon}_2^{\frac{1}{n}-1}\exp\left(\frac{E_a + PV_a}{nRT}\right) \tag{5.16}$$

where the symbols and values are given in table 5.1 (Karato and Wu, 1993; Turcotte and Schubert, 2002). These two rheologies are then combined to give the effective viscosity.

$$\eta_{\text{effective}} = \left(\frac{1}{\eta_{\text{diffusion}}} + \frac{1}{\eta_{\text{dislocation}}}\right)^{-1} \tag{5.17}$$

| Symbol | Meaning | Diffusion | Dislocation | Units |
|---|---|---|---|---|
| $\eta$ | viscosity | | | Pa s |
| T | temperature | | | K |
| P | pressure | | | Pa |
| $\sigma$ | stress | | | MPa |
| n | stress exponent | 1 | 3.5 | |
| R | gas constant | 8.314 | 8.314 | $JK^{-1}$ $mol^{-1}$ |
| $E_a$ | activation energy | 300 | 540 | kJ $mol^{-1}$ |
| $V_a$ | activation volume | $6\times10^{-6}$ | $20\times10^{-6}$ | $m^3$ $mol^{-1}$ |
| A | pre-exponential factor | $1.92\times10^{-11}$ | $2.42\times10^{-16}$ | $Pa^{-n}s^{-1}$ |

Table 5.1: Symbols, meanings and values used in viscosity calculations (Karato and Wu, 1993; Turcotte and Schubert, 2002)

### 5.2.3 Brittle Failure

In a viscoelastic material, the threshold between the viscous and elastic response is governed by temperature and pressure. In the viscous regime, large stresses lead to ductile deformation, but in the elastic regime stresses are accumulated until they cause brittle failure. To apply this concept to the viscoelastic model, the maximum stresses that can be supported by the lithosphere at a particular depth need to be determined.

Slip on a fault will occur when the dynamic frictional stress $\tau_{fd}$ is equal to or greater than the static frictional stress $\tau_{fs}$, that is,

$$\tau_{fd} = \tau_{fs} \tag{5.18}$$

$$= f_s \sigma_n \tag{5.19}$$

which is Amonton's law (Turcotte and Schubert, 2002), where $f_s$ is the coefficient of static friction and $\sigma_n$ is the normal stress, meaning large normal stresses make it difficult for sliding to initiate. In the upper lithosphere in the presence of water, this is modified to

$$|\tau| = f_s(\sigma_n - P_w) \tag{5.20}$$

where $P_w$ is hydrostatic pressure, making it easier for the rock to fail. Byerlee's law (Byerlee, 1978) gives empirically derived values for $f_s$:

$$\tau = \begin{cases} 0.85\sigma & \text{if } \sigma < 200\text{MPa} \\ 0.6\sigma + 50\text{MPa} & \text{if } 200 < \sigma < 1700\text{MPa} \end{cases}$$

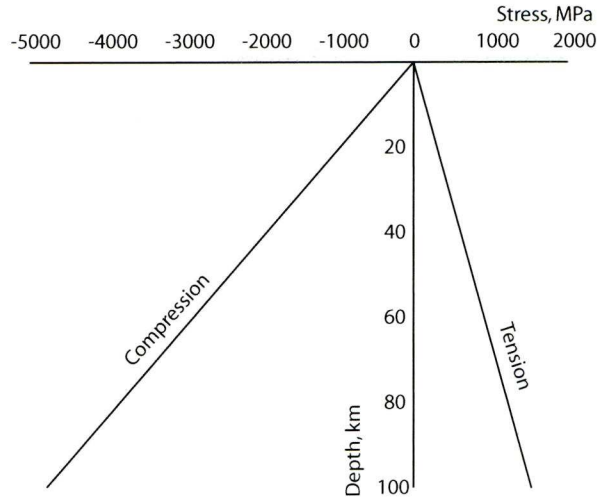


Figure 5.2: The lithosphere strength envelope (Turcotte and Schubert, 2002)

The horizontal and vertical stresses at a particular depth $z$ are given by

$$\sigma_x = \rho g z + \Delta\sigma_x \tag{5.21}$$

$$\sigma_z = \rho g z \tag{5.22}$$

where $\rho$ is the rock density, $g$ is gravity, and $\Delta\sigma_x$ is the horizontal tectonic stress. This can be used to find the normal and tangential stresses on the fault,

$$\sigma_n = \rho g z + \frac{\Delta\sigma_x}{2}(1 + \cos 2\theta) \tag{5.23}$$

$$\tau = -\frac{\Delta\sigma_x}{2}\sin 2\theta \tag{5.24}$$

These can be substituted into Amonton's law to give

$$\sigma_{xx} = \frac{\pm f_s(\rho g z - \rho_w g z)}{(1 + f_s^2)^{1/2} \mp f_s} \tag{5.25}$$

where $\rho_w$ is water density, and the upper signs are used for compression, the lower ones for tension. This can be used to find the the lithosphere strength envelope shown in figure 5.2. If stresses occur in the lithosphere that are outside the strength envelope then brittle faulting occurs, relieving the stress.

### 5.2.4 Implementing the viscoelastic model

To implement the viscoelastic model, the equations described above must be solved. First, the vertical slice of lithosphere is discretised as shown in figure 5.3.

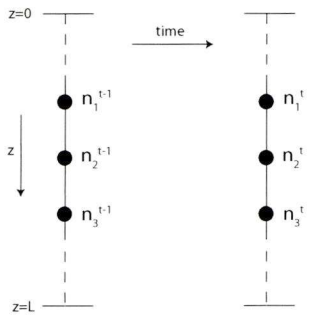


Figure 5.3: Discretisation of the lithosphere by depth and time

Each node suffers stresses, strains, and forces as described in equation 5.11; these are evaluated then combined with the total stress to give the new total stress at each node. This can be written

$$\sigma_x^{new} = \sigma_x^{old} + \dot{\sigma}_x \Delta t \tag{5.26}$$

where $\sigma_x^{new}$ is the total stress for each node at the new timestep, $\sigma_x^{old}$ is the total stress for each node at the old timestep, and $\Delta t$ is the timestep. Using values at the old timestep to calculate values at the new timestep is described as the forward difference method. This is stable as long as the timestep is kept appropriately small: in this case, the timestep is required to be

$$\Delta t < \frac{\eta_{min}}{E} \tag{5.27}$$

where $\eta_{min}$ is the minimum value of viscosity in the domain, and $E$ is Young's modulus.

The time derivative of stress for each node is performed numerically, calculating each nodal component as discussed, and using the trapezoidal rule to perform the integration. For each iteration, the total stress calculated is tested against the failure envelope described in section 5.2.3; if the stress at any node is outside the envelope, its value is reduced and the total stress for all the nodes recalculated, as if the node had suffered failure and its stresses had been redistributed through the lithosphere.

## 5.3 Applying the viscoelastic model to the lithosphere

The viscoelastic model described in section 5.2 gives the general formulation of how the constitutive equations are approximated and solved numerically to find horizontal stress in the lithosphere. This formulation is now applied to our vertical slice of lithosphere during its periods of cooling and subducting. The time derivative of horizontal stress in its basic form is given by

$$\dot{\sigma}_x = \frac{E}{L}\int_0^L \left(\dot{\varepsilon}^v + \frac{\dot{\sigma}_x^0}{E}\right) dz - E\dot{\varepsilon}^v + \dot{\sigma}_x^0 \tag{5.28}$$

where $\sigma_x$ is horizontal stress, $\varepsilon^v$ is viscous strain, $\sigma^0$ is initial stress for brittle failure, and $E$ is Young's modulus.

There are additional stresses and strains that act on the lithosphere before and during subduction, affecting the total stress state. Prior to subduction, the lithosphere is subject to the ridge push force, and thermal stresses due to cooling. During subduction, stresses are generated by bending, heating, the basalt to eclogite transition, and slab pull. Only the body forces of ridge push and slab pull are renewable sources of stress, that is, they are continually applied. These stress sources can be added into equation 5.28 so that the change in total horizontal stress with time is given by

$$\dot{\sigma}_x = \frac{E}{L}\int_0^L \left(\dot{\varepsilon}^v + \dot{\varepsilon}^T + \dot{\varepsilon}^{ecl} + \frac{\dot{\sigma}_x^0}{E}\right) dz - E\dot{\varepsilon}^v - E\dot{\varepsilon}^T - E\dot{\varepsilon}^{ecl} + \dot{\sigma}_x^0 + \dot{\sigma}^B + \frac{\dot{F}^{RP}}{L} + \frac{\dot{F}^{SP}}{L} \tag{5.29}$$

where $\dot{\varepsilon}^v$ is viscous strain rate, $\dot{\varepsilon}^T$ is thermal strain rate, $\dot{\varepsilon}^{ecl}$ is strain rate due to the transformation of basalt to eclogite, $\sigma^B$ is bending stress, $\mathrm{F}^{RP}$ is the ridge push force, $\mathrm{F}^{SP}$ is the slab pull force and L is the lithosphere thickness. Table 5.2 summarises all symbols and values, which will now be discussed in more detail.

### 5.3.1 Thermal strain

As material heats or cools, it expands or contracts. This change in volume with temperature can be written as

$$\Delta V = V\alpha_v \delta T \tag{5.30}$$

where V is volume, $T$ is temperature, and $\alpha^v$ is the volumetric thermal coefficient of expansion, $3.5\times10^{-5}\mathrm{K}^{-1}$ for the lithosphere (Turcotte and Schubert, 2002). The change in size induces thermal strain in the material, which is calculated as

$$\varepsilon^T = \alpha_l \Delta T \tag{5.31}$$

| Symbol | Meaning | Value | Units |
|---|---|---|---|
| $\sigma$ | Stress | | Pa |
| $\sigma^0$ | Initial stress at brittle failure | | Pa |
| $\sigma^B$ | Bending stress | | Pa |
| $\varepsilon^v$ | Viscous strain | | |
| $\varepsilon^T$ | Thermal strain | | |
| $\varepsilon^{ecl}$ | Basalt to eclogite volumetric strain | | |
| $F^{RP}$ | Ridge push force | $-2.8 \times 10^{12}$ | $\mathrm{Nm}^{-1}$ |
| $F^{SP}$ | Slab pull force | $5 \times 10^{12}$ | $\mathrm{Nm}^{-1}$ |
| L | Lithosphere thickness | 100 | km |
| E | Young's modulus | 100 | GPa |
| $\nu$ | Poisson's ratio | 0.25 | |
| $\alpha$ | Coefficient of thermal expansion | $3.5\times10^{-5}$ | $\mathrm{K}^{-1}$ |
| T | Temperature | | K |
| $\eta$ | Viscosity | | Pa.s |
| $f_s$ | Coefficient of friction | 0.6 | |
| $\rho$ | Density of the lithosphere | 3300 | kg $m^{-3}$ |
| $\rho_w$ | Density of water | 1000 | kg $m^{-3}$ |
| g | Gravity | 9.81 | $ms^{-1}$ |
| z | Depth | | m |

Table 5.2: Parameters used in the viscoelastic model (Turcotte and Schubert, 2002)

where $\varepsilon^T$ is the thermal strain, and $\alpha_l$ is the linear coefficient of thermal expansion. The viscoelastic model assumes that any volumetric change due to thermal expansion or contraction occurs equally in all directions, although this is not necessarily the case due to the constraints acting upon the lithosphere. However, in the context of a 1D model, and given the relatively small effect the thermal strain has upon the total stress, this is considered to be an acceptable approximation.

### 5.3.2 Bending stress

The subducting slab starts bending just before the subduction zone to allow subduction to commence; when it is below the overriding plate it begins to unbend.

The bending stress in the x direction along the neutral core of the plate is written as

$$\sigma^B = \frac{-E}{1-\nu^2}\,\varepsilon^B \tag{5.32}$$

where $E$ is Young's modulus, $\nu$ is Poisson's ratio, and $\varepsilon^B$ is bending strain (Turcotte and Schubert, 2002). The bending strain is given by

$$\varepsilon = -(z - \frac{L}{2})\,\frac{\partial^2 w}{\partial x^2} \tag{5.33}$$

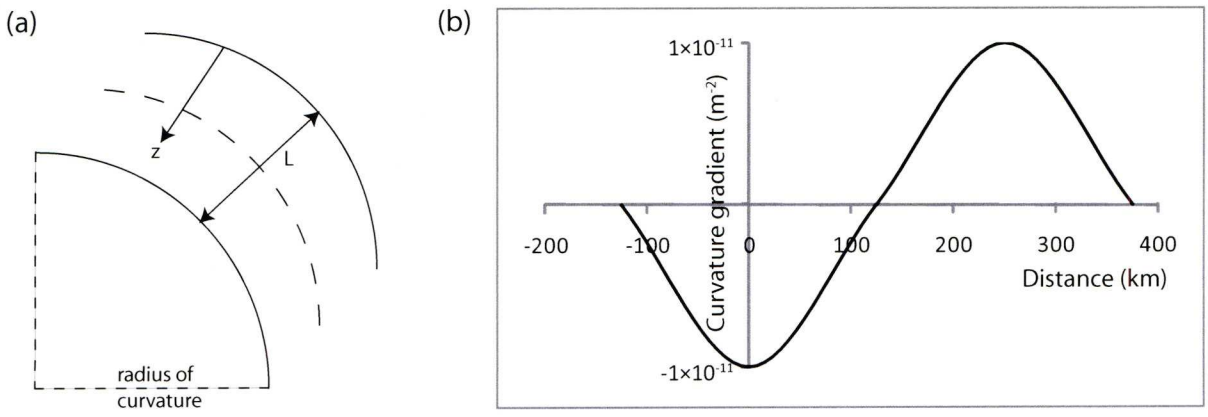


Figure 5.4: Bending stresses in the subducting slab: (a) lithosphere bending geometry; (b) applying the curvature gradient to the slab.

where $z - \frac{L}{2}$ is the vertical distance from the central neutral fibre of the lithosphere based on z-coordinate and lithosphere thickness $L$ as shown in figure 5.4, and $w$ is the deflection. The bending strain rate can then be calculated as

$$\dot{\varepsilon}_x^B = (z - \frac{L}{2}) \frac{\partial}{\partial t} \frac{\partial^2 w}{\partial x^2} \tag{5.34}$$

$$= (z - \frac{L}{2}) \frac{\partial x}{\partial t} \frac{\partial}{\partial x} \frac{\partial^2 w}{\partial x^2} \tag{5.35}$$

$$= (z - \frac{L}{2}) v_{sub} \frac{\partial^3 w}{\partial x^3} \tag{5.36}$$

where $v_{sub}$ is the subduction velocity, and $\partial^3 w / \partial x^3$ is the curvature gradient of the slab, assuming that the profile shape is constant in space and time. A typical value of curvature gradient of $1 \times 10^{-11} \mathrm{m}^{-2}$ (Theodoridou, 2008) is applied here sinusoidally over a wavelength of 500km (Chase et al., 2009), as shown in figure 5.4b. In the sign convention used here, the minimum curvature gradient which occurs at the trench is associated with the highest bending rate. The maximum curvature gradient which occurs about 250km away from the trench indicates the highest unbending rate.

### 5.3.3 Basalt to eclogite transition

The basaltic oceanic crust makes up the top 7km of the lithosphere; during subduction, the increase in temperature and pressure transforms the basalt to eclogite. Since eclogite is denser than basalt, this transformation is associated with a volumetric reduction of approximately 10%, inducing tension in the crust and compression in the mantle beneath (Kirby et al., 1996).

In the 1D model, this strain is applied linearly to the top 7km representing the slab crust whilst it is between the temperatures of 200°C and 700°C (Hacker et al., 2003). A simplistic temperature-pressure relationship is assumed here, so pressure is neglected.

$$\varepsilon^{ecl} = \begin{cases} 0 & \text{T} < 200^{\circ}\text{C} \\ 0.1 \times \frac{T-200}{700-200} & 200^{\circ}\text{C} < \text{T} < 700^{\circ}\text{C} \\ 0 & \text{T} > 700^{\circ}\text{C} \end{cases}$$

where $\varepsilon^{ecl}$ is the strain due to the metamorphism, and T is the temperature. The strain generated by the basalt to eclogite transition is approximately two orders of magnitude greater than the thermal strain for the same change in temperature.

### 5.3.4 Ridge push

While the oceanic plate is still at the surface prior to subduction, it is subject to the ridge push force. This is due to gravitational sliding of the newly-formed plate down and away from the topographic high of the ridge (Fowler, 2005), as shown in figure 5.5. A typical value for the ridge push force is estimated to be $-2.8 \times 10^{12}$ $\text{Nm}^{-1}$ (Dahlen, 1981), generating stresses of 20-30MPa in the lithosphere (Bott and Kusznir, 1984). This force is applied uniformly to the oceanic lithosphere prior to subduction.

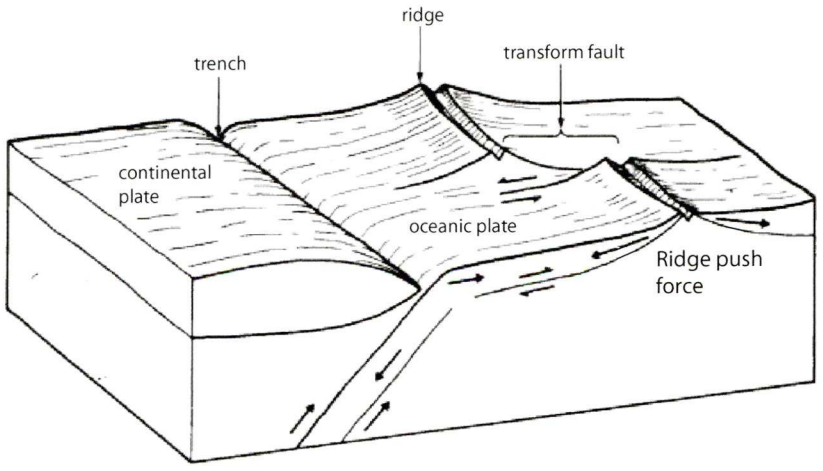


Figure 5.5: The ridge push force acting on the oceanic plates (Brown and Mussett, 1981)

Although the ridge push force is not the largest source of stress, it is a renewable stress source because its presence persists even though the strain it produces is being dissipated (Bott and Kusznir, 1984). If the slab is subject to these cumulative stresses

for a long time prior to subduction, this could have a significant effect on the total stress state at the start of subduction.

### 5.3.5 Slab pull

The negative buoyancy of the slab makes it sink into the mantle and is known as slab pull, shown in figure 5.6.

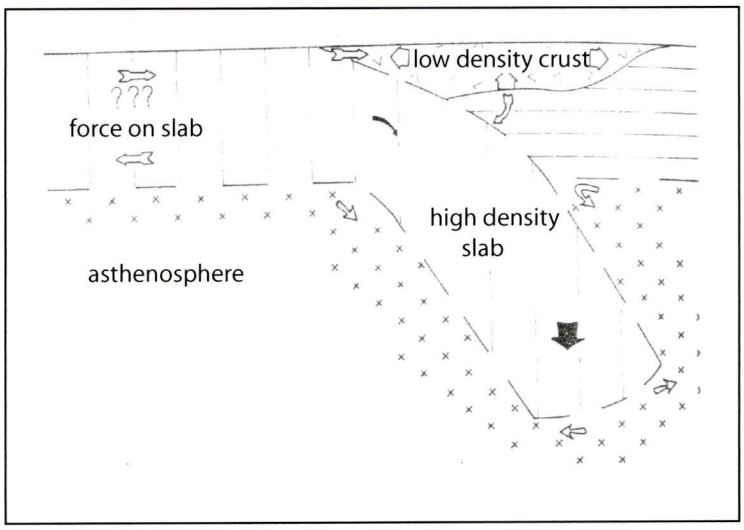


Figure 5.6: The slab pull force acting on the oceanic plate (Sleep, 1979)

Slab pull is estimated at $5 \times 10^{12}$ $\mathrm{Nm}^{-1}$ (Bott, 1993). Although this is larger than the ridge push force, it is counteracted by forces such as slab resistance, and bending (Bott and Kusznir, 1984). Slab pull is also a renewable stress, so whilst non-renewable stresses are being dissipated, slab pull is still being applied meaning that at great depths it may be the only cause of stress that persists.

The slab pull acting on any given point would be expected to decrease down the length of the slab, but the 1D viscoelastic model assumes a constant slab pull throughout the duration of subduction based on an estimate of the total average force acting. However, the small impact of the slab pull on the total stress state of the slab means this approximation is unlikely to introduce significant errors.

## 5.4 Thermal model

Stresses in the lithosphere arising from cooling prior to subduction, heating during subduction and the basalt to eclogite transition are all temperature-dependent processes. Additionally, the temperature-dependent rheology controls the response of

the lithosphere to stress and deformation by creep. The high sensitivity of the total stress profile in the slab to temperature means that using an accurate thermal model is very important.

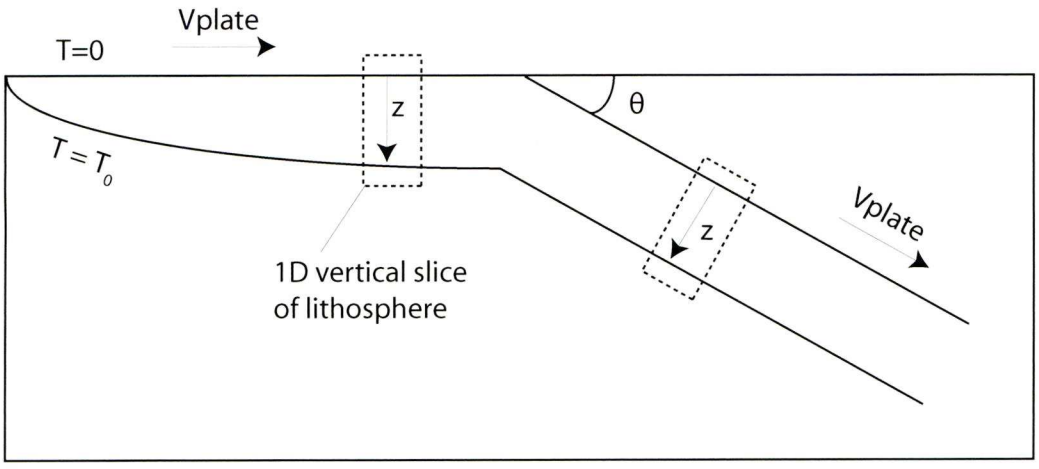


Figure 5.7: The model domain and parameters

The lithospheric temperatures required by the viscoelastic model can be calculated in one or two dimensions using the finite difference method to solve the thermal advection-diffusion equation. Given that the temperature of the lithosphere is affected by its interaction with the thermal state of the whole domain, a two-dimensional temperature calculation is likely to give more accurate results. Here a 2D thermal model is described, from which the temperatures in the lithosphere are extracted for each timestep and used in the viscoelastic model. The model subduction zone is shown in figure 5.7.

### 5.4.1 Solving the thermal advection-diffusion equation with the finite difference method

The thermal advection-diffusion equation can be written

$$\frac{\partial T}{\partial t} = \frac{1}{\rho C_p} \nabla.(k \nabla T) - \underline{v}.\nabla T \tag{5.37}$$

where $T$ is temperature, $t$ is time, $\underline{v}$ is velocity, $\rho$ is density, $C_p$ is specific heat capacity, and $k$ is is thermal conductivity.

Treating time as a series of timesteps, if the the change in temperature with time $\partial T/\partial t$ is found from equation 5.37, then this can be used with the temperature at time

$t_{old}$ to calculate the new temperature at time $t_{new}$,

$$T(t_{new}) = T(t_{old}) + \frac{\partial T}{\partial t}\Delta t \tag{5.38}$$

where $\Delta t$ is the time step. This is known as the explicit, or forward difference method, which has a maximum timestep for stability of

$$\Delta t \leq \frac{k\,(min(\Delta x, \Delta z))^2}{2\,\rho C_p} \tag{5.39}$$

where $\Delta x$ and $\Delta z$ are the grid spacings used to discretise the domain.

In order to solve the thermal advection-diffusion equation and find $\partial T/\partial t$, a finite difference scheme is used. The domain is discretised into regularly spaced nodes as shown in figure 5.8, and where each node is initiated with a temperature.

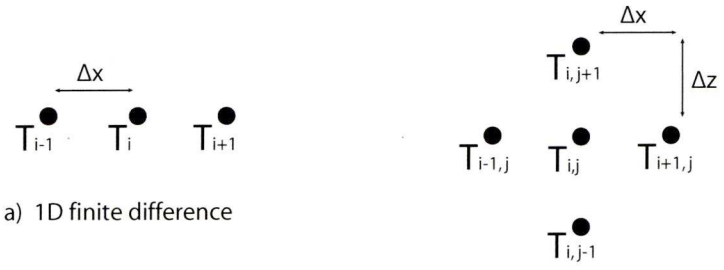


Figure 5.8: Discretisation of domain into nodal points

The governing thermal differential equation is then approximated by calculating spatial derivatives for temperature at each node. In a one-dimensional situation such as shown in figure 5.8a, this can be calculated numerically using the central difference approximation (Majumdar, 2005),

$$\frac{\partial T}{\partial x} = \frac{T_{i+1} - T_{i-1}}{2\Delta x} \tag{5.40}$$

In a similar way, second derivatives can be calculated,

$$\frac{\partial^2 T}{\partial x^2} = \frac{T_{i+1} + T_{i-1} - 2T_i}{\Delta x^2} \tag{5.41}$$

In two dimensions as shown in fig 5.8b, the second derivative can be found using

$$\nabla^2 T = \frac{\partial^2 T}{\partial x^2} + \frac{\partial^2 T}{\partial z^2} \tag{5.42}$$

$$= \left( \frac{T_{i-1,j} + T_{i+1,j} - 2T_{i,j}}{\Delta x^2} \right) + \left( \frac{T_{i,j+1} + T_{i,j-1} - 2T_{i,j}}{\Delta z^2} \right) \tag{5.43}$$

Using values of $\rho = 3300 kgm^{-3}$, $C_p = 1000 Jkg^{-1}K{-}1$, and $k = 3.5 Wm^{-1}K^{-1}$ (Turcotte and Schubert, 2002), the diffusion part of equation 5.37 can be calculated. To calculate the advection term, the velocities in the subduction zone must be found.

### 5.4.2 Velocities in the subduction zone

In order to find the advection term of the thermal finite difference formulation, the velocities in the subduction zone need to be found. Velocity, $\underline{v}$ is calculated from the cornerflow solution of Batchelor (1967) for both the arc and oceanic corners. The velocity in polar coordinates is

$$\underline{V} = \left[ \frac{1}{r} \frac{\partial \psi}{\partial \theta}, -\frac{\partial \psi}{\partial r} \right] \tag{5.44}$$

which can be divided into angular and radial components

$$v_r = \frac{1}{r} \frac{\partial \psi}{\partial \theta} = \frac{1}{r} \frac{\partial}{\partial \theta} (r f(\theta)) = f'(\theta) \tag{5.45}$$

$$v_\theta = -\frac{\partial \psi}{\partial r} = \frac{\partial}{\partial r} (r f(\theta)) = f(\theta) \tag{5.46}$$

The stream function can be written as

$$\psi = r f(\theta) = r\Theta \tag{5.47}$$

where

$$\nabla^2 [\nabla^2 \psi] = 0 \tag{5.48}$$

$$\nabla^2 [\nabla^2 \psi] = \frac{1}{r^3} \left( \frac{\partial^4 \Theta}{\partial \Theta^4} + \frac{2\partial^2 \Theta}{\partial \Theta^2} + \Theta \right) = 0 \tag{5.49}$$

which has the general solution

$$f(\theta) = A \sin\theta + B \cos\theta + C\theta \sin\theta + D\theta \cos\theta \tag{5.50}$$

Solving to find these constants in the arc and oceanic corners and substituting back into the equation gives angular and radial velocities as follows.

Arc corner:

$$v_r = \frac{U}{\theta_a^2 - \sin^2\theta_a}\left[\sin\theta_a(\theta\theta_a\sin\theta - \sin\theta + \theta\cos\theta) + \cos\theta_a(\theta_a\sin\theta + \theta\theta_a\cos\theta)\right]$$
$$v_\theta = \frac{-U}{\theta_a^2 - \sin^2\theta_a}\left[(\theta_a - \theta)\sin\theta_a\sin\theta - \theta_a\theta\sin(\theta_a - \theta)\right] \tag{5.51}$$

Oceanic corner:

$$v_r = \frac{-U}{\theta_o + \sin\theta_o}\left[\sin(\theta_o - \theta) - \sin\theta + (\theta_o - \theta)\cos\theta - \theta\cos(\theta_o - \theta)\right]$$
$$v_\theta = \frac{U}{\theta_o + \sin\theta_o}\left[(\theta_o - \theta)\sin\theta + \theta\sin(\theta_o - \theta)\right] \tag{5.52}$$

where $U$ is the scaling velocity and $\theta_a$ and $\theta_o$ are the arc and oceanic angles respectively.

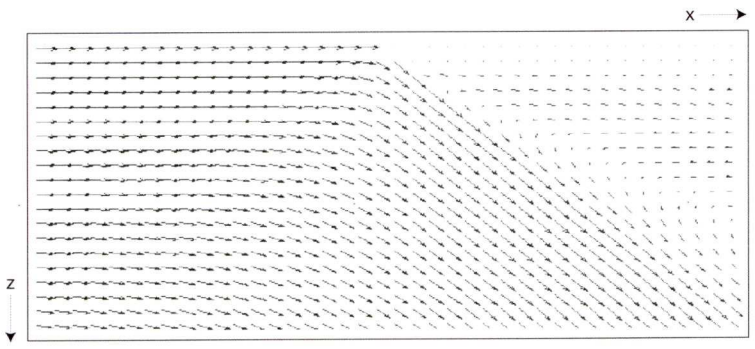


Figure 5.9: Corner flow velocity vectors for the subduction zone

Figure 5.9 shows the velocity vectors this produces for the subduction zone, which are then used in the finite difference calculation to develop temperatures for the subduction zone.

### 5.4.3 Temperatures produced by the 2D thermal model

The thermal model solves the thermal advection-diffusion equation using the corner-flow velocities, and calculates the temperatures across the subduction zone using the parameters of velocity, plate age, and slab dip. Typical temperatures calculated for a subduction zone are shown in figure 5.10.

To incorporate these temperatures into the 1D viscoelastic model, the coordinates of the vertical slice lithosphere under consideration are used to map the position of the 1D slice onto the 2D thermal model as shown in figure 5.11, and the temperatures for each node are extracted.

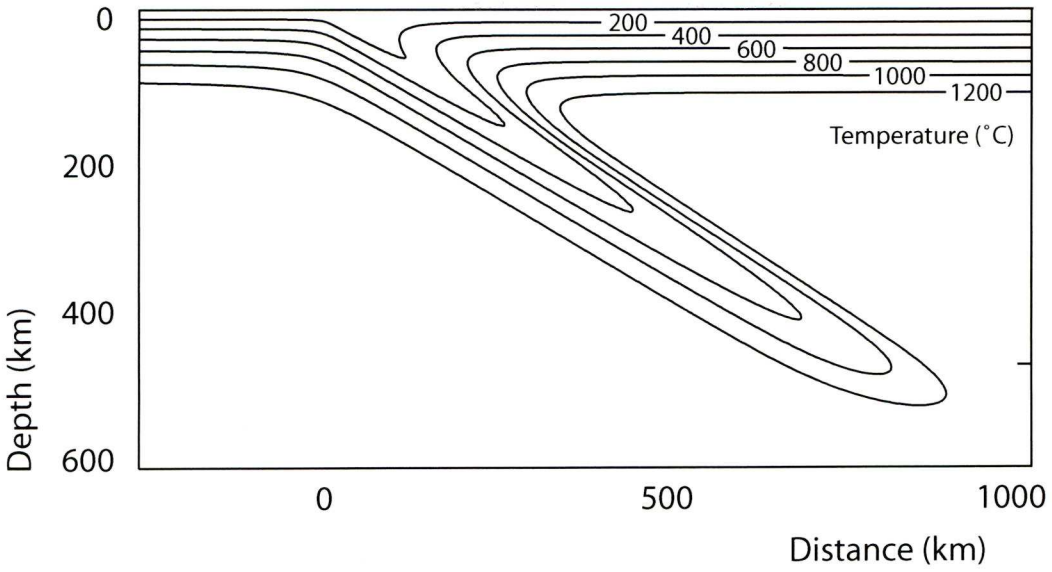


Figure 5.10: Temperature contours for the subduction zone as calculated in 2D thermal advection-diffusion model

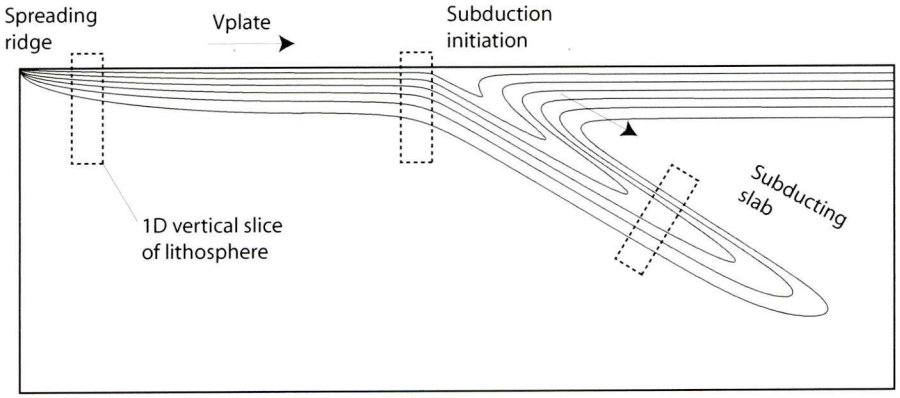


Figure 5.11: Mapping of 1D viscoelastic model onto 2D thermal model to extract temperatures

## 5.5 Summary of the viscoelastic model

The one-dimensional model follows a vertical slice of lithosphere from the spreading ridge to the trench and into the subduction zone, predicting stress development. Before subduction, thermal stresses and the ridge push force determine the stress-depth profile of the slab; during subduction the slab is subject to viscous stresses, thermal stresses, metamorphic stresses, bending stresses and the slab pull force. The total stress profile is heavily dependent on slab temperatures, which are extracted from a two-dimensional thermal model. Stress memory, stress transfer, and brittle failure

are all included in the viscoelastic model. The stresses in the lithosphere prior to and during subduction can be found by calculating the stresses acting on the slab at each timestep and propagating this forwards with time.

Chapter 6 presents sensitivity tests and results from this model and applies them to observations from subduction zones. Chapters 7 and 8 use the model to investigate stress accumulation in subduction in north Chile and northeast Japan.

# Chapter 6

# Stress accumulation in the subducting slab: results from the one-dimensional viscoelastic model

## 6.1 Introduction

The viscoelastic model described in chapter 5 is formulated to investigate stress development in the subducting lithosphere. A one-dimensional, vertical slice of the lithosphere is tracked from the mid-ocean ridge and down through the subduction zone, as shown in figure 6.1. Forces such as ridge push and slab pull, and strains from bending and volume changes act upon the slab to induce stresses. Since this is a viscoelastic model and the slab has a stress memory, large stresses can accumulate in the cool, high viscosity regions. Renewable stresses produce creep in the warmer regions of the lithosphere, transferring the stress to the elastic upper lithosphere. If this stress exceeds the brittle strength of the lithosphere, it will fracture and fail, causing seismicity.

The results of this viscoelastic model are presented here. The importance of the stress history from the cooling ocean basin is explored, as well as the differences that result from using different temperature profiles. The sensitivity of the model to the various sources of stress is investigated, using models that include or exclude each stress source in turn. The sensitivity of the stresses to the model variables of plate age, slab dip, and subduction velocity are examined. These numerical experiments will help to determine what the primary controls on the slab stress profile are, and how the stresses develop over time.

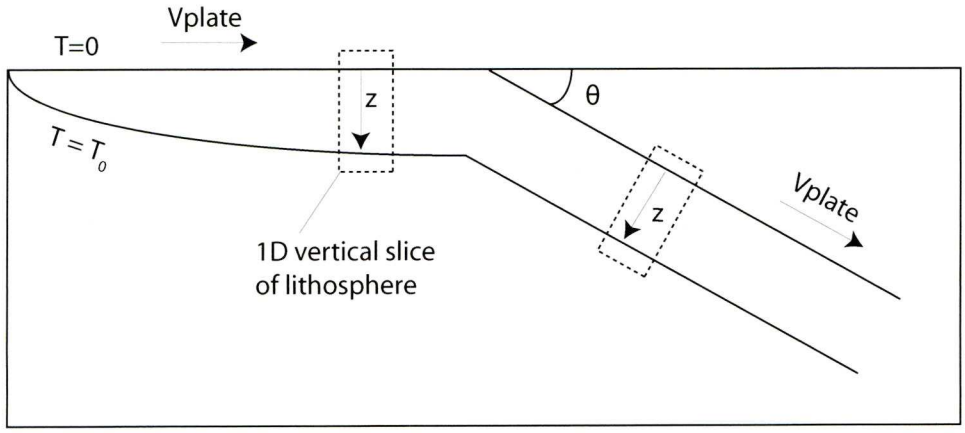


Figure 6.1: The 1D viscoelastic model, following a vertical slice of lithosphere from the ocean ridge to subduction

## 6.2 Stress development in the lithosphere prior to and during subduction

Between the mid-ocean ridge and the subduction zone, the lithosphere accumulates stresses from the ridge push force, and from cooling. Immediately prior to subduction the lithosphere begins to bend, inducing tensile stresses in the upper lithosphere and compressive stresses in the lower lithosphere. During subduction more stresses arise from the thermal expansion associated with heating, the basalt to eclogite transition, unbending, and the slab pull force.

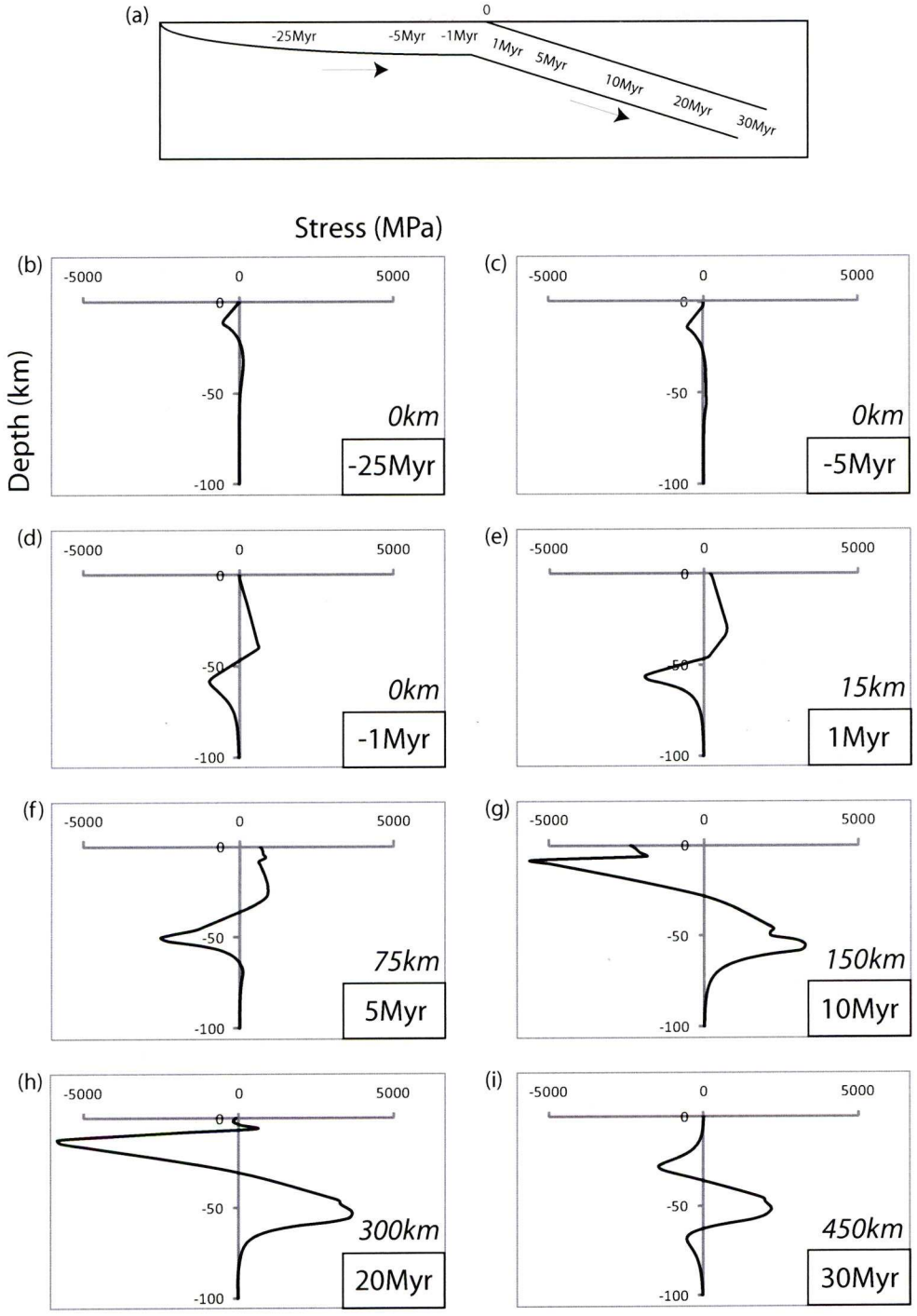


Figure 6.2: Evolution of stresses in the subducting slab before and during subduction. The oceanic lithosphere starts subducting at time t=0. Values in italics indicate the depth of the top of the slab.

Figure 6.2 shows the stresses that are induced in the lithosphere during a typical evolutionary history. Using temperatures extracted from the 2D thermal model as described in chapter 4, the lithosphere cools for 100Myr on its way to the collision zone, then is subducted at 30° and 3cm/yr. All values used in this model are listed in table 6.1; these parameters will be explored in depth later in this chapter.

For this and all subsequent figures, subduction is initiated at time=0, and the vertical depth scale is the perpendicular distance from the top of the slab. The stress sign convention is negative for compression, positive for tension.

| Parameter | Value |
|---|---|
| Plate velocity | 3cm/yr |
| Plate age | 100Myr |
| Dip angle | 30° |
| Ridge push force | -2.8 $\times$ $10^{12}$Nm$^{-1}$ |
| Thermal coefficient of expansion, $\alpha$ | $3\times10^{-5}$ |
| curvature gradient | $1\times 10^{-11}$ Nm$^{-1}$ |
| Volumetric change due to basalt to eclogite transition | 10% |
| Temperature range of the basalt to eclogite transition | 200-700°C |
| Slab pull force | $5 \times 10^{12}$ Nm$^{-1}$ |
| Viscosity: combined diffusion and dislocation | |

Table 6.1: Parameter values used for model shown in figure 6.2

Prior to subduction, the ridge push force and the cooling of the lithosphere generate the stresses that are compressive in the upper 25km of the lithosphere, and tensile beneath, as shown in figures 6.2b and 6.2c. The bending of the lithosphere in the forebulge immediately before subduction reverses this stress pattern to tension over compression (figure 6.2d). This 'bending' polarity continues as the slab begins to subduct and additional stresses act upon it (figure 6.2e); the stresses from the basalt to eclogite transition can be seen in the top few kilometers of the lithosphere after about 5Myr of subduction (figure 6.2f). When the slab begins to unbend at about 10Myr, the stresses revert to compression over tension (figure 6.2g), which for this model occurs at approximately 150km depth. This 'unbending' stress pattern is still observed 20Myr into subduction (figure 6.2h), although a thin band of tension can be seen at the top of the lithosphere relating to the metamorphism in the crust. By 30Myr the slab is very warm and has rapidly decreasing viscosity, leading to stress decay throughout the lithosphere (figure 6.2i); the only sources of stress still acting are thermal stresses and slab pull.

The sensitivity of the stresses in the lithosphere to the model parameters and stress sources listed in table 6.1 will now be explored.

## 6.3 Stresses accumulated by the lithosphere prior to subduction

The stress history of the lithosphere is an important feature of the viscoelastic formulation, allowing stresses to accumulate within the slab. Between the mid-ocean ridge and the subduction zone, the lithosphere is subject to the ridge push force, and stresses induced by cooling. These stresses are frozen into the lithosphere, and when subduction begins, they are advected with the slab, affecting its subsequent stress development. Figure 6.3 shows the thermal evolution as the oceanic lithosphere cools after formation at the mid ocean ridge, and the stresses this produces.

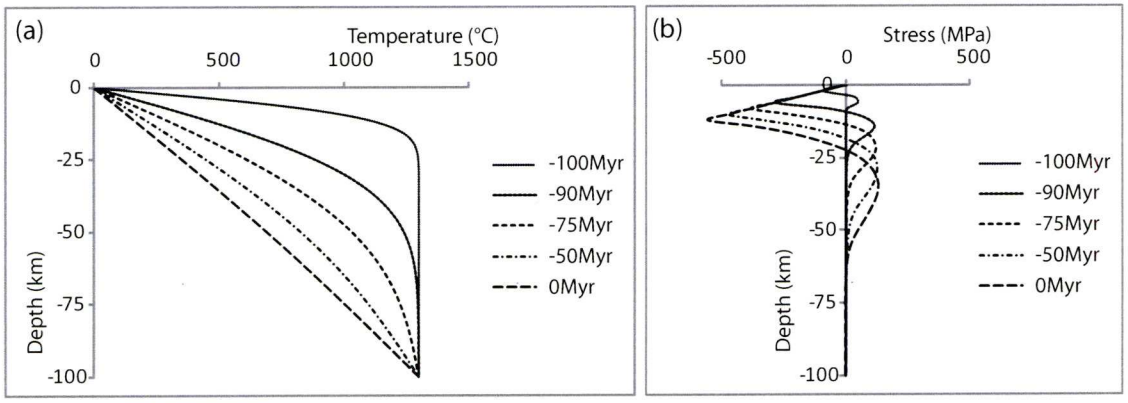


Figure 6.3: Temperature and stress evolution of the lithosphere from its creation at the mid-ocean ridge. Time is with respect to subduction at time t=0.

Figure 6.4 compares the total stresses in the slab with and without these pre-subduction stresses. The stress states look quite different at 5Myr and 3Myr before subduction, but the bending that begins in the forebulge is of such a large magnitude that it soon eclipses almost all the stresses from the ocean basin history. Some minor differences can still be seen 5Myr after subduction initiation, but they are quite small.

## 6.4 Dependence of predicted stresses on the temperature model

The temperature of the slab is an important parameter in the viscoelastic model, controlling the viscosity, thermal stresses and metamorphic reactions. The temperature profile used here can either be calculated by a 1D model, or extracted from a more sophisticated 2D thermal advection-diffusion model, as discussed in chapter 5. Figure

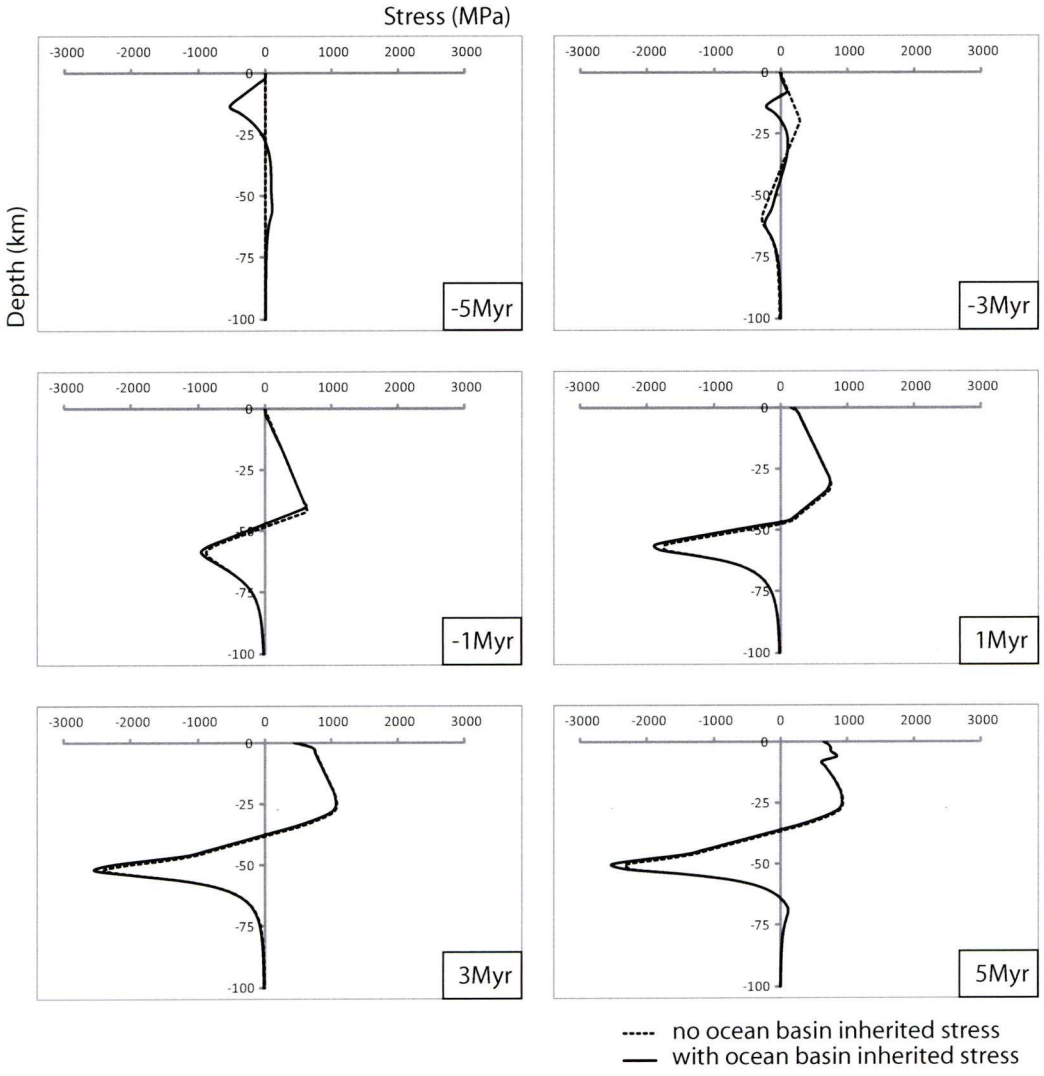


Figure 6.4: Comparison of total stress evolution in the subducting slab with (solid line) and without (dashed line) stresses from cooling history

6.5 shows the temperatures through the slab from (a) the 1D model and (b) the 2D model, where times are with respect to subduction initiation.

Figure 6.5 also shows the difference in the total stress at 1, 5 and 10Myr after the start of subduction, using these two different temperature profiles. The 2D temperature calculation predicts lower temperatures, resulting in higher viscosity so the slab is able to accumulate higher stresses. The temperature dependence of the thermal strain, viscous strain, and metamorphic stresses also combine to produce quite a different stress profile.

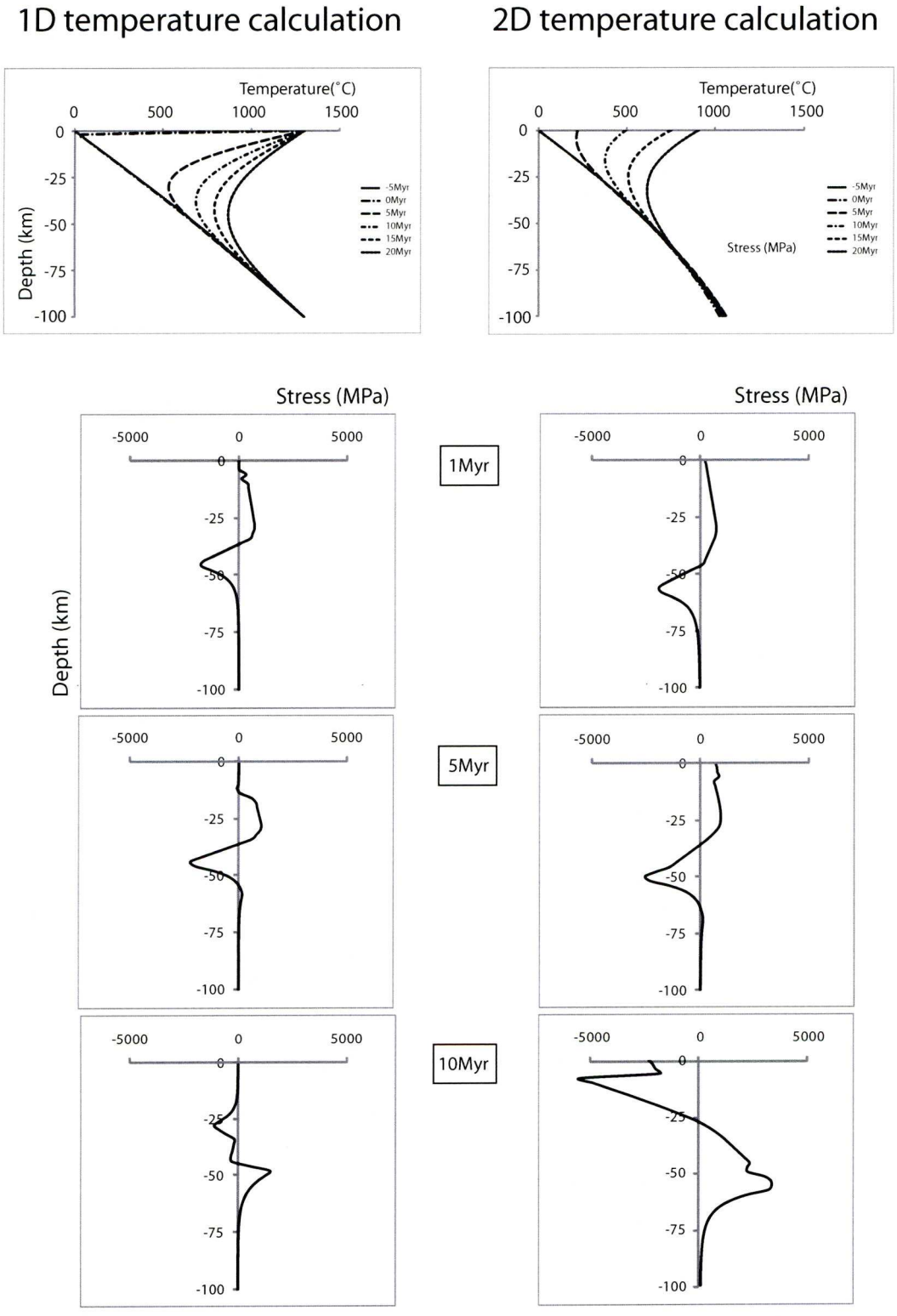


Figure 6.5: Temperature profiles calculated (a) within the 1D viscoelastic model (b) in the stand-alone 2D thermal advection-diffusion model, and their associated stress profiles

## 6.5 Dependence of stresses on rheology

The rheology of the lithosphere has a first-order effect on the slab stress profile so the choice of viscosity formulation is very important. Figure 6.6 shows the viscosity structure and the resulting stress evolution in the slab using diffusion creep versus a combined diffusion and dislocation creep rheology.

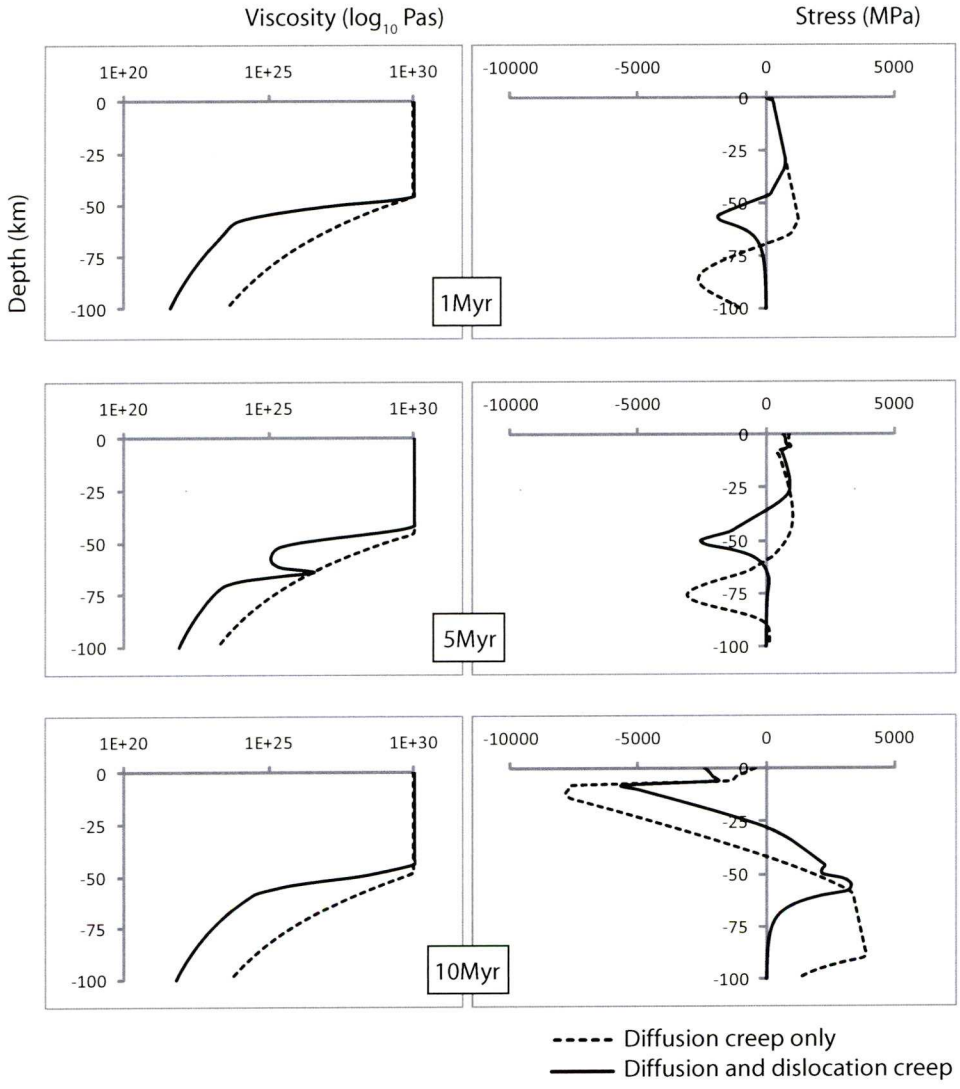


Figure 6.6: Comparison of viscosities calculated using diffusion creep only (dashed line), or diffusion and dislocation creep (solid line), and the corresponding total stresses produced

Hotter and higher stress regions flow by dislocation creep, whereas cooler and lower stress regions flow by diffusion creep (Karato and Wu, 1993), therefore a model incorporating both rheologies gives more accurate results for the subduction zone.

In the viscoelastic model shown in figure 6.6, the model using only diffusion creep gives higher viscosities, resulting in significantly higher stresses that persist to greater depths.

## 6.6 Sensitivity of stress profile to the various stress sources

### 6.6.1 Thermal strain

Thermal strain in the lithosphere is induced when the cold slab begins to warm up as it descends into the hot mantle. The amount that it expands is controlled by its thermal coefficient of expansion, $\alpha$.

Figure 6.7 shows stress prediction using only thermal stresses, while figure 6.8 is the stress prediction without any thermal stresses; note the scale difference between the two figures. The effect of the thermal strain is too small to be seen up to about 10Myr; after this a small contribution is apparent although it only has a small effect on the total stress.

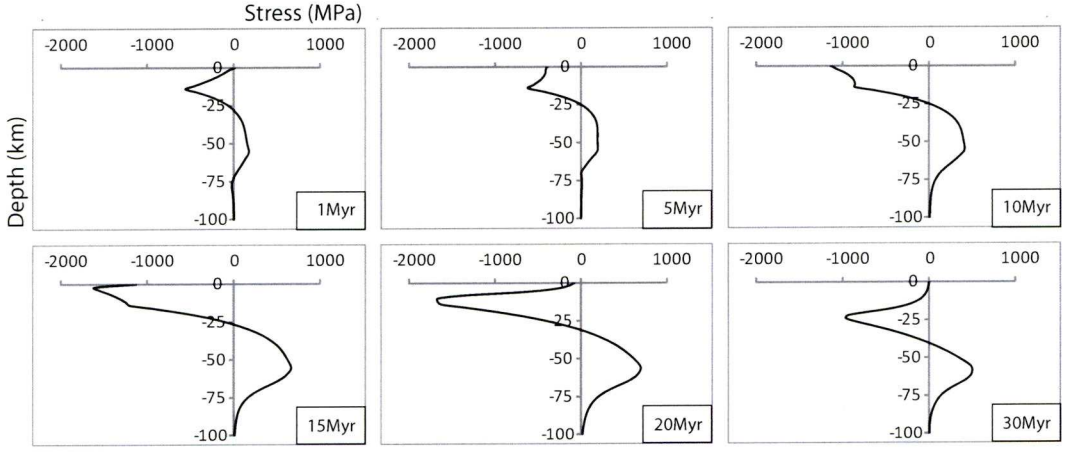


Figure 6.7: Stress evolution due to the thermal stresses in the slab only

Figure 6.9 shows a model using $\alpha$=3.5$\times 10^{-5}$K$^{-1}$ compared with values of 2.4$\times 10^{-5}$K$^{-1}$ and 4.6$\times 10^{-5}$K$^{-1}$. The difference between the generated stresses is minimal due to the small contribution of thermal stress to the total stresses produced.

### 6.6.2 Bending stresses

The lithosphere bends at the collision zone for the initiation of subduction, then unbends in the upper mantle. This creates large stresses of opposite sign about the neutral core of the slab; bending causes tension in the upper layer and compression in

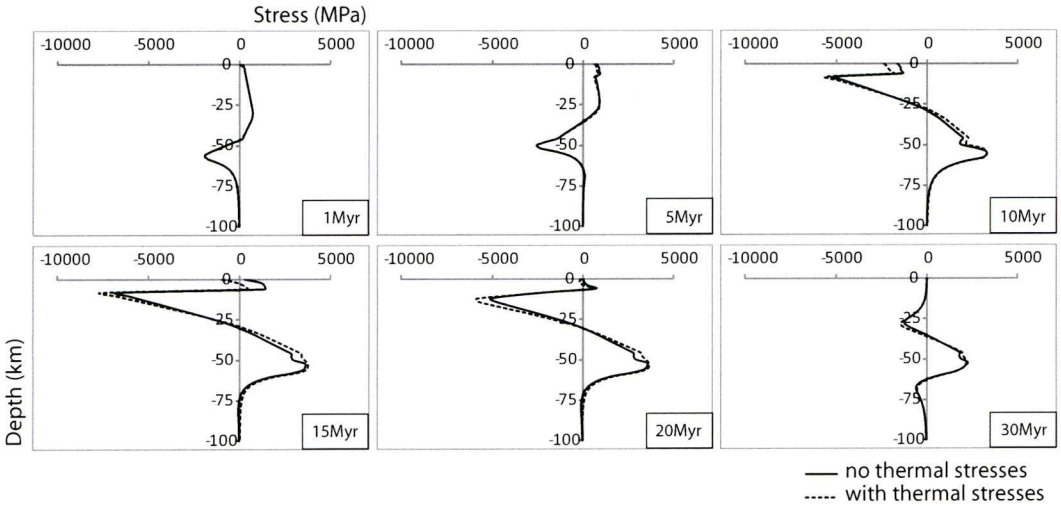


Figure 6.8: Stress evolution without thermal stresses is indicated by solid line. Dashed line shows reference model

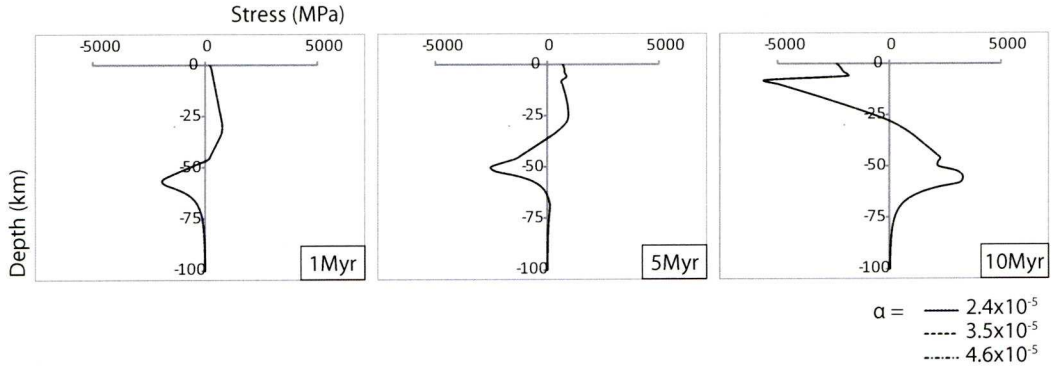


Figure 6.9: Sensitivity of total stress evolution to the thermal stresses: comparison of coefficient of thermal expansion $\alpha$ of $2.4\times10^{-5}$, $3.5\times10^{-5}$, and $4.6\times10^{-5}$

the lower layer, unbending induces the reverse. The majority of the focal mechanisms recorded in double Wadati-Benioff zones show this unbending pattern of compression over tension (Fujita and Kanamori, 1981), so modelling these bending stresses is an important part of the stress analysis (Wang, 2002). A typical subduction zone geometry and its curvature gradient is shown in figure 6.10 (Theodoridou, 2008).

Figures 6.11 and 6.12 show the model using bending stresses only, and with no bending stress. Of all the sources of stress in the slab, the bending stresses are the most influential, exerting very strong control over the shape of the stress profile for most of the subduction duration.

The curvature gradient has a first-order control on the bending stress, and therefore on the stress profile. Figure 6.13 shows the sensitivity of total stress evolution

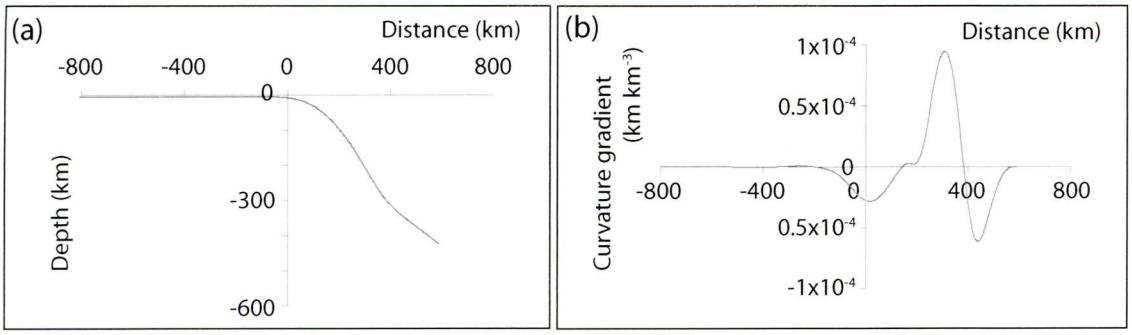


Figure 6.10: Plate geometry and associated curvature gradient, from Theodoridou (2008).

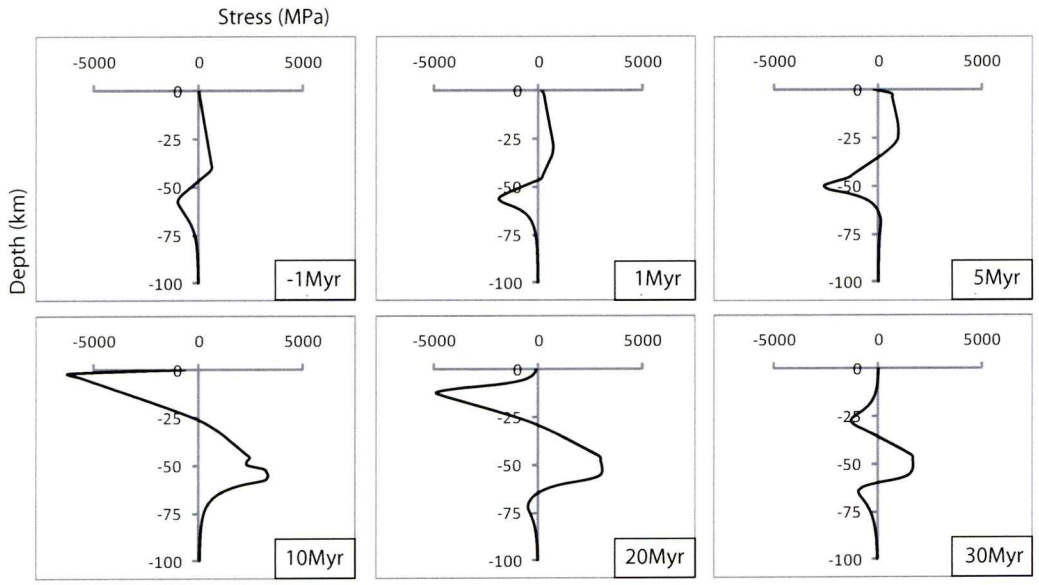


Figure 6.11: Stress evolution due to the bending and unbending of the slab only

to the curvature gradient. The reference value of $1\times10^{-11}\mathrm{m}^{-2}$ (Theodoridou, 2008) is compared against values of half and double this number. In the early stages of subduction, the stress profiles for all three curvature gradients are very similar. However, as the slab reaches its maximum point of unbending at 10Myr, the total stresses diverge in both magnitude and shape; the model with the smallest curvature gradient even produces stress of a different sign in the crust. The choice of curvature gradient is therefore undertaken carefully.

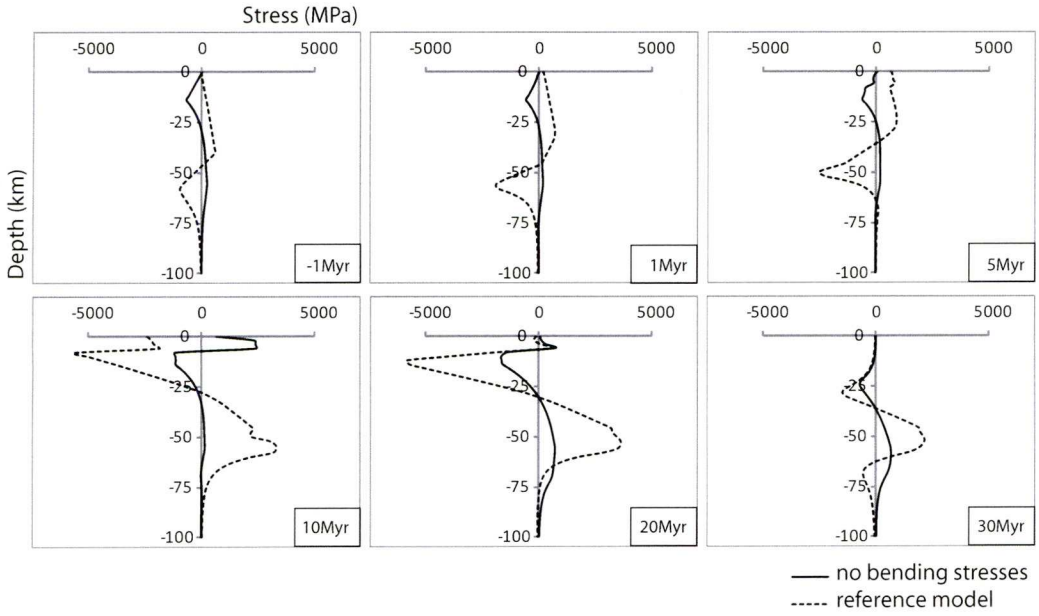


Figure 6.12: Stress evolution with (dashed line) and without (solid line) the inclusion of bending stresses

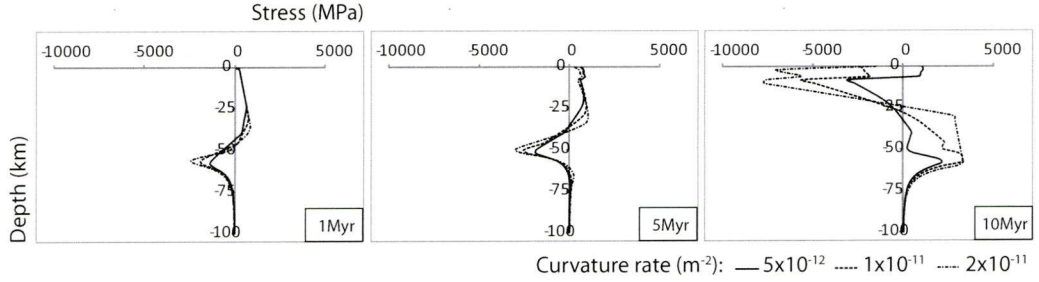


Figure 6.13: Total stress in the lithosphere as a function of curvature gradient; comparison of $\frac{\partial^3 w}{\partial x^3} = 5\times10^{-12}$, $1\times10^{-11}$, and $2\times10^{-11}$ m$^{-2}$

### 6.6.3 Basalt to eclogite transition

The top few kilometers of the subducting lithosphere are composed of a basaltic crust. As the slab subducts, the basalt is transported to conditions of high temperature and pressure, where it undergoes transformation into eclogite. This metamorphism is associated with an increase in density and a decrease in volume, inducing strain in the slab (Kirby et al., 1996). It has been suggested that this is the cause of the upper layer of seismicity in triple Wadati-Benioff zones (Wang, 2002).

Figure 6.14 shows the stresses due to the basalt to eclogite transition; figure 6.15 shows a model without these stresses. These metamorphic stresses are at their maximum at around 10-15Myr where they have a moderate effect on the total stress profile

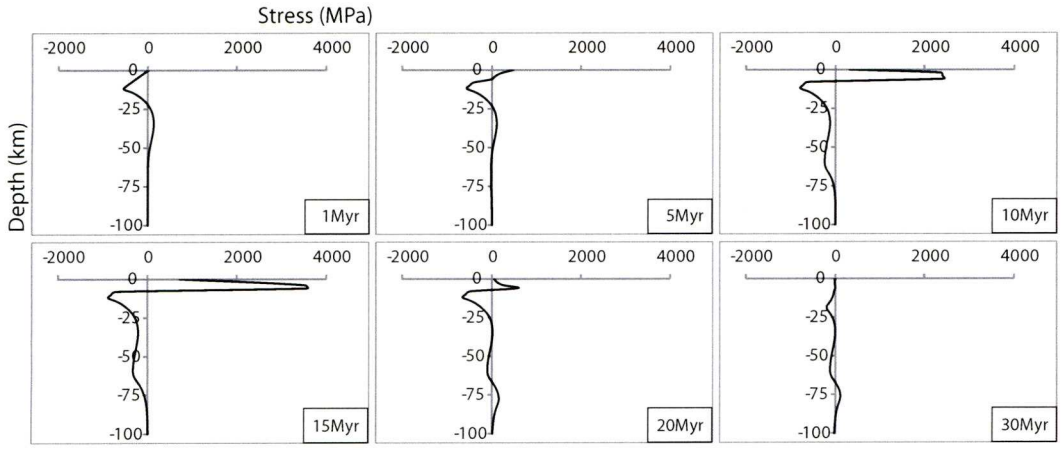


Figure 6.14: Stress evolution due to the basalt to eclogite transition only.

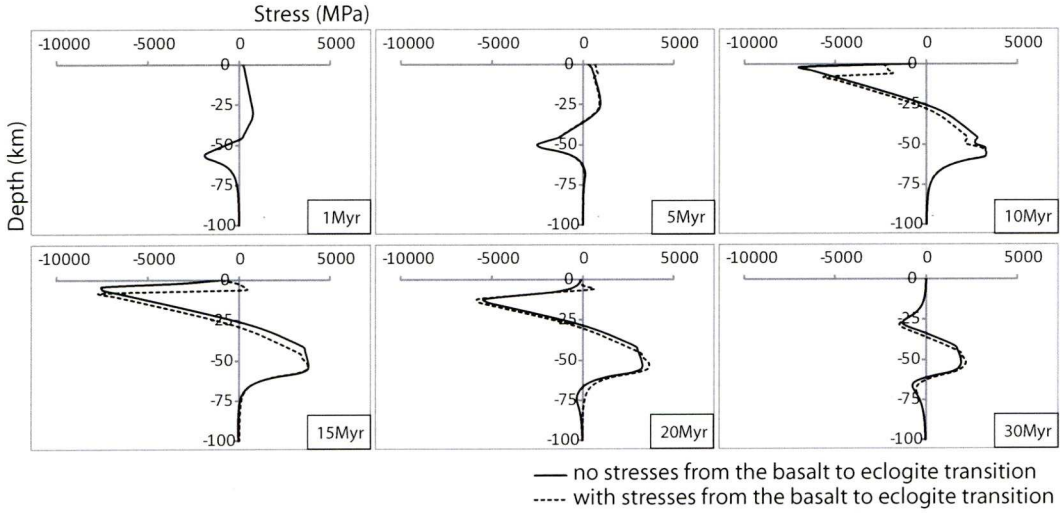


Figure 6.15: Total stress evolution without stresses from the metamorphism of basalt to eclogite is indicated by solid line. Dashed line shows reference model.

and magnitude.

Figure 6.16 shows the sensitivity of the total stress profile to the basalt to eclogite transformation. Comparing a volumetric change of 5%, 10%, and 20%, the profiles are very similar until about 10Myr, whereupon differences can be seen both at the top of the slab in the crust, and lower down in the slab due to the stress redistribution through creep. Figure 6.17 shows the sensitivity of the model to the temperature range of the metamorphism. At both 5Myr and 10Myr into subduction, the model with the biggest temperature range shows the highest magnitudes of stress. Although the total volume change is the same, applying it over a longer period increases the stresses accumulated from metamorphism because they are not dissipated so quickly.

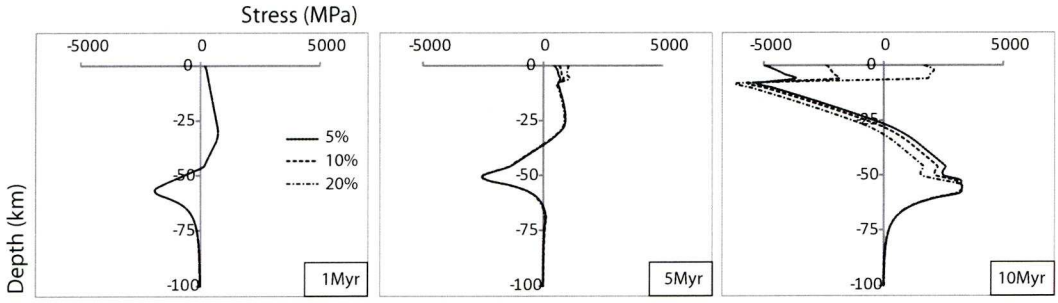


Figure 6.16: Sensitivity of total stress evolution to the basalt to eclogite transition: comparison of 5%, 10% and 20% volumetric change

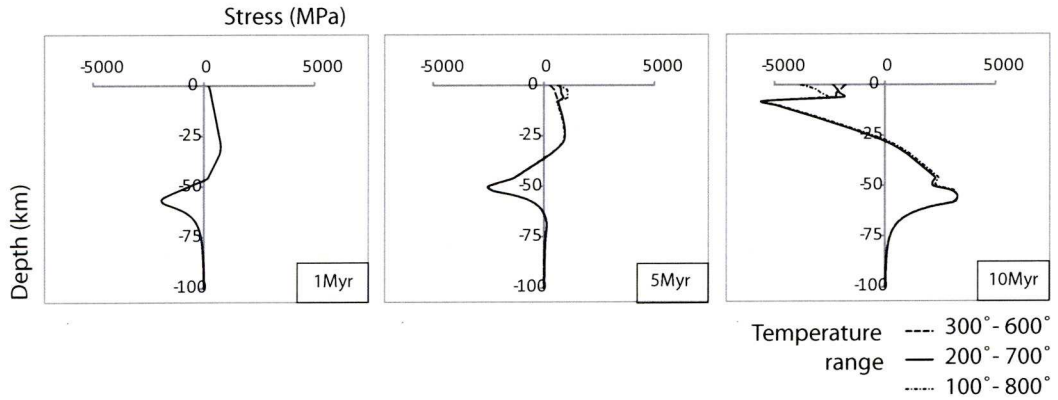


Figure 6.17: Sensitivity of total stress evolution to temperature range for the basalt to eclogite transition: comparison of 300-600°C, 200-700°C, and 100°-800°C

### 6.6.4 Slab pull

The negative buoyancy of the cold, dense slab is the main driving force for subduction, and is estimated at $5 \times 10^{12} \mathrm{Nm}^{-1}$ (Turcotte and Schubert, 2002). Unlike the other stress sources, it is a renewable source of stress in the slab (Bott and Kusznir, 1984), meaning it is applied throughout subduction; when all the stresses from the other sources have dissipated, stresses arising from slab pull are still renewable.

Figure 6.20 shows the total stress evolution using a slab pull force of 1, 5, or 10 $\times 10^{12} \mathrm{Nm}^{-1}$. The response of the total stress profile is very minor, so varying the value of the slab pull force make little difference.

Figure 6.18a shows the stresses generated by slab pull when it is applied to a piece of lithosphere with no ocean basin cooling history. Figure 6.18b shows the stresses generated by slab pull when the lithosphere already has a stress profile from cooling and the ridge push force prior to subduction. Figure 6.19 shows the model with no slab pull force included. The stresses that slab pull induces in the subducting lithosphere

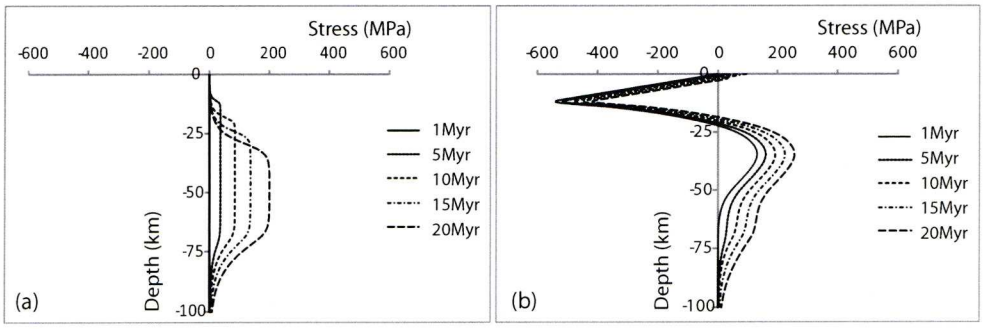


Figure 6.18: Stress evolution due to the slab pull force applied to (a) a neutral stress state (b) the stress profile produced by ocean basin cooling prior to subduction.

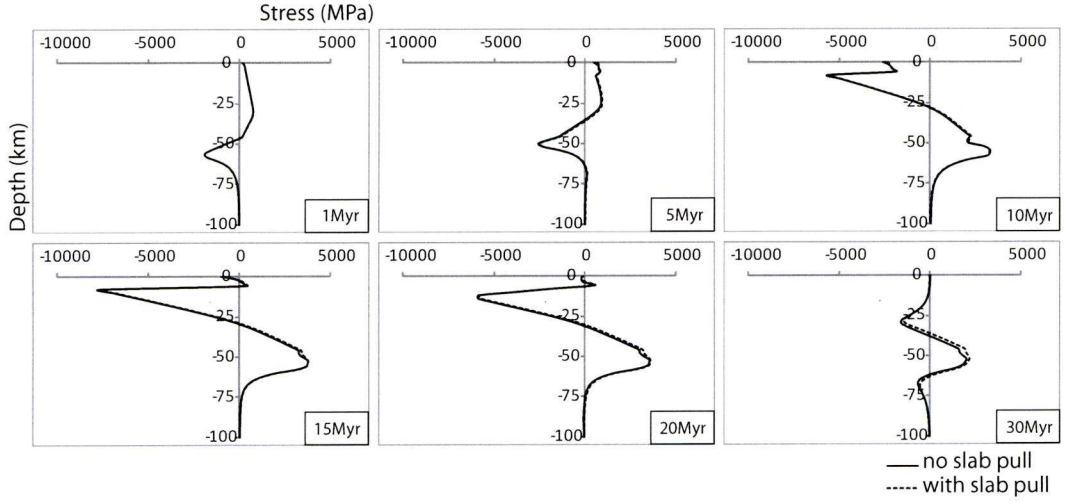


Figure 6.19: Stress evolution with (dashed line) and without (solid line) the slab pull force.

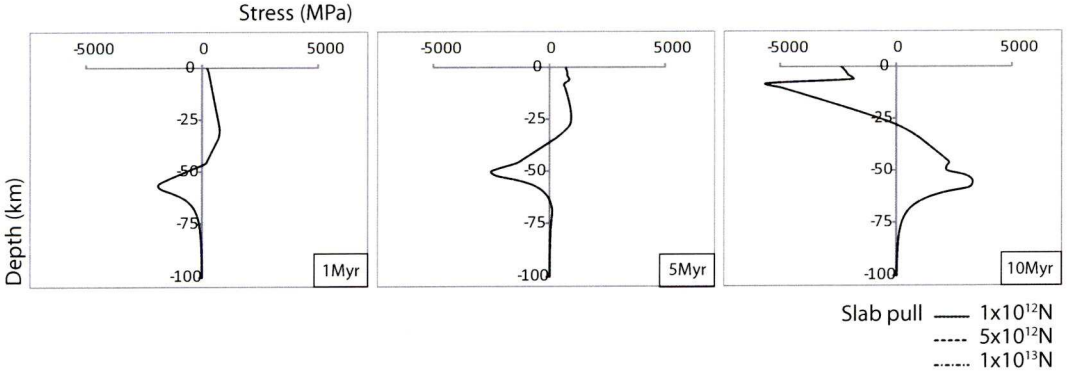


Figure 6.20: Sensitivity of total stress evolution to the slab pull force: comparison of 1, 5, and 10 $\times 10^{12}$Nm$^{-1}$

are about an order of magnitude smaller than the stresses generated through bending, so the contribution to the total stress state is small, although does grow over time rather than dissipate.

Figure 6.20 shows the sensitivity of the total stresses when the slab pull force is $1\times10^{12}$, $2\times10^{12}$, and $10\times10^{12}$Nm$^{-1}$. The influence of slab pull on the total stresses is so small that the differences between these stress profiles is negligible.

## 6.7 Dependence of stresses in the lithosphere on slab dip, plate age, and velocity

The principal controls over the development of the subducting slab are the age of the oceanic lithosphere, the angle at which the slab subducts, and the convergence velocity. All three variables have a direct effect on the temperatures, viscosities, and the stresses within the slab. By modelling how the total stress profile changes with parameter values, the various relationships can be investigated, giving insight into the processes of stress accumulation leading to Wadati-Benioff zone seismicity. In the following models comparing the sensitivity of the slab stresses to plate age, dip angle and plate velocity, all the stress sources are included.

### 6.7.1 Sensitivity of slab stresses to the age of the lithosphere

The age of the oceanic lithosphere at the start of subduction controls the temperature of the slab, as well as other related mechanisms. An older slab will be colder, which means that during subduction it will take longer to heat up to ambient temperatures, affecting stresses arising from thermal expansion and metamorphism. The accumulation of stresses in the slab will also be affected. Figure 6.21 compares models that use a plate age of 25, 50, or 100Myr, keeping the dip angle at 30° and the plate velocity at 3cm/yr.

The model in 6.21a is the warmest, with a plate age of 25Myr at the point of subduction. Only the top third of the slab is cold and rigid enough to accumulate any stresses; the bottom two-thirds deform by viscous creep if stress is applied. The maximum stresses occur approximately 10Myr after subduction initiation, and appear to be mostly due to the metamorphic and bending stresses. By 20Myr the slab has warmed up so much that almost all the stresses have dissipated.

The model in 6.21c has a much colder plate, with an age of 100Myr at the start of subduction. The low temperatures mean that the top 75km of the slab is able to accumulate stresses. The low temperatures also mean that the slab takes a long time

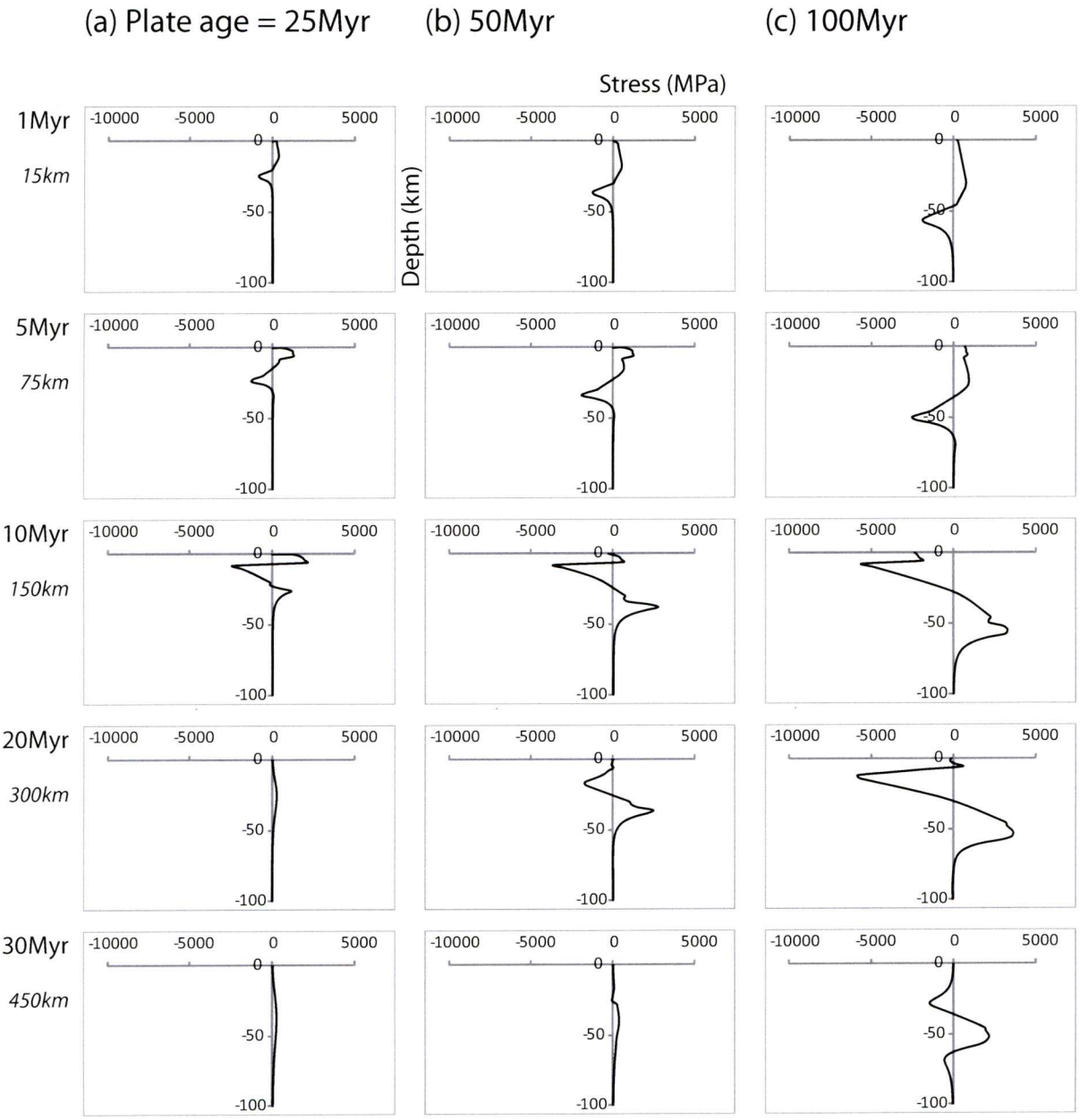


Figure 6.21: Sensitivity to plate age. Comparison of models with 25, 50 and 100Myr old slabs. Dip angle is 30°, convergence velocity is 3cm/yr. Numbers in italics refer to the depth of the top of the slab.

to heat up, so these stresses persist for over 30Myr, which for this model of 3cm/yr and 30° dip translates to 450km depth, covering the intermediate depths where double seismic zones are observed.

The 100Myr old slab shows a very strong unbending stress pattern around 10Myr-20Myr into subduction (150km-300km depth) relating to focal mechanisms of compression over tension observed in the majority of double seismic zones (Fujita and

Kanamori, 1981). The two cooler plates of ages 25Myr and 50Myr both show a triple stress pattern of tension in the crust, followed by compression over tension, relating to focal mechanisms observed in triple seismic zones (Igarashi et al., 2001).

### 6.7.2 Sensitivity of slab stresses to the plate dip angle

The dip angle of the oceanic plate may or may not depend on slab pull (Uyeda and Kanamori, 1979; Cruciani et al., 2005), and seems to vary with time (Lallemand et al., 2005). Values of slab dip angle worldwide range from 11° to 90°, but most are around intermediate values of 30° to 50° (Uyeda and Kanamori, 1979). The dip angle controls the radius of curvature of the slab, and with it the bending stresses. The dip angle also affects how quickly the cold slab reaches the hot mantle, and therefore affects thermal, metamorphic, and viscous stresses.

Dip angle is introduced into the 1D viscoelastic model in two ways. First, the dip angle controls the curvature gradient used to calculate the bending stress; a steeper angle means a smaller radius of curvature and therefore higher bending stresses. Second, the 2D thermal model which provides the temperatures in the slab has dip angle included explicitly as one of its controlling parameters, affecting the lithosphere isotherms. Figure 6.22 compares models with different dip angles, keeping the plate age at 100Myr and the plate velocity at 3cm/yr.

Figure 6.22a shows a model with a dip angle of 15°. The low angle means the bending stresses are small, and due to the dominance of the bending stresses in the stress profile, the total stress magnitudes are reduced. The smaller bending stresses also mean that more of the contributions of the other stress sources can be seen, especially the tensile peak from the basalt to eclogite transition. The lower angle means the slab takes longer to heat up, so the stresses that are accumulated take longer to dissipate; the unbending stress shape is still very prominent at 30Myr.

Figure 6.22c shows a model where the slab dips at 45°. The bending stresses are large due to the steeper angle of subduction especially in the unbending phase. The high angle also means the cold slab enters the hot mantle more rapidly, increasing the temperature-related stresses associated with thermal expansion and the basalt to eclogite transition. The combination of these mechanisms occurring together mean that between 10Myr and 20Myr the slab accumulates very high stresses.

All three models are dominated by the bending and unbending stresses, and all show the unbending pattern 10Myr into subduction, as frequently observed in double seismic zones. The model with the steepest angle of 45° shows a very strong unbending pattern at 10-20Myr (200-400km depth). The model with the low dip angle of

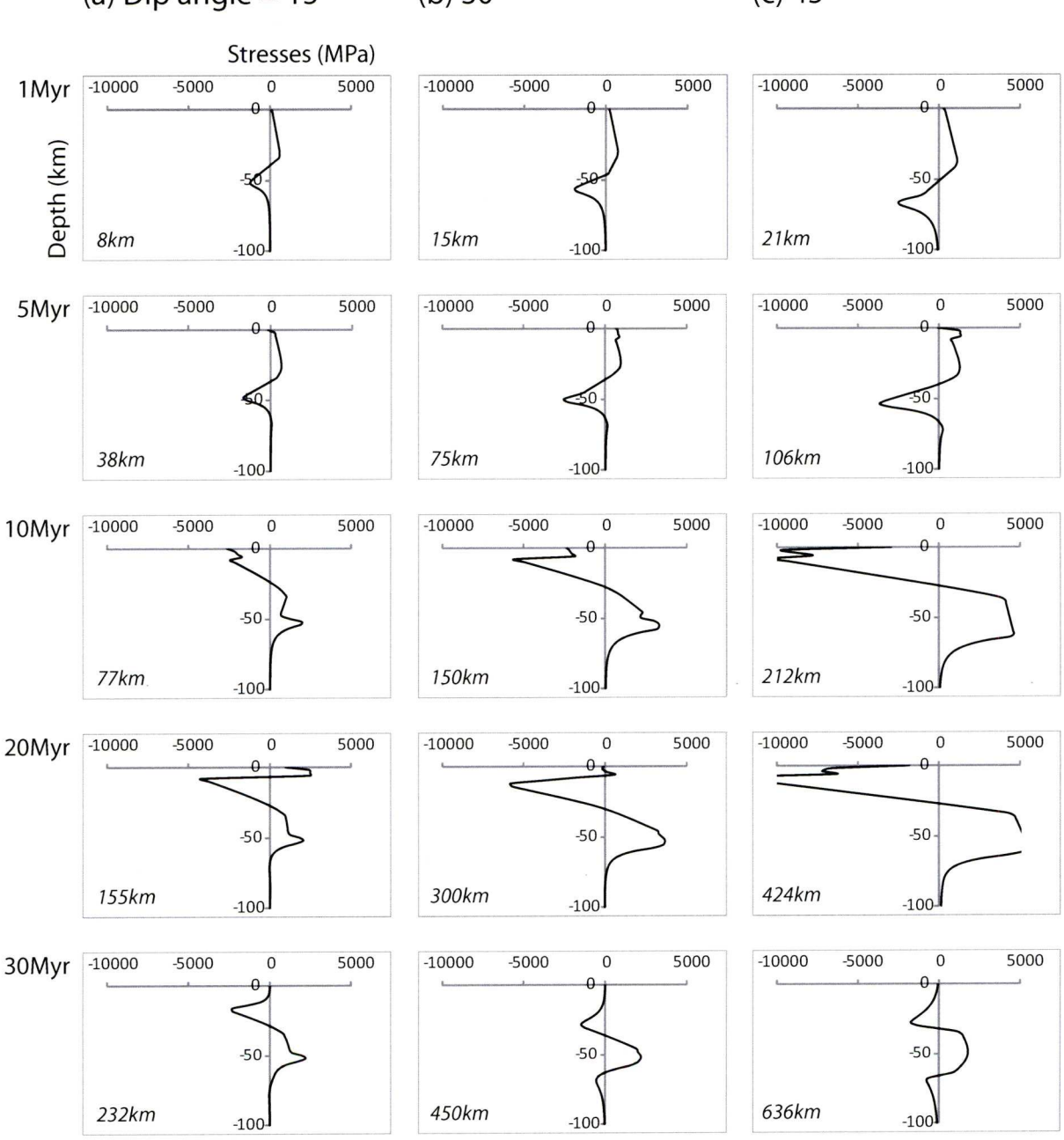


Figure 6.22: Comparison of models with a slab dip angle of 15°, 30°, and 45°. All models have a convergence velocity of 3cm/yr, and a plate age of 100Myr. Numbers in italics refer to the depth of the top of the slab.

15° has smaller bending stresses and shows a triple seismic zone at 20Myr, or 150km depth, the right signs and depths to be in agreement with recorded focal mechanisms in northeast Japan (Igarashi et al., 2001).

### 6.7.3 Sensitivity of slab stresses to the plate velocity

Assuming the oceanic lithosphere moves uniformly and does not stretch or thicken, the plate velocity at the surface will be the same as the slab velocity during subduction. The speed of descent affects the rate of heating and the associated stresses that arise from thermal, viscous, and metamorphic strains. It also controls the magnitude of the bending stresses.

The plate velocity is introduced into the 1D viscoelastic model as one of the factors for calculating the bending stress, where a faster plate will bend more rapidly, generating higher stresses. It is also one of the parameters in the 2D thermal model, controlling speed of descent into the mantle and therefore the temperatures in the slab. Figure 6.23 shows models comparing plate velocities of 1, 3 and 5cm/yr, keeping the plate age at 100Myr, and the dip angle at 30°.

Figure 6.23a has a very slow plate velocity of 1cm/yr, and so does not even begin to unbend until approximately 20Myr after the start of subduction. The low velocity means that stress accumulation occurs at a modest rate, but it also means that the slab stays colder for longer so the stresses do not dissipate as quickly.

Figure 6.23c shows stresses from a model with a plate velocity of 5cm/yr. This high speed means that the stresses due to bending start and end quickly, are significantly higher, and dominate the stress profile. The velocity also means that the slab moves into the hot mantle very quickly, heating rapidly and accruing greater temperature-dependent stresses such as thermal and metamorphic stress. However the fast heating also means that the slab is too hot to maintain any more stresses by the time it has subducted for 30Myr, which for this model is about 750km depth.

All three models have total stresses that indicate bending at shallow depths, followed by the unbending pattern of compression over tension, in accordance with observed focal mechanisms from many seismic zones. Additionally, all three show periods of triple zone stress patterns, both before and after the unbending maxima.

## 6.8 Summary of the viscoelastic model results

Using a viscoelastic formulation to model the lithosphere is advantageous because it includes behaviour such as stress transfer and stress memory. These aspects mean that stresses that are generated can accumulate in the upper lithosphere until they exceed the brittle strength of the lithosphere, causing the seismicity in Wadati-Benioff zones. The interplay between the stress sources is the origin of the observed double and triple bands.

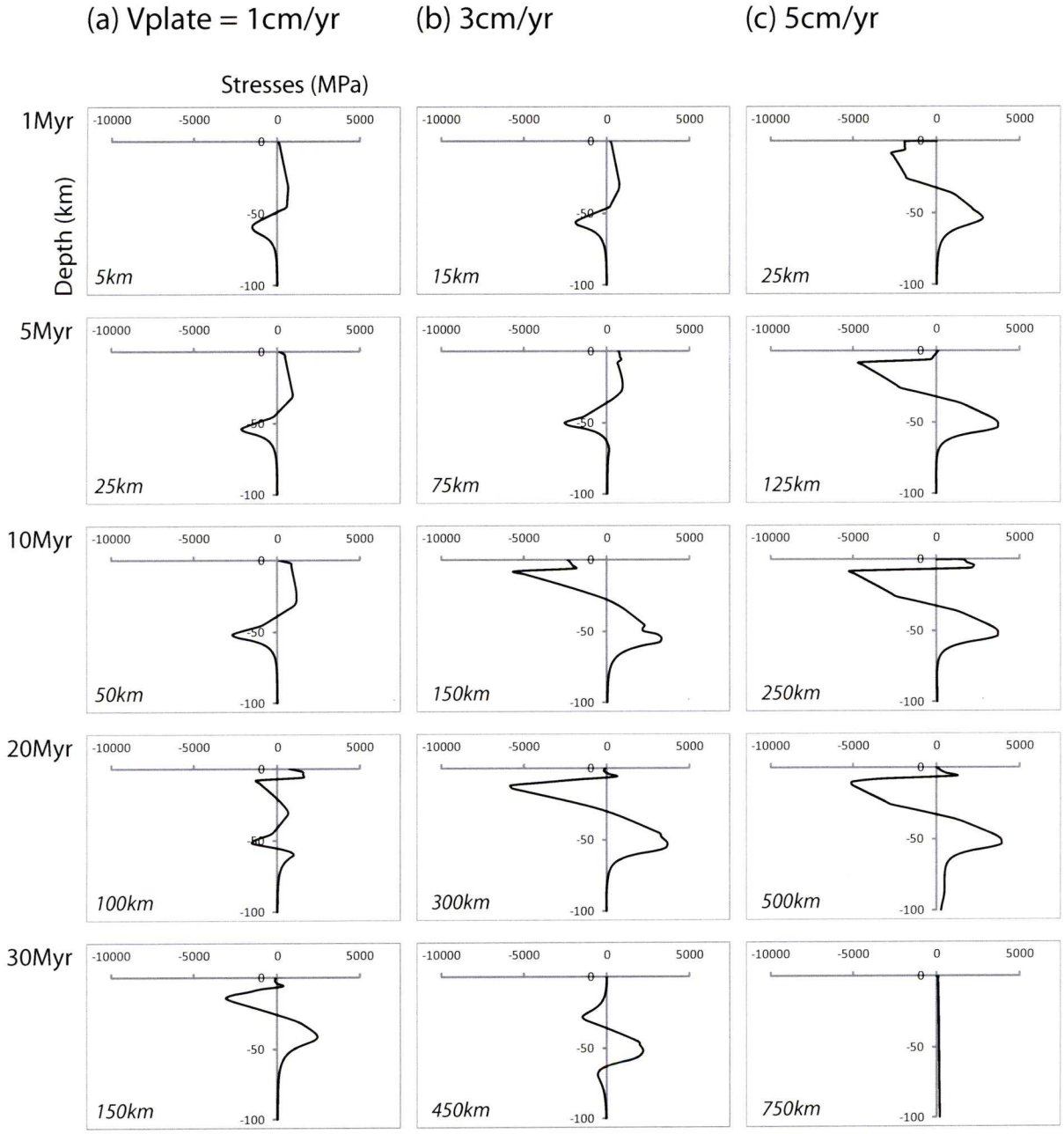


Figure 6.23: Comparison of models with plate velocities of 1, 3, and 5cm/yr. All models have a plate age of 100Myr and a dip angle of 30°. Numbers in italics refer to the depth of the top of the slab.

This one-dimensional viscoelastic model explores the consequences of subducting a viscoelastic slab into the mantle. The results presented here show the dependence of the stresses in the lithosphere on temperature, stress history from the ocean basin, the various stress sources, and the three controlling parameters of plate age, dip angle, and plate velocity.

A two-dimensional thermal advection-diffusion corner-flow model is used to obtain temperatures for the subducting slab. This produces a more accurate, colder temperature profile than the 1D temperature model, meaning the stresses throughout the slab are higher and persist for longer.

Prior to subduction, the oceanic lithosphere accumulated stresses as it cooled, which were then advected with the slab. These have a small influence on the total stress within the first million years of subduction, but are quickly overwhelmed by the other stresses arising in the slab.

Viscosity is an important factor in the development of stresses in the slab; here a combined rheology of diffusion and dislocation creep is used, reflecting the deformation mechanisms of the different regions of the upper mantle. Temperature, pressure and stress all influence the viscosity, which controls how stresses in the slab are dissipated or transferred to the upper lithosphere.

The most influential stress source is the bending and unbending of the slab, dominating the stresses at all depths. The basalt to eclogite transition is also quite an important source of stress, but is confined to the top few kilometers of the slab. The thermal strain has a small but noticeable effect on the stress profile, and whilst slab pull only has a small effect on the stress state, it is the only renewable stress source so is most influential at greater depths when the other stresses have dissipated.

Plate age, dip angle, and convergence velocity all affect the stresses accumulated by the slab primarily through their influence on the slab temperature. A higher angle or a faster velocity means that the cold lithosphere heats up more quickly as it rapidly penetrates the hot regions of the mantle, meaning the slab will accumulate higher temperature-related stresses from the volumetric changes associated with thermal and metamorphic effects. An older slab is colder and more viscous, accumulating higher stresses that take longer to dissipate because it takes longer for it to warm up.

Plate age, dip angle, and convergence velocity also control the slab bending, which generates the largest stresses in the slab. Plate velocity is one of the factors in calculating the bending stress, so a faster plate will generate higher stresses. Large bending stresses are also caused by high dip angles, since the angle dictates the curvature gradient, the other factor in the bending stress calculation. Bending stresses are also affected by the age of the slab, which controls the temperature and the viscosity. An older slab will be thicker and stiffer, accumulating higher stresses throughout more of the slab.

The stress patterns produced here are largely dominated by the bending and unbending stresses at intermediate depths, which is in good agreement with the majority of focal mechanisms recorded at double Wadati-Benioff zones (Sleep, 1979; Fujita and

Kanamori, 1981). Additionally, some models also show tension in the crust due to the basalt to eclogite transition, which agrees with the focal mechanisms recorded for triple seismic zones. The magnitudes of the stresses are in the GPa range, which is on the right order of magnitude suggested by observations (Andersen et al., 2008; John et al., 2009) and other models (Cížková et al., 2007; Babeyko and Sobolev, 2008). This therefore makes this viscoelastic model a useful and relevant tool for investigating the causes of subduction zone seismicity.

# Chapter 7

# Modelling stress accumulation in the subducting lithosphere beneath north Chile

## 7.1 Introduction

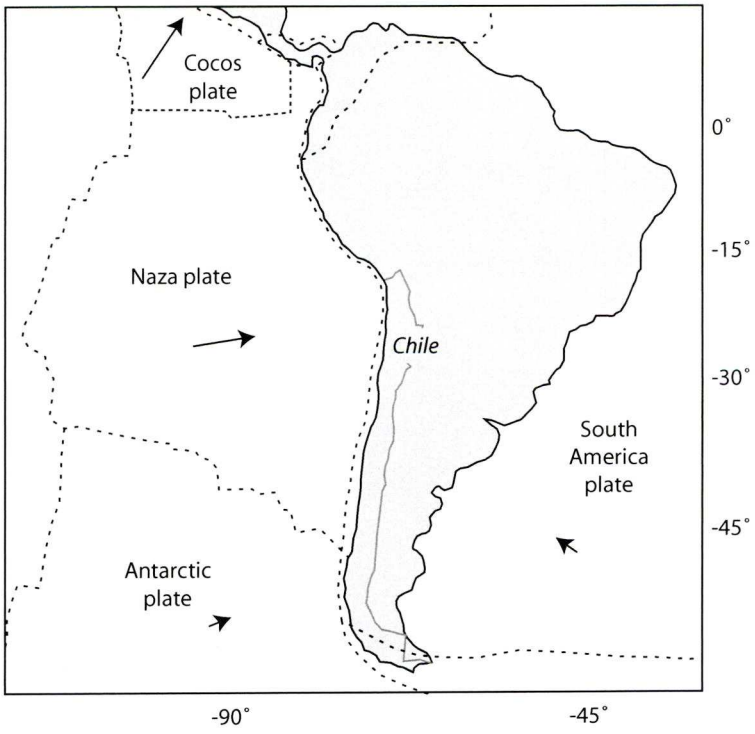


Figure 7.1: Chile, South America, and the local tectonic plates system, after Schellart and Rawlinson (2010). Arrows indicate plate motion.

The subduction of the Nazca plate underneath the South American plate (figure 7.1) takes place over a 3,000km length, with earthquakes recorded up to depths of 650km, although there is a break in seismicity between depths of 320km and 525km (Barazangi and Isacks, 1976). In northern Chile, between about 19°-24°S, and 66°-71°W, a double seismic zone is observed between 90km and 150km depth (Comte and Suarez, 1994; Comte and Suárez, 1995; Rietbrock and Waldhauser, 2004).

The 2D viscous model and the 1D viscoelastic model described and demonstrated in chapters 3-6 are here applied to the north Chile subduction zone to investigate stress accumulation in the downgoing slab, and the causes of the observed Wadati-Benioff zone seismicity.

## 7.2 Key parameters of the north Chile subduction zone

The subducting Nazca plate is geologically young at around 50 million years old (Muller et al., 1997, 2008), being relatively close to the East Pacific Rise. The seafloor isochrons are reconstructed from magnetic anomalies, gravity anomalies, and plate rotations, and are accurate to within 5Myr for Chile. The plate age is introduced into both the 1D and 2D models through the temperature of the oceanic lithosphere at the point of subduction.

| Parameter | Value |
|---|---|
| Plate age | 50Myr |
| Dip angle | 25° |
| Plate velocity | 6cm/yr |
| Rollback velocity | 2cm/yr |
| curvature gradient | $2\times10^{-11}\mathrm{m}^{-2}$ |

Table 7.1: Parameters for the north Chile subduction zone used in the viscous and viscoelastic models.

As with all subduction zones, the dip angle is somewhat open to interpretation due to the difficulty in defining the exact geometry of the slab. Schurr et al. (1999) estimate the dip angle of the slab between depths of 75km and 275km as 35°; Norabuena et al. (1998) model the dip angle of the slab in three progressively steeper segments of 10°, 18°, then 26° until 50km; whilst Lallemand et al. (2005) find an average of 19° for the first 125km, then 45° below. Oleskevich et al. (1999) use a shallow dip angle of 13° for the locked portion of the slab beneath the accretionary prism.

For the 2D viscous model the dip angle is primarily imposed through the geometry of the weak decoupling zone which extends from the surface to 100km depth;

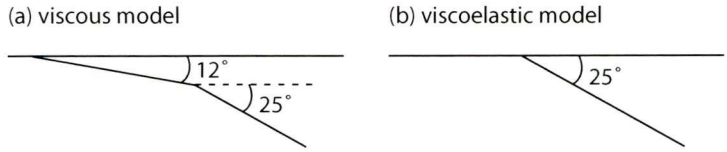


Figure 7.2: Dip angles for the (a) 2D viscous model and (b) 1D viscoelastic model

beneath this the low viscosity mantle wedge continues at the same angle for another 50km. To represent the gradual onset of the subduction dip and the influence of the accretionary wedge, I impose a shallow dip angle of 12° for the first 40km as indicated by Norabuena et al. (1998) and Oleskevich et al. (1999); below this I use an angle of 25°, as a weighted average of the values estimated by Lallemand et al. (2005), given that beneath 150km there is no imposed dip angle and the slab is free to move. For the 1D viscoelastic model, the dip angle is primarily used to calculate the temperatures in the thermal model. The constraints of this model require a single dip angle, so the 25° angle is used throughout. The dip angles used in the 1D and 2D models are shown in figure 7.2.

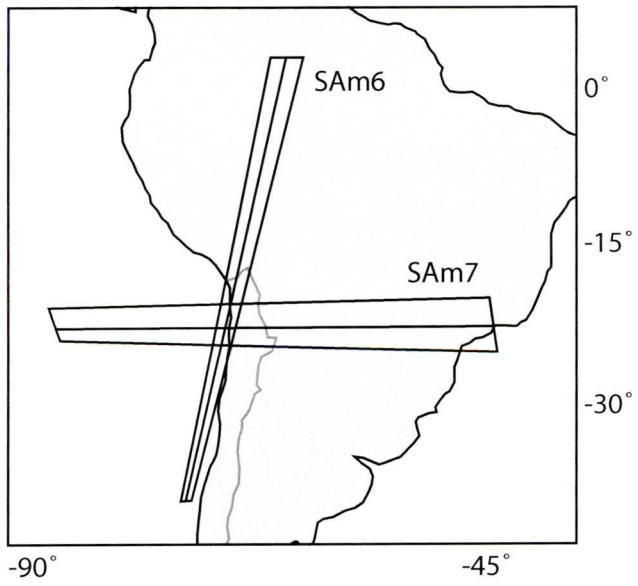


Figure 7.3: Profiles (a) SAm6 and (b) SAm7 in north Chile as defined by Theodoridou (2008)

The velocity of the Nazca plate is estimated variously as 2.9cm/yr (Lallemand et al., 2005), 6.8cm/yr (Norabuena et al., 1998), 6.8cm/yr (Schellart and Rawlinson, 2010), and 9.5 (Jarrard, 1986), with a rollback velocity of 1.9cm/yr (Schellart and Rawl-

inson, 2010), 2.3cm/yr (Jarrard, 1986) and 3.9cm/yr (Lallemand et al., 2005). From these values I use a plate velocity of 6cm/yr and a rollback velocity of 2cm/yr. In the 2D viscous model, the plate velocity is applied through a horizontal boundary condition on the top of the oceanic plate far from the trench, and the rollback velocity is introduced by a relative movement between the overriding plate and the bottom of the model representing the core mantle boundary. In the 1D viscoelastic model only the plate velocity is used, where it is one of the parameters of the thermal model and also used in the calculation of the bending stresses.

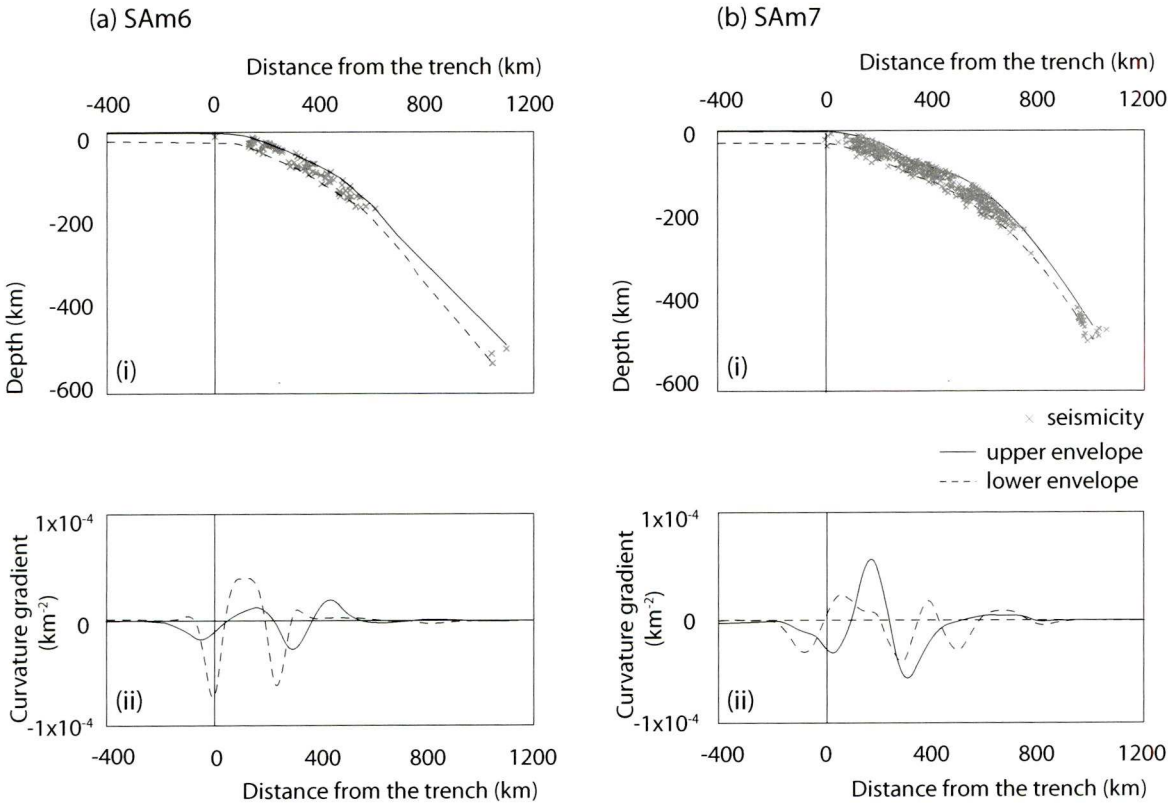


Figure 7.4: curvature gradient for the N Chile subduction zone, using profiles (a) SAm6 and (b) SAm7 as defined in Theodoridou (2008)

The 1D viscoelastic model also requires the curvature gradient of the slab to calculate the bending stresses. If the shape of the subducting slab is found by fitting a spline to the Wadati-Benioff zone seismicity, the curvature gradient is the third derivative of this spline. The curvature gradients used to model the north Chile subduction zone are taken from the work by Theodoridou (2008). The cross-sectional profiles along which the observations are taken are shown in figure 7.3. The seismicity, upper and lower fitted splines, and curvature gradients are shown in figure 7.4; the curvature gradient is very sensitive to the slab profile. The curvature gradient is applied to the

1D viscoelastic model sinusoidally: using the data shown in figure 7.4, the amplitude is estimated at $2\times10^{-11}\mathrm{m}^{-2}$ with a wavelength of 500km, shown in figure 7.5.

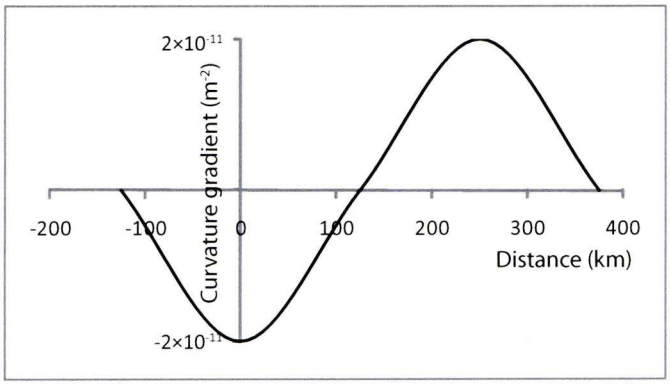


Figure 7.5: curvature gradient as applied to the 1D model

The current phase of subduction beneath Chile began approximately 25Myr ago, when the Farallon plate broke up into the Cocos and Nazca plates (Wortel, 1984; Wdowinski and Bock, 1994), significantly increasing convergence velocity, decreasing plate age, and resulting in a lower dip angle (Pilger, 1984). However, subduction in the region is much older than this, and the new phase of subduction began with a fully-formed slab in the subduction zone. Unfortunately the 2D model cannot be run long enough to model the time prior to 25Myr; instead, it begins with an unperturbed domain where the oceanic plate is kinematically driven to initiate subduction. The 1D model, on the other hand, uses a formulation for the region that allows the subduction zone to develop to a quasi-steady state before the 25Myr period begins, more closely approximating the subduction history of the region.

Using these parameters for dip angle, plate age, plate velocity, rollback velocity and curvature gradient, together with the full formulation of the models as described in chapters 3 and 5, the stress accumulation within the subducting slab over the most recent 25Myr period can be explored.

## 7.3 Modelling stress accumulation in the subducting lithosphere in north Chile with the 2D viscous model

The subduction zone development of north Chile is here explored using the 2D thermomechanical model described in chapters 3 and 4, which uses a viscous rheology, kinematic boundary conditions and dynamic driving forces to investigate the generation

of stress in the lithosphere.

The parameters listed in table 7.1 are used to describe the north Chile subduction zone. The plate age is represented in the model by the temperature of the downgoing slab at the start of subduction, the dip angle is imposed with the geometry of the weak decoupling zone and the low viscosity mantle wedge, the plate velocity is imposed as a boundary condition on the top surface of the oceanic plate, and the rollback velocity is represented as a horizontal motion of the bottom boundary relative to the overriding plate. The viscous model can then be used to predict slab development over time, and the stresses that are generated.

Figure 7.6 shows snapshots of the downdip stress development for the north Chile parameters. Figure 7.6a shows the model 5Myr after subduction initiation, where the stress pattern of tension over compression indicates bending of the slab. Figures 7.6b and c show the model at 10Myr and 15Myr respectively, with the bending stress pattern until approximately 70km depth, after which the slab begins to unbend. Figures 7.6d and e show the model after 20Myr and 25Myr, where the slab has the unbending pattern until 200km, then inverts to bending again.

The tectonic history of the region means that figure 7.6e, with 25Myr of development, represents the current state of subduction beneath north Chile. Figure 7.7 shows the shape of the subducting slab beneath Chile, as inferred from Wadati-Benioff zone seismicity by Comte and Suarez (1994) and Araujo and Suarez (1994). The Chilean slab is known to be divided into several segments (Barazangi and Isacks, 1976), each with different geometries, as can be seen in figure 7.7b as the profiles move south. The region classed as north Chile covers approximately 19°S-24°S, which is shown in figures 7.7a and 7.7b(i); these correlate quite well with the slab shown in figure 7.6e where the slab subducts smoothly and without flattening.

Figure 7.8 shows the temperature, dynamic topography, downdip stresses and velocities for the present-day model shown in 7.6e. Overlaid on top of the temperature contours shown in figure 7.8a are the positions of cross sections s1, s2 and s3, taken perpendicular to the slab top at 100km, 150km, and 200km depth respectively. The downdip stresses along each of these profiles is shown in figure 7.8c. These profiles show a strong double layer of compression over tension within the slab, indicating the slab is unbending. Additionally, there is a small layer of tension above the slab in profiles s1 and s2; this appears to occur in the weak decoupling layer between the downgoing and overriding plates, which represents the subducting oceanic crust. Profile s3 does not show this tensile band, and figure 7.6e reveals that this is the point at which the slab changes from unbending to bending.

Figure 7.8b shows the dynamic topography for the present day model. Amplitudes

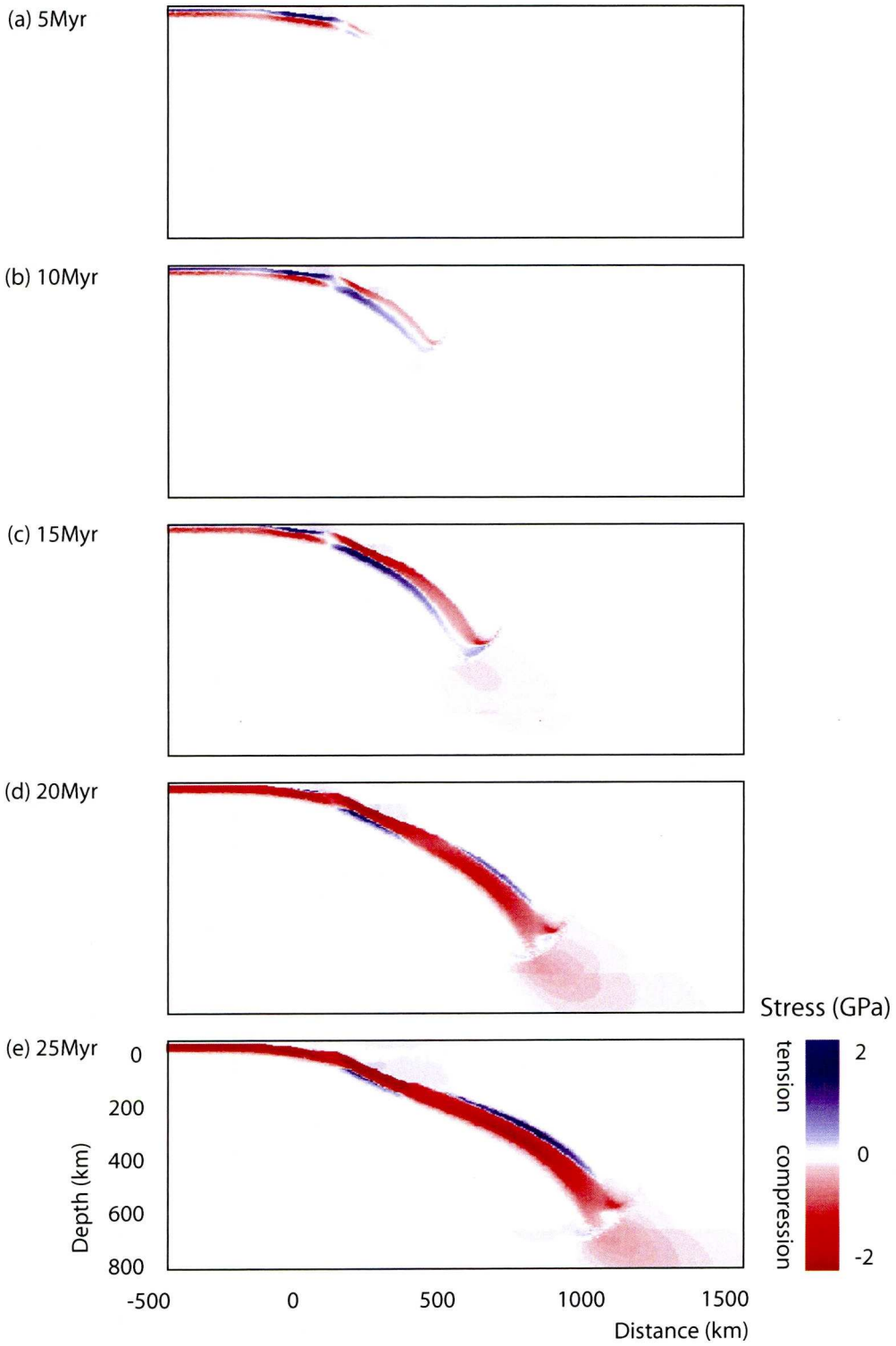


Figure 7.6: Downdip stresses predicted for north Chile by the 2D viscous model. Figures shown here are at (a)5Myr (b) 10Myr (c) 15Myr (d) 20Myr (e) 25Myr after subduction initiation.

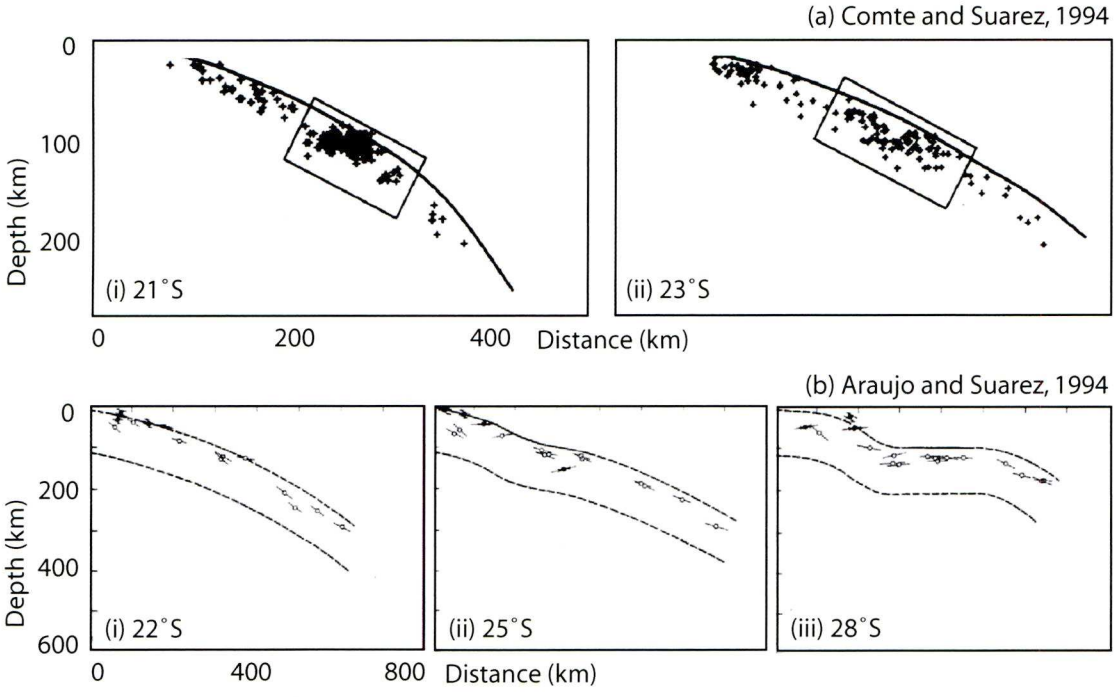


Figure 7.7: The subducting slab underneath Chile. Figure (a) shows seismic events and an estimate of the top of the slab Comte and Suarez (1994); figure (b) shows tensional events (open circles) and compressional events (filled circles) within the slab Araujo and Suarez (1994).

for the trench, arc, and basin are all reasonable, within an order of magnitude of observations and predictions from other models (Zhong and Gurnis, 1992; Billen and Gurnis, 2001). However, the large forebulge and the depression just before it are not seen in subduction zones and models. It could be possible that this decoupling layer somehow undermines the dynamic topography calculation, producing this anomaly; however this seems unlikely as the dynamic topographies presented in chapter 4 also use this decoupling layer but do not show this anomaly. It seems more likely that this is the result of using a geometry for the decoupling zone with a shallow and a deep angle, essentially causing a double trench, although it is surprising that this two-angle geometry which is supposed to be a more accurate representation of the north Chile subduction zone would have a detrimental effect on the dynamic topography. Further investigation of the effects of subduction thrust geometry and boundary conditions on dynamic topography would hopefully resolve this issue.

Figure 7.8d shows the velocities for the subduction zone where the white arrows show the velocity vectors, and the background colours represent the magnitude. The rollback velocity is apparent in the small but uniform velocity away from the slab. The mantle wedge shows a small anticlockwise circulation which occurs in approximately

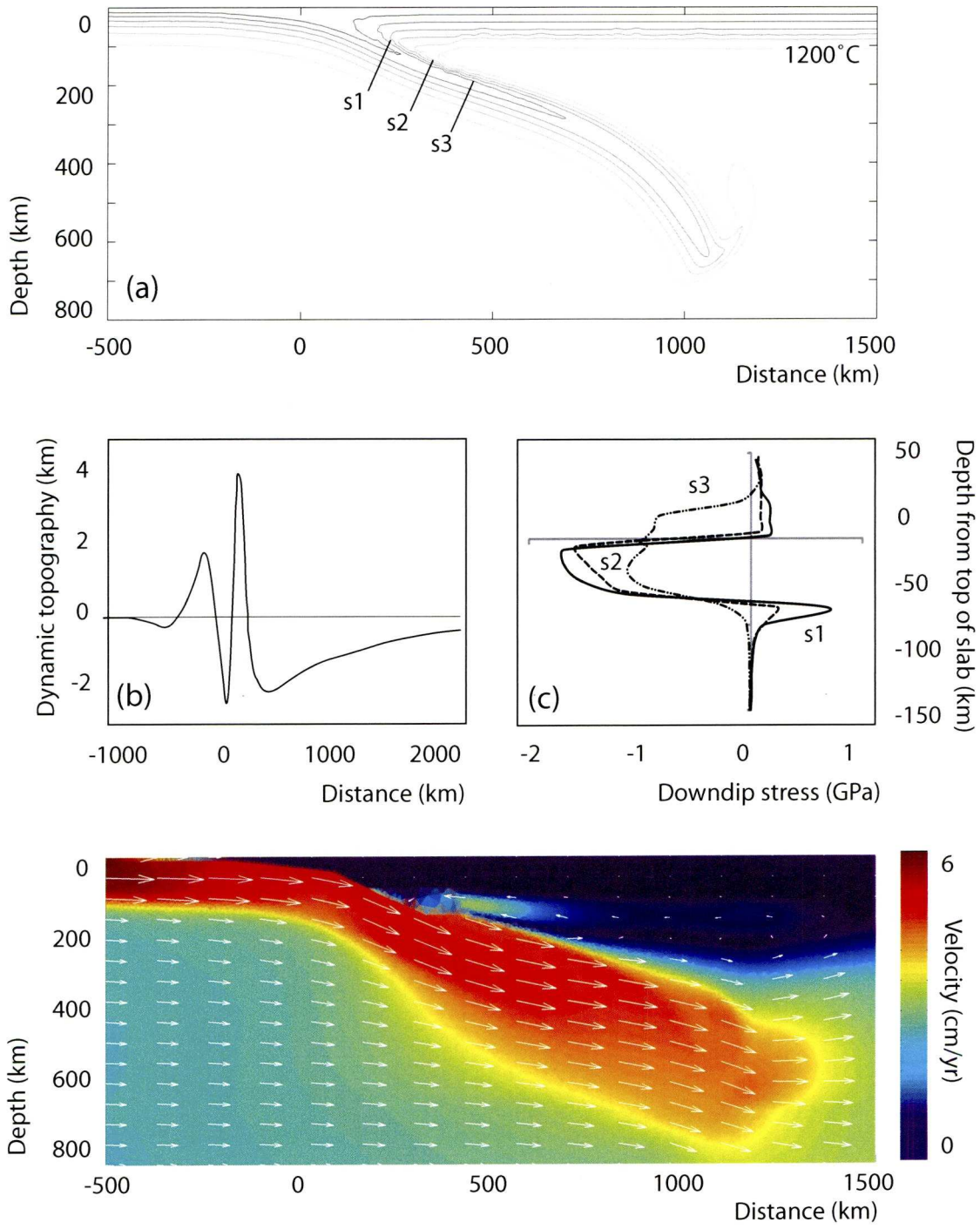


Figure 7.8: Outputs for north Chile from the 2D viscous model shown in 7.6c: (a) temperature; (b) dynamic topography; (c) downdip stresses along perpendicular cross sections shown in (a); (d) velocity.

the same region as the slab unbending stress pattern shown in figure 7.6e. It is possible that this circulation in the wedge provides an upwards force on the top of the slab,

inducing the unbending of the slab observed in figures 7.6e and 7.8c.

### 7.3.1 Sensitivity of predicted stresses from the 2D viscous model for north Chile

The 2D viscous model uses estimated values for dip angle, plate age, plate velocity and rollback velocity as input parameters to model the north Chile subduction zone. Each of the values listed in table 7.1 has an uncertainty associated with it; by repeating the numerical experiment and varying the parameters within the uncertainties, the sensitivity of the results to the input values can be assessed.

Figure 7.9 shows the differences in the models within the value ranges for (i) the 800°C temperature contour and (ii) the downdip stresses for a cross-section through the slab when the slab top reaches 100km (slice s1 in figure 7.8).

The dip angle is estimated at 25°±5°, in light of the work by Jarrard (1986), Lallemand et al. (2005) and Cruciani et al. (2005). Figure 7.9a shows that this dip angle has some effect on the shape of the slab and the magnitude of the downdip stresses, but the unbending pattern of compression over tension is still apparent.

The age of the subducting slab beneath north Chile is estimated as 50Myr±5Myr (Muller et al., 2008). Although this is a 10% difference, figure 7.9b shows that this has almost no effect on slab development or downdip stresses.

The plate velocity is estimated here as 6cm/yr, and the rollback velocity as 2cm/yr based on the work by Cruciani et al. (2005), Norabuena et al. (1998) and Schellart and Rawlinson (2010). Uncertainties of ±1cm/yr are estimated for both. Figures 7.9c and 7.9d show that for both the variation in plate velocity and rollback velocity the shape of the slab is changed as it enters the transition zone, but is relatively invariant at intermediate depths. The downdip stresses are very similar for all values of plate and rollback velocities in both shape and magnitude.

The results indicate that the slab development predicted by these parameters for north Chile is fairly robust, and the small variations in slab shape are not dissimilar to what is observed in south Chile (figure 7.7). The slab shape and downdip stresses at intermediate depths are particularly invariant within the uncertainties, giving confidence in the model predictions.

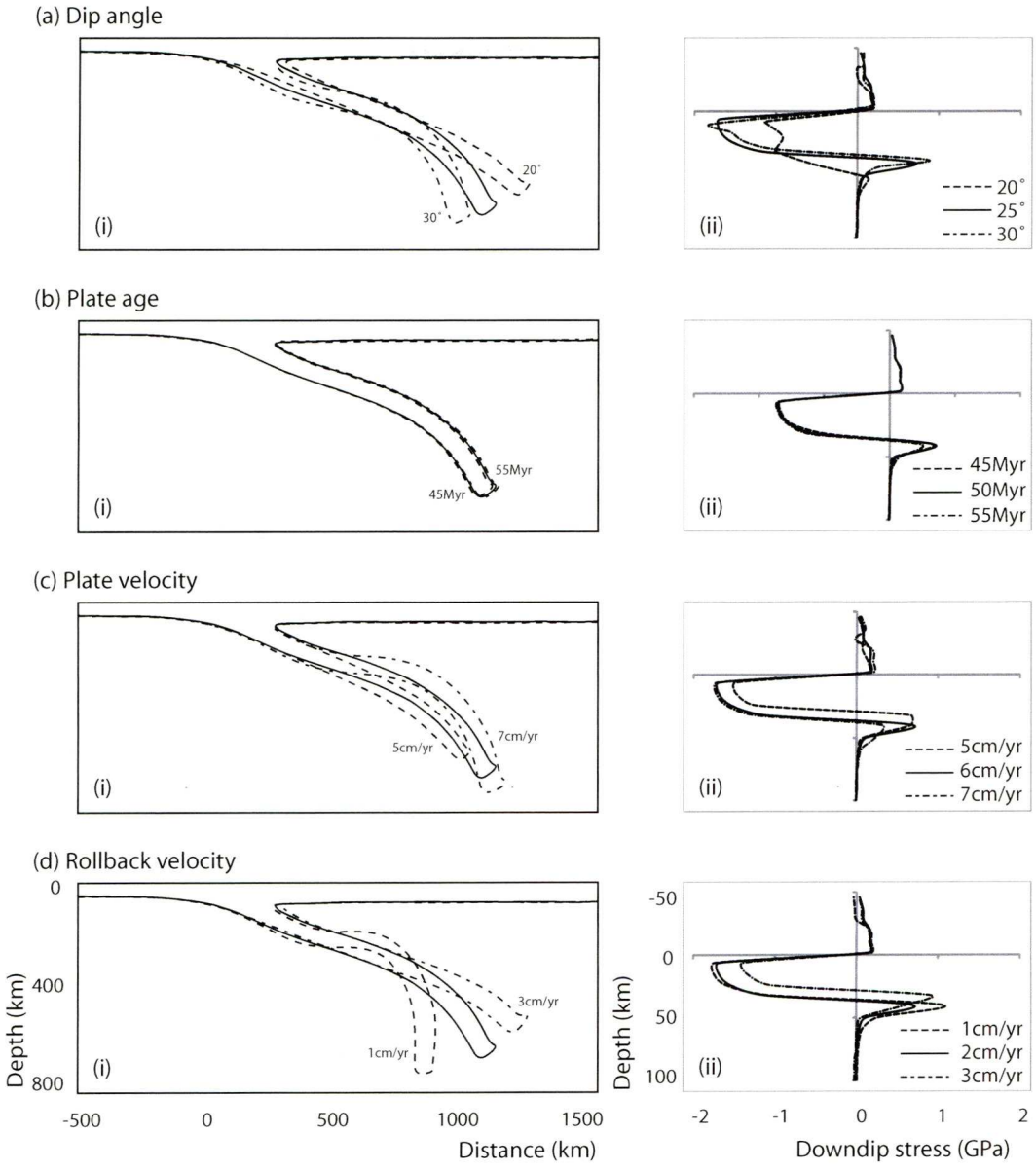


Figure 7.9: Sensitivity of slab development to the four parameters of (a) dip angle (b) plate age (c) plate velocity (d) rollback velocity. The 800°C temperature contour is shown in (i), and the downdip stresses along s1 is shown in (ii). In all figures the solid line indicates the reference model.

## 7.4 Modelling stress accumulation in the subducting lithosphere in north Chile with the 1D viscoelastic model

The one-dimensional viscoelastic model tracks a vertical slice of lithosphere from the ocean ridge to the trench and through the subduction zone. Prior to subduction the oceanic lithosphere accumulates stresses from cooling and the ridge push force, and

immediately before subduction stresses are generated from bending in the forebulge. During subduction, stresses are accumulated from heating, bending and unbending, the basalt to eclogite transition, and slab pull.

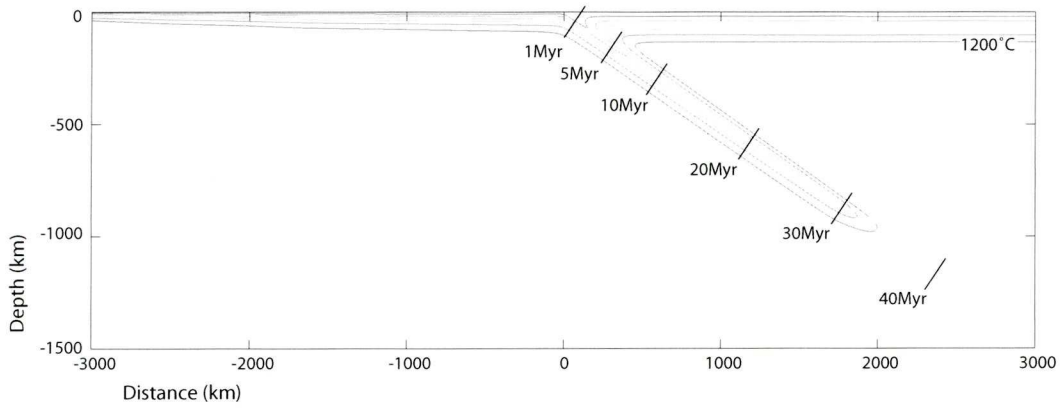


Figure 7.10: The temperature contours for Chile as calculated by the 2D thermal model. Cross sections relate to the stresses shown in figure 7.11.

As described in chapter 4, the temperatures used in the viscoelastic model are extracted from a stand-alone two-dimensional thermal model. The isotherms generated by this model for the north Chile subduction zone are shown in figure 7.10. Temperature is one of the most important parameters in calculating the stresses in the viscoelastic model as it determines the thermal stresses and the basalt to eclogite transition. It also influences the viscosity of the lithosphere which controls how much of the lithosphere is able to accumulate stress, and how much undergoes viscous creep.

The key parameters to model the north Chile subduction zone with the viscoelastic model are a plate velocity of 6cm/yr, a dip angle of 25°, a plate age of 50Myr, and a curvature gradient of $2\times\ 10^{-5}$. The plate velocity, dip angle, and plate age are all primarily introduced as parameters for the thermal model and therefore enter the viscoelastic model through the temperatures this generates. The plate velocity and the curvature gradient are also used directly in the viscoelastic model as factors in the calculation of the bending stress.

The stresses generated by the viscoelastic model are shown in figure 7.11; the cross-sections in figure 7.10 show the origin of their temperatures in the thermal model. The stresses generated by cooling and ridge push during the oceanic lithosphere's time as the ocean basin can be seen in figure 7.11a, 3 million years before subduction initiation. These stresses are rapidly overwritten by the bending stress in the forebulge which is applied 125km before the trench; this bending pattern of tension over compression is apparent 1Myr into subduction, shown in figure 7.11b. At 3Myr (figure 7.11c), the slab

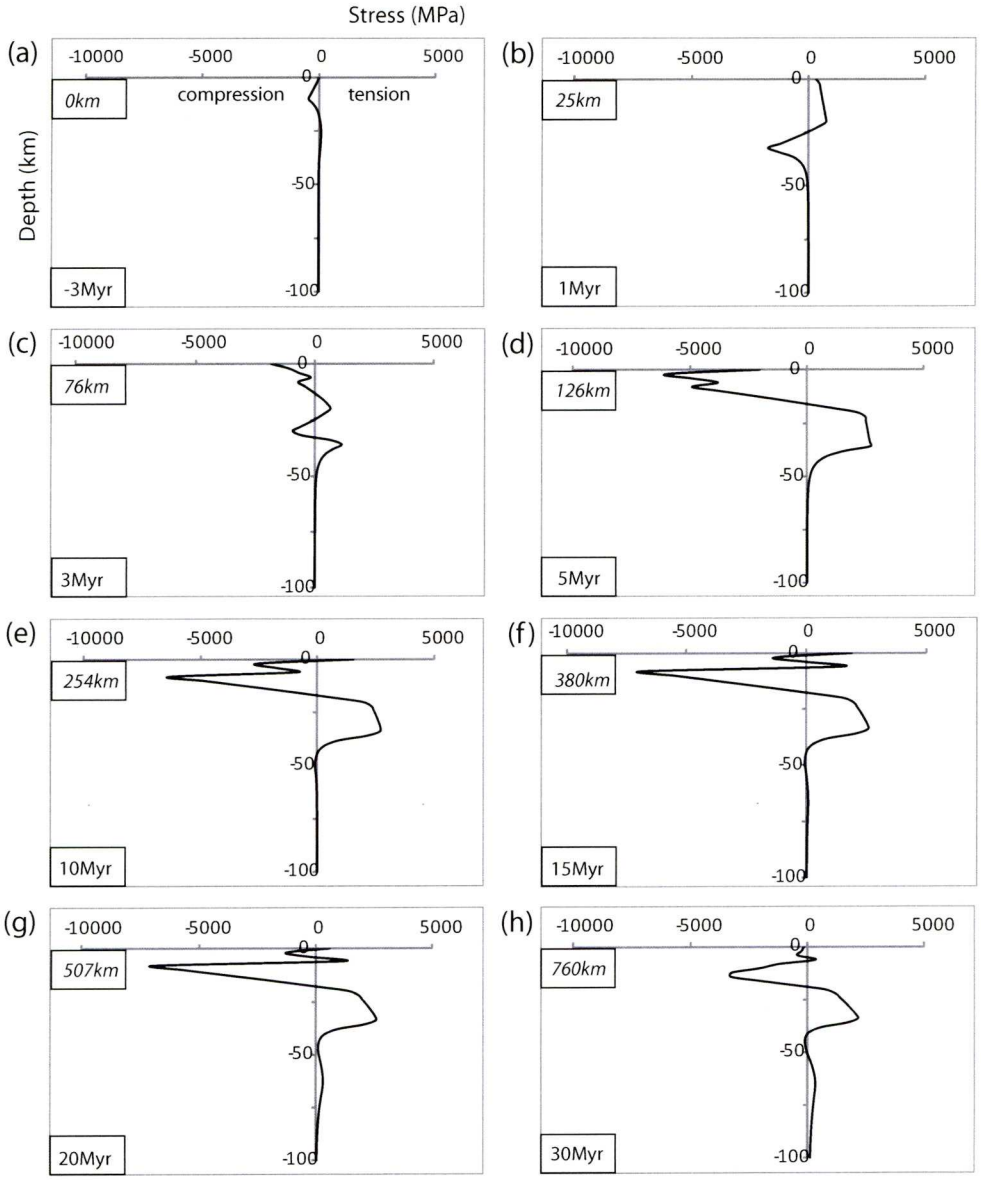


Figure 7.11: Stresses in the lithosphere as calculated by the 1D viscoelastic model. Numbers in italics refer to the depth of the top of the slab.

is moving from bending to unbending; this transition is completed by 5Myr (figure 7.11d) and the unbending stress pattern of compression over tension is clear, occurring here at intermediate depths.

The unbending stress pattern can be seen throughout figures 7.11d-h, persisting even after the unbending is complete due to the stress memory of the viscoelastic lithosphere. The contribution to the stress from the basalt to eclogite transition can also be seen in the lithosphere crust in these figures, eventually generating enough stress to put the subducted oceanic crust into tension, creating a triple layer of stresses

in figures 7.11f-h. By 30Myr (figure 7.11g), the slab is very warm and the stresses are dissipating though viscous creep, although slab pull as a renewable stress is still being applied.

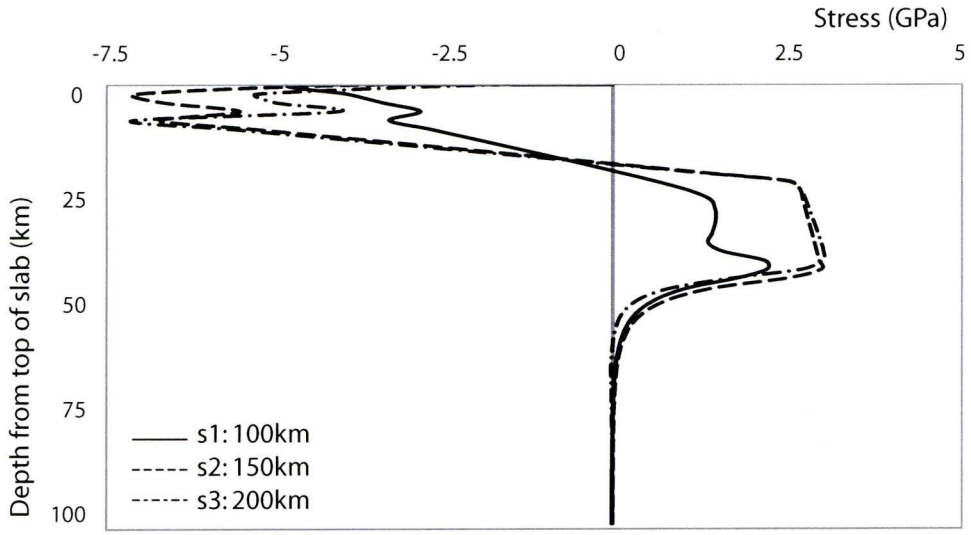


Figure 7.12: Stresses in the lithosphere taken along cross-sections s1,s2,s3, shown in figure 7.8a.

Figure 7.12 shows downdip stresses taken when the slab top is at 100km, 150km, and 200km, analogous to sections s1, s2 and s3 for the viscous model shown in figure 7.8a. The stresses for the 1D model are dominated by the unbending of the slab: all three cross sections have a layer of compression over a layer of tension, the same as the lower two sections in figure 7.8c. They do not, however, have the tensile layer in the subducted oceanic crust; the stresses generated by the basalt-to-eclogite transition are apparent but not large enough here to change the polarity of the stress.

The magnitudes of the stresses predicted by the 1D model are about two to three times higher than predicted by the 2D model, but still within an order of magnitude of the stress drops associated with seismicity in subduction zones. Conservative estimates put this in the range 750MPa to 1.5GPa (Andersen et al., 2008; John et al., 2009), but not all of the stress accumulated in the lithosphere will be dissipated in a single seismic event, so the maximum stresses predicted here are quite plausible.

### 7.4.1 Sensitivity of predicted stresses from the 1D viscoelastic model for north Chile

The stresses predicted for the north Chile slab from the 1D viscoelastic model are shown in figure 7.11. These are calculated using values estimated from the literature

(table 7.1), although each has an associated uncertainty. Sensitivity analysis is performed for the north Chile model, varying the four parameters of dip angle, plate age, plate velocity and curvature gradient within the estimated uncertainties to explore the response of the model.

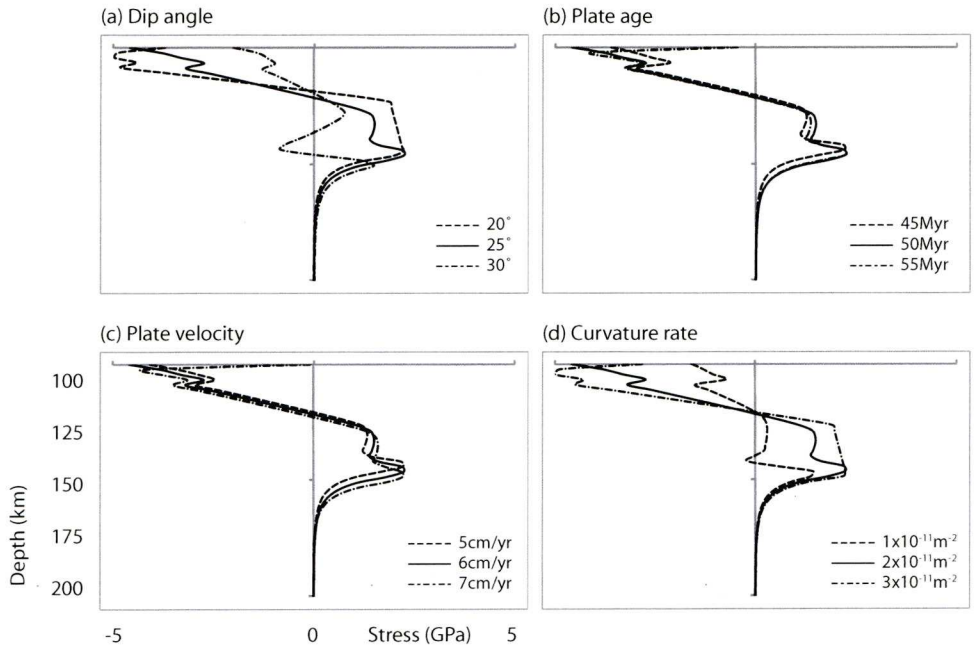


Figure 7.13: Sensitivity of slab stresses to the four parameters of (a) dip angle (b) plate age (c) plate velocity (d) curvature gradient.

The dip angle of the slab beneath north Chile is estimated as $25° \pm 5°$, as discussed for the 2D model. Figure 7.13a shows that there is some variation in stress pattern and magnitude over these angles (here the dip angle is varied independently to the curvature gradient). The dip angle influences the temperature contours across the subduction zone, so the lower angle model stays colder, giving higher stresses.

The plate age is estimated as 50Myr$\pm$5Myr (Muller et al., 2008); figure 7.13b shows the insensitivity of the predicted stresses within this range. The stresses are also very similar for the range of plate velocities 6cm/yr $\pm$1cm/yr (as discussed previously), shown in figure 7.13c.

The curvature gradient is estimated at $2 \times 10^{-11} \pm 1 \times 10^{-11} \mathrm{m}^{-2}$ (Theodoridou, 2008) owing to the difficulty in defining the topology of the slab, and the high sensitivity of the curvature gradient to the slab shape. The bending stresses resulting from the curvature gradient dominate the predicted stresses at intermediate depths, so these large uncertainties significantly change the resulting stress shape, as shown in figure 7.13d.

The point at which these stresses are taken is around the region where the slab changes from the bending regime to unbending, to highlight differences between the models. The stresses predicted by the model are relatively insensitive to plate age and plate velocity, and more sensitive to dip angle and curvature gradient, but overall, the predicted stresses are fairly robust.

## 7.5 Comparison of calculated stresses with observed seismicity

Although the presence of a Wadati-Benioff zone beneath Chile has been known for some time (Benioff, 1954; Barazangi and Isacks, 1976), it is only relatively recently that the narrowly-spaced double-planed structure has been observed (Comte and Suárez, 1995). The polarities of the stresses in the two planes were originally reported as having tension in the upper band and compression in the lower band as shown in figure 7.14 (Comte and Suarez, 1994; Comte and Suárez, 1995), but a later study concluded there was no clear pattern (Comte et al., 1999). The most recent work shows downdip tension in both bands, which are separated by only 9km (Rietbrock and Waldhauser, 2004), shown in figure 7.15.

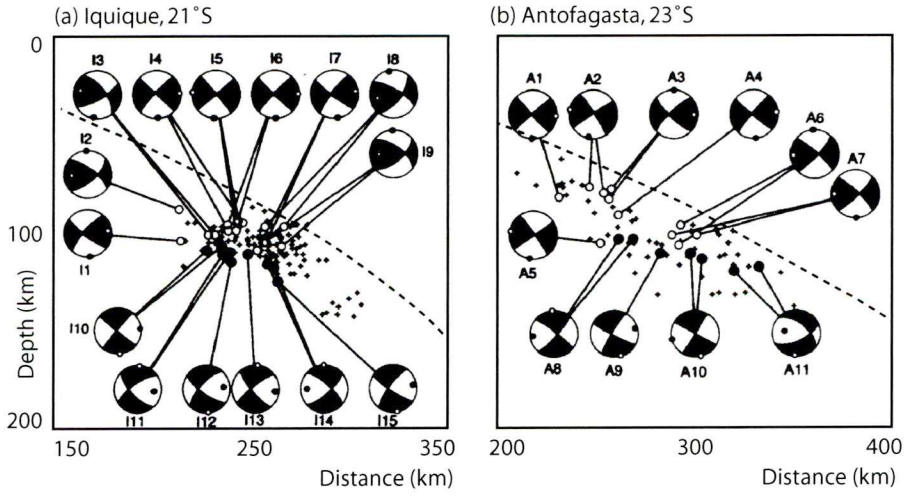


Figure 7.14: The double seismic zone in north Chile, with a layer of tensional events (open circles) over a layer of compressional events (coloured circles) in a side-looking projection. The slab top is indicated by the dashed line. (Comte and Suarez, 1994).

Both the 1D viscous and the 2D viscoelastic models presented here predict a double layer of stress at intermediate depths, but with the more usual double seismic zone pattern of compression over tension. Both have an additional layer of tension at the

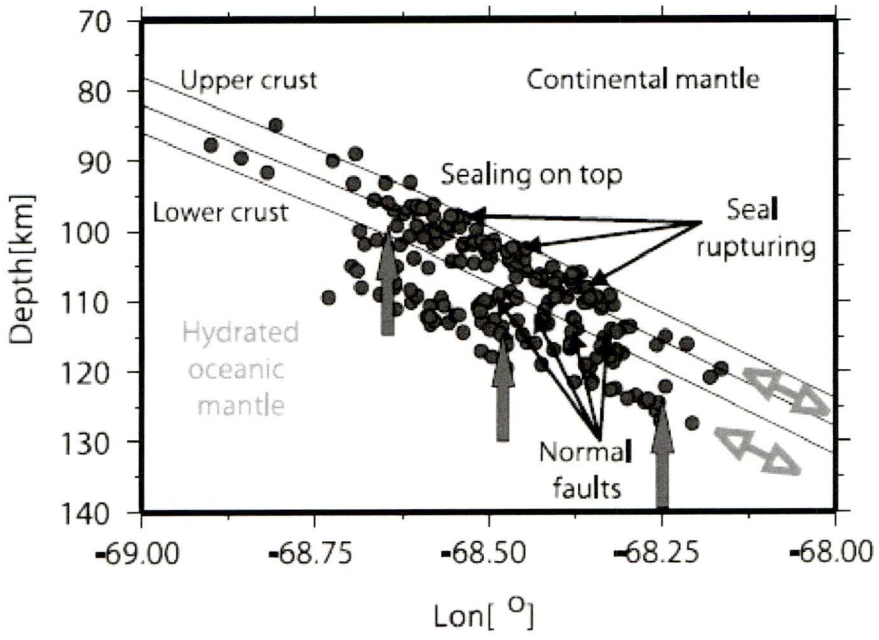


Figure 7.15: The double seismic zone in north Chile (Rietbrock and Waldhauser, 2004), with downdip tension in both bands.

top of the slab, although this occurs below intermediate depths in the 1D viscoelastic model. Neither model predicts downdip tension in both bands, and the assumption of stresses integrating to zero in the viscoelastic model would appear to specifically prohibit this. Isacks and Molnar (1971) and Rietbrock and Waldhauser (2004) attribute the downdip tension in the Nazca plate to slab pull, however in both the 2D viscous and 1D viscoelastic models slab pull has very little effect on the intermediate depth stresses. The results of the models presented here suggest a few alternative possibilities.

First, given the lack of agreement in the literature about the sign of the events, it is possible that the double layer pattern may be a transient effect. The 2D viscous model at 25Myr shows two changes in stress polarity along the slab length (figure 7.6e), all occurring at intermediate depths. The 1D model also has periods between bending and unbending where the stresses are quite complex. It may be that the slab beneath Chile is currently in the process of changing from one regime to another.

Another possibility is the two layers observed by Comte and Suarez (1994) and Rietbrock and Waldhauser (2004) are each two of the three layers of a triple seismic zone which has a stress pattern of tension over compression over tension: could Comte and Suarez (1994) be seeing the top two bands, and Rietbrock and Waldhauser (2004) be seeing the top and bottom band? The 2D viscous model predicts this triple stress struc-

ture at intermediate depths for north Chile; the top band is attributed to decoupling in the weak zone above the slab, and the lower two bands to unbending caused by circulation in the mantle wedge. The 1D viscoelastic model generates a double layer of stress at intermediate depths due to slab unbending, and a triple layer at depths of approximately 400km where the top band is attributed to the basalt-to-eclogite transition in the crust. It is not unreasonable to speculate that if the temperatures used in the 1D viscoelastic calculation were slightly higher, this triple layer could occur at intermediate depths. However, the problem of this hypothesis is that the two bands of tensile stress reported by Rietbrock and Waldhauser (2004) are only separated by about 9km, whilst the 1D viscoelastic and the 2D viscous models predict the distance between top and bottom stress layers to be at least 30km.

A closer inspection of the shape of the slab deduced by Theodoridou (2008) shown in figure 7.16 shows that the slab appears to bend and unbend twice, first around the trench, and again at about 175km depth. The 1D viscous model for north Chile imposes a single bending event which is shown in figure 7.5, where the curvature gradient is applied sinusoidally over a wavelength of 500km. If two smaller bending events are applied instead of one large event, the slab is essentially straight between about 50km and 150km depth.

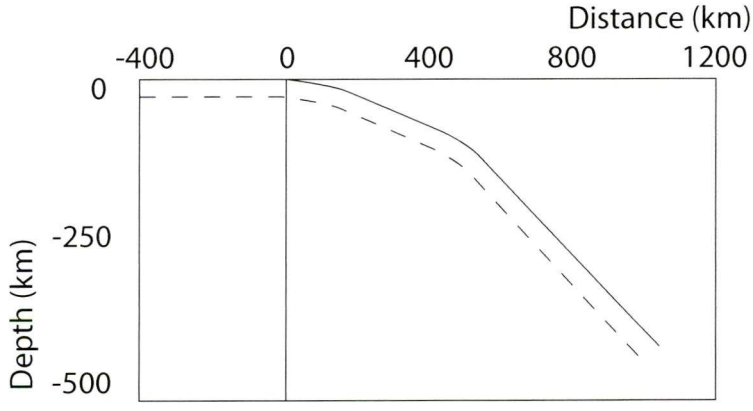


Figure 7.16: Estimate of slab shape based on Theodoridou (2008) (from figures 7.4(i)a and b): the slab bends twice during its descent.

Figure 7.17 shows the stresses generated by the 1D viscoelastic model when the bending occurs twice, where the curvature gradient of $2\times10^{-11}\mathrm{m}^{-2}$ is applied sinusoidally over a wavelength of (a) 250km and (b) 350km, centered about 25km and 175km depth. By shifting the curvature away from intermediate depths, the stresses along profiles s1-3 are no longer dominated by the bending stresses. This allows a more variable stress regime to emerge, where the basalt-to-eclogite transition plays a

more important role, putting the top of the slab into tension below 100km depth. Additionally, the two tensile bands are now separated by as little as 15km, which is close to the separation of tensile bands reported by Rietbrock and Waldhauser (2004).

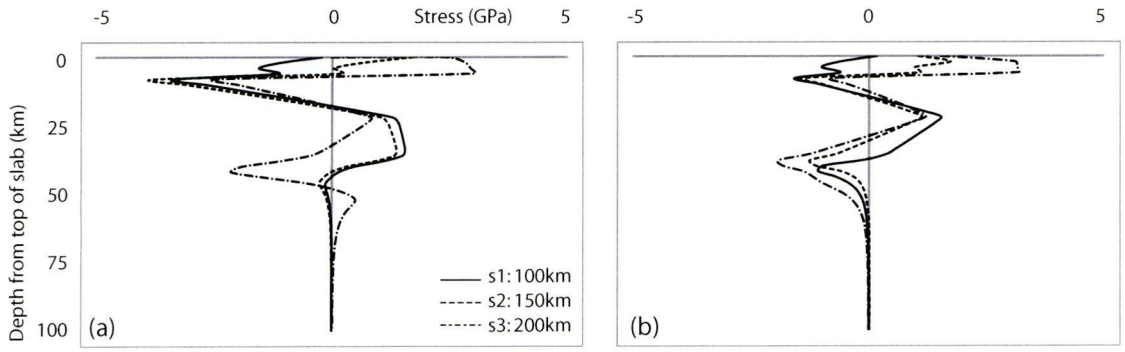


Figure 7.17: Stresses predicted by the 1D model when the bending is applied twice: at 25km and 175km depth, using a wavelength of (a) 250km and (b) 350km.

This is only a preliminary experiment, and has the basic flaw that whilst the bending is applied twice in the viscoelastic calculation, the thermal model can only calculate temperatures for a subduction zone with a single angle. Nevertheless, the diminished bending stresses and the development of a slab with multiple layers of stress appears to be fairly robust for the three profiles and two models. This would indicate that double seismic zones with anomalous stress polarities could be the result of a complex stress structure composed of multiple layers. Further investigation into the relationship between slab curvature and predicted stresses is recommended to explore this hypothesis.

## 7.6 Summary of predicted stresses for north Chile

Despite the 2D viscous and 1D viscoelastic models having different formulations and implementing different rheologies, they generate quite similar stresses for the subduction zone.

The 2D viscous model predicts a strong double layer of compression over tension which appears to be due to slab unbending under the influence of circulation in the mantle wedge. There is also a small layer of tension at the top of the slab in the weak decoupling zone.

Using the standard formulation of the 1D viscoelastic model where the slab only bends once, the unbending stresses of compression over tension dominate the total stress profile for most of the duration of subduction. An additional tensile band is

observed in the crust due to the basalt to eclogite transition, but not at intermediate depths. However, if the slab curvature is applied in two halves so that the slab is straight between 50km and 100km depth, the reduction in bending stresses allows a finer scale structure to emerge, where three or more bands of stress are seen in the slab at intermediate depths.

These predicted stresses give some insight into the processes that govern the seismicity observed in north Chile. Both models are strongly controlled by the bending and unbending of the slab, although the mechanisms causing this bending and unbending differ; both models also predict a layer of tension in the crust under certain conditions. The prediction by both models that stresses of alternating polarity are arranged in multiple layers in the slab leads to the hypothesis that double seismic zones are underdeveloped or underobseved triple seismic zones, as suggested by previous studies (Wang, 2002; Rietbrock and Waldhauser, 2004), although observational evidence is yet to be found.

# Chapter 8

# Modelling stress accumulation in the subducting lithosphere beneath northeast Japan

## 8.1 Introduction

One of the best-known sites of Wadati-Benioff zone seismicity is beneath northeastern Japan, where the Pacific plate subducts underneath the Okhotsk plate, as shown in figure 8.1. Seismicity is recorded over a large area, from 138° to 143°E, and 35° to 44°N. It is one of the most seismically active regions in the world, and the first place where a double seismic zone was observed (Hasegawa et al., 1978). It is also the only subduction zone observed so far which shows a triple layer of seismicity (Igarashi et al., 2001).

Seismicity in subduction zones is a direct consequence of stress accumulation and dissipation in the subducting slab. The two-dimensional thermo-mechanical viscous model formulated and demonstrated in chapters 3 and 4, and the one-dimensional viscoelastic model from chapters 5 and 6 are here used to investigate stress accumulation in the subducting lithosphere in northeastern Japan.

## 8.2 Key parameters of the northeast Japan subduction zone

By the time the Pacific plate begins to subduct underneath Japan, it has been cooling for approximately 130Myr (Muller et al., 1997, 2008), making it extremely old, cold, and dense. The plate age is introduced into both the 2D viscous and the 1D viscoelastic

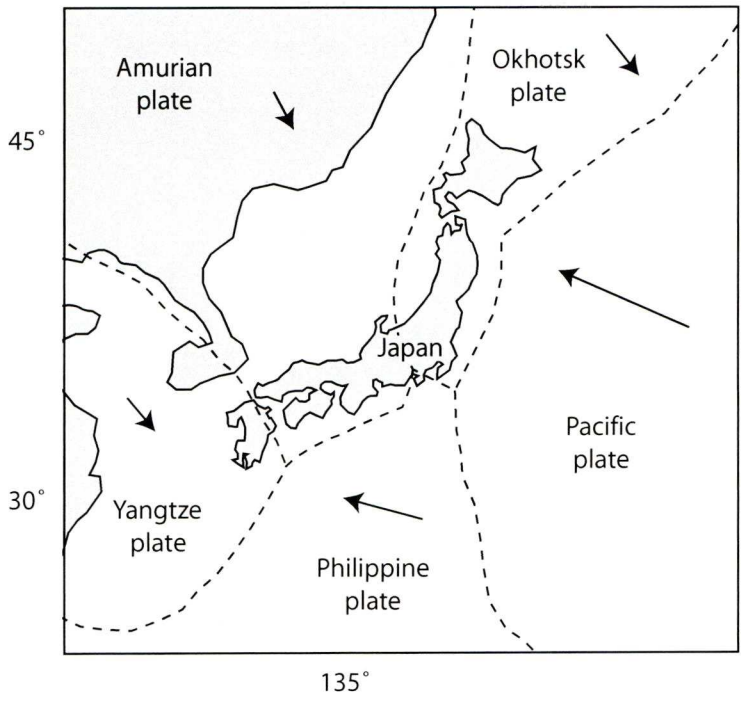


Figure 8.1: Japan and the local tectonic plate system, after Schellart and Rawlinson (2010). Arrows indicate plate motion.

models as the temperature of the oceanic lithosphere at the trench. In the viscoelastic model the temperatures are extracted from a two-dimensional kinematic temperature model, as discussed in chapter 5.

| Parameter | Value |
|---|---|
| Plate age | 130Myr |
| Dip angle | 25° |
| Plate velocity | 8cm/yr |
| Rollback velocity | 1.5cm/yr |
| curvature gradient | $1\times10^{-11}\mathrm{m}^{-2}$ |

Table 8.1: Parameters for the North East Japan subduction zone used in the viscous and viscoelastic models.

Although it is often assumed that an old slab will generate a high dip angle, this has not proved to be the case (Cruciani et al., 2005), and the dip of the slab under Japan averages approximately 25° (Lallemand et al., 2005). In the viscous model a shallow angle of 12° is prescribed for the upper 40km to represent the gradual onset of the dip angle and the presence of an accretionary prism (Yoshii, 1978). This 25° dip is then prescribed until 150km depth by the geometry of the weak zone and low viscosity

mantle wedge, but beneath this it is free to develop. In the viscoelastic model, the single dip angle of 25° is used in the thermal model which calculates the temperature of the lithosphere. The angles used in both models are shown in figure 8.2.

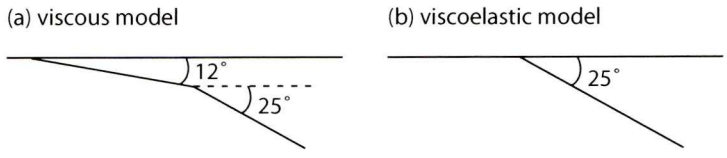


Figure 8.2: Dip angles for the (a) 2D viscous model and (b) 1D viscoelastic model

The combination of a fast spreading rate at the East Pacific Rise and the large slab pull at the subduction zone mean that the plate velocity is estimated at between 8cm/yr and 11cm/yr (Jarrard, 1986; Lallemand et al., 2005; Cruciani et al., 2005; Schellart and Rawlinson, 2010), with a rollback velocity of 0.5cm/yr (Jarrard, 1986), 1.5cm/yr (Schellart and Rawlinson, 2010), and 2cm/yr (Lallemand et al., 2005). To model the subduction zone I use the conservative values of an 8cm/yr plate velocity, and a rollback velocity of 1.5cm/yr, from Schellart and Rawlinson (2010). In the viscous model, plate velocity is imposed as a kinematic boundary condition on the top of the oceanic plate, and rollback velocity is represented by a relative horizontal motion between the lower boundary and the overriding plate. In the viscoelastic model, the plate velocity is one of the factors in the bending stress calculation, and influences the temperatures via the thermal model.

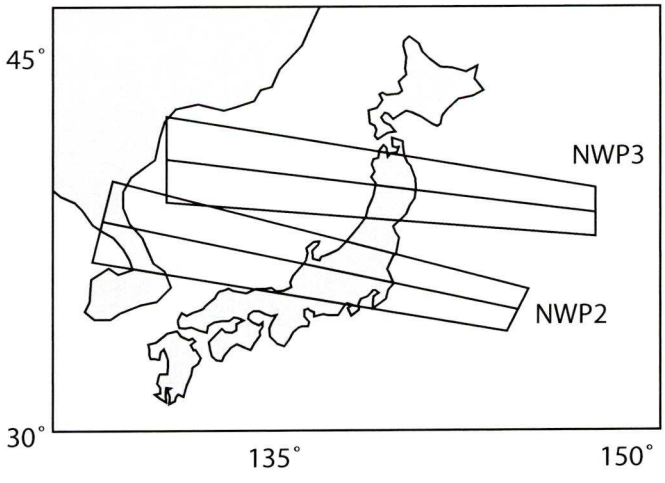


Figure 8.3: Profiles (a) NWP2 and (b) NWP3 in northeast Japan as defined in Theodoridou (2008)

The curvature gradient of the slab is also used to calculate bending stresses in the viscoelastic model. The rate of curvature for two sections of the northeastern Japan subduction zones are taken from Theodoridou (2008), where their locations are shown in figure 8.3. Theodoridou (2008) fits splines to the upper and lower extents of the Wadati-Benioff zone seismicity, and the third derivative of these fitted lines gives the curvature gradient, as shown in figure 8.4. A conservative estimate of an appropriate bending stress to use in the viscoelastic model based on these figures is $1\times10^{-11}\mathrm{m}^{-2}$. This is applied sinusoidally across the subduction zone, as shown in figure 8.5.

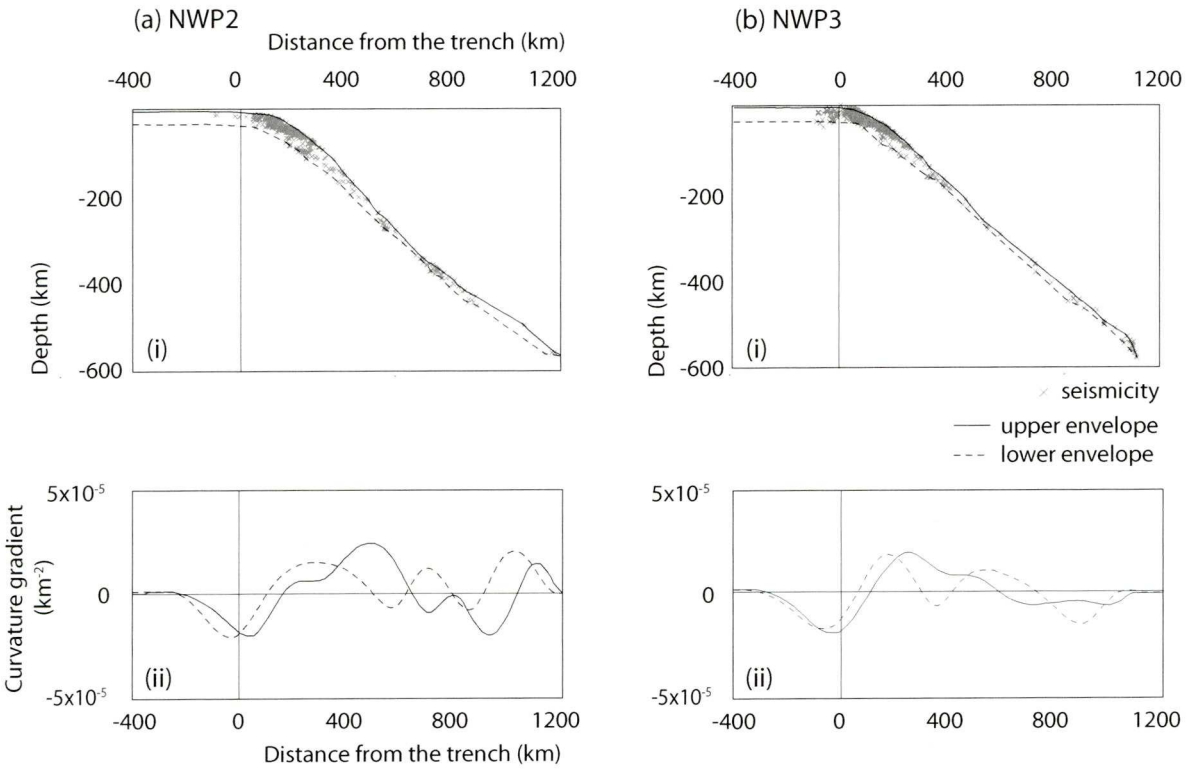


Figure 8.4: curvature gradient for the northeast Japan subduction zone, using profiles (a) NWP2 and (b) NWP3 as defined in Theodoridou (2008)

The major upheaval in the tectonic regime approximately 20-30Myr ago changed the direction and velocity of the Pacific plate and began the latest stage of subduction beneath northeastern Japan (Uyeda and Miyashiro, 1974; Uyeda, 1982). The viscous and viscoelastic models are therefore run for 25Myr to develop a subduction zone that represents the present day. However, although the new phase of subduction beneath Japan began with a mature subduction zone, the formulation of the 2D viscous model mean it begins with an unperturbed domain. The 1D viscoelastic model has no such

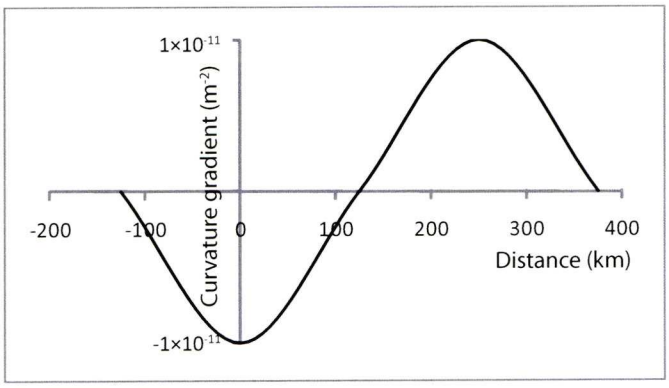


Figure 8.5: curvature gradient as applied to the 1D model

caveats, and uses a fully-formed subduction zone from the outset. The parameters listed in table 8.1 are used to describe the northeastern Japanese subduction zone in the viscous and viscoelastic models, and the slab development and generated stresses provide an insight into the processes that occur in the subducting lithosphere.

## 8.3 Modelling stress accumulation in the subducting lithosphere in northeast Japan with the 2D viscous model

The viscous model developed in chapters 3 and 4 is a two-dimensional thermo-mechanical model using a viscous rheology incorporating diffusion creep, dislocation creep, and a yield stress. Kinematic boundary conditions are used to impose plate and rollback velocities, but the rest of the model is driven by internal body forces. Using the parameters listed in table 8.1, the downdip stresses generated for the Japan subduction zone by the viscous model are shown in figure 8.6.

Figure 8.6a shows the downdip stresses in the subduction zone. At 5Myr after subduction initiation, shown in figure 8.6a, there is a layer of tension over compression as the slab bends to begin subducting. After 10Myr (8.6b), there is bending until approximately 100km depth, then the stress polarities reverse to compression over extension, indicating the unbending of the slab. At times 15-25Myr (figures 8.6c-e), there are stress patterns indicating unbending in the upper regions of the slab and bending in the lower portions. Based on the tectonic history of the region, the model with 25Myr of development shown in figure 8.6e represents the present day. The dashed box shows the intermediate depth regions for comparison with the subduction zones shown in figure 8.7.

The shape of the slab subducting under northeast Japan is fairly well constrained

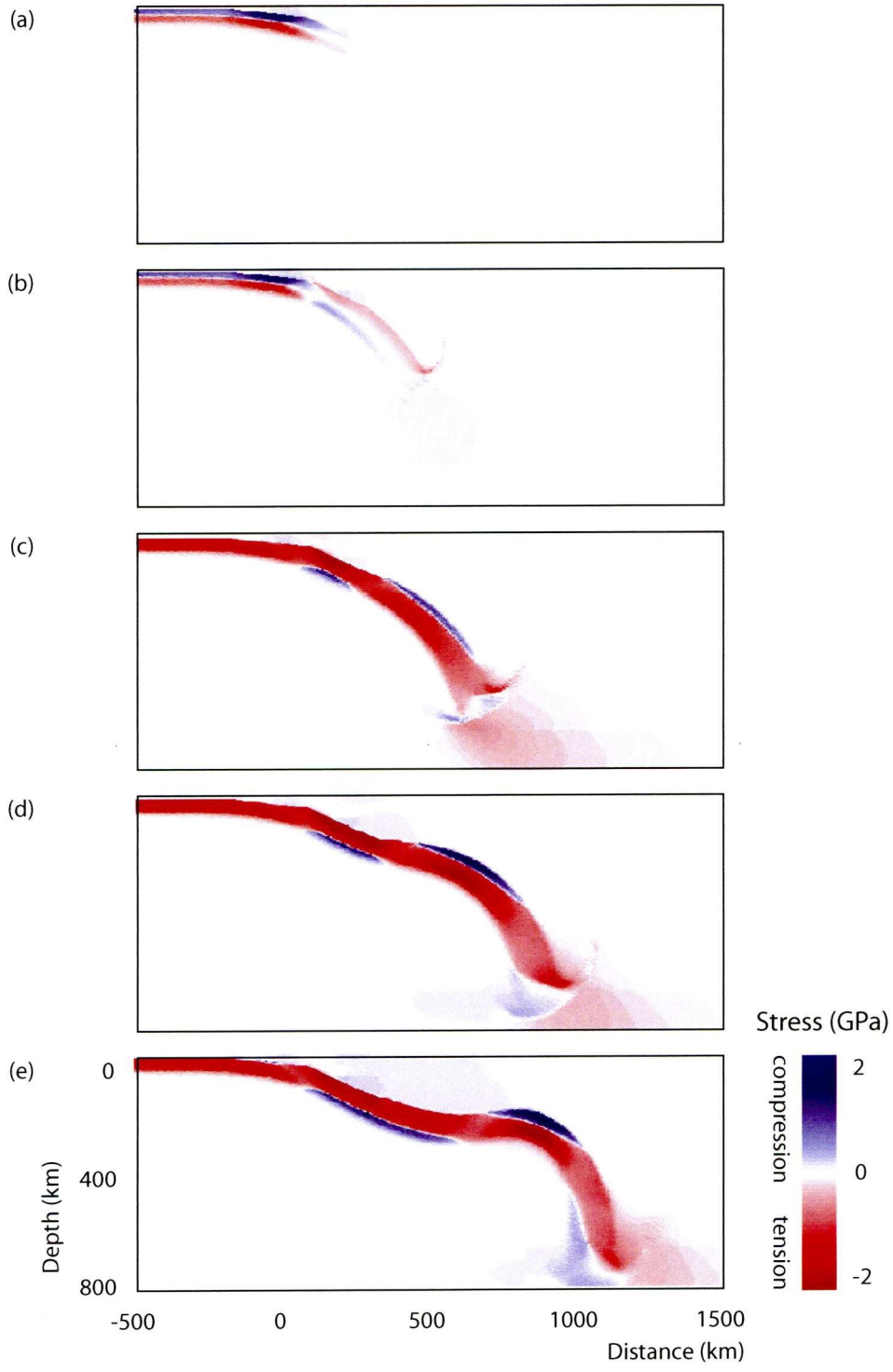


Figure 8.6: Downdip stresses in the lithosphere as calculated by the 2D viscous model. Figures shown here are at (a)5Myr (b) 10Myr (c) 15Myr (d) 20Myr (e) 25Myr after subduction initiation. Dashed box is for comparison with figure 8.7.

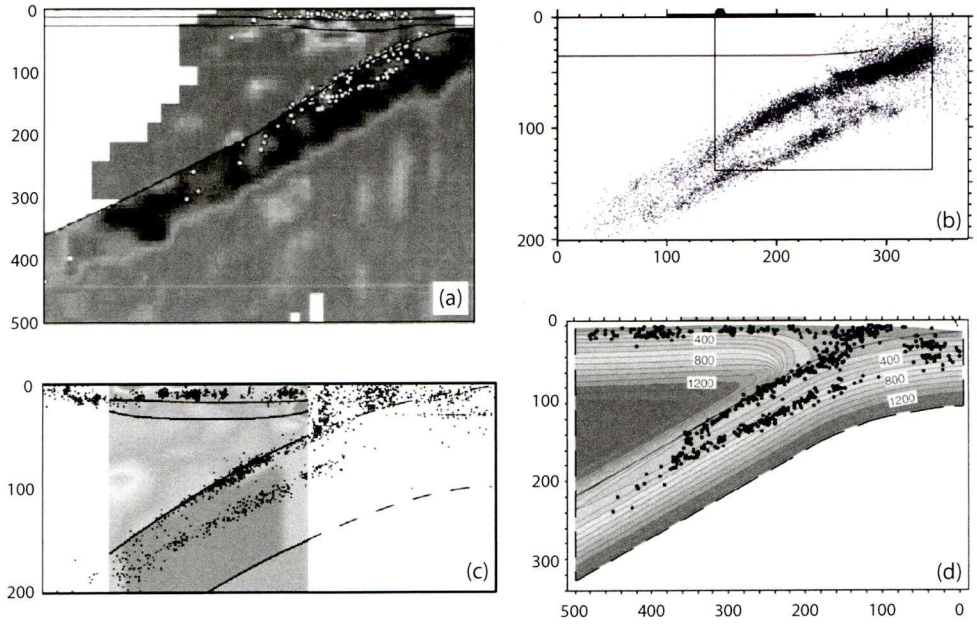


Figure 8.7: The subducting slab underneath northeast Japan, from (a) Zhao et al. (1994) (b) Igarashi et al. (2001) (c) Nakajima et al. (2001) (d) Peacock (2001)

for the first 400km depth and approximately 400km from the trench, as determined by tomography and seismicity (Zhao et al., 1994; Igarashi et al., 2001; Nakajima et al., 2001; Peacock, 2001), as shown in figure 8.7. Seismicity shown in figure 8.4 indicates the position of the slab below intermediate depths, but the focal mechanisms become sparse, especially in the more northern segment, NWP3. The intermediate depths of the present day model shown in the dashed box figure 8.6e compare well to the slab shapes shown in figure 8.7, with the top of the slab arriving at approximately 150km depth after 300km of horizontal motion (figures 8.7b and d). However, beyond this the 2D model predicts a flat subduction model, which is not observed in Japan.

Other output parameters for the present day model (25Myr, figure 8.6e) are shown in figure 8.8. Figure 8.8a shows the temperatures contours for the model. Overlaid are three cross sections s1, s2, and s3 starting at 100km, 150km and 200km depth respectively, which run perpendicular to the slab top, and cover the region in which the double and triple Wadati-Benioff zones are observed (figure 8.7). The downdip stresses along each of these lines are shown in figure 8.8c; the stresses for slice s3 which starts at 200km is shifted slightly higher than the other two as the slab is beyond the region where the dip angle is specified, and is pulled upwards by the flow in the mantle wedge. All three cross-sections show a layer of compressive stress over a layer of tensile stress, which is in agreement with the focal mechanisms recorded by Hasegawa et al. (1978) for the two dominant bands of the northeast Japan subduction

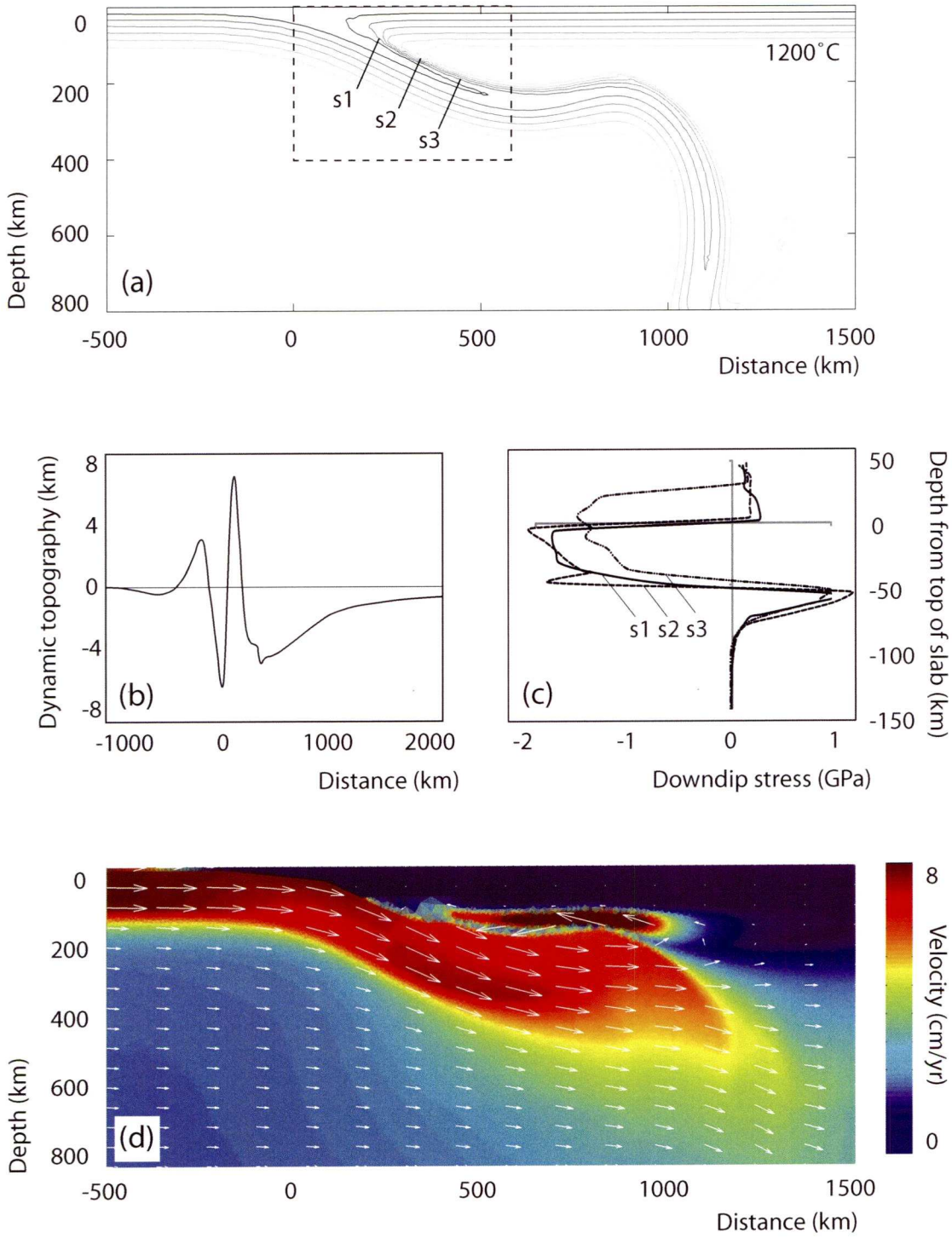


Figure 8.8: Outputs for northeast Japan from the 2D viscous model at present day, shown in 8.6d: (a) temperature; (b) dynamic topography; (c) downdip stresses along perpendicular cross sections shown in (a); (d) velocity.

zone. Additionally, there is a small tensile layer of stress at the top of the slab in the weak zone, which correlates with the third band of seismicity observed by Igarashi

et al. (2001). The compressive stresses are the larger of the two, with a maximum of 2GPa, which compares well to other models and observations (Andersen et al., 2008; John et al., 2009; Cížková et al., 2007).

Figure 8.8b shows the dynamic topography for the region. Like the dynamic topography calculated for north Chile, the trench, arc, and outer rise are all visible, with maxima that are high but still fairly similar to those predicted by Zhong and Gurnis (1992). However, the very high forebulge and the depression immediately before it are not seen in observations or models. As discussed in chapter 7, it is possible that this is due to a boundary condition issue involving the weak decoupling layer, or due to a superposition of a mini trench caused by the shallow dip angle of 12° representing the accretionary wedge. Further investigation into the causes of this anomaly will hopefully shed more light on this issue.

Figure 8.8d shows the velocities in the region, where the white arrows are the velocity vectors, and the coloured background indicates magnitude. The circulation in the mantle wedge is immediately obvious, with velocities of a similar magnitude to the plate velocity; the effect of the rollback velocity can be seen in the constant background mantle flow.

Figures 8.6 and 8.8b show the stresses in the subducting slab, which culminate in present-day conditions of a strong layer of compression over a layer of tension, with a small layer of tension at the top of the slab. The two main bands of compression over tension indicate slab unbending, however this unbending cannot be a result of stresses accumulated during an earlier phase of bending, as this is a viscous model and has no stress memory. An alternative possibility is that the induced flow in the mantle wedge shown in figure 8.8d unbends the slab by pulling the top surface upwards, often called trench suction (Forsyth and Uyeda, 1975). This flow-induced slab unbending appears to cause the compression over tension double seismic layer seen at intermediate depths in figures 8.6b-e. In these models, when the negative buoyancy of the slab finally exceeds the upwards pull of the trench suction, the slab bends back downwards again and the stress polarity is reversed, but this is not supported by observations.

### 8.3.1 Sensitivity of results from the 2D viscous model for northeast Japan

The values of the controlling parameters shown in table 8.1 each have an associated error; by varying these values within the uncertainty range, the robustness of the results presented in figures 8.6 and 8.8 can be examined. Figure 8.9 shows the results of

these sensitivity tests. Column (i) shows the shape of the slab, as defined by the 800°C contour. Column (ii) shows the downdip stresses extracted perpendicular to the top of the slab starting at 100km depth, referred to as s1 in figure 8.8c.

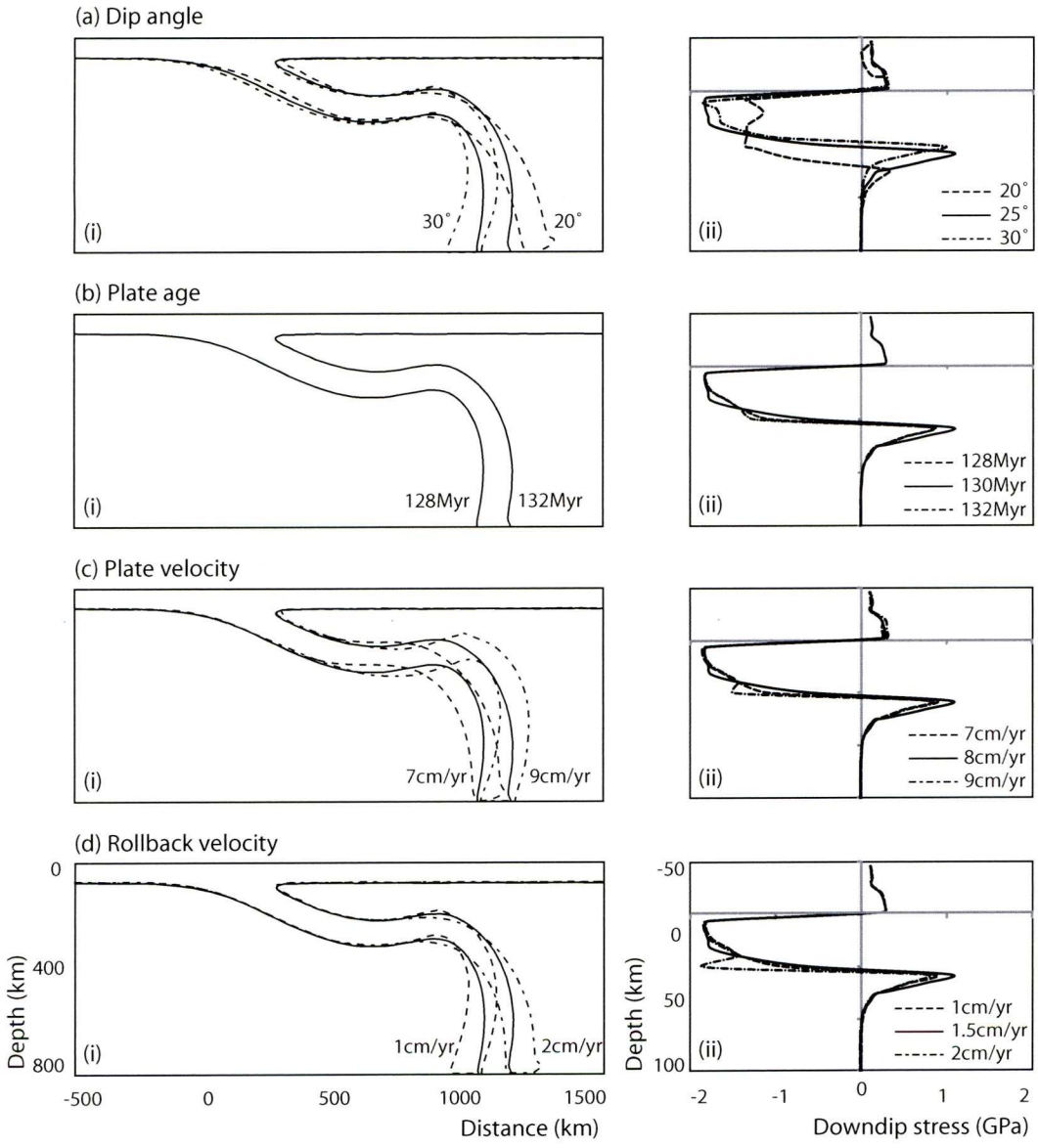


Figure 8.9: Sensitivity of slab shape and downdip stresses to the four parameters of (a) dip angle (b) plate age (c) plate velocity (d) rollback velocity. All models shown at 25Myr development.

The dip angle is estimated as 25°±5°, based on the range of values measured by Jarrard (1986), Lallemand et al. (2005) and Cruciani et al. (2005). Figure 8.9a shows the model run with 20°, 25°, and 30° dips. The shallower the dip angle, the straighter the slab and the smaller the stresses, although all three are quite similar.

The plate age is estimated as 130Myr old, with a small uncertainty of ±2Myr (Muller

et al., 2008). Figure 8.9b shows models with a plate age of 128Myr, 130Myr, and 132Myr. The model is hardly affected by this variation at all: the shape of the slab is nearly identical, and the stresses are also very close.

The plate velocity of 8cm/yr and rollback velocity of 1.5cm/yr are taken from Schellart and Rawlinson (2010); in the context of values given by Jarrard (1986), Lallemand et al. (2005) and Cruciani et al. (2005), uncertainties of $\pm$1cm/yr and $\pm$0.5cm/yr respectively are estimated. Figure 8.9c shows the model run with a plate velocity of 7, 8, and 9cm/yr; interestingly the slab tip is in almost the same place for all three velocities, with more distortion of the slab in the faster models. The stresses are also very similar, although the fastest model has a depression in the compressive part, possibly due to the effects of the plasticity since it is colder.

Figure 8.9d shows models with a rollback velocity of 0.5cm/yr, 1cm/yr and 1.5cm/yr; the slab shapes are virtually identical for the first 800km horizontally, after which the rollback causes divergence between the three. The stresses are also much the same, again with the effects of the stress-limiting plasticity appearing in the model with the fastest rollback.

Overall the model is fairly robust within its estimated uncertainties, especially in the intermediate depths which are the most important when analysing double seismic zones. The shape and magnitude of the downdip stresses always show a strong layer of compression over tension, with a small layer of tension just above the slab.

## 8.4 Modelling stress accumulation in the subducting lithosphere in northeast Japan with the 1D viscoelastic model

The viscoelastic model described in chapters 5 and 6 follows a 1D slice of lithosphere in a Lagrangian manner as it moves from the mid-ocean ridge to the trench and through the subduction zone. Temperatures are extracted from a stand-alone 2D thermal model and used to calculate viscosity. Stresses are accumulated in the slab arising from thermal expansion or contraction, slab bending, the basalt to eclogite transition, ridge push, and slab pull. The total stresses these generate in the lithosphere can then be investigated.

The temperatures for the subduction zone as calculated by the 2D thermal model using the values listed in table 8.1 are shown in figure 8.10. The overlaid markers indicate the position of the lithosphere slice at the various times in its development used in figure 8.11.

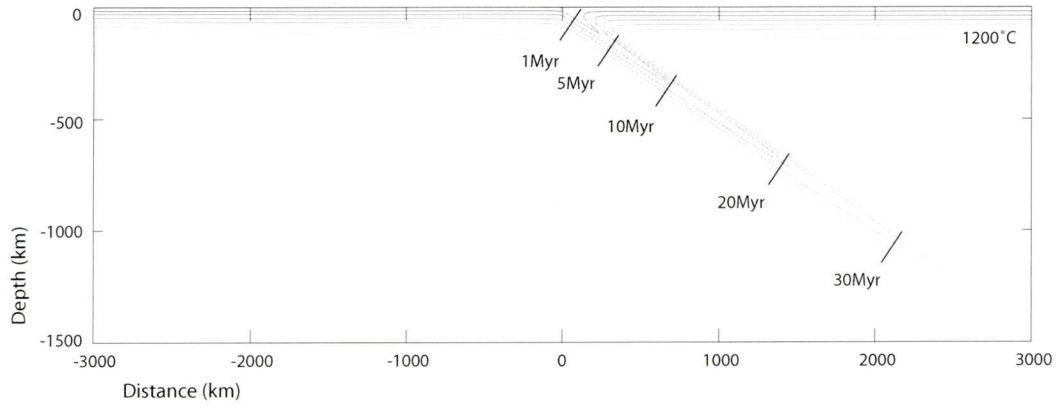


Figure 8.10: The temperature contours for Japan as calculated by the 2D thermal model.

Figure 8.11 shows the stresses in the lithosphere, where the depth indicates the distance from the top of the slab. At 1Myr before subduction (figure 8.11a), the stresses are a result of ridge push and slab cooling. At 1Myr after subduction initiation (figure 8.11b) the bending is at its peak, creating tension in the top of the slab and compression below. At 3Myr (figure 8.11c), the slab is beginning to unbend, reversing the stress polarities. By 5Myr (figure 8.11d) the unbending stress pattern is well-developed, and this shape stays fairly constant for the next 10Myr of subduction (figure 8.11d-f). At 15Myr (figure 8.11f) the stresses from the basalt-to-eclogite transition in the crust have created a small band of tension at the top of the slab. This stress pattern of tension-compression-tension persists until 30Myr (figures 8.11f-h), where the only mechanism still acting is the slab pull force.

The low temperatures at high pressures encountered by the model at 25Myr and 30Myr (figures 8.11g and h) cause the breakdown of the model; it appears that the bottom 25km is too high viscosity for the stresses to dissipate. However, this is only encountered at these extreme conditions, which occur at depths of 850-1000km, so does not invalidate the stresses predicted at shallower depths.

Figure 8.12 shows stresses in the lithosphere taken along the same cross-sections s1, s2, s3 as shown in figure 8.8. Each slice runs perpendicular to the top of the slab, starting at 100km, 150km, and 200km depth respectively. In slices s2 and s3, the stresses arising from the basalt-to-eclogite transition can be seen in the top 10km, and the shape of the brittle strength envelope on the tensile stresses is also apparent 30-60km below the top of the slab. The s1 slice captures the stresses in the lithosphere as it moves from the bending regime to unbending, which can be seen in figure 8.11c.

Comparing figure 8.12 for the 1D viscoelastic model with figure 8.8c for the 2D viscous model, it is clear that all the slices have broadly the same stress configuration

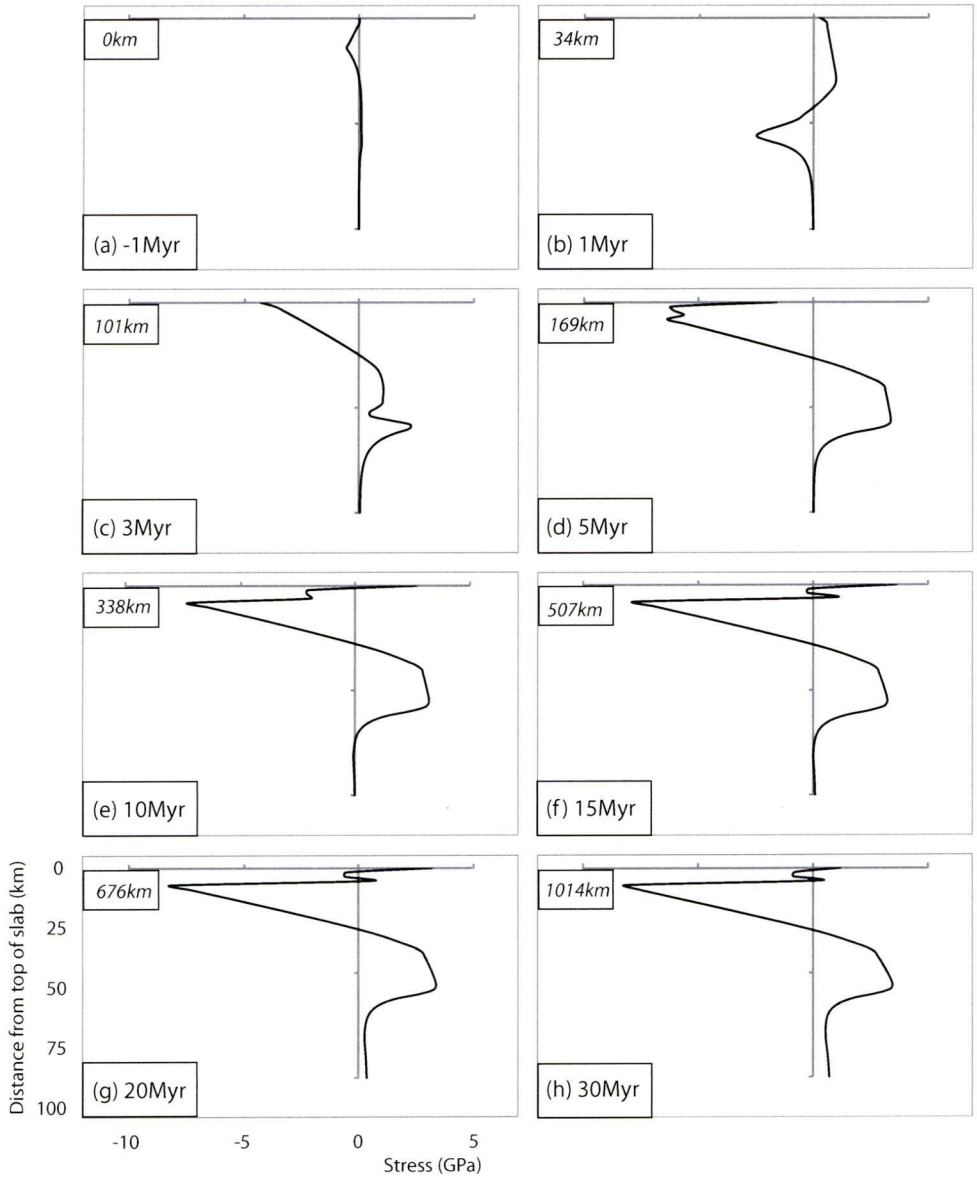


Figure 8.11: Stresses in the lithosphere as calculated by the 1D viscoelastic model.

of compression over tension, indicating unbending in the slab. The differences in the shapes of the stress profiles reflects the differences in the calculations for the 1D viscoelastic and 2D viscous models: the 1D model calculates the stresses generated by the various mechanisms and allows brittle failure, whilst the 2D model calculates flow within the slab and mantle which is tempered by a stress-limiting rheology. The magnitudes of the stresses predicted from the 1D model are somewhat higher than those predicted by the 2D model, possibly due to the lack of yield stress in the rheology formulation, or because of an overestimate in quantities such as the curvature gradient, however both models are still within half an order of magnitude of each other.

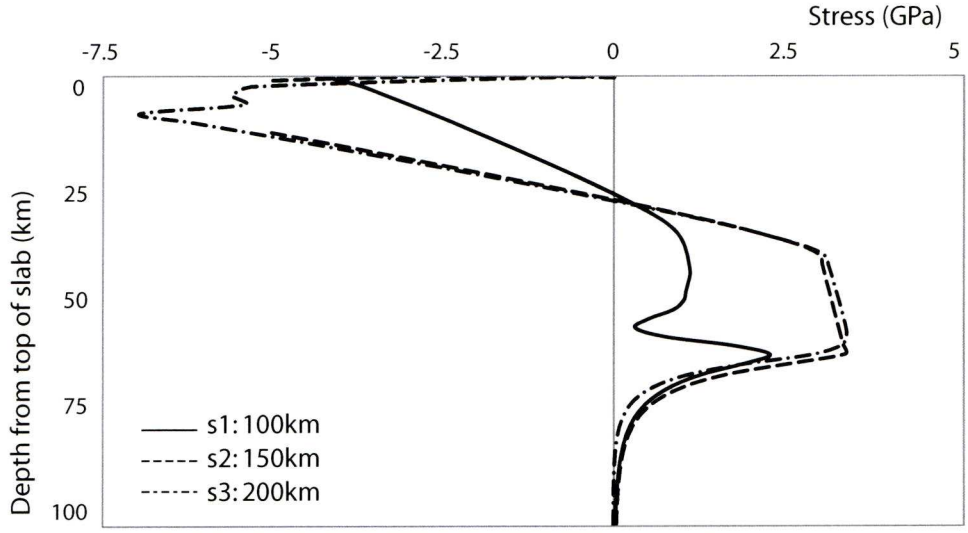


Figure 8.12: Stresses in the lithosphere taken along cross-sections s1,s2,s3,shown in figure 8.8.

Focal mechanisms recorded for the northeast Japan subduction zone indicate a triple layer of tension-compression-tension in the slab at intermediate depths (Hasegawa et al., 1978; Igarashi et al., 2001). The bands of compression over tension indicate unbending in the slab, and are apparent throughout much of the slab development history shown in figure 8.11, and predicted at intermediate depths as shown in figure 8.12. The later stages of development shown in figure 8.11 show a triple layer of stress, where the unbending double layer is topped by a small layer of tension due to the basalt to eclogite transition, although in this model this occurs at approximately 1000km depth. Estimates of stress drops due to subduction zone seismicity are in the range 750MPa-1.5GPa (Andersen et al., 2008; John et al., 2009), but as seismicity is not expected to release all the accumulated stresses at once, the stresses predicted here seem plausible.

### 8.4.1 Sensitivity of results from the 1D viscoelastic model for northeast Japan

To predict stresses for the northeast Japan subduction zone using the 1D viscoelastic model requires estimation of the four parameters of dip angle, plate age, plate velocity and curvature gradient. To investigate the sensitivity of the model results to these four parameters, each is varied within its estimated uncertainties in the same manner as for the 2D viscous model in section 8.3.1, and the stresses in the lithosphere when the slab

top reaches 100km (cross section s1 in figure 8.8a) are compared.

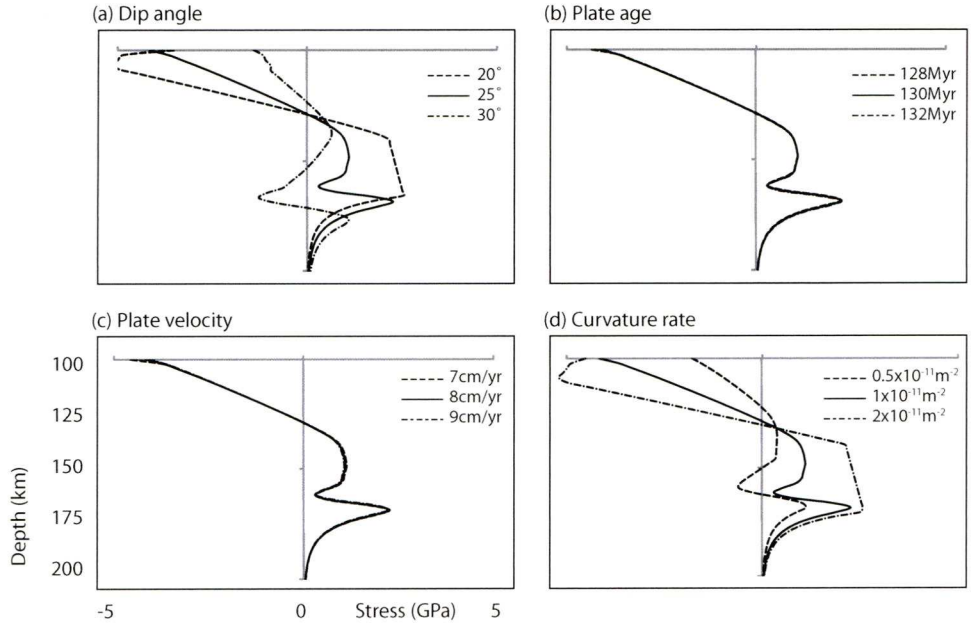


Figure 8.13: Sensitivity of slab stresses to the four parameters of (a) dip angle (b) plate age (c) plate velocity (d) curvature gradient.

The dip angle used is $25° \pm 5°$ (see section 8.3.1); figure 8.13a shows that the model is quite sensitive to this uncertainty, significantly changing the shape of the stress profile. The 30° model also has a different stress pattern, vacillating between compression and tension a number of times as it changes from the bending regime to unbending.

The plate age is estimated as 130Myr±2Myr (Muller et al., 2008), and figure 8.13b shows that the model is almost unchanged within this small range of values. The predicted stresses are also quite insensitive to the plate velocity (figure 8.13), which is estimated as 8cm/yr±1cm/yr as discussed in section 8.3.1.

A conservative value of the curvature gradient is estimated as $1 \times 10^{-11} \mathrm{m}^{-2}$ with an error of approximately half an order of magnitude so the model is run with half and double this figure, based on the work by Theodoridou (2008) shown in figure 8.4. The curvature of the slab is calculated as the third derivative of the fitted spline, and is therefore very sensitive to small variations in the slab topography deduced from earthquake focii. The stresses are influenced quite strongly by the curvature gradient, and these large errors have a significant effect on the shape and magnitude of the predicted stress profiles.

Overall, the 1D model is sensitive to dip angle and curvature gradient, especially at the depth range 100-200km, when the slab is transitioning from bending to unbending. However, the model is quite insensitive to variations in the plate age and plate velocity.

## 8.5 Comparison of calculated stresses with observed seismicity

The subduction zone beneath northeastern Japan was originally thought to be a double seismic zone (Hasegawa et al., 1978) but more recent observations indicate it is a triple seismic zone (Igarashi et al., 2001), with a layer of tension at the top, compression below, and tension again below that, as shown in figure 8.14.

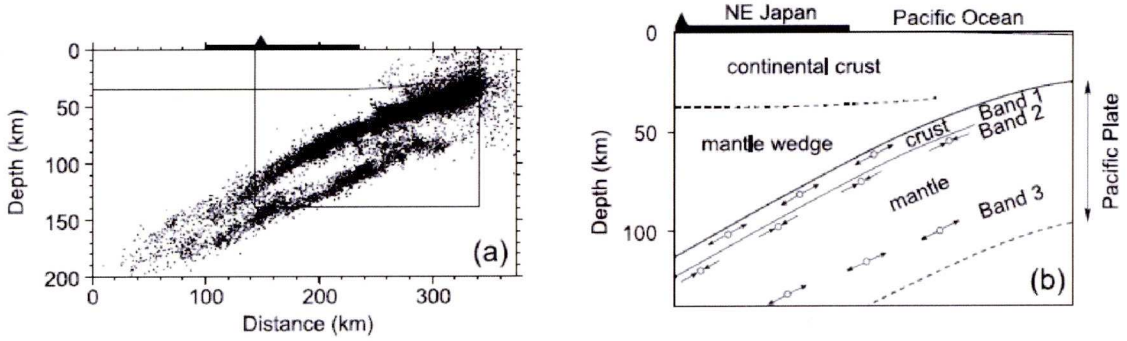


Figure 8.14: The triple seismic zone beneath northeast Japan, (a) observed seismicity (Igarashi et al., 2001), (b) focal mechanisms (Wang, 2002).

The stresses predicted here by both the 2D viscous and 1D viscoelastic models show the unbending stress pattern of compression over tension at intermediate depths, corresponding to the bands of compression over tension observed in the Japanese subduction zone. In the viscoelastic model this is attributed to the slab unbending due to the elasticity; in the viscous model there is no elasticity but the unbending stress pattern is still seen, and it is proposed that this is the result of circulation in the mantle wedge causing unbending via slab suction.

Both models also show a small tensile stress immediately above the slab at certain points of development, corresponding to the top band of seismicity observed in the Japan subduction zone. In the 1D viscoelastic model this top layer is attributed to the basalt-to-eclogite transition, but appears too deep to be responsible for intermediate depth seismicity, although if the slab acts as a stress guide it is possible that these stresses are transmitted upwards. Alternatively, given the model sensitivity to temperature, dip angle, and curvature gradient, it is possible that more accurate estimates of these values could move this band into intermediate depths. In the viscous model this band does appear at intermediate depths, and appears to be due to the decoupling in the weak zone at the top of the slab.

The lower two bands of seismicity showing compression over tension for the north-

eastern Japan subduction zone have often been attributed to unbending in the slab (Engdahl and Scholz, 1977; Sleep, 1979). Both the 2D viscous and 1D viscoelastic models would support this assertion, although the mechanisms behind the unbending are quite different. Additionally, it has been proposed that the top band of tension is due to the basalt to eclogite transition in the crust (Wang, 2002). In the 2D viscous model the top band is seen at intermediate depths but there is no mechanism for this transition in the model formulation; instead the band is attributed to decoupling in the weak layer. In the 1D viscoelastic model this tensile band does originate from the basalt metamorphism, but occurs below intermediate depths. It is possible that warmer subduction zone temperature would decrease the depths at which this tensile band is seen; alternatively, smaller unbending stresses might permit the earlier appearance of this tensile band.

## 8.6 Summary of predicted stresses for northeast Japan

Both the 2D viscous and the 1D viscoelastic models for northeast Japan predict a double layer of stress at intermediate depths, with compression over extension in agreement with observations. In the 1D viscoelastic model these bands indicate unbending as a direct consequence of stresses accumulated during prior bending. In the 2D viscous model these stresses are attributed to slab unbending due to circulation in the mantle wedge.

Additionally, the 2D viscous model predicts a small layer of tensile stress at the top of the slab, due to the weak decoupling layer representing the subducting oceanic crust. This correlates well with the band of seismicity in the crust reported by Igarashi et al. (2001). The 1D viscoelastic model predicts a layer of tensile stress in the crust due to the basalt to eclogite transition, but not at intermediate depths.

Both models give very similar results despite the differences in their formulations, and further investigation is necessary to determine which is a more accurate description of the subduction beneath Japan.

# Chapter 9

# Discussion

In this work I formulated two independent models to investigate stress accumulation in the subducting lithosphere which leads to Wadati-Benioff zone seismicity. The first is a two-dimensional model of the subduction zone using thermo-mechanical code and a viscous rheology. The second is a one-dimensional model of a subducting slice of lithosphere using a viscoelastic rheology. General results from these models were presented in chapters 4 and 6; these models were then both applied to the case studies of Chile and Japan in chapters 7 and 8. Despite differences in their formulation and rheology, both models consistently predict stresses that indicate slab bending followed by slab unbending, with the unbending pattern of compression over tension dominating the stresses at intermediate depths. An additional band of stress in the slab crust is also often predicted above these unbending stresses. This chapter discusses general trends, sensitivities and errors, and interpretation of these models.

## 9.1 Stresses predicted by the 2D viscous model

The 2D model uses a viscous rheology with kinematic boundary conditions and dynamic driving forces to predict the development of the subduction zone over a horizontal region of 6,000km extent, and from the Earth's surface to the core-mantle boundary. The thermo-mechanical formulation calculates temperatures, velocities, and pressures; these are then used to calculate viscosities, densities and stresses.

#### General trends in stresses predicted by the 2D viscous model

For all the models shown in this work, the 2D model predicts two bands of opposite-signed stress centered about a neutral plane running down the length of the subducting slab. All of the models are dominated by the unbending stress pattern of compres-

sion over tension at intermediate depths, although in very early and very late stages of development there is some variation. A typical subduction zone development generated by the 2D model is shown in figure 9.1.

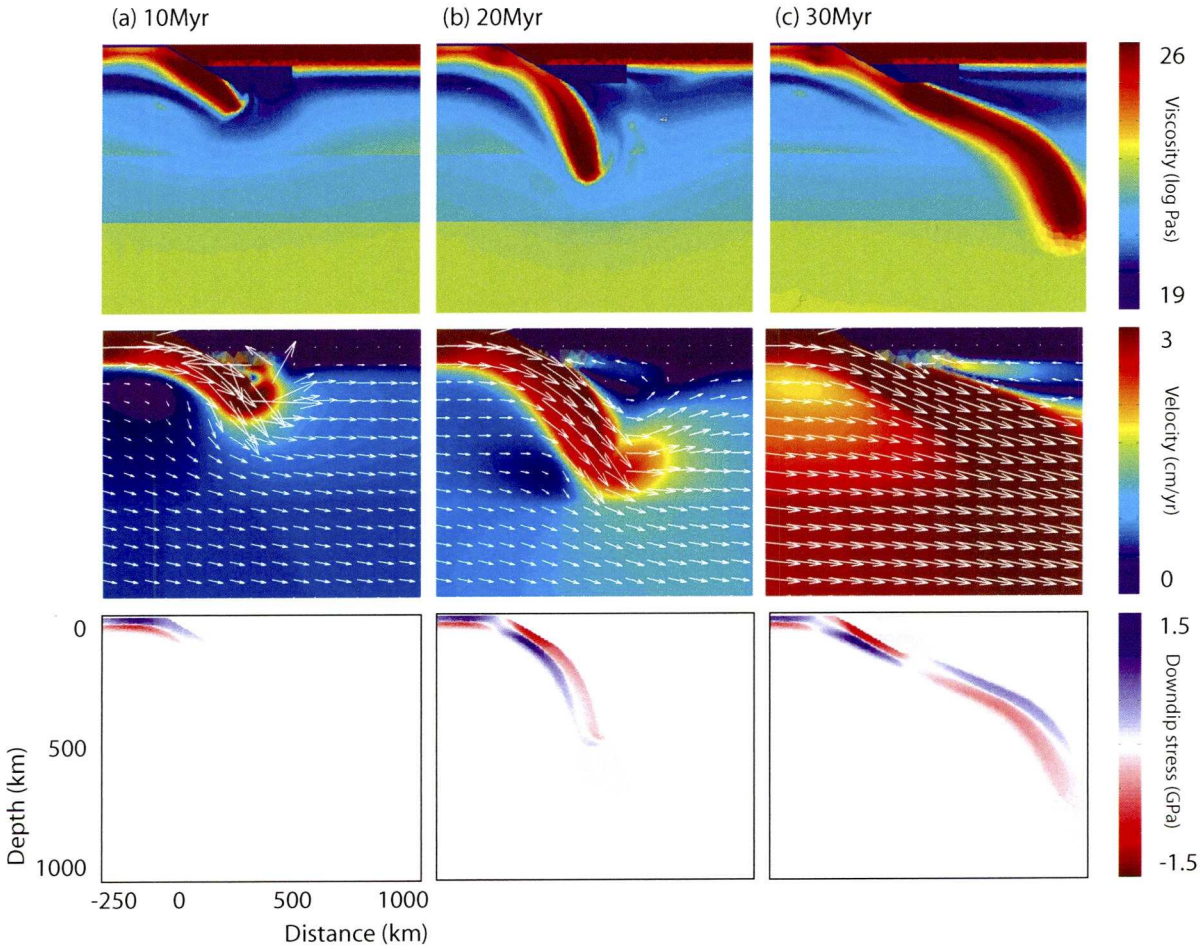


Figure 9.1: Viscosity (i), velocities (ii), and downdip stresses (iii) shown after (a) 10Myr (b) 20Myr (c) 40Myr. Model parameters are $v_p$=3cm/yr, $v_r$=0, plate age = 100Myr, dip angle = 30°.

After 10Myr of development (figure 9.1a), the whole slab still has quite a high viscosity. The flow vectors show that there is some flow in the mantle wedge, and slab bending is the dominant motion resulting in slab stresses that are mostly tension over compression.

At 20Myr (figure 9.1b), there is a distinct core of high viscosity material running the length of the slab. The movement of the slab induces circulation in the mantle wedge and mantle flow underneath the slab, and the stresses in the slab consist of a band of compression above the stiff core, and a band of tension beneath.

At 40Myr (figure 9.1c), the high viscosity core runs all the way down the slab, but

as the slab passes the bottom of the prescribed low-viscosity mantle wedge it briefly widens. The flow vectors show that there is still circulation in the mantle wedge, but the flow in the whole mantle has been accelerated to the plate velocity. The resulting stresses in the slab show an unbending pattern until approximately 200km depth, then an inversion to a bending pattern of tension over compression. This change in stress polarity coincides with the bottom of the mantle wedge where the high viscosity core is at its widest, but a high viscosity in itself would not be cause for low or fluctuating stresses. It appears that the slab widens as it passes the bottom of the prescribed low-viscosity mantle wedge, lowering the stresses and increasing the slab viscosity. When the stresses resume their two-layer structure below this point, they have reversed their polarity to tension over compression, implying that the there is now more downward than upward force acting.

**Sensitivities and errors in the 2D viscous model**

The sensitivity tests in chapter 3 demonstrated the invariance of the stress pattern to viscosity structure, yield stress, density and conductivity, although the viscosity structure and density did have a small effect on the shape of the slab. The inclusion of the weak regions used in the low viscosity zone and mantle wedge to decouple the oceanic plate from the overriding plate were shown to be vital in initiating and maintaining subduction, and the presence of a weak layer at the surface of the oceanic plate to approximate a free surface was also very important. These aspects are quite prescriptive but unavoidable; however they do appear to be an adequate approximation of the Earth system in this model as reflected in quality checks on the other model predictions such as dynamic topography.

Four key parameters of plate age, dip angle, plate velocity and rollback velocity control the 2D model. The age of the plate at the point of subduction only really affects the width of the stress layers: an older slab has more cold material and thus wider bands of stress. The dip angle influences the shape of the plate somewhat, but the stresses are largely unaffected. The plate velocity has the most influence on the slab development through the mantle flow it induces: faster slabs create more mantle flow which accelerates their progress. The slab stress state is closely linked to slab development, so the plate velocity also affects the resulting stresses after a set period of time. The rollback velocity affects the shape of the slab via the action of the viscous mantle, but the stress patterns are largely unchanged.

The slab stress pattern development shown in figure 9.1 is therefore quite robust; the shape of the slab has some small variation, but the double stress pattern of compression over tension at intermediate depths is almost always seen.

### Interpretation of 2D viscous model stresses

The most common intermediate depth stress pattern of compression over tension has often been attributed to the unbending of the subducted lithosphere due to its elasticity (Isacks and Barazangi, 1977), where stresses are 'frozen in' to the slab during bending at shallow depths (Wang, 2002). The 2D model predicts the same stress pattern of compression over tension using a viscous rheology, with no elastic components such as stress memory that would be necessary for the slab to spontaneously unbend. An alternative explanation of this slab unbending is therefore required.

One possibility is that the stress pattern of compression over tension is the result of a slab with a stiff core being unbent by a vigorous flow in the mantle wedge (see figure 9.2). Figure 9.1b demonstrates the three elements of this hypothesis: the high viscosity core of the slab due to its temperature and stress dependent rheology; the induced mantle flow with an upwards component in the mantle wedge, and the generated stress pattern of compression over tension. As the slab continues to move horizontally, at some point the downward force of the slab pull exceeds the upwards force of the mantle wedge circulation, as seen in figure 9.1c; the slab then begins to sink under its own weight, reverting to the bending stress pattern of tension over compression.

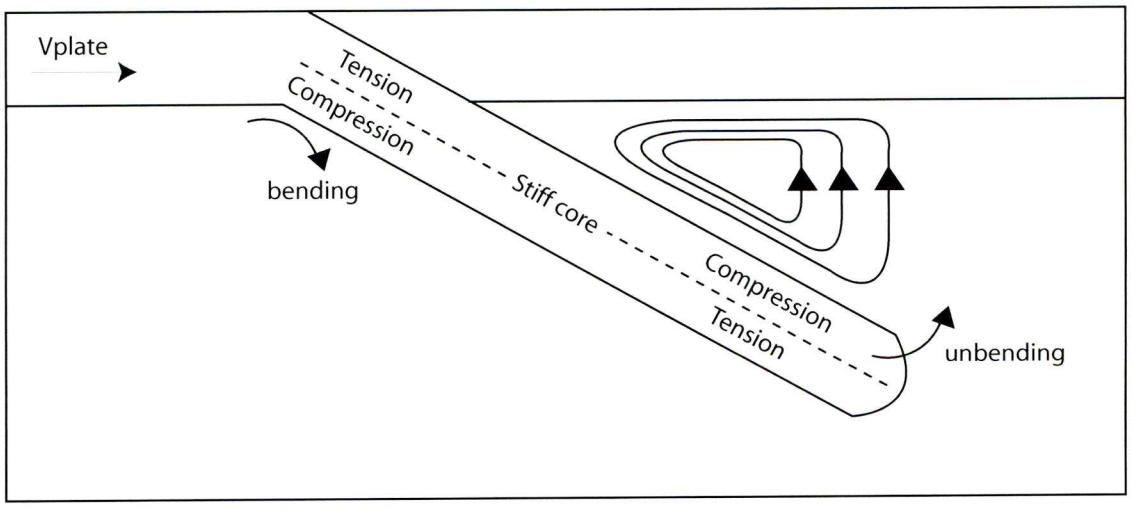


Figure 9.2: Schematic diagram of the circulatory flow in the mantle wedge acting to unbend the slab about its stiff central core

The two key components of this hypothesis are rheology and mantle flow. The rheology used in this 2D model is viscous, calculated as the harmonic mean of diffusion, dislocation, and plasticity. These are dependent upon temperature and stress; an olivine mineralogy is used throughout. This rheology results in high viscosity in areas of low temperature, for example, in the core of the slab, giving the slab a rigidity that

ensures the slab subducts rather than drips (Kaus and Becker, 2008). Any forces acting on the slab that are not exclusively down-dip would cause flexion about this stiff core, resulting in a band of stress on either side of the core with opposite signs.

The flow in the mantle wedge is an important aspect of this model, bringing warm, low viscosity material into the subduction zone and helping to keep the overriding and subducting plates decoupled. If the flow in the mantle wedge forms a small circulatory cell, and if this circulation is strong enough, it may exert an upwards force on the slab, causing it to unbend. This circulation has been described as slab suction (or trench suction), and is defined as the poloidal flow in the mantle wedge above the subducting slab due to the viscous coupling between the subducting and overriding plates (Forsyth and Uyeda, 1975). Poloidal mantle flow induced by a subducting slab has been predicted by both laboratory experiments (Schellart, 2004) and numerical models (Piromallo et al., 2006). Studies investigating the relative contributions of the slab suction and slab pull forces on driving plate motion found that they are of comparable magnitude (Conrad and Lithgow-Bertelloni, 2002), with slab suction from mantle flow accounting for 30% to 40% of the force acting on the slab (Conrad and Lithgow-Bertelloni, 2004). Given the potential strength of slab suction, it seems entirely possible that it is capable of influencing the shape of the subducting slab.

**Comparison of stresses predicted by the 2D viscous model with observations**

Although the double seismic zone pattern of compression over extension is the most common, there is some variation in observations, including extension over compression, tension in both planes, and along strike components (Kao and Rau, 1999; Brudzinski et al., 2007). A number of subduction zones have been reported with different mechanisms within a small distance along the trench, for example north Chile (Comte and Suarez, 1994; Rietbrock and Waldhauser, 2004) or the Aleutians (Brudzinski et al., 2007). Figure 9.3 summarises some of the stress patterns observed, which are listed in table 2.2.

The 2D viscous model predicts a double layered stress zone that reflects not only the local conditions acting upon the slab but also the local conditions created by the slab, via mantle flow. As the conditions change with the development of the subduction zone, so do the stresses, typically from bending to unbending, to a combination of both (figure 9.1(iii)). Both the compression-over-tension and tension-over-compression stress patterns are observed in the stresses generated by the 2D model (see figure 9.3), so it is possible that this transitory nature of stress development could explain the variety in seismicity focal mechanisms observed in subduction zones. It could also be possible that regions with more than one reported stress pattern are

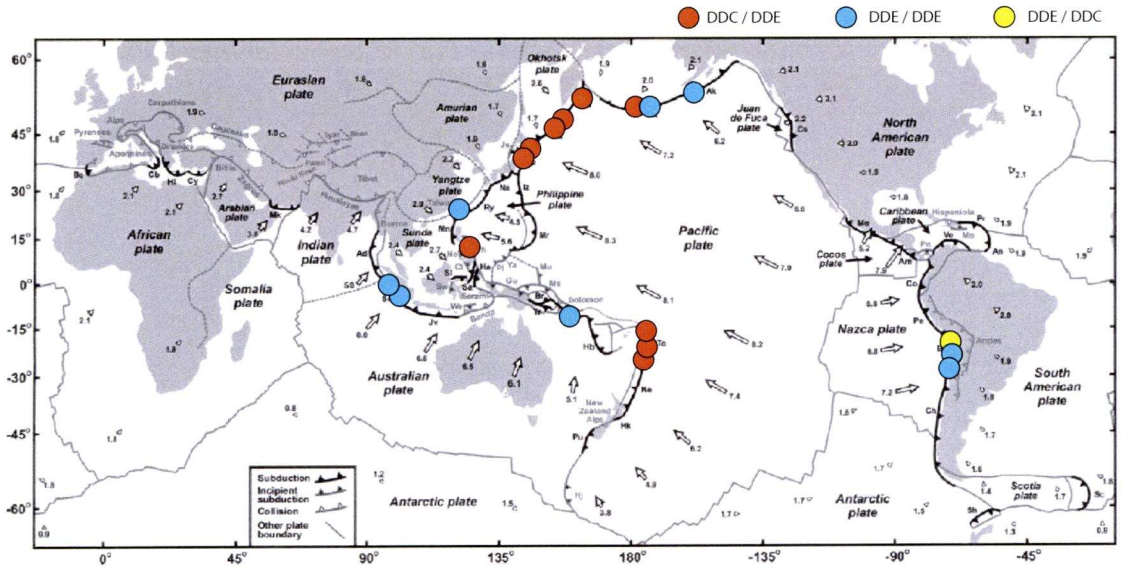


Figure 9.3: Double seismic zone patterns worldwide, as listed in table 2.2 (Hasegawa et al., 1978; Kawakatsu, 1986; Samowitz and Forsyth, 1981; Engdahl and Scholz, 1977; Kao and Chen, 1994; Gorbatov et al., 1994; Ratchkovsky et al., 1997; Kao and Rau, 1999; Reyners and Robinson, 1997; Smith et al., 1993; Comte and Suarez, 1994; Rietbrock and Waldhauser, 2004; McGuire and Wiens, 1995; Brudzinski et al., 2007). DDC=downdip compression, DDE=downdip extension.

either laterally segmented (Araujo and Suarez, 1994), or are caught in the transition between one regime and another.

Double seismic zones with downdip tension in both planes are, however, not predicted by the viscous model. The 2D model always predicts two strong bands of downdip stress in the slab with opposing polarities, and the hypothesis of slab flexion about a high viscosity core would expressly prohibit the occurrence of two bands with the same polarity. However, a closer investigation of the downdip stresses perpendicular to the slab reveals that at intermediate depths there is always a small band of tension at the top of the slab in the 2D model, as shown in figure 9.4, which would make the intermediate-depth stress pattern a triple-layered stress zone. It has been postulated that all double seismic zones are in fact underdeveloped triple seismic zones, where unbending causes the two main bands of compression over tension, and metamorphism in the slab crust produces a bend of tension above (Wang, 2002). The 2D viscous model does not compute process-specific stresses such as metamorphism, but tensile stresses are generated at the top of the slab in the low-viscosity zone present in slices s1 and s2 of figure 9.4, due to the decoupling of the subducting and overriding plates in the weak slab crust.

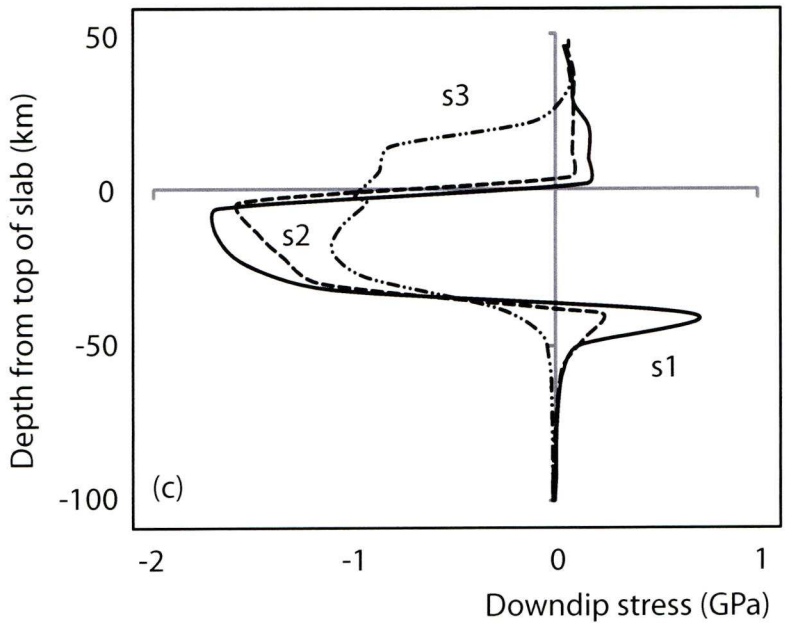


Figure 9.4: Downdip stresses taken perpendicular to the top of the slab at 100km (s1), 150km (s2), and 200km (s3) depth, from the present-day Chile model in figure 7.7.

The 2D viscous model suggests the possibility that regions that report downdip extension in both bands are observing the top and bottom bands of a triple seismic zone, and regions with tension over compression are observing the top two layers of a triple seismic zone. However, in the case of north Chile, the separation between the layers is less than 10km (Rietbrock and Waldhauser, 2004), whereas the separation between tensile layers predicted by the 2D viscous model is closer to 50km. An adjustment of the temperatures or viscosities in the 2D model might narrow this gap, but would then imply a gap of less than 5km between the lower two layers of compression and tension, which is not observed.

If the 2D model implies that the top layer of tension is due to the weak decoupling layer representing the subducting slab crust, then to produce the tension-over-tension stresses observed in north Chile requires that the top of the subducting oceanic lithosphere is also in tension. Alternative ways of generating this tensile stress include a geometry that forces bending rather than unbending at intermediate depths, but this would require a major re-formulation of model geometry and boundary conditions. It is also possible that as the slab changes from bending to unbending the hiatus in bending stresses allows other stress-generating mechanisms to be observed, such as slab pull, although this is not seen in the 2D viscous model due to the restrictions in resolution.

## 9.2 Stresses predicted by the 1D viscoelastic model

The 1D model uses a viscoelastic rheology to model a vertical slice of lithosphere as it moves from the ocean ridge to the trench and into subduction. Prior to subduction, stresses arise from the ridge push force, and from volumetric reduction associated with thermal cooling. Immediately before subduction, the slab starts to bend; this bending continues into subduction until it is replaced by unbending. Other sources of stress during subduction include the volumetric reduction due to the basalt to eclogite transition, the volumetric expansion due to slab heating, and the slab pull force. The net effect of these stress sources is a complex and transitory stress profile generated for the subducting lithosphere.

#### General trends in stresses predicted by the 1D viscoelastic model

The pre-subduction stresses due to cooling and ridge push have a bimodal distribution, with compression in the upper part of the lithosphere, and tension below. The compressive stress accumulation is restricted by the strength envelope, and the applied brittle failure redistributes the stresses. As the slab bending begins in the forebulge, the stress polarities are inverted to tension in the upper lithosphere, and compression below. These bending stresses are the largest of all the generated stresses, almost completely overprinting the stresses accumulated during ocean floor cooling. When the bending changes to unbending the stresses revert to compression over tension, where they remain for most of the duration of subduction. The basalt to eclogite transition is the next most influential stress source, producing stresses that in some cases can be large enough to put the slab crust back into tension, creating a tri-modal stress distribution of tension over compression over tension in the slab. The thermal stresses have much less influence on the total stresses, being approximately one order of magnitude smaller than the bending stresses. The slab pull force is also a relatively minor effect, although it is the only one to be continually applied throughout subduction.

In the model results presented in chapters 6, 7 and 8, the general trend in stress profile is compression over tension (figure 9.5a) until bending begins (figure 9.5b), then tension over compression until bending changes to unbending (figure 9.5c); this unbending pattern usually dominates for most of the rest of the duration of subduction. The unbending pattern of compression over tension sometimes has an additional band of tension at the top of the slab due to the basalt to eclogite transition in the slab crust (figure 9.5d). As the slab warms to ambient mantle temperatures, these stresses are dissipated away.

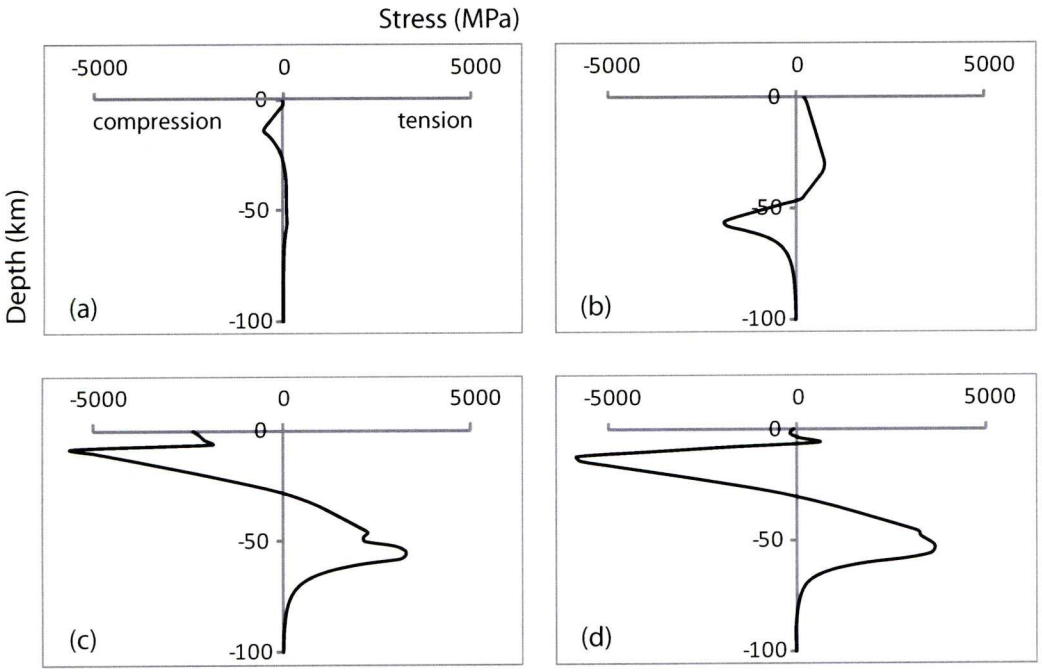


Figure 9.5: General pattern of stresses in the lithosphere as generated by the 1D model, taken from figure 6.2

### Sensitivities and errors in the 1D viscoelastic model

The stresses generated by the 1D model are relatively unaffected by variations in pre-subduction stresses, thermal stresses, and slab pull, but are quite sensitive to bending stresses and the stresses arising from the basalt to eclogite transition, as these dominate the total stress profile. Within the errors estimated for each, the prevalent trend of bending then unbending stress polarities remains the same but the magnitudes of the stresses show some variation. The main difference in the stress profile is whether the tensile band due to the basalt metamorphism in the crust is seen.

The 1D model is also quite sensitive to rheology; using a linear diffusion creep gives significantly higher viscosity, and therefore higher stresses, than using a combined diffusion and dislocation creep. The values used to calculate both diffusion and dislocation creep are fairly well constrained but some variation in viscosity is possible within the error estimates (Karato and Wu, 1993; Hirth and Kohlstedt, 2003).

The four controlling parameters for the 1D model are plate age, dip angle, plate velocity and curvature rate; of these, plate age is quite well constrained (Muller et al., 2008), and plate velocity only has a small effect on the total stresses. The dip angle and the curvature rate on the other hand are both relatively poorly constrained, and exert strong control over the predicted stresses. However, although varying the parame-

ters within the estimated errors affects the magnitude of the stresses, the fundamental shape of the stresses remains the same.

### Comparison of stresses predicted by the 1D viscoelastic model with observations

As discussed in section 9.1, the most common stress pattern observed in double seismic zones is compression over tension, often attributed to the unbending of the slab (Engdahl and Scholz, 1977; Wang, 2002). In the 1D viscous model, stresses at intermediate depths always have a strong band of compression over tension resulting from the unbending of the slab, supporting this hypothesis. Wang (2002) also suggests that in triple seismic zones, the extra band of tension at the top of the slab is due to the metamorphism of the subducting slab crust. The results from the 1D model also support this, with a third band of tension in the slab crust due to the basalt to eclogite transition seen in many models.

This tensile band is more likely to occur at intermediate depths in younger plates with a shallower dip angle; old, cold plates and those with high dip angles do not accumulate sufficient tensile stresses from metamorphism until greater depths. This relationship between early-onset basalt dehydration and young and shallow dipping slab is supported by observations (Green and Harry, 1999); in light of this, it is surprising that the only well-established triple seismic zone is observed in northeast Japan (Igarashi et al., 2001), where the oceanic plate is 130Ma at the point of subduction, the oldest in the world (Muller et al., 2008). As the separation of Wadati-Benioff zone layers has been linearly related to slab age (Brudzinski et al., 2007), it is possible that the large separation between the layers in such an old slab is the reason why the they are able to be resolved into three layers. This also suggests the possibilities that other seismic zones may really be triple seismic zones, as postulated by Wang (2002), and furthermore that double seismic zones with alternative stress patterns have seismicity that results from the top two bands, or top and bottom bands, of a triple seismic zone.

The double seismic zone of north Chile, however, does not quite fit this hypothesis: the separation between the bands is only 9km, and the 1D viscoelastic model of north Chile predicts approximately 30km between bands of tensile stress. It is possible that an alternative temperature and viscosity formulation could reduce the gaps between predicted bands of stress, although this seems unlikely and would imply that the unbending bands of compression over tension both occur at the top of the oceanic lithosphere. An alternative is suggested by the preliminary results from a model that applies slab bending at 25km and 175km depth so the slab is largely straight through intermediate depths. This drastically reduces the dominance of the bending stresses, generating a stress pattern that is quite complex, where multiple layers of stress are

separated by as little as 5-10km. The relationship between slab curvature and stress generation is clearly very important, and further investigation is recommended.

## 9.3 Overview of the 2D viscous and 1D viscoelastic models

Seismicity in subduction zones is generated through stress accumulation and dissipation. Stresses are accumulated through mechanisms such as slab pull and slab resistance, bending and unbending, thermal effects, and metamorphism. Stresses are dissipated by brittle failure under special conditions such as dehydration embrittlement, shear instabilities, or transformational faulting. The two models used in this work focus on the stress accumulation aspect of this dichotomy, predicting stress generation in the subducting lithosphere according to local conditions.

Both the 2D viscous and 1D viscoelastic models predict stresses that are almost always compression over tension at intermediate depths, but the significant differences in their formulation and rheology leads to two different explanations of these stresses. In the 2D model this stress pattern was proposed to be a result of induced poloidal flow in the mantle wedge unbending the slab about a high viscosity core. In the 1D model, this stress pattern was attributed to stresses arising from unbending due to the slab's elastic nature. Additionally, both models show the presence of a small band of tension at the top of the slab; in the 2D model this is due to decoupling in the weak zone; in the 1D model this is due to the basalt-to-eclogite transition in the slab crust.

We are therefore presented with something of a conundrum: which, if either, of these interpretations is the correct one? From the work presented here it is difficult to say. Both models correlate well with observations, predicting double stress zones of compression over tension which is most commonly seen in subduction zones, and an additional small band of tension at the top of the slab, as seen in the Japanese triple seismic zone. The 2D model predicts stresses that are similar to those predicted by other numerical models (Cížková et al., 2007; John et al., 2009). The 1D model predicts stresses that are 2-3 times higher than the 2D model, which is high but not implausible; they are approximately an order of magnitude higher than stress drops inferred from observations (Andersen et al., 2008), but not all of the accumulated stress is assumed to be dissipated in a single seismic event.

If the lithosphere and mantle are best described with a visco-elastic-plastic rheology, then each model has an incomplete rheological formulation: visco-elastic for the 1D model and visco-plastic for the 2D model. The advantage of the 2D visco-plastic

| | 2D model | 1D model | Cizkova et al, 2007 | Babeyko et al, 2008 | Dorbath et al, 2008 | Kaus et al, 2009 |
|---|---|---|---|---|---|---|
| 2D | ✓ | | ✓ | ✓ | ✓ | ✓ |
| Viscoelastic | | ✓ | | ✓ | ✓ | |
| Viscoplastic | ✓ | | ✓ | | ✓ | ✓ |
| Dynamic driving forces | ✓ | | ✓ | | | ✓ |
| Subduction zone evolves over time | ✓ | | ✓ | | | |
| Investigates influence of mantle flow | ✓ | | | | | ✓ |
| Large model domain | ✓ | ✓ | ✓ | | | |
| Predicts DSZs | ✓ | ✓ | ✓ | ✓ | ✓ | ✓ |
| Predicts TSZs | ✓ | ✓ | | | ✓ | |
| Individual contributions from stress sources | | ✓ | | | | |

Table 9.1: Comparison of the 1D viscoelastic and 2D viscous models with other numerical models.

model is that it is two-dimensional and therefore can provide significant insight into the whole subduction zone system. Minimal kinematic boundary conditions are imposed and the model is driven internally through dynamic conditions of density and viscosity. However, it does not have any elastic component of rheology, and therefore can only compute instantaneous stresses without stress memory. The 1D model on the other hand does have stress memory, and therefore can accumulate stresses over time, contributing to the high stresses predicted. However, it is a highly prescriptive model and the limitation to one dimension is quite restrictive. Extending both the 1D and 2D models to a visco-elastic-plastic rheology would be the next step in investigating the influence of model formulation on predicted stresses.

Both models unequivocally show that unbending is responsible for the compression-over-extension stress pattern generated at intermediate depths. Both models also predict a top tensile band of stress for certain models, but through different mechanisms. Each model has its merits, and therefore neither of the explanations for the generated stress patterns can be ruled out; it may be that both, or neither hypotheses are correct. More investigation into the causes of Wadati-Benioff zone seismicity, and particularly using a two-dimensional visco-elastic-plastic model, is thus required.

# Chapter 10

# Summary and further work

This work set out to investigate stress accumulation and dissipation in the subducting lithosphere that leads to Wadati-Benioff zone seismicity, particularly at intermediate depths. Earthquakes caused by subduction cause immense devastation and loss of life, yet remain somewhat enigmatic. Stresses may accumulate in the oceanic lithosphere due to forces such as ridge push and slab pull, or strains induced by changes in shape or size such as bending, thermal expansion, or metamorphism. When stresses become so large that they exceed the strength of the lithosphere, brittle failure occurs, dissipating the stresses. However, at intermediate depths and below, the confining pressure is too high for frictional sliding to occur yet seismicity continues. Alternative mechanisms of stress dissipation are therefore required; these include dehydration embrittlement, shear instabilities, and transformational faulting.

Seismicity in some Wadati-Benioff zones is organised into two or three planes with separations of 5-40km, which merge at depth. Focal mechanisms from these areas show that the most common stresses experienced in double seismic zones is compression in the upper band and tension beneath, although other polarities have also been observed; both of these bands are generally assumed to occur in the subducted oceanic lithosphere. In the triple seismic zone beneath Japan, there is an additional band of tension at the top of the slab, thought to occur in the slab crust. These bands of seismicity provide extra clues about the stresses within the lithosphere, for example, the compression-over-tension pattern implies that the slab is unbending. In this thesis, I used two different computational models to investigate the stress accumulation that leads to such double and triple seismic zones.

The two-dimensional viscous model is thermo-mechanical, using kinematic boundary conditions, and dynamic driving forces. The temperature and stress dependent rheology means that the slab has a core of high viscosity material. In all of the results

for this model, the slab has two bands of stress with opposite polarities running the length of the slab, one on either side of this high viscosity core. Most of the results for this model follow the same general trend: in the early stages of subduction, the slab has stresses that are down-dip tension in the upper band and down-dip compression below as the slab bends downwards. After this stage, the stresses in the slab invert to compression over tension as the slab unbends. In the absence of stress memory the slab cannot spontaneously unbend; instead, it is proposed to unbend as a result of poloidal circulation in the mantle wedge pulling the top of the slab upwards, flexing it about its stiff core. Closer inspection of the intermediate depth stresses reveals a third band of tension at the top of the slab, which may be due to decoupling in the weak layer representing the slab crust. In later stages of slab development as the slab moves past the circulatory region, the downward force of slab pull eventually exceeds the upwards force of slab suction. The stresses in the lower portion of the slab then revert to tension over compression as the slab bends downwards again.

The four parameters that control this model are plate age, slab dip, plate velocity and rollback velocity. Variation of these parameters affects the shape of the slab somewhat, but the stress patterns are relatively invariant, particularly the intermediate depth unbending stresses of compression over tension. For the specific examples of north Chile and northeast Japan, these parameters were estimated, including their errors. Within the error bars there was some variation in slab shape, but little variation in the intermediate depth stresses.

The one-dimensional viscoelastic model follows the development of a vertical slice of oceanic lithosphere from the ridge to the trench and into the subduction zone. It predicts stresses arising before subduction due to cooling and the ridge push force, and during subduction from bending, heating, the basalt to eclogite transition and slab pull. The viscoelastic rheology means the lithosphere has a stress memory, so the stresses accumulate over time and are advected with the slab. Deformation by diffusion or dislocation creep in the lower lithosphere transfers stresses to the elastic upper lithosphere; if the stresses exceed the strength envelope brittle failure occurs.

The stresses generated by the 1D model follow a general trend. Prior to subduction, the ridge push force and the thermal stresses due to cooling cause stresses that are compressive for the upper lithosphere and tensile below. When the slab begins to bend in the forebulge, the bending stresses of tension over compression almost completely overwrite the stresses previously accumulated. These stresses return to the pattern of compression over tension when the slab begins to unbend again at depth, and dominate the stress pattern for most of the rest of subduction duration. The basalt to eclogite transition is the next largest source of stress after bending, generating ten-

sion in the crust that is sometimes large enough to overprint the unbending stresses, creating a triple-layered stress pattern of tension-compression-tension. Stresses arising from heating and slab pull are less influential, although stresses due to slab pull continue to act throughout subduction. The stresses are dissipated as the slab warms to mantle temperatures.

The controlling parameters in the 1D model are plate age, slab dip, plate velocity, and curvature rate. Slab dip and curvature rate have the largest estimated errors and the most effect on the stresses generated in the slab. Nevertheless, the dominant stress pattern of compression over tension is quite robust through intermediate depths.

Both the 2D viscous and 1D viscoelastic models predict stresses at intermediate depths to be dominated by unbending, generating strong bands of compression over tension. This is in agreement with the majority of observations of double Wadati-Benioff zones. Additionally, both models frequently predict a smaller band of tension in the slab crust, which agrees with observations of the triple seismic zone in northeast Japan. The 2D model ascribes the two main bands to unbending as a result of induced mantle flow, whilst the 1D model attributes these to unbending due to stress memory and elasticity. Where a top band of tensive stress is predicted, it is attributed to decoupling in the weak crust in the 2D model, and the basalt to eclogite transition in the 1D model.

From the work presented in this thesis, the main bands of compression over tension at intermediate depths are the result of slab unbending, whilst the smaller top band of stress is due to decoupling or metamorphism, or a combination of both. The causes of the slab unbending are still a topic for consideration. The triple Wadati-Benioff zone observed beneath Japan may therefore be the result of two main bands of stress in the oceanic mantle due to slab unbending, and a top band of tension due to processes in the crust. The most common type of double Wadati-Benioff zone may be due to the two unbending bands only, with the top band underdeveloped or unobserved. Double Wadati-Benioff zones with other patterns could be either the top two bands, or the top and bottom bands, of a triple seismic zone. Alternatively, they could be the result of special cases of slab curvature that reduce the dominance of bending stresses at intermediate depths, allowing complex multi-layered stresses to be seen.

**Further work**

The most obvious progression from the work would be to build a model that combines the most realistic parts of the two models used here, that is, a two-dimensional visco-elastic model. The 2D viscous and 1D viscoelastic models both have their mer-

its, and each provides an insight into stress generation in the subducting lithosphere, but are ultimately restricted by their respective rheology and dimensions. A 2D viscoelastic model would be able to investigate whether unbending in the slab is due to mantle flow or stresses accumulated during prior bending, and would be able to explore whether the tension in the subducting slab crust originates from decoupling or metamorphism. Hopefully this would give a more conclusive insight into the causes of subduction zone stresses, and double and triple seismic zones.

Other recommendations for future work centre around the numerical implementation of a model. A less prescriptive model setup would be a benefit and a challenge; fixed material domains, kinematic boundary conditions, and free surface formulation are currently unavoidable artificialities. Increases in domain size and resolution would improve the model, but depend mainly on computing power.

Finally, the values of the parameters used to model specific subduction zones were subject to some significant errors, notably in dip angle and curvature rate; uncertainties are also undoubtedly present in the viscosity formulation. Better estimations of these values, and additional sensitivity testing, would help to generate more accurate models.

# Appendix A

# Code testing and benchmarking

The 2D viscous model used in this work is built upon the finite element package MILAMIN (Dabrowski et al., 2008), which includes a thermal and a mechanical solver. The original version of MILAMIN is Lagrangian and non-dimensional, and the thermal code solves for steady-state; the version used in this work is Eulerian and dimensional, and uses a transient thermal solver. Additionally, the mechanical solver is used iteratively to find nonlinear viscosity, and the velocities from the mechanical solver are used to advect the temperature field when the two solvers are coupled together. Some simple tests are therefore performed here to check these elements are working correctly, and to ensure the validity of the 2D model.

**Mechanical test: original version of MILAMIN**

The original version of MILAMIN compares well to other finite element solvers such as IFISS (Silvester et al., 2009) and FEMLAB in terms of both solution and performance, as discussed in Dabrowski et al. (2008). A test of the mechanical solver is provided with the MILAMIN package: a box made of a viscous material has a rigid inclusion in the centre, and the condition of pure shear is applied to the box, squeezing it from top and bottom. Figure A.1a shows this model domain, and the calculated solutions for velocity and pressure. The velocity vectors show movement out to either side; the pressure solution shows overpressure above and below the inclusion, and underpressure on the left and right.

The same test is performed in a paper by Beuchert and Podladchikov (2010) using a different FE solver, and shown in figure A.2a; they also include an analytical solution from Schmid and Podladchikov (2002), which is shown in figure A.2b. The very close similarity of figures A.1c, A.2a and A.2b provides a good benchmark of the mechanical MILAMIN solver.

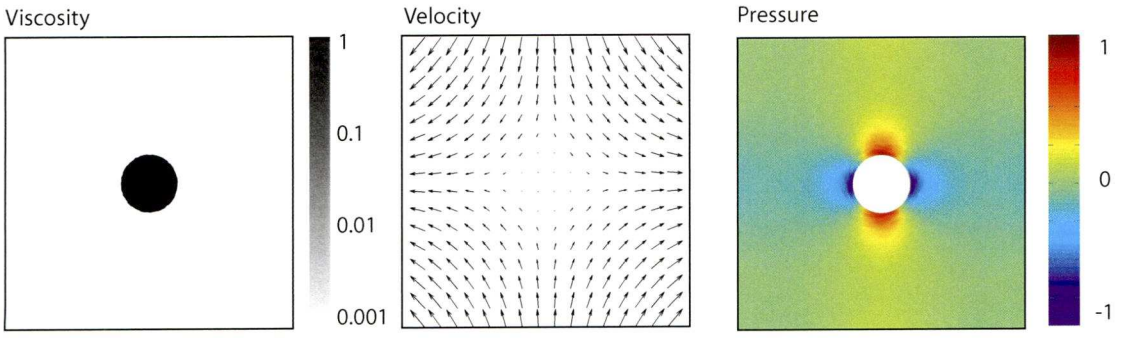


Figure A.1: Mechanical test, original version of MILAMIN: Pure shear applied vertically to a viscous box with a rigid inclusion.

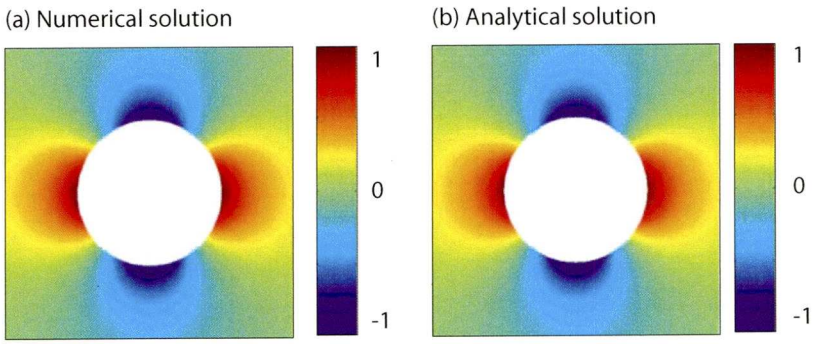


Figure A.2: Mechanical test: Pure shear applied horizontally to a viscous box with a rigid inclusion, (a) numerical solution from Beuchert and Podladchikov (2010), (b) analytical solution from Schmid and Podladchikov (2002).

### Mechanical test: adapted version of MILAMIN

The version of the mechanical MILAMIN code used in this work has been adapted to the Eulerian reference frame, and takes dimensionalised parameters. Figure A.3 shows the same test as figure A.1, but using the adapted code. The two tests are identical; the change in reference frame and unit length does not affect the solution in any way.

### Nonlinear viscosity test

In the 2D model, the viscosity used is a combination of linear diffusion creep and nonlinear dislocation creep.

To calculate the viscosity due to the dislocation creep, the mechanical solver is used as part of a Picard iteration. In this method (Dabrowski, 2008), the mechanical solver computes the velocities for the region, from which the strain rates are found. These strain rates are then used to calculate the viscosity, but as the viscosity affects the strain

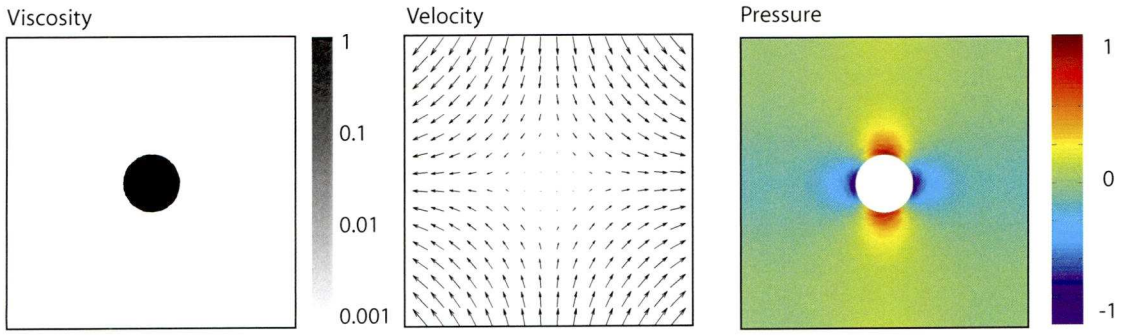


Figure A.3: Mechanical test, adapted version of MILAMIN: Pure shear applied to a viscous box with a rigid inclusion.

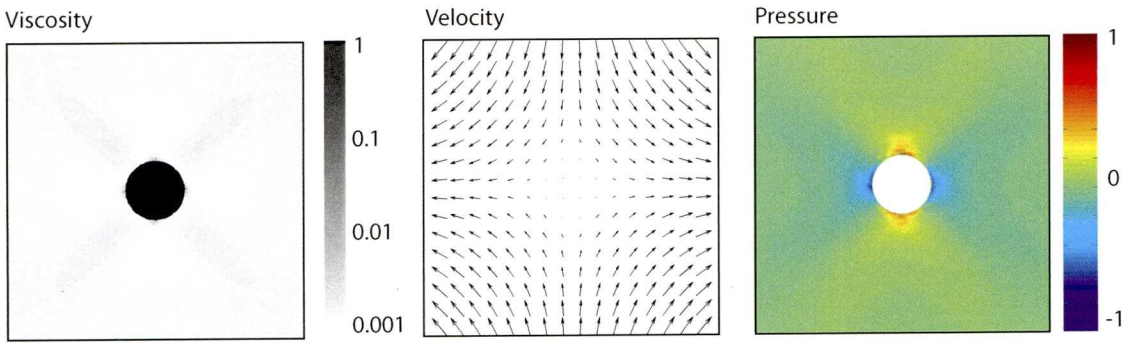


Figure A.4: Nonlinear viscosity test: Pure shear applied to a box with nonlinear viscosity, and a rigid inclusion.

rate, this process must be iterated until an acceptably steady state is reached.

Figure A.4 shows the same test as figure A.3, but using a nonlinear viscosity. The initial viscosity is the same as for the mechanical test (figure A.3a), but after a number of iterations it has been modified to that shown in figure A.4a, due to the stress-dependent viscosity. The resulting velocity field in figure A.4b is very similar to the velocity field for the linear viscosity test, but the shape of the pressure field in figure A.4c has smaller magnitudes and a slightly different shape, due to the change in viscosity.

### Thermal test

To test the thermal solver, a box is initialised with zero background temperature, a hot region off-centre, and edge conditions of zero temperature. Figure A.5 shows the model development as the heat diffuses away, indicating the thermal code is working correctly.

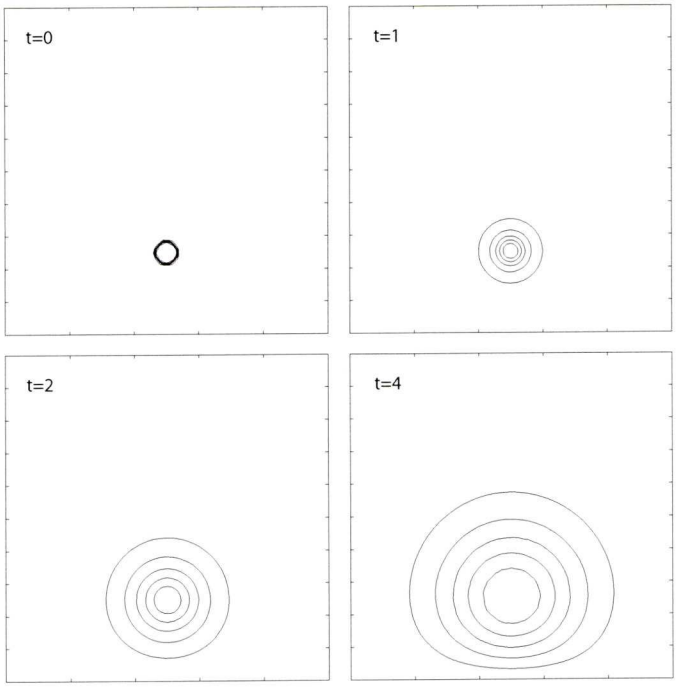


Figure A.5: Thermal test: temperature contours showing heat diffusion from a hot spot.

**Advection test**

The coupling of the thermal and viscous solvers together is achieved by using the temperatures from the thermal solver to calculate temperature-dependent density and viscosity; these are used as inputs into the viscous solver, which calculates the resulting pressures and velocities. The velocities are then used to advect the temperatures through the region.

Advection can be applied through a variety of methods; here I use the semi-Lagrangian scheme which has small numerical diffusion and is quite stable (Schmid et al., 2008). In the basic semi-Lagrangian method, the path of a particle through the domain is calculated. By projecting backwards in time, the location of the particle at the last timestep is found, and the temperature at this point is interpolated from the local gridpoints. Assuming that the velocity does not change over one timestep, this is the same temperature of the particle at the current position. However, if the velocity field does change, an iterative version of the semi-Lagrangian method yields more accurate results. This involves finding the centred velocity of the particle by interpolating the local velocity field at a series of partial timesteps, and using this more accurate velocity field to find the previous location of the particle.

To test the advection of the temperatures and the coupling of the solvers, a box with

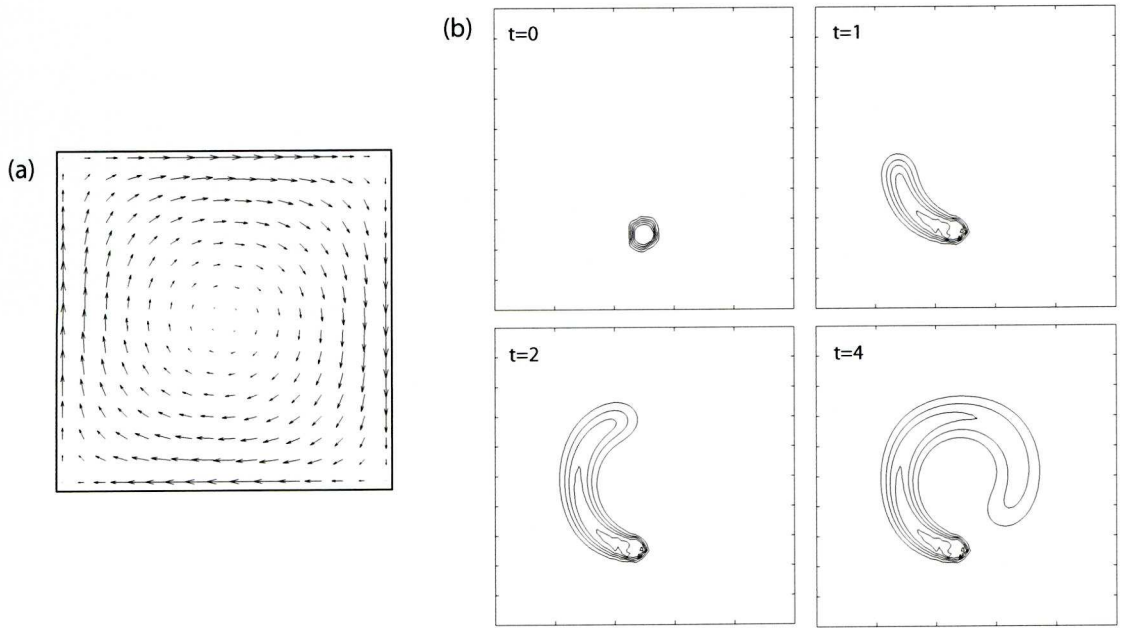


Figure A.6: Advection test, where rotation is applied to a box with an off-centre hot region: (a) applied velocities (b) resulting temperature contours

a zero background temperature has a solid-body rotation applied to it (Dabrowski, 2008), and an off-centre hot spot is applied at a stationary point. Figure A.6a shows the applied velocities; figure A.6b shows the development over time as the rotation advects the hot material along the streamlines.

# BIBLIOGRAPHY


Abers, G. A., P. E. van Keken, E. A. Kneller, A. Ferris, and J. C. Stachnik (2006). The thermal structure of subduction zones constrained by seismic imaging: implications for slab dehydration and wedge flow. *Earth Planet. Sci. Lett. vol 241*, 387–397.

Andersen, T. B., K. Mair, H. Austrheim, Y. Y. Podladchikov, and J. C. Vrijmoed (2008). Stress release in exhumed intermediate and deep earthquakes determined from pseudotachylyte. *Geology vol 36*, 995–998.

Andrews, D. J. and N. H. Sleep (1974). Numerical modelling of tectonic flow behind island arcs. *Geophys. J. R. Astr. Soc. vol 38*.

Araujo, M. and G. Suarez (1994). Geometry and state of stress of the subducted nazca plate beneath central Chile and Argentina: evidence from teleseismic data. *Geophys J Int vol 116*, 283–303.

Babeyko, A. Y. and S. V. Sobolev (2008). High-resolution numerical modeling of stress distribution in visco-elasto-plastic subducting slabs. *Lithos vol 103*, 205–216.

Barazangi, M. and B. L. Isacks (1976). Spatial distribution of earthquakes and subduction of the nazca plate beneath South America. *Geol Soc America vol 4*, 686–692.

Batchelor, G. K. (1967). *Introduction to Fluid Dynamics*. Cambridge University Press.

Bellahsen, N., C. Faccenna, and F. Funiciello (2005). Dynamics of subduction and plate motion in laboratory experiments: insights into the "plate tectonics" behaviour of the earth. *J. Geophys. Res. vol 110*.

Benioff, H. (1954). Orogenesis and deep crustal structure. *Bulletin of the Geological Society of America vol 65*, 385–400.

Beuchert, M. and Y. Y. Podladchikov (2010). Viscoelastic mantle convection and lithospheric stresses. *Geophys. J. Int. In revision*.

Billen, M. I. and M. Gurnis (2001). A low viscosity wedge in subduction zones. *Earth Planet. Sci. Lett. vol 193*, 227–236.

Billen, M. I. and G. Hirth (2005). Newtonian versus non-newtonian upper mantle viscosity: implications for subduction initiation. *Geophys. Res. Lett. vol 32*, 19.

Bott, M. H. P. (1993). Modelling the plate-driving mechanism. *J. Geol. Soc. vol 150*.

Bott, M. H. P. and N. J. Kusznir (1984). The origin of tectonic stress in the lithosphere. *Tectonophysics vol 105*, 1–13.

Brown, G. C. and A. E. Mussett (1981). *The Inaccessible Earth*. Taylor and Francis.

Brudzinski, M. R., C. H. Thurber, B. R. Hacker, and E. R. Engdahl (2007). Global prevalence of double Benioff zones. *Science vol 316*, 1472–1474.

Byerlee, J. (1978). Friction of rocks. *Pageoph vol 116*.

Capitanio, F. A., G. Morra, and S. Goes (2007). Dynamic models of downgoing plate-buoyancy driven subduction: subduction motions and energy dissipation. *Earth Planet. Sci. Lett. vol 262*, 284–297.

Cathles, L. M. (1975). *The viscosity of the Earth's mantle*. Princeton University Press.

Chase, C. G., A. J. Sussman, and D. D. Coblentz (2009). Curved Andes: geoid, forebulge, and flexure. *Lithosphere vol 1*.

Chen, M., J. Tromp, D. Helberger, and H. Kanamori (2007). Waveform modeling of the slab beneath Japan. *J. Geophys. Res. vol 112*, B02305.

Chen, P. F., C. R. Bina, and E. A. Okal (2004). A global survey of stress orientations in subducting slabs as revealed by intermediate-depth earthquakes. *Geophys. J. Int. vol 159*, 721–733.

Chen, W. P. and P. Molnar (1983). Focal depths of intracontinental and intraplate earthquakes and their implications for the thermal and mechanical properties of the lithosphere. *J. Geophys. Res. vol 88*, 4183–4214.

Chopelas, A. and R. Boehler (1992). Thermal expansivity in the lower mantle. *Geophys. Res. Lett. vol 19, no 19*, 1983–1986.

Cížková, H., J. van Hunen, and A. van den Berg (2007). Stress distribution within subducting slabs and their deformation in the transition zone. *Phys. Earth Planet. Inter. vol 161*, 202–214.

Cížková, H., J. van Hunen, A. P. van den Berg, and N. J. Vlaar (2002). The influence of rheological weakening and yield stress on the interaction of slabs with the 670km discontinuity. *Earth Planet. Sci. Lett. vol 199*, 447–457.

Cloos, M. (1982). Flow melanges: numerical modeling and geologic constraints on their origin in the franciscan subduction complex, california. *Geol. Soc. Am. Bull. v93*, 330–345.

Comte, D., L. Dorbath, M. Pardo, T. Monfret, H. Haessler, L. Rivera, M. Frogneux, B. Glass, and C. Meneses (1999). A double-layered seismic zone in Arica, Northern Chile. *Geophys. Res. Lett. vol 26, no 13*, 1965–1968.

Comte, D. and G. Suarez (1994). An inverted double seismic zone in Chile: evidence of phase transformation in the subducted slab. *Science vol 263*, 212–215.

Comte, D. and G. Suárez (1995). Stress distribution and geometry of the subducting Nazca plate in northern Chile using teleseismically recorded earthquakes. *Geophys. J. Int. vol 122*, 419–440.

Conrad, C. P. and B. H. Hager (1999). Effects of plate bending and fault strength at subduction zones on plate dynamics. *J. Geophys. Res. vol 104, no B8*, 17551–17571.

Conrad, C. P. and C. Lithgow-Bertelloni (2002). How mantle slabs drive plate tectonics. *Science vol 298*, 207–209.

Conrad, C. P. and C. Lithgow-Bertelloni (2004). The temporal evolution of plate driving forces: importance of "slab suction" versus "slab pull" during the cenozoic. *J. Geophys. Res. vol 109*, B10407.

Cruciani, C., E. Carminati, and C. Doglioni (2005). Slab dip vs lithosphere age: no direct function. *Earth Planet. Sci. Lett. vol 238*, 298–310.

Dabrowski, M. (2008). personal communication.

Dabrowski, M., M. Krotkiewski, and D. Schmid (2008). Milamin: Matlab-based finite element method solver for large problems. *Geochemistry, Geophysics, Geosystems vol 9*, Q04030.

Dahlen, F. A. (1981). Isostasy and the ambient state of stress in the oceanic lithosphere. *J. Geophys. Res. vol 86, no B9*, 7801–7807.

Deubelbeiss, Y. and B. J. P. Kaus (2008). Comparison of eulerian and lagrangian numerical techniques for the stokes equations in the presence of strongly varying viscosity. *Phys. Earth Planet. Inter. vol 171*.

Dorbath, C., M. Gerbault, G. Carlier, and M. Guirard (2008). Double seismic zone of the nazca plate in northern Chile: High-resolution velocity structure, petrological implications, and thermomechanical modeling. *Geochemistry, Geophysics, Geosystems vol 9, no 7*, Q07006.

Engdahl, E. R. and C. H. Scholz (1977). A double benioff zone beneath the central Aleutians: an unbending of the lithosphere. *Geophys. Res. Lett. vol 4, no 10*.

Forsyth, D. and S. Uyeda (1975). On the relative importance of the driving forces of plate motion. *Geophys. J. R. Astr. Soc. vol 43*, 163–200.

Forte, A. M., W. R. Peltier, and A. M. Dziewonski (1991). Inferences of mantle viscosity from tectonic plate velocities. *Geophys. Res. Lett. vol 18, no 9*, 1747–1750.

Fowler, C. M. R. (2005). *The Solid Earth*. Cambridge University Press.

Fujita, K. and H. Kanamori (1981). Double seimsmic zones and stresses of intermediate depth earthquakes. *Geophys. J. R. Astr. Soc. vol 66*, 131–156.

Goes, S. (2009). personal communication.

Gorbatov, A., G. Suárez, V. Kostoglodov, and E. Gordeev (1994). A double-planed seismic zone in Kamchatka from local and teleseismic data. *Geophys. Res. Lett. vol 21, no 16*, 1675–1678.

Green, H. W. and P. C. Burnley (1989). A new self-organizing mechanism for deep-focus earthquakes. *Nature vol 341*, 733–737.

Green, H. W. and H. Houston (1995). The mechanisms of deep earthquakes. *Annual Review of Earth and Planetary Sciences vol 23*, 169–213.

Green, N. L. and D. L. Harry (1999). On the relationship between subducted slab age and arc basalt petrogenesis, cascadia subduction system, north america. *Earth Planet. Sci. Lett. vol 171*, 367–381.

Grellet, C. and J. Dubois (1982). The depth of trenches as a function of the subduction rate and age of the lithosphere. *Tectonophysics vol 82*, 45–56.

Griffiths, R. W., R. I. Hackney, and R. D. van der Hilst (1995). A laboratory investigation of effects of trench migration on the descent of subducted slabs. *Earth Planet. Sci. Lett. vol 133*, 1–17.

Guest, A., G. Schubert, and C. W. Gable (2003). Stress field in the subducting lithosphere and comparison with deep earthquakes in Tonga. *J. Geophys. Res. vol 108, B6*.

Guest, A., G. Schubert, and C. W. Gable (2004). Stresses along the metastable wedge of olivine in a subducting slab: possible explanation for the Tonga double seismic layer. *Phys. Earth Planet. Inter. vol 141*, 253–267.

Gurnis, M., C. Eloy, and S. Zhong (1996). Free-surface formulation of mantle convection - ii. implications for subduction-zone observables. *Geophys. J. Int. vol 127*, 719–727.

Gurnis, M. and B. Hager (1988). Controls of the structure of subducted slabs. *Nature vol 335*.

Hacker, B. R., G. A. Abers, and S. M. Peacock (2003). Theoretical mineralogy, densities, seismic wave speeds, and $h_2o$ contents. *J. Geophys. Res. vol 108*, 2029.

Hacker, B. R., S. M. Peacock, G. A. Abers, and S. D. Holloway (2003). Subduction factory ii. are intermediate-depth earthquakes in subducting slabs linked to metamorphic dehydration reactions? *J. Geophys. Res. vol 108*, 2030.

Hager, B. H. (1984). Subducted slabs and the geoid: constraints on mantle rheology and flow. *J. Geophys. Res. vol 89, no B7.*

Han, L. and M. Gurnis (1999). How valid are dynamic models of subduction and convection when plate motions are prescribed? *Phys. Earth Planet. Inter. vol 110*, 235–246.

Hasegawa, A., N. Umino, and A. Takagi (1978). Double-planed deep seismic zone and upper-mantle structure in the northeastern Japan arc. *Geophys. J. R. Astr. Soc. vol54*, 43–58.

Hauck, S. A., R. J. Phillips, and A. M. Hofmeister (1999). Variable conductivity: Effects on the thermal structure of subducting slabs. *Geophys. Res. Lett.s vol 26, no 21*, 3257–3260.

Hirth, G. and D. Kohlstedt (2003). Rheology of the upper mantle and the mantle wedge: a view from the experimentalists. *Inside the Subduction Factory: Geophysical Monograph vol 138*, 83–104.

Hirth, G. and D. L. Kohlstedt (1996). Water in the oceanic upper mantle: implications for rheology, melt extraction and the evolution of the lithosphere. *Earth and Planetary Science Letters vol 144*, 93–108.

Hobbs, B. E. and A. Ord (1988). Plastic instabilities: implications for the origin of intermediate and deep focus earthquakes. *J. Geophys. Res. vol 93, no B9*, 10521–10540.

Hofmeister, A. M. (1999). Mantle values of thermal conductivity and the geotherm from phonon lifetimes. *Science vol 283*, 1699–1706.

House, L. S. and K. H. Jacob (1982). Thermal stresses in subducting lithosphere can explain double seismic zones. *Nature vol 295.*

Igarashi, T., T. Matsuzawa, N. Umino, and A. Hasegawa (2001). Spatial distribution of focal mechanisms for interplate and intraplate earthquakes associated with the subducting Pacific plate beneath the northeastern Japan arc: A triple-planed seismic zone. *J. Geophys. Res. vol 106, B2*, 2177–2191.

II, H. W. G. (2007). Shearing instabilities accompanying high-pressure phase transformations and the mechanics of deep earthquakes. *Proc Natl Acad Sci USA vol 104 (22)*, 9133–9138.

Isacks, B. and P. Molnar (1971). Distribution of stresses in the descending lithosphere from a global survey of focal-mechanism solutions of mantle earthquakes. *Reviews of Geophysics and Space Physics vol 9, no 1*, 103–174.

Isacks, B. L. and M. Barazangi (1977). Geometry of Benioff zones: Lateral segmentation and downwards bending of the subducted lithosphere. *Island Arcs, Deep Sea Trenches, and Back-arc Basins, AGU.*

Jarrard, R. D. (1986). Relations among subduction parameters. *Reviews of geophysics vol 24, no 2*, 217–284.

John, T., S. Medvedev, L. H. Rüpke, T. B. Andersen, Y. Y. Podladchikov, and H. Austrheim (2009). Generation of intermediate-depth earthquakes by self-localizing thermal runaway. *Nature Geoscience vol 2*, 137–140.

Kameyama, M., D. A. Yuen, and S. I. Karato (1999). Thermal-mechanical effects of low-temperature plasticity (the Peierls mechanism) on the deformation of a viscoelastic shear zone. *Earth Planet. Sci. Lett. vol 168*, 159–172.

Kanamori, H., D. L. Anderson, and T. H. Heaton (1998). Frictional melting during the rupture of the 1994 Bolivian earthquake. *Science vol 279.*

Kao, H. and W. P. Chen (1994). The double seismic zone in Kuril-Kamchatka: the tale of two overlapping single zones. *J. Geophys. Res. vol 99, B4*, 6913–6930.

Kao, H. and L. G. Liu (1995). A hypothesis for the seismogenesis of a double seismic zone. *Geophys J Int vol 123*, 71–84.

Kao, H. and R. J. Rau (1999). Detailed structures of the subducted Philippine Sea plate beneath northeast Taiwan: a new type of double seismic zone. *J. Geophys. Res. vol 104, no B1*, 1051–1033.

Karato, S., M. R. Riedel, and D. A. Yuen (2001). Rheological structure and deformation of subducted slabs in the mantle transition zone: implications for mantle circulation and deep earthquakes. *Phys. Earth Planet. Inter. vol 127*, 83–108.

Karato, S. I. (2003). *The dynamic structure of the deep earth.* Princeton University Press.

Karato, S. I. and P. Wu (1993). Rheology of the upper mantle: a synthesis. *Science vol 260*, 771–778.

Kaus, B. J. P. and T. W. Becker (2008). A numerical study on the effects of surface boundary condition and rheology on slab dynamics. *GeoMod2008 22-24 September.*

Kaus, B. J. P., Y. Liu, T. W. Becker, D. A. Yuen, and Y. Shi (2009). Lithospheric stress-states predicted from long-term tectonic models: influence of rheology and possible application to Taiwan. *Journal of Asian Earth Sciences vol 36*, 119–134.

Kawakatsu, H. (1986). Downdip tensional earthquakes beneath the Tonga arch: a double seismic zone? *J. Geophys. Res. vol 91, no B6*, 6432–6440.

Kelemen, P. B. and G. Hirth (2007). A periodic shear-heating mechanism for intermediate-depth earthquakes. *Nature vol 446*, 787–790.

King, S. D. and G. Masters (1992). An inversion for radial viscosity structure using seismic tomography. *Geophys. Res. Lett. vol 19, no 15*, 1551–1554.

Kirby, S. (1987). Localized polymorphic phase transformations on high-pressure faults and applications to the physical mechanism of deep earthquakes. *J. Geophys. Res. vol 92, no B13*, 13789–13800.

Kirby, S. (1995). Intraslab earthquakes and phase changes in subducting lithosphere. *Rev. Geophys. vol 33 supplement*.

Kirby, S., W. Durham, and L. Stern (1991). Mantle phase changes and deep-earthquake faulting in subducting lithosphere. *Science vol 252, no 5003*, 216–225.

Kirby, S., E. R. Engdahl, and R. Denlinger (1996). Intermediate-depth intraslab earthquakes and arc volcanism as physical expressions of crustal and uppermost mantle metamorphism in subducting slabs. *AGU Geophysical Monograph Subduction: top to bottom*, 195–214.

Kusznir, N. J. (1977). The distribution of stress with depth in the lithosphere: thermo-rheological and goedynamic constraints. *Phil Trans R Soc London A vol 337 ,pages =*.

Kusznir, N. J. and M. H. P. Bott (1977). Stress concentration in the upper lithosphere caused by underlying visco-elastic creep. *Tectonophysics vol 43*.

Lallemand, S., A. Heuret, and D. Boutelier (2005). On the relationships between slab dip, back-arc stress, upper plate absolute motion, and crustal nature in subduction zones. *Geochemistry, Geophysics, Geosystems vol 6, no 9*, Q09006.

Majumdar, P. (2005). *Computational methods for heat and mass transfer*. Taylor and Francis Group.

Manea, V. and M. Gurnis (2007). Subduction zone evolution and low viscosity wedges and channels. *Earth Planet. Sci. Lett. vol 264*, 22–45.

Marton, F. C., C. R. Bina, S. Stein, and D. C. Rubie (1999). Effects of slab mineralogy on subduction rates. *Geophys. Res. Lett. vol 26*, 119–122.

Marton, F. C., T. J. Shankland, D. C. Rubie, and Y. Xu (2005). Effects of variable thermal conductivity on the mineralogy of subducting slabs and implications for mechanisms of deep earthquakes. *Phys. Earth Planet. Inter. vol 149*, 53–64.

McGuire, J. J. and D. A. Wiens (1995). A double seismic zone in New Britain and the morphology of the Solomon plate at intermediate depths. *Geophys. Res. Lett. vol 22, no 15*, 1965–1968.

McKenzie, D. (1969). Consequenses and causes of plate motions. *Geophys. J. R. Astr. Soc. vol 18*, 1–32.

Mithen, D. P. (1982). Stress amplification in the upper crust and the development of normal faulting. *Tectonophysics vol 83*, 259–273.

Mitrovica, J. X. and A. M. Forte (2004). A new inference of mantle viscosity based upon joint inversion of convection and glacial isostatic adjustment data. *Earth Planet. Sci. Lett. vol 225.*

Molnar, P., D. Freedman, and J. S. F. Shih (1979). Lengths of intermediate and deep seismic zones and temperatures in downgoing slabs of lithosphere. *Geophys. J. R. Astr. Soc. vol 56*, 41–54.

Muller, R. D., W. R. Roest, J. Y. Royer, and J. G. Gahagan (1997). Digital isochrons of the world's ocean floor. *J. Geophys. Res. vol 102, no B2*, 3211–3214.

Muller, R. D., M. Sdrolias, C. Gaina, and W. R. Roest (2008). Age, spreading rates, and spreading asymmetry of the world's ocean crust. *Geochemistry, geophysics, geosystems vol 9*, 18–36.

Nakajima, J., T. Marsuzawa, and A. Hasegawa (2001). Three-dimensional structure of Vp, Vs, and Vp/Vs beneath northeastern Japan: implications for arc magmatism and fluids. *J. Geophys. Res. vol 106, no B10*, 21843–21857.

Norabuena, E., L. Leffler-Griffin, A. Mao, T. Dixon, S. Stein, I. S. Sacks, L. Ocola, and M. Ellis (1998). Space geodetic observations of Nazca-South America convergence across the Central Andes. *Science vol 279*, 358–362.

Ogawa, M. (1987). Shear instability in a viscoelastic material as the cause of deep focus earthquakes. *J. Geophys. Res. vol 92, no B13*, 13801–13810.

Oleskevich, D. A., R. D. Hyndman, and K. Wang (1999). The updip and downdip limits to great subduction earthquakes: thermal and structural models of Cascadia, south Alaska, SW Japan, and Chile. *J. Geophys. Res. vol 104, no B7*, 14965–14991.

Peacock, S. M. (2001). Are the lower planes of double seismic zones caused by serpentine dehydration in subducting oceanic mantle? *Geology vol 29*, 299–302.

Pilger, R. H. (1984). Cenozoic plate kinematics, subduction and magmatism: South American Andes. *J. Geol. Soc. London vol 141*, 793–802.

Piromallo, C., T. W. Becker, F. Funiciello, and C. Faccenna (2006). Three-dimensional instantaneous mantle flow induced by subduction. *Geophys. Res. Lett. vol 33*, L08304.

Plafker, G. (1965). Tectonic deformation associated with the 1964 Alaska earthquake. *Science vol 148.*

Ponko, S. C. and S. M. Peacock (1995). Thermal modelling of the southern Alaska subduction zone: Insight into the petrology of the subducting slab and overlying mantle wedge. *J. Geophys. Res. Vol 100 B11*, 22117–22128.

Raleigh, C. B. (1967). Tectonic implications of serpentinite weakening. *Geophys. J. R. Astr. Soc. vol 14*.

Raleigh, C. B. and M. S. Paterson (1965). Experimental deformation of serpentinite and its tectonic implications. *J. Geophys. Res. vol 70, no 16*.

Ratchkovsky, N. A., J. Pujol, and N. N. Biswas (1997). Stress pattern in the double seismic zone beneath Cook Inlet, south-central Alaska. *Tectonophysics vol 281*, 163–171.

Reddy, J. N. and D. K. Gartling (2001). *The finite element method in heat transfer and fluid dynamics*. CRC Press.

Reyners, M. and P. Robinson (1997). Plate coupling in the northern South Island and southernmost North Island, New Zealand, as illuminated by earthquake focal mechanisms. *J. Geophys. Res. vol 102, no B7*, 15197–15210.

Ricard, Y., C. Vigny, and C. Froidevaux (1989). Mantle heterogeneities, geoid and plate motion: a monte carlo inversion. *J. Geophys. Res. vol 94, no B10*.

Rietbrock, A. and F. Waldhauser (2004). A narrowly spaced double-seismic zone in the subducting Nazca plate. *Geophys. Res. Lett. vol 31*, L10608.

Samowitz, I. R. and D. W. Forsyth (1981). Double seismic zone beneath the Mariana island arc. *J. Geophys. Res. vol 86, no B8*, 7013–7021.

Schellart, W. P. (2004). Kinematics of subduction and subduction-induced flow in the upper mantle. *J. Geophys. Res. vol 109*, B07401.

Schellart, W. P. and N. Rawlinson (2010). Convergent plate margin dynamics: new perspectives from structural geology, geophysics and geodynamic modelling. *Tectonophysics vol 483*, 4–19.

Schmeling, H., A. Y. Babeyko, A. Enns, C. Faccenna, F. Funicello, T. Gerya, G. J. Golcbek, S. Grigull, B. J. P. Kaus, G. Morra, S. M. Schmalholz, and J. van Hunen (2008). A benchmark comparison of spontaneous subduction models - toward a free surface. *Phys. Earth Planet. Inter. vol 171*, 198–223.

Schmid, Dabrowski, Rupke, and Kaus (2008). Introduction to the finite difference method.

Schmid, D. W. and Y. Y. Podladchikov (2002). Muskhelishcili's method applied to elliptical and lubricated circular inclusion in general shear. *E-Collections Contribution, ETH*, 10.3929.

Schubert, G. and D. L. Turcotte (1972). One-dimensional model of shallow-mantle convection. *J. Geophys. Res. vol 77, no 5*, 945–951.

Schubert, G., D. L. Turcotte, and P. Olson (2001). *Mantle convection in the earth and planets.* Cambridge University Press.

Schurr, B., G. Asch, A. Rietbrock, R. Kind, M. Pardo, B. Heit, and T. Monfret (1999). Seismicity and average velocities beneath the Argentine Puna plateau. *Geophys. Res. Lett. vol 26, no 19*, 3025–3028.

Seno, T. and Y. Yamanaka (1996). Double seismic zones, compressional deep trench-outer rise events, and superplumes. *AGU Geophysical Monograph Subduction: Top to Bottom.*

Shewchuck, J. (1996). Triangle: engineering a 2d quality mesh generator and delaunay triangulator. *Applied Computational Geometry vol 1148.*

Silvester, D. J., H. C. Elman, and A. Ramage (2009).

Sleep, N. H. (1979). The double seismic zone in downgoing slabs and the viscosity of the mesosphere. *J. Geophys. Res. vol 84, no B9*, 4565–4571.

Smith, S., J. Knapp, and R. McPherson (1993). Seismicity of the Gorda plate, structure of the continental margin, and an eastward jump of the mendocino triple junction. *J. Geophys. Res. vol 98, no B5*, 8153–8171.

Sobolev, S. V. and A. Y. Babeyko (2005). What drives orogeny in the Andes? *Geology vol 33, no 8*, 617–620.

Stein, C. A. and S. Stein (1992). A model for the global variation in oceanic depth and heat flow with lithspheric age. *Nature vol 359*, 123–129.

Steinberger, B. and R. Holme (2002). An explanation for the shape of earth's gravity spectrum based on viscous mantle flow models. *Geophys. Rese. Lett. vol 29, no 21*, 2019.

Stuwe, K. (2002). *Geodynamics of the Lithosphere.* Springer.

Sykes, L. R. (1966). The seismicity and deep structure of island arcs. *J. Geophys. Res. vol 71*, 2981–3006.

Tackley, P. J. (2000). Mantle convection and plate tectonics: toward an integrated physical and chemical theory. *Science vol 288*, 2002–2007.

Theodoridou, S. (2008). Determination of subducting lithosphere bending and stress distributions from the curvature of wadati-benioff zone seismicity. *PhD thesis.*

Toksoz, M. N. and A. T. Hsui (1978). Numerical studies of back-arc convection and the formation of marginal basins. *Tectonophysics vol 50.*

Turcotte, D. L. and G. Schubert (2002). *Geodynamics*. Cambridge University Press.

Uyeda, S. (1982). Subduction zones: an introduction to comparative subductology. *Tectonophysics 81*, 133–159.

Uyeda, S. and H. Kanamori (1979). Back-arc opening and the mode of subduction. *J. Geophys. Res. vol 84, no B3*, 1049–1061.

Uyeda, S. and A. Miyashiro (1974). Plate tectonics and the Japanese islands: a synthesis. *Geol Soc Am Bull vol 85*, 1159–1170.

van Hunen, J., A. van den Berg, and N. Vlaar (2000). A thermo-mechanical model of horizontal subduction below an overriding plate. *Earth Planet. Sci. Lett. vol 182*, 157–169.

van Keken, P. E., B. Kiefer, and S. M. Peacock (2002). High-resolution models of subduction zones: Implications for mineral dehydration reaction and the transport of water into the deep mantle. *Geochemistry, Geophysics, Geosystems vol 3, no 10*, 1056.

Vassiliou, M. S., B. H. Hager, and A. Raefsky (1984). The distribution of earthquakes with depth and stress in subducting slabs. *J. Geodynamics vol 1*, 11–28.

Wada, I. and K. Wang (2009). Common depth of slab-mantle decoupling: reconciling diversity and uniformity of subduction zones. *Geochemistry, Geophysics, Geosystems vol 10, no 10*, Q10009.

Wada, I., K. Wang, J. He, and R. D. Hyndman (2008). Weakening of the subduction interface and its effects on surface heat flow, slab dehydration, and mantle wedge serpentinization. *J. Geophys. Res. vol 113*, B04402.

Wadati, K. (1928). Shallow and deep earthquakes. *Geophysical Magazine vol 1.*

Wadati, K. (1935). On the activity of deep-focus earthquakes in the japan islands and neighbourhoods. *Geophysical Magazine vol 8.*

Wang, K. (2002). Unbending combined with dehydration embrittlement as a cause for double and triple seismic zones. *Geophys. Res. Lett. vol 29*, 36.

Wdowinski, S. and Y. Bock (1994). The evolution of deformation and topography of high elevated plateaus 2. application to the central Andes. *J. Geophys. Res. vol 99, no B4*, 7121–7130.

Wiens, D. A., J. J. McGuire, and P. J. Shore (1993). Evidence for transformational faulting from a deep double seismic zone in Tonga. *Nature vol 364*, 790–793.

Wiens, D. A., J. J. McGuire, P. J. Shore, M. G. Bevis, K. Draunidalo, G. Prasad, and S. P. Helu (1994). A deep earthquake aftershock sequence and implications for the rupture mechanism of deep earthquakes. *Nature vol 372*, 540–543.

Wiens, D. A. and S. Stein (1983). Age dependence of oceanic intraplate seismicity and implications for lithospheric evolution. *J. Geophys. Res. vol 88, no B8*, 6455–6568.

Wortel, M. J. R. (1984). Spatial and temporal variations in the Andean subduction zone. *J. Geol. Soc. vol 141*, 783–791.

Wortel, R. (1982). Seismicity and rheology of subducted slabs. *Nature vol 296*.

Yamasaki, T. and T. Seno (2003). Double seismic zone and dehydration embrittlement of the subducting slab. *J. Geophys. Res. vol 108, B4*, 2212.

Yoshii, T. (1978). A detailed cross-section of the deep seismic zone beneath northeastern Honshu, Japan. *Tectonophysics 55, issues 3-4*, 349–360.

Zhao, D., A. Hasgawa, and H. Kanamori (1994). Deep structure of Japan subduction zone as derived from local, regional, and teleseismic events. *J. Geophys. Res. vol 99, no B11*, 22313–22329.

Zhong, S. and M. Gurnis (1992). Viscous flow model of a subduction zone with a faulted lithosphere: long and short wavelength topography, gravity and geoid. *Geophys. Res. Lett. vol 19, no 18*, 1891–1894.

Zhong, S. and M. Gurnis (1994). Controls on trench topography from dynamic models of subducted slabs. *J. Geophys. Res. vol 99, no B8*, 15683–15695.

Zhong, S., M. Gurnis, and L. Moresi (1996). Free-surface formulation of mantle convection - i. basic theory and application to plumes. *Geophys J Int vol 127*, 708–718.

Zienkiewicz, O. C., R. L. Taylor, and J. Z. Zhu (2005). *Finite Element Method - Its Basis and Fundamentals (6th Edition)*. Butterworth-Heinemann.